Mesure de l'amplitude de transition b en u et de la phase CKM gamma a l'aide des desintegrations B0 en D0K*0 reconstruites avec l'experience Babar

V. Sordini

LAL 08-59
Juin 2008

THÈSE

présentée le 6 juin 2008
par

Viola Sordini

pour obtenir le grade de
Docteur es sciences
de l'Université Paris XI Orsay
et
Università di Roma La Sapienza

Measurements of $b \to u$ amplitude and CKM weak phase γ using $B^0 \to D^0 K^{*0}$ decays reconstructed with the *BABAR* detector

soutenue devant la commission d'examen composée de:

M.	F.	Ferroni	Directeur de thèse
M.	A.	Jawahery	
M.	J.-P.	Lees	Rapporteur
M.	G.	Martinelli	
M.	O.	Schneider	Rapporteur
M.	A.	Stocchi	Directeur de thèse
M.	G.	Wormser	Président

Contents

Introduction

The Standard Model of elementary particles is the theory that describes three of the four fundamental interactions (the strong, weak and electromagnetic ones) in a coherent framework. This theory gives an excellent description of all the phenomena observed in the particle physics domain up to energies explored by LEP, SLL and Tevatron.

Nonetheless the Standard Model is known to be incomplete, since it does not account for some experimental evidences, such as the presence of dark matter, the fermion masses hierarchy and the quantitative asymmetry between matter and antimatter of the universe. In order to find effects that go beyond the Standard Model theory, needed to explain these missing pieces, it is very important to constraint the Standard Model parameters as precisely as possible.

In the 90's, experiments started to study B physics and thus to test the Standard Model in the fermion sector. With the B-factory experiments having collected data for almost ten years, flavour physics is now in its mature age. A primary main goal of these experiments is to access and test, in an indirect way, the presence of New Physics effects beyond the Standard Model at scales that will be directly accessible only after the start of the Large Hadron Collider experiments. The fermion sector of the Standard Model concerns the masses of the quarks and charged leptons and the quark mixing matrix, named CKM (from the names of N. Cabibbo, M. Kobayashi and T. Maskawa). In the Standard Model, the couplings of weak interactions among quarks are described by this matrix, translating the fact that the quarks that participate to the weak interactions are a linear combination of the mass eigenstates. The CKM matrix contains four free parameters (A, λ, ρ, η), one of which (η) is complex and alone accounts for all the CP violation phenomena in the Standard Model. The unitarity of the CKM matrix can be visualized as a triangle (the Unitarity Triangle) in the (ρ-η) plane, with height given by the value of η. Many quantities depending on ρ and η can be measured and, if the Standard Model is correct, they should give compatible results, within the errors, for these two parameters. To do that, the sides and angles (α, β, γ) of the Unitarity Triangle have to be measured and the B-factories have played a central role in this physics program. In the first part of the thesis (chapters 1, 2) these subjects are detailed and explained.

The main topics of this thesis are the studies of CP violation in the B mesons sector and in particular the measurements of the angle γ of the Unitarity Triangle using data collected with the *BABAR* detector (described in chapter 3). Being the relative weak phase between V_{ub} and V_{cb} elements of the CKM matrix, the angle γ is accessible from the studies of interference between $b \to u$ and $b \to c$ transitions.

The efforts within the scientific community have lead to measurements of the angle γ, from the combination of several different experimental techniques, up to a precision that

was not supposed to be accessible at the B-factories experiments. Despite this fact, this parameter is one of the less precisely known. The reason for that is that the sensitivity to γ is driven by the value of the ratios r between $b \to u$ and $b \to c$ amplitudes for each particular decay mode used for the measurement. The values of these parameters are small and have to be determined on data. In particular, up to now, the angle γ of the Unitarity Triangle has been determined, using different methods, from the study of charged B decays into final states with a neutral $D^{(*)}$ meson and a charged $K^{(*)}$ meson. The present knowledge on γ and the different methods used for its determination are described in chapter 2.

The experimental work presented in this thesis is composed of two measurements of γ and the ratio r, using the decays of neutral B mesons into final states with a neutral D meson and a neutral K^* meson. These decays are less abundant than the charged ones, but the value of the ratio r (called r_S, in these channels) is expected to be larger and thus to give a good sensitivity to γ. The analyses techniques are described in chapter 4.

The neutral B decay channels studied in this thesis are: $B^0 \to \bar{D}^0(D^0)K^{*0}$ with $K^{*0} \to K^+\pi^-$ and similarly $\bar{B}^0 \to D^0(\bar{D}^0)\bar{K}^{*0}$ with $\bar{K}^{*0} \to K^-\pi^+$. The electric charge of the kaons produced in neutral K^* decays identifies unambiguously the flavor of the neutral B mesons allowing for a measurement of γ (chapter 2). In the first analysis presented in this thesis (chapter 5), neutral D mesons are reconstructed into $K^\mp\pi^\pm$, $K^\mp\pi^\pm\pi^0$ and $K^\mp\pi^\pm\pi^\pm\pi^\mp$ final modes and studied with the ADS method, allowing for a determination of r_S.

In the second analysis presented in this thesis (chapter 6), neutral D mesons are reconstructed in three-body CP eigenstate mode $K_s\pi^+\pi^-$ and analysed with the Dalitz technique. This analysis, combined with the ADS one, allows for a first determination of the angle γ using neutral B decays.

In chapter 7, we conclude and we discuss the perspectives of the measurements of γ and r_S from neutral B decays in higher luminosity scenarios.

Chapter 1

CP violation in the Standard Model and the CKM matrix

Symmetries are very important in physics, since they establish relations within quantities in principle uncorrelated. In a field theory described by a Lagrangian $\mathcal{L}$, a transformation is a symmetry of the theory if $\mathcal{L}$ does not change under the transformation. On a generic state, described by a four 4-vector $(t, \vec{x})$, one can define the following operations:

- parity P: $P\ (t, \vec{x}) = (t, -\vec{x})$;
- time inversion T: $T\ (t, \vec{x}) = (-t, \vec{x})$;
- charge conjugation, that transforms a particle in its antiparticle.

Those are discrete symmetries that can be combined, for example the operation *CP* changes a particle in its antiparticle and inverts its momentum and helicity. The transformation *CPT* must be a symmetry for every local field theory [1] and it is confirmed to be conserved by all experimental searches up to now.

There is no experimental evidence that strong and electromagnetic interactions violate C, P or T, while weak interactions violate C and P separately, conserving, in first approximation, their product *CP*. The *CP* violation of the weak interactions has been observed for the first time in 1964 [3] in the study of rare decays in the neutral kaon system and recently observed also in B meson decays, thanks to the data collected by the B-factory experiments.

The Standard Model of elementary particles is the theory that describes in a common framework the strong, electromagnetic and weak interactions. This theory successfully describes all *CP* violation related measurements up to now.

This chapter describes the Standard Model picture of the *CP* violation (1.1), which leads to the Cabibbo-Kobayashi-Maskawa quark mixing matrix (1.2) and the Unitarity Triangle.

1.1 *CP* violation in the Standard Model

The Standard Model describes in a common framework the strong, electromagnetic and weak interactions starting from the elementary particles, that are:

- six leptons (and six antileptons), organized in three families;

$$\begin{pmatrix} \nu_e \\ e \end{pmatrix} \ , \ \begin{pmatrix} \nu_\mu \\ \mu \end{pmatrix} \ , \ \begin{pmatrix} \nu_\tau \\ \tau \end{pmatrix}$$

- six flavors of quarks (and six antiquarks), organized in three generations;

$$\begin{pmatrix} u \\ d \end{pmatrix} \ , \ \begin{pmatrix} c \\ s \end{pmatrix} \ , \ \begin{pmatrix} t \\ b \end{pmatrix}$$

- a *gauge* boson for the electromagnetic interaction, the photon γ;
- three *gauge* bosons for the weak interaction: W^+ , W^- and Z^0;
- eight *gauge* bosons for the strong interaction, the gluons;
- the Higgs boson, H (not yet experimentally observed).

The Standard Model is built on the symmetry group $SU(3)_C \otimes SU(2)_I \otimes U(1)_Y$, where $SU(3)_C$ describes the *color* symmetry of strong interactions, $SU(2)_I$ the *weak isospin* symmetry and $U(1)_Y$ the symmetry under *hypercharge* transformations.

The Lagrangian for this theory will be the sum of the strong interactions term $\mathcal{L}_{QCD}$ and the term that accounts for electroweak interactions $\mathcal{L}_{EW}(SU(2)_I \otimes U(1)_Y)$.

The quarks are organized in multiplets:

$$Q_L^{int.} = \begin{pmatrix} U_L^{int.} \\ D_L^{int.} \end{pmatrix} = (3,2)_{+1/6}$$

$$u_R^{int.} = (3,1)_{+2/3} \ \ d_R^{int.} = (3,1)_{-1/3}$$

and a similar structure holds for the leptons:

$$\Psi_L^{int.} = \begin{pmatrix} \nu_L^{int.} \\ l_L^{int.} \end{pmatrix} = (3,2)_{-1/2}$$

$$l_R^{int.} = (3,1)_{-1} \ \ \nu_R^{int.} = (3,1)_0$$

where, for example, $(3,1)_{-1}$ is a triplet in $SU(3)$ (color) a singlet of weak isospin $SU(2)$ and has hypercharge $Y = Q - I_3 = -1$, $\phi_{L/R}(x) = (1 \mp \gamma_5)\phi(x)$ are the left handed $(1-\gamma_5)$ and right handed $(1+\gamma_5)$ helicity components of the field ϕ.

The electroweak term of the Lagrangian is:

$$\begin{aligned} \mathcal{L}_{EW} = i\{ \, & \overline{Q}_L^{int.}(x)\gamma_\mu \mathcal{D}^\mu Q_L^{int.}(x) + \overline{u}_R^{int.}(x)\gamma_\mu \mathcal{D}^\mu u_R^{int.}(x) + \overline{d}_R^{int.}(x)\gamma_\mu \mathcal{D}^\mu d_R^{int.}(x) + \\ & \overline{\Psi}_L^{int.}(x)\gamma_\mu \mathcal{D}^\mu \Psi_L^{int.}(x) + \overline{\nu}_R^{int.}(x)\gamma_\mu \mathcal{D}^\mu \nu_R^{int.}(x) + \overline{l}_R^{int.}(x)\gamma_\mu \mathcal{D}^\mu l_R^{int.}(x) \ \} \end{aligned}$$

where the covariant derivative $\mathcal{D}^\mu$ is defined by the expression:

$$\mathcal{D}^\mu = \partial^\mu + i\frac{g}{2}\tau_j W_j^\mu + 2ig'Y B^\mu \tag{1.1}$$

g and g' are the coupling constants associated to the gauge fields W_j ($j = 1, 2, 3$) and B (related to the isospin $SU(2)$ and hypercharge $U(1)$ symmetry groups) and τ_j are the Pauli matrices in the $SU(2)_L$ space.

The $W^{\pm}$ bosons are related to the $W_{1,2}$ components of the W_j gauge field, the photon and the Z^0 to the W_3 component and to the B field through the weak angle θ_W [4]). In more detail, for the charged boson one defines the field:

$$W^{\mu+}(x) = \frac{W_1^{\mu} - iW_2^{\mu}}{\sqrt{2}}$$

and its hermitian conjugate, related to W^+ and W^- respectively. For the neutral bosons one can write:

$$\begin{aligned} W_3^{\mu} &= \cos\theta_W Z^{\mu} - \sin\theta_W A^{\mu} \\ B^{\mu} &= -\sin\theta_W Z^{\mu} + \cos\theta_W A^{\mu} \end{aligned}$$

where $\sin^2\theta_W = 0.2326 \pm 0.0008$, Z^{μ} is the field associated to the Z^0 and A^{μ} with the photon.

The following relation holds for the weak angle:

$$\frac{g}{\sin\theta_W} = \frac{g'}{\cos\theta_W} = e$$

with e the positron electric charge.

The Lagrangian can be split into a free theory and an interaction part: $\mathcal{L}_{EW} = \mathcal{L}_0 + \mathcal{L}_I$. The interaction Lagrangian is composed of a charged current term $\mathcal{L}_{CC}$ and a neutral current term $\mathcal{L}_{NC}$.

The charged current term can be written in terms of the observable boson fields:

$$\mathcal{L}_{CC} = \frac{g_W}{2\sqrt{2}} \left(J_{\mu}^{+}(x) W^{\mu}(x) + J_{\mu}^{-}(x) W^{\dagger\mu}(x) \right)$$

where:

$$\begin{aligned} J_{\mu}^{+} = {} & \bar{u}^{int.}\gamma_{\mu}(1-\gamma_5)d^{int.} + \bar{c}^{int.}\gamma_{\mu}(1-\gamma_5)s^{int.} + \bar{t}^{int.}\gamma_{\mu}(1-\gamma_5)b^{int.} + \\ & \bar{\nu}_e^{int.}\gamma_{\mu}(1-\gamma_5)e^{int.} + \bar{\nu}_{\mu}^{int.}\gamma_{\mu}(1-\gamma_5)\mu^{int.} + \bar{\nu}_{\tau}^{int.}\gamma_{\mu}(1-\gamma_5)\tau^{int.} \end{aligned}$$

and the neutral current one:

$$\mathcal{L}_{NC} = eJ_{\mu}^{em}(x)A^{\mu}(x) + \frac{g_W}{2\cos\theta_W} J_{\mu}^{0}(x) Z^{0\mu}(x)$$

where

$$\begin{aligned} J_{\mu}^{em} &= \sum_f Q_f \bar{f}\gamma_{\mu} f \\ J_{\mu}^{0} &= \sum_f \bar{f}\gamma_{\mu}(v_f - a_f\gamma_5) f \\ v_f &= \tau_3^f - 2Q_f \sin^2\theta_W \quad a_f = \tau_3^f \end{aligned}$$

and the index f runs over all the flavors.

Experimentally the W^+, W^- and Z^0 bosons have been observed to have non zero masses. These masses are explained in the theory thanks to the presence of the Higgs field and the spontaneous symmetry breaking mechanism.

The Higgs field is an isospin doublet of complex scalar fields:

$$\Phi = \begin{pmatrix} \phi_+ \\ \phi_0 \end{pmatrix} \quad \tilde{\Phi} = i \cdot \tau_2 \cdot \Phi = \begin{pmatrix} \phi_0^* \\ \phi_- \end{pmatrix}$$

The Lagrangian for the Higgs field is written as follows:

$$\mathcal{D}^\mu \Phi^\dagger \mathcal{D}_\mu \Phi - \mu^2 \Phi^\dagger \Phi - \lambda (\Phi^\dagger \Phi)^2$$

where the covariant derivative is defined in eq. 1.1:

The Higgs field potential ($V(\Phi) = -\mu^2 \Phi^\dagger \Phi - \lambda(\Phi^\dagger \Phi)^2$) has a relative maximum at $\Phi(x) = 0$ and reaches an absolute minimum for all the points belonging to the circle $\Phi(x) = \sqrt{\frac{-\mu^2}{2\lambda}}$. This means that the state of minimum energy, the vacuum state, is not unique but is degenerate. The choice of one of the infinite possible vacuum states implies the spontaneous symmetry breaking, in which some symmetries of the Lagrangian are lost and some of the massless particles acquire a non zero mass.

With the spontaneous breaking, the symmetry group $SU(2)_I \otimes U(1)_Y$ is reduced to $U(1)_Q$ (with Q the electric charge) and the three gauge bosons (W^+, W^- and Z^0) acquire a mass (the photon, related to the electric charge conservation, stays massless).

The choice of the minimum energy state is operated by assigning a non zero expectation value for the Higgs field in the vacuum state. A usual choice is:

$$\langle 0|\Phi|0\rangle = \begin{pmatrix} 0 \\ \frac{v}{\sqrt{2}} \end{pmatrix}$$

with $v = \sqrt{\frac{-\mu^2}{2\lambda}}$.

The mass terms for the $W^\pm$ and Z^0 bosons arise from the kinetic term and the masses have the values $M_W = \frac{vg}{2}$ and $M_Z = \frac{vg}{2cos\theta_W}$.

Leptons and quarks masses arise from the Yukawa coupling terms of leptons and quarks with the Higgs field:

$$\mathcal{L}_M = Y_{ij}^d \, \overline{Q}_{L_i}^{int.} \, \Phi \, d_{R_j}^{int.} + Y_{ij}^u \, \overline{Q}_{L_i}^{int.} \, \tilde{\Phi} \, u_{R_j}^{int.} + Y_{ij}^l \, \overline{L}_{L_i}^{int.} \, \Phi \, l_{R_j}^{int.} + h.c.$$

Writing explicitly the Φ field, one obtains for the quarks:

$$\mathcal{L}_M = M_{ij}^d \, \overline{d}_{L_j}^{int.} \, d_{R_j}^{int.} + M_{ij}^u \, \overline{u}_j^{int.} \, u_{R_j}^{int.} + h.c.$$

where

$$M_{ij}^{u,d} = \frac{Y_{ij}^{u,d} \cdot v}{\sqrt{2}}$$

is the quark mass matrix.

It can be shown that the conservation of the symmetry *CP* is described by the matrix M being real. Any complex term would on the other hand transform under *CP* into its complex conjugate, hence producing *CP* violation. Generally speaking, the M matrix is not diagonal in the weak interaction eigenstates basis (that we have used up to now), since the weak interaction eigenstates are not also mass eigenstates. One can always pass to the mass eigenstates basis simply by diagonalizing the M matrix; this can be done with a pair of unitary matrices, V_L and V_R:

$$\mathcal{M}^{u,d} = V_L^{u,d} M^{u,d} V_R^{u,d}$$

with $\mathcal{M}^f$ diagonal ($f = u,\, d$). These unitary matrices change the interaction eigenstates into mass eigenstates.

$$d_{L_i} = (V_L^d)_{ij} d_{L_j}^{int.} \;\; ; \;\; d_{R_i} = (V_R^d)_{ij} d_{R_j}^{int.}$$
$$u_{L_i} = (V_L^u)_{ij} u_{L_j}^{int.} \;\; ; \;\; u_{R_i} = (V_R^u)_{ij} u_{R_j}^{int.}$$

In the mass eigenstates basis, the Lagrangian mass term is diagonal and the electroweak charged current term becomes:

$$\mathcal{L}_{CC} = i\frac{g}{2}\overline{u}_{L_i}\gamma^\mu (V^u_{L_{ik}} V^{d\dagger}_{L_{kj}}) d_{L_j} \tau_a W^a_\mu .$$

$V = V^u_{L_{ik}} V^{d\dagger}_{L_{kj}}$ being a 3×3 matrix, it can always be parametrized with three Euler angles (real parameters) and six phases (complex parameters). Five of these six phases disappear under transformations that redefine the phase of the quark fields in the quark mass eigenstate basis and leave the diagonal mass matrix unchanged. One of the six phases is irreducible. The presence of this phase accounts for the *CP* violation in the Standard Model.

The choice of operating in the quark mass eigenstates basis has hence moved the *CP* violation description from the mass sector to the electroweak Lagrangian sector, where it is described by the quark mixing matrix $V = V^u_{L_{ik}} V^{d\dagger}_{L_{kj}}$.

This matrix, that is the generalization of the Cabibbo mechanism to the three quark generations case, is know as CKM matrix (from Cabibbo, Kobayashi and Maskawa) [2]:

$$V_{CKM} = V^u_{L_{ik}} V^{d\dagger}_{L_{kj}}$$

1.2 The CKM matrix

The CKM matrix, the unitary matrix that relates the weak interaction eigenstates with the mass eigenstates, can be written as:

$$V_{CKM} = \begin{pmatrix} V_{ud} & V_{us} & V_{ub} \\ V_{cd} & V_{cs} & V_{cb} \\ V_{td} & V_{ts} & V_{tb} \end{pmatrix}$$

where $V_{q_1 q_2}$ is the coupling related to the transition $q_2 \to q_1$. Many parametrizations exist in the literature, the most used are the *standard parametrization* [5], and a generalization of the *Wolfenstein parametrization* [6] as presented in [7].

In the standard parametrization, also used by the Particle Data Group [8], the CKM matrix is written as:

$$V_{CKM} = \begin{pmatrix} c_{12}c_{13} & s_{12}c_{13} & s_{13}e^{-i\delta} \\ -s_{12}c_{23} - c_{12}s_{23}s_{13}e^{i\delta} & c_{12}c_{23} - s_{12}s_{23}s_{13}e^{i\delta} & s_{23}c_{13} \\ s_{12}s_{23} - c_{12}c_{23}s_{13}e^{i\delta} & -s_{23}c_{12} - s_{12}c_{23}s_{13}e^{i\delta} & c_{23}c_{13} \end{pmatrix}$$

where $c_{ij} = \cos\theta_{ij}$ and $s_{ij} = \sin\theta_{ij}$ with θ_{ij} the mixing angles between the different families and δ is the $\mathcal{CP}$ violating phase. Because s_{13} and s_{23} are small and of the order of $O(10^{-3})$ and $O(10^{-2})$ respectively, the standard choice for the four independent parameters is:

$$s_{12} = |V_{us}| \ , \ s_{13} \sim |V_{ub}| \ , \ s_{23} \sim |V_{cb}| \quad \text{and} \quad \delta$$

Starting from the consideration that the mixing angles are small, the Wolfenstein parametrization [6] emphasizes a hierarchy in the magnitudes of the V_{CKM} elements: the ones on the diagonal are of order 1, and the others become smaller the more they are far from the diagonal. In the Wolfenstein parametrization, the matrix elements are the result of an expansion in terms of a small parameter $\lambda = |V_{us}| \sim 0.22$. The four independent parameters are in this case:

$$\lambda \ , \ A \ , \ \rho \quad \text{and} \quad \eta.$$

where η is the *CP* violating phase and the matrix is written:

$$V_{CKM} = \begin{pmatrix} 1 - \frac{\lambda^2}{2} & \lambda & A\lambda^3(\rho - i\eta) \\ -\lambda & 1 - \frac{\lambda^2}{2} & A\lambda^2 \\ A\lambda^3(1 - \rho - i\eta) & -A\lambda^2 & 1 \end{pmatrix} + O(\lambda^4) \tag{1.2}$$

If we define:

$$s_{12} = \lambda \ , \ s_{23} = A\lambda^2 \ , \ s_{13}e^{i\delta} = A\lambda^3(\rho - i\eta) \tag{1.3}$$

to all orders in λ, then

$$\rho = \frac{s_{13}}{s_{12}s_{23}}\cos\delta \ , \ \eta = \frac{s_{13}}{s_{12}s_{23}}\sin\delta$$

and the CKM matrix, as a function of (λ, A, ρ, η), satisfies the unitarity condition exactly. Substituting the expressions given in 1.3 into the standard parametrization one obtains the CKM parameters as Taylor expansions with terms of order $O(\lambda^4)$ and higher orders.

With respect to the Wolfenstein parametrization, given in 1.2, the corrections to diagonal elements and to V_{ts} are of order $O(\lambda^4)$, corrections to V_{cd} and V_{td} are of order $O(\lambda^5)$, while additional terms to V_{us} and V_{cb} only appear at the orders $O(\lambda^7)$ and $O(\lambda^8)$ and the expression for V_{ub} stay unchanged. The main corrections to imaginary parts are $\Delta V_{cd} = -iA^2\lambda^5\eta$ and $\Delta V_{ts} = -iA\lambda^4\eta$.

Thanks to the use of the variables:

$$\overline{\rho} = \rho(1 - \frac{\lambda^2}{2}) \ , \ \overline{\eta} = \eta(1 - \frac{\lambda^2}{2})$$

the orders $O(\lambda^5)$ can be included in the expression of V_{td}

$$V_{td} = A\lambda^3(1 - \bar{\rho} - i\bar{\eta})$$

and the CKM matrix can be expressed as:

$$V_{CKM} = \begin{pmatrix} 1-\frac{\lambda^2}{2}-\frac{\lambda^4}{8} & \lambda & A\lambda^3(\bar{\rho}-i\bar{\eta}) \\ -\lambda+\frac{A^2\lambda^5}{2}(1-2(\bar{\rho}+i\bar{\eta})) & 1-\frac{\lambda^2}{2}-\lambda^4(1/8+A^2/2) & A\lambda^2 \\ A\lambda^3(1-\bar{\rho}-i\bar{\eta}) & -A\lambda^2+\frac{1}{2}A\lambda^4+A\lambda^4(\bar{\rho}+i\bar{\eta}) & 1-\frac{A^2\lambda^4}{2} \end{pmatrix} + O(\lambda^6)$$

1.3 The Unitarity Triangle

The unitarity of the V_{CKM} matrix,

$$V_{CKM}V_{CKM}^{\dagger} = V_{CKM}^{\dagger}V_{CKM} = \mathbf{1},$$

implies several relations between its elements:

$$\sum_{i=1}^{3} V_{ij}V_{ik}^{*} = \delta_{jk} \text{ and } \sum_{j=1}^{3} V_{ij}V_{kj}^{*} = \delta_{ik}.$$

The six independent vanishing relations are listed below:

$$\begin{aligned}
V_{ud}^{*}V_{us} + V_{cd}^{*}V_{cs} + V_{td}^{*}V_{ts} &= 0 \quad \text{(three terms of the order, respectively, } \lambda, \lambda, \lambda^5 \text{) ;} \\
V_{ub}^{*}V_{ud} + V_{cb}^{*}V_{cd} + V_{tb}^{*}V_{td} &= 0 \quad \text{(three terms of the order, respectively, } \lambda^3, \lambda^3, \lambda^3 \text{) ;} \\
V_{us}^{*}V_{ub} + V_{cs}^{*}V_{cb} + V_{ts}^{*}V_{tb} &= 0 \quad \text{(three terms of the order, respectively, } \lambda^4, \lambda^2, \lambda^2) \text{ .} \\
V_{ud}V_{cd}^{*} + V_{us}V_{cs}^{*} + V_{ub}V_{cb}^{*} &= 0 \quad \text{(three terms of the order, respectively, } \lambda, \lambda, \lambda^5 \text{) ;} \\
V_{td}V_{ud}^{*} + V_{ts}V_{us}^{*} + V_{tb}V_{ub}^{*} &= 0 \quad \text{(three terms of the order, respectively, } \lambda^3, \lambda^3, \lambda^3 \text{) ;} \\
V_{cd}V_{td}^{*} + V_{cs}V_{ts}^{*} + V_{cb}V_{tb}^{*} &= 0 \quad \text{(three terms of the order, respectively, } \lambda^4, \lambda^2, \lambda^2) \text{ .}
\end{aligned}$$

Each one of these relations can be represented as a triangle in the $(\overline{\rho}, \overline{\eta})$ plane, where the ones obtained by product of neighboring rows or columns are nearly degenerate. The areas of all these triangles are equal to half of the Jarlskog invariant J, which is a phase convention measurement of *CP* violation, defined by:

$$\mathcal{I}m\{V_{ij}V_{kl}V_{il}^{*}V_{kj}^{*}\} = J \sum_{m,n=1}^{3} \epsilon_{ikm}\epsilon_{jln}$$

where ϵ_{abc} is the antisymmetric tensor. The presence of a non-zero CKM phase, and hence of *CP* violation, requires $J \neq 0$.

Within the six relations, we choose the second one, $V_{ub}^{*}V_{ud} + V_{cb}^{*}V_{cd} + V_{tb}^{*}V_{td} = 0$, whose elements can be determined by B physics measurements. This triangle is particularly attracting from the experimental point of view, since it has all the sides of order λ^3. Dividing all the terms of the relation by $|V_{cb}^{*}V_{cd}|$, one obtains:

$$\frac{V_{ub}^{*}V_{ud}}{V_{cb}^{*}V_{cd}} + 1 + \frac{V_{tb}^{*}V_{td}}{V_{cb}^{*}V_{cd}} = 0$$

which is represented by the triangle in Fig. 1.1.

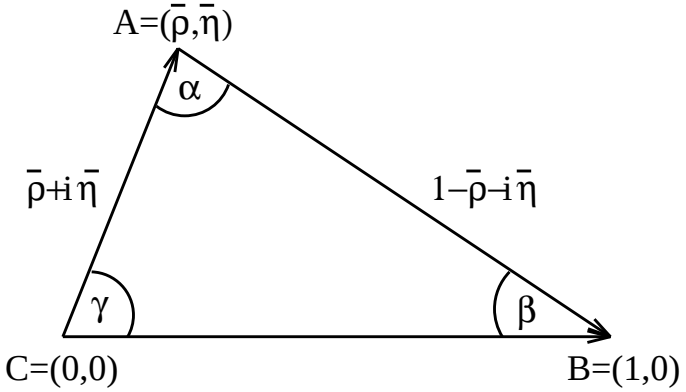

Figure 1.1: Unitarity Triangle, represented in the $(\bar{\rho}, \bar{\eta})$ plane.

The imaginary coordinate of the apex is $\bar{\eta}$, the *CP* violating phase and, as already stated, the presence of *CP* violation, i.e. $\bar{\eta} \neq 0$, is described by the area of the triangle being non-vanishing. The sides of the triangle can be expressed in terms of $\overline{\rho}$ and $\overline{\eta}$:

$$\begin{aligned} \overline{AC} &= R_b = \frac{|V_{ub}^* V_{ud}|}{|V_{cb}^* V_{cd}|} = \sqrt{\overline{\rho}^2 + \overline{\eta}^2} \\ \overline{AB} &= R_t = \frac{|V_{tb}^* V_{td}|}{|V_{cb}^* V_{cd}|} = \sqrt{(1-\overline{\rho})^2 + \overline{\eta}^2}, \end{aligned}$$

and each angle is the relative phase between two adjacent sides:

$$\begin{aligned} \alpha &= \arg\Big[\frac{V_{ub}^* V_{ud}}{V_{tb}^* V_{td}}\Big] \\ \beta &= \arg\Big[\frac{V_{tb}^* V_{td}}{V_{cb}^* V_{cd}}\Big] \\ \gamma &= \arg\Big[\frac{V_{cb}^* V_{cd}}{V_{ub}^* V_{ud}}\Big]. \end{aligned}$$

In the Wolfenstein parametrization the only complex elements, up to terms of order $O(\lambda^5)$, are V_{ub} and V_{td} and the phases γ and β can be directly related to them:

$$V_{td} = |V_{td}| e^{-i\beta} \quad , \quad V_{ub} = |V_{ub}| e^{-i\gamma}.$$

The angles of the Unitarity Triangle, or quantities strictly related to them, are accessible by different experimental techniques.

1.4 Numerical Unitarity Triangle analysis

Various methods have been proposed for the data statistical treatment to obtain the combined constraint on the $\bar{\rho} - \bar{\eta}$ plane from the different results: we refer here to the Bayesian method. In this method, the probability density functions (*pdf*) for the free parameters that

have to be determined are written in terms of quantities that are either experimentally measured or theoretically calculated. With a simulation procedure (called Toy Monte Carlo) a large sample is extracted for the free parameters and to each extraction a weight is assigned. The extractions are made in reasonable intervals and following homogeneous *a-priori* distributions. The weight for each extraction is given by $e^{-\prod_i f_i}$, where f_i are the experimental *pdf* for the measured quantities; in other words the result of each extraction is considered more or less likely, depending on the agreement of the corresponding measured quantities with the actual experimental results.

In this way an *a-posteriori pdf* for each parameter is obtained, generally different from the *a-priori* one, because of the weighting procedure. More details on the Bayesian approach to Unitarity Triangle fits are given in [9].

Several measurements, resulting in different constraints on the $\bar{\rho} - \bar{\eta}$ plane, are included in the Unitarity Triangle analysis:

- $|V_{ub}|$ **and** $|V_{cb}|$
  B mesons can decay through the $b \to c$ and $b \to u$ transitions. Semileptonic decays offer a relatively large branching fraction ($\simeq 10$ %) and corresponding measurements can be interpreted using a well established theoretical framework. The relative rate of charmless over charmed b-hadron semileptonic decays is proportional to the square of the ratio:
  $$\frac{|V_{ub}|}{|V_{cb}|} = \frac{\lambda}{1 - \frac{\lambda^2}{2}} \sqrt{\bar{\rho}^2 + \bar{\eta}^2} \ , \tag{1.4}$$
  and it allows to measure the length of the side AC of the Unitarity triangle.

- Δm_d
  In the Standard Model, $B^0 - \bar{B}^0$ oscillations occur through a second-order process, a box diagram, with a loop that contains W and up-type quarks. The box diagram with the exchange of a *top* quark gives the dominant contribution. The time oscillation frequency, which can be related to the mass difference between the light and heavy mass eigenstates of the $B_d^0 - \overline{B_d^0}$ system, is expressed, in the SM, as[1]:
  $$\Delta m_d \ = \ \frac{G_F^2}{6\pi^2} m_W^2 \ \eta_b S(x_t) \ A^2\lambda^6 \ [(1-\bar{\rho})^2 + \bar{\eta}^2] \ m_{B_d} \ f_{B_d}^2 \hat{B}_{B_d} \ , \tag{1.5}$$
  where $S(x_t)$ is the Inami-Lim function [12] and $x_t = m_t^2/M_W^2$, m_t is the top quark mass and η_b is the perturbative QCD short-distance NLO correction. The scale for the evaluation of those corrections entering into η_b and the running of the t quark mass have to be defined in a consistent way. The value of $\eta_b = 0.55 \pm 0.01$ has been obtained in [13] and, in order to be consistent, the measured value of the pole top quark mass, obtained by CDF and D0 collaborations, $m_t = (172.6 \pm 1.4)\,\mathrm{GeV}/c^2$ [14], has to be corrected downwards by $(7 \pm 1)\,\mathrm{GeV}/c^2$.

  The remaining factor, $f_{B_d}^2 \hat{B}_{B_d}$, encodes the information of non-perturbative QCD. The constant f_{B_d} translates the size of the B meson wave function at the origin. The bag factor $\hat{B}_{B_d}$ is also introduced to take into account all possible deviation from vacuum

[1] Δm_q is usually expressed in ps^{-1} unit. 1 ps^{-1} corresponds to 6.58 10^{-4} eV.

saturation approximation. The values of the non-perturbative QCD parameters f_{B_d}, $\hat{B}_{B_d}$ are obtained from lattice QCD calculations. The measurement of Δm_d gives a constraint on the length of the side AB of the Unitarity Triangle.

- $\Delta m_d/\Delta m_s$
  The $B_s^0 - \overline{B_s^0}$ time oscillation frequency, which can be related to the mass difference between the light and heavy mass eigenstates of the $B_s^0 - \overline{B_s^0}$ system, is proportional to the square of the $|V_{ts}|$ element. Neglecting terms of order $O(\lambda^4)$, $\mid V_{ts} \mid$ is independent of $\bar{\rho}$ and $\bar{\eta}$. The measurement of Δm_s then give a strong constraint on the non-perturbative QCD parameter $f_{B_s}^2 \hat{B}_{B_s}$. The ratio between the values of the mass difference between the mass eigenstates measured in the B_d and in the B_s systems can be used in the Unitarity Triangle analyses:

$$\frac{\Delta m_d}{\Delta m_s} = \frac{m_{B_d} f_{B_d}^2 \hat{B}_{B_d}}{m_{B_s} f_{B_s}^2 \hat{B}_{B_s}} \left(\frac{\lambda}{1-\frac{\lambda^2}{2}}\right)^2 \frac{(1-\bar{\rho})^2 + \bar{\eta}^2}{\left(1 + \frac{\lambda^2}{1-\frac{\lambda^2}{2}}\bar{\rho}\right)^2 + \lambda^4 \bar{\eta}^2} \,. \tag{1.6}$$

  Using the ratio $\frac{\Delta m_d}{\Delta m_s}$, instead of Δm_d and Δm_s separately, exploits the fact that $\xi = f_{B_s}\sqrt{\hat{B}_{B_s}}/f_{B_d}\sqrt{\hat{B}_{B_d}}$ is better determined from lattice QCD than the individual quantities entering into its expression. The measurement of the ratio $\Delta m_d/\Delta m_s$ gives a similar type of constraint as Δm_d, on the length of the side AB of the Unitarity triangle.

- ϵ_K
  Indirect *CP* violation in the $\mathrm{K}^0 - \overline{K^0}$ system is usually expressed in terms of the ϵ_K parameter, which is the fraction of *CP*-violating component in the mass eigenstates. In the SM, the following equation is obtained

$$\begin{aligned} \epsilon_K &= C_\varepsilon \; A^2 \lambda^6 \; \bar{\eta} \times \\ &\left[-\eta_1 S(x_c) \left(1 - \frac{\lambda^2}{2}\right) + \eta_2 S(x_t) A^2 \lambda^4 \left(1 - \bar{\rho}\right) + \eta_3 S(x_c, x_t) \right] \hat{B}_K \end{aligned} \tag{1.7}$$

  where $C_\varepsilon = \frac{G_F^2 f_K^2 m_K m_W^2}{6\sqrt{2}\pi^2 \Delta m_K}$. $S(x_i)$ and $S(x_i, x_j)$ are the appropriate Inami-Lim functions [12] depending on $x_q = m_q^2/m_W^2$, including the next-to-leading order QCD corrections [13, 15, 10]. An important theoretical uncertainty comes from the non-perturbative QCD bag parameter $\hat{B}_K$, that is evaluated from lattice QCD calculations. The constraint brought by the measurement of ϵ_K corresponds to an hyperbola in the $(\bar{\rho}, \bar{\eta})$ plane.

- ***CP* violation measurements in the B sector**
  The advent of the B-factories has allowed the measurement of many observables related to the Unitarity Triangle angles. The studied decays and constrained quantities are briefly listed below.

  - $\sin 2\beta$, the first *CP*-violating quantity measured by the B-factories that is now a precision measurement, can be determined from the mixing induced *CP* asymmetry in $b \to c\bar{c}s$ decays. The golden observable is $A_{J/\Psi K^0}$ in $B_d^0 \to J/\Psi K_S(K_L)$ decays, which has a very small theoretical uncertainty.

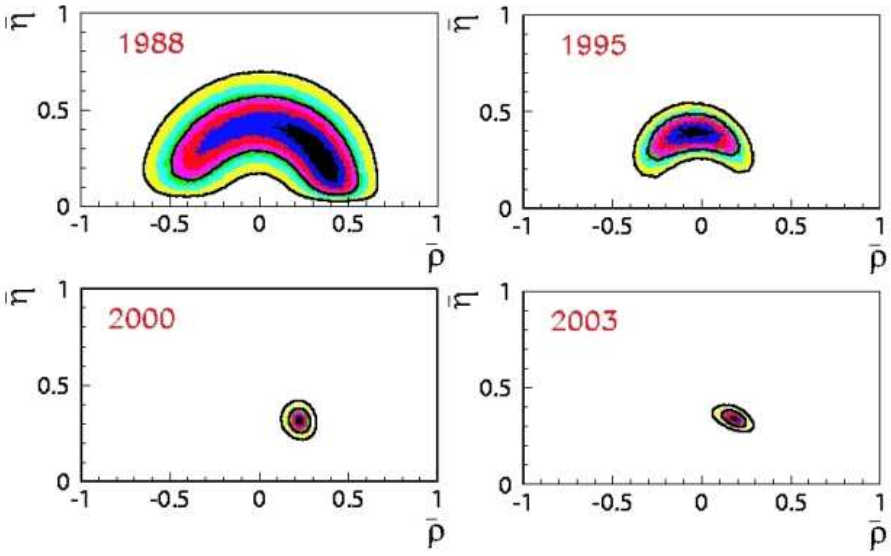

Figure 1.2: Selected regions for $(\overline{\rho}, \overline{\eta})$ from the Unitarity Triangle analysis during the years.

- the angle α is constrained by the study of $B \to \pi\pi$, $B \to \rho\rho$ and $B \to \rho\pi$ decays.
- the angle γ, the main topic of this thesis, is measured in several $B \to DK$ decays.
- the combination of Unitarity Triangle angles $2\beta + \gamma$, is constrained using $B^0 \to D\pi$, $B^0 \to D^*\pi$, $B^0 \to D\rho$ and $B^0 \to DK^0\pi$ decays;
- $\cos 2\beta$ or directly the angle β, can be determined from $B \to J/\psi K^{*0}(K_S\pi^0)$ and $B^0 \to D^0\rho^0$ decays. These measurements do not give a very precise measurement of the phase β, but are useful in removing the ambiguity between β and $\pi/2 - \beta$ coming from the measurement of $\sin 2\beta$.

If these observables were determined with infinite precision, they would be represented by a curve in the $\bar{\rho} - \bar{\eta}$ plane. Assuming the validity of the Standard Model, all these curves would intersect in one point, $(\overline{\rho}, \overline{\eta})$: the apex of the Unitarity Triangle. In real life, these measured quantities are known with experimental and theoretical errors and each constraint results, not in a curve, but in a region on the $\bar{\rho} - \bar{\eta}$ plane. The Unitarity Triangle analyses determines the region in which the apex of the Unitarity Triangle has to be with a given probability.

The increasing precision of the measurements and of the theoretical calculations in the last twenty years, significantly improved the knowledge on the allowed region for the apex position $(\overline{\rho}, \overline{\eta})$ (Fig. 1.2).

The measurements of *CP*-violating quantities from the *B*-factories are nowadays so abundant and precise that the CKM parameters can be constrained using only the determination of the Unitarity Triangle angles, as can be seen in Fig. 1.3, right plot. On the other hand, an independent determination can be obtained using experimental information on *CP*-conserving processes ($\frac{|V_{ub}|}{|V_{cb}|}$ from semileptonic B decays, Δm_d and Δm_s from the $B_d - \bar{B}_d$ and

$B_s - \bar{B}_s$ oscillations) and the direct CP violation measurements in the kaon sector, ϵ_K (see Fig. 1.3, left plot). This was indeed the strategy used to predict the value of $\sin 2\beta$ before the precise *BABAR* and Belle measurements [16].

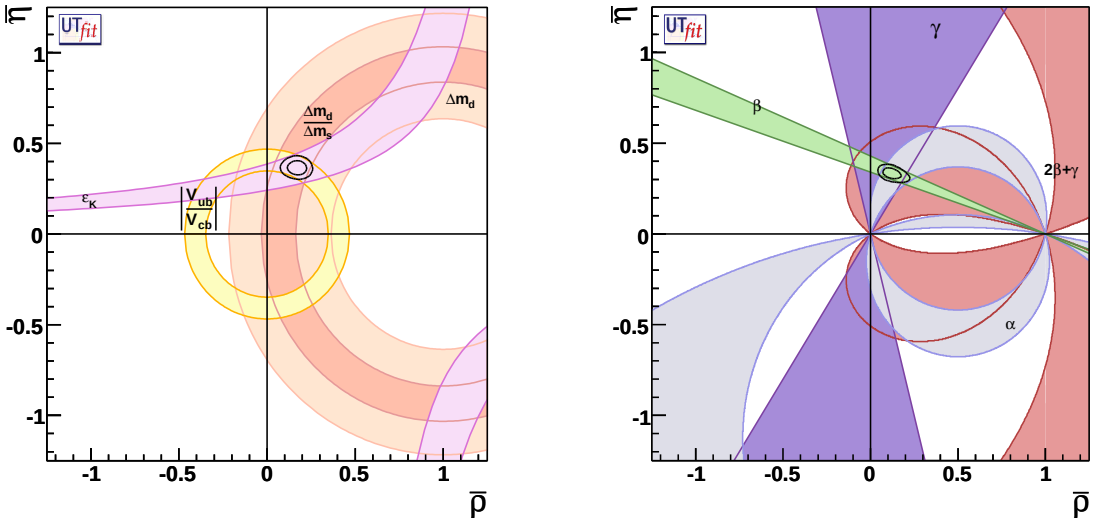

Figure 1.3: Allowed regions for $\overline{\rho}-\overline{\eta}$, as given by the measurement of $|V_{ub}|/|V_{cb}|$, Δm_d, Δm_s and ϵ_K (left plot) and as given by the measurements of the angles α, $\sin 2\beta$, γ, $2\beta+\gamma$, β and $\cos 2\beta$ (right plot). The closed contours show the 68% and 95% probability regions for the triangle apex, while the colored zones are the 95% probability regions for each constraint. The experimental values are updated using results presented at the 2008 winter conferences.

In Fig. 1.4, we show the allowed regions for $\bar{\rho}$ and $\bar{\eta}$, as given by all the available measurements. Numerical results are summarized in Tab. 1.1.

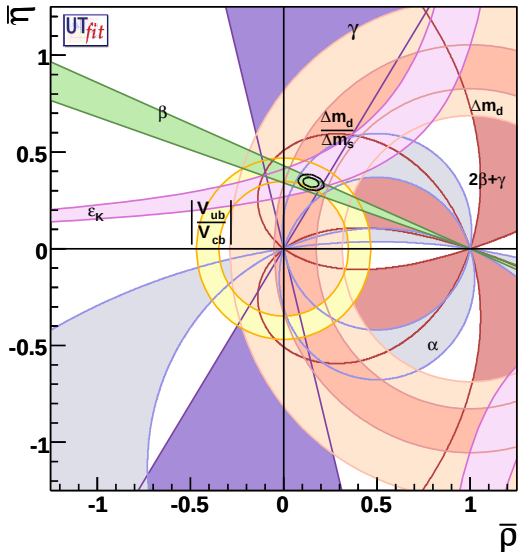

Figure 1.4: Allowed regions for $\overline{\rho}-\overline{\eta}$, as given by $|V_{ub}|/|V_{cb}|$, Δm_d, Δm_s, ϵ_K, α, $\sin 2\beta$, γ, $2\beta+\gamma$, β and $\cos 2\beta$. The closed contours show the 68% and 95% probability regions for the triangle apex, while the colored zones are the 95% probability regions for each constraint. The experimental values are updated using results presented at the 2008 winter conferences.

Parameter	68% probability	95% probability
$\overline{\rho}$	0.146 ± 0.028	[0.092,0.202]
$\overline{\eta}$	0.342 ± 0.016	[0.311,0.374]
$\alpha[^\circ]$	91.1 ± 4.3	[82.9,99.8]
$\beta[^\circ]$	21.8 ± 0.9	[20.0,23.7]
$\gamma[^\circ]$	66.8 ± 4.4	[58.1,75.2]

Table 1.1: 68% and 95% probability regions for the Unitarity Triangle parameters, obtained with the experimental values updated to the 2008 winter conferences results.

Other Unitarity Triangle analyses use a frequentistic approach, based on a χ^2 minimization [17] or scanning methods [18].

1.5 Search for New Physics: looking for discrepancies

As a general fact, as it can be seen in Fig. 1.4, the Standard Model description of *CP* violation through the CKM mechanism appears as a very successful framework, able to account for

all the measured observables up to the current precision. In this situation, any effect from physics beyond the Standard Model should appear as a correction to the CKM picture.

The agreement of all the measured quantities is somehow quantified in the so called *compatibility plots* [19], in which the comparison between indirect parameter determinations and their direct experimental measurement can be used as a test for the Standard Model description of flavour physics. The indirect determination of a particular quantity obtained performing the Unitarity Triangle complete fit, including all the available constraints except from the direct measurement of the parameter of interest, gives a prediction of the quantity based on formulas which are valid in the Standard Model. The comparison between this prediction and a direct measurement can thus quantify the agreement of the single measurement with the overall fit and possibly reveal new physics phenomena.

In Unitarity Triangle fits based on a χ^2 minimization, a conventional evaluation of compatibility stems automatically from the value of the χ^2 at its minimum. The compatibility between constraints in the Bayesian approach is simply done by comparing two different p.d.f.'s.

Let us consider, for instance, two p.d.f.'s for a given quantity obtained from the Unitarity Triangle fit, $f(x_1)$, and from a direct measurement, $f(x_2)$: their compatibility is evaluated by constructing the p.d.f. of the difference variable, $x_2 - x_1$, and by estimating the distance of the most probable value from zero in units of standard deviations. The latter is done by integrating this p.d.f. between zero and the most probable value and converting it into the equivalent number of standard deviations for a Gaussian distribution [1]. The advantage of this approach is that no approximation is made on the shape of p.d.f.'s. In the following analysis, $f(x_1)$ is the p.d.f. predicted by the Unitarity Triangle fit while the p.d.f of the measured quantity, $f(x_2)$, is taken Gaussian for simplicity. The number of standard deviations between the measured value, $\bar{x}_2 \pm \sigma(x_2)$, and the predicted value (distributed according to $f(x_1)$) is plotted as a function of $\bar{x}_2$ (x-axis) and $\sigma(x_2)$ (y-axis). The compatibility between x_1 and x_2 can be then directly estimated on the plot, for any central value and error of the measurement of x_2.
The compatbility plots for α, $\sin 2\beta$, γ and Δm_s are shown in Fig. 1.5. The direct values obtained for α and Δm_s are in very good agreement, within 1σ, with the indirect determination, although for the latter the effectiveness of the comparison is limited by the precision on the theoretical inputs, inducing a big error (compared to the experimental one) on the prediction from the rest of the fit.

The determination of γ from direct measurement yields a value slightly higher, $(80 \pm 13)^o$, than the indirect one from the overall fit, $(65 \pm 7)^o$; the two determinations are compatible within 1σ.

We also observe that the direct determination for $\sin 2\beta$ from the measurement of the *CP* asymmetry in $B^0 \to J/\psi K^0$ is slightly shifted, with respect to the indirect determination, still being compatible with it within 2σ. This effect is visually evident in Fig. 1.6, left, where the 68% and 95% probability regions for $\bar{\rho}$ and $\bar{\eta}$, as given by $|V_{ub}|/|V_{cb}|$, Δm_d, Δm_s and ϵ_K are compared with the 95% probability regions given by the measurements of angles.

[1] In the case of Gaussian distributions for both x_1 and x_2, this quantity coincides with the pull, which is defined as the difference between the central values of the two distributions divided by the sum in quadrature of the r.m.s of the distributions themselves.

This slight tension in the Unitarity Triangle fit has been studied in the latest years [20] and can be related to the fact that the present experimental measurement of $\sin 2\beta$ favours a value of $|V_{ub}|$ that is more compatible with the direct determination of $|V_{ub}|$ using exclusive methods rather than the one obtained using the inclusive ones. In Fig. 1.6, right, we show the compatibility separately for the exclusive and the inclusive direct determination of $|V_{ub}|$.

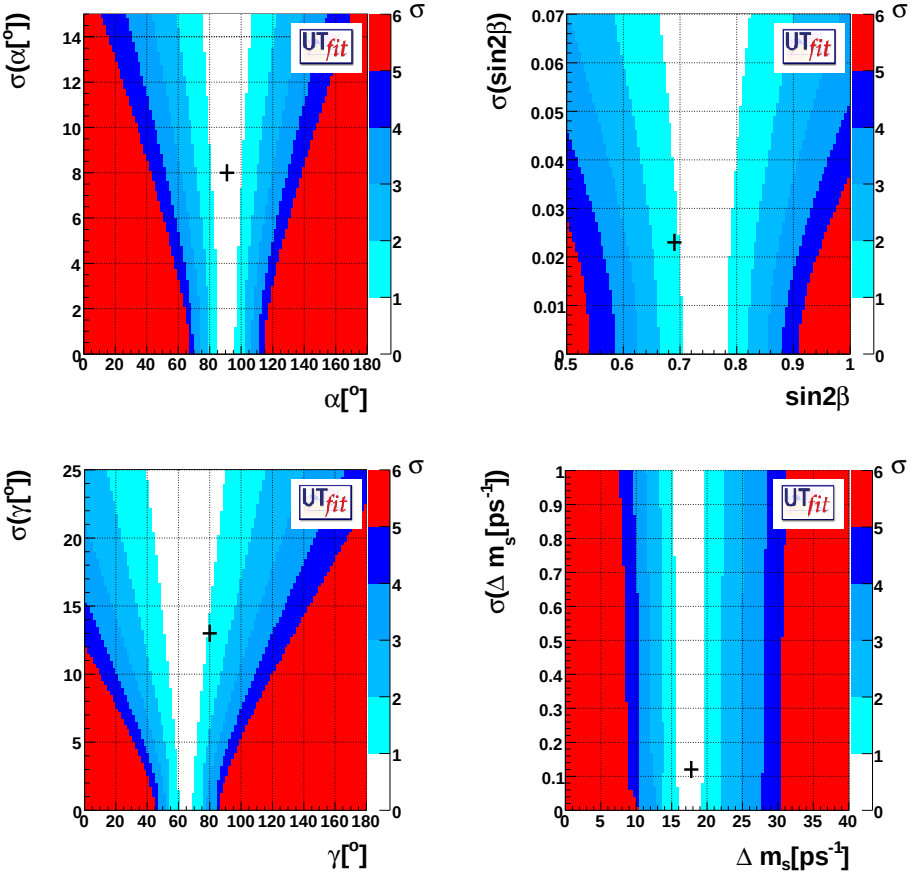

Figure 1.5: Compatibility plots for α, $\sin 2\beta$, γ and Δm_s. The color code indicates the compatibility between direct and indirect determinations, given in terms of standard deviations, as a function of the measured value and its experimental uncertainty. The crosses indicate the direct world average measurement values respectively for α, $\sin 2\beta$ from the measurement of the CP asymmetry in $B^0 \to J/\psi K^0$, γ and Δm_s.

In conclusion, it is interesting to monitor the compatibility of each single measurement with the overall Unitarity Triangle fit, because any effect from new physics beyond the Standard Model, would appear as a disagreement in such comparisons. Given the present experimental measurements, no significant deviation from the CKM picture is observed.

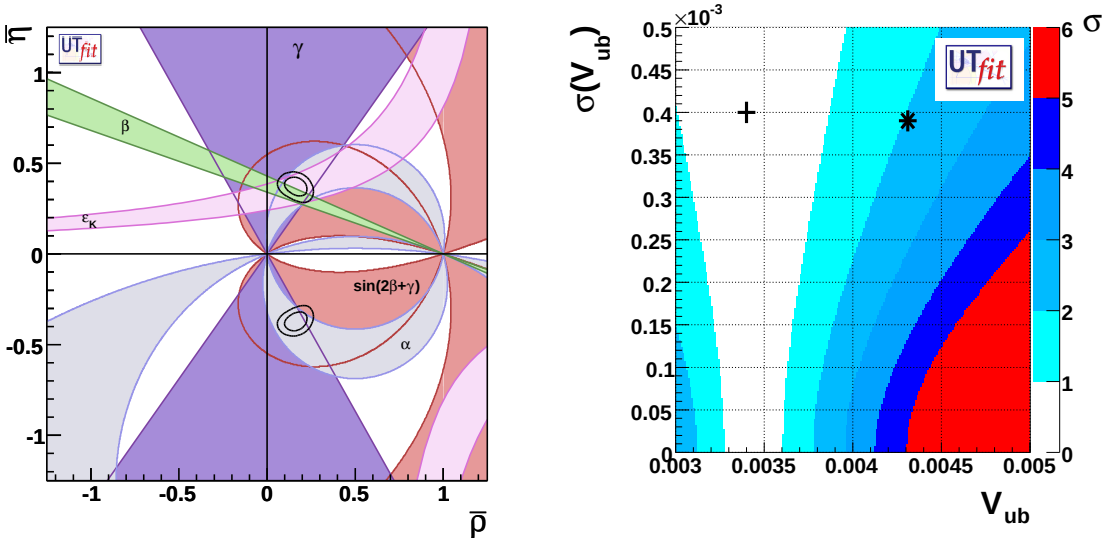

Figure 1.6: Left plot: allowed regions for $\bar{\rho}$ and $\bar{\eta}$ obtained by using the measurements of $|V_{ub}|/|V_{cb}|$, Δm_d, Δm_s and ϵ_K. The coloured zones indicate the 68% and 95% probability regions for the angles measurements, which are not included in the fit. Right plot: compatibility plot for V_{ub}. The color code indicates the compatibility between direct and indirect determinations, given in terms of standard deviations, as a function of the measured value and its experimental uncertainty. The cross and the star indicate the exclusive and inclusive measurement values respectively

Chapter 2

Measurements of the angle γ of the Unitarity Triangle

In the Wolfenstein parametrization, γ is the weak phase of the CKM element $V_{ub}^* = |V_{ub}|e^{i\gamma}$.

Several methods aim to access this phase exploiting the interference between $b \to u$ and $b \to c$ transitions in $B \to DK$ decays. After a brief introduction (sec. 2.1) on $B \to DK$ phenomenology, in section 2.2 the common characteristics of γ measurements in $B \to DK$ decays are presented. In sections 2.2.1, 2.2.2 and 2.2.3, the different experimental methods are described. The present knowledge of γ comes from the combination of several analyses of charged $B \to DK$ channels using all these methods. These results are listed in section 2.3, where the current constraint on γ, from their combination, is also shown.

The work presented in this thesis concerns measurements of γ in neutral $B \to DK$ decays, that are introduced in section 2.6.

Some analyses also try to measure γ from charmless B decay, where $b \to u$ transitions appear in *penguin* diagrams, making use of the $SU(3)$ symmetry. In this thesis, these methods will not be discussed.

2.1 Phenomenology of $B \to DK$ decays

The amplitudes for the $B \to DK$ decays of interest can be expressed as:

$$\begin{aligned}
&A\left(B^+ \to \overline{D}^0 K^+\right) = V_{us}\, V_{cb}^*(T + C)\ ; \\
&A\left(B^0 \to \overline{D}^0 K^0\right) = V_{us}\, V_{cb}^* C\ ; \\
&A\left(B^+ \to D^0 K^+\right) = V_{cs}\, V_{ub}^*(\bar{C} + A)\ ; \\
&A\left(B^0 \to D^0 K^0\right) = V_{cs}\, V_{ub}^* \bar{C}\ .
\end{aligned}$$

where T, C, $\bar{C}$ and A refer to the *tree*, *color-suppressed* and *annihilation* topologies respectively. In Fig. 2.1 and 2.2, the possible diagrams for the $B^+ \to \overline{D}^{(*)0} K^{(*)+}$ and $B^0 \to \overline{D}^{(*)0} K^{(*)0}$ respectively are shown. In the amplitudes we have written for the charged $B \to DK$ decays, the T parameter will account for the *tree* diagram (a), C and $\bar{C}$ for the *color-suppressed* diagrams (b) and (c) respectively and A for the (d) *annihilation* diagram.

For the neutral $B \to DK$ decays, both the diagrams for the $b \to c$ and $b \to u$ transitions are *color-suppressed* and their amplitudes are described by the C and $\bar{C}$ parameters respectively.

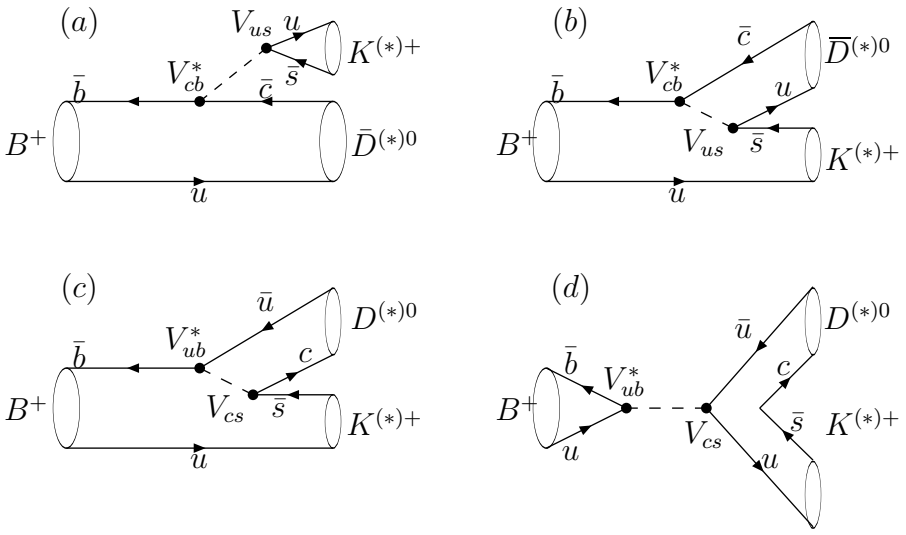

Figure 2.1: Feynman diagrams for the decay $B^+ \to \overline{D}^{(*)0} K^{(*)+}$ (a and b) and $B^+ \to D^{(*)0} K^{(*)+}$ (c and d).

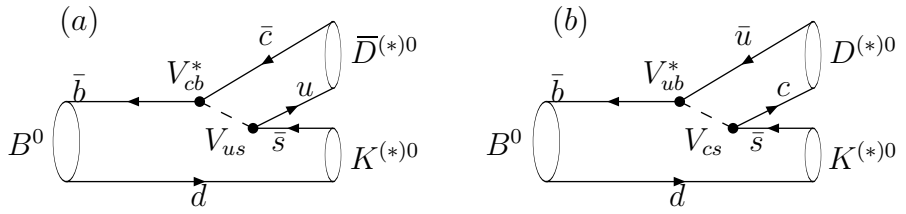

Figure 2.2: Feynman diagrams for the decays $B^0 \to \overline{D}^{(*)0} K^{(*)0}$ (a) and $B^0 \to D^{(*)0} K^{(*)0}$ (b).

This parametrization, with the different contributions arising from the diagrams shown in fig 2.1 and 2.2, is often used but it is not exact. The correct treatment, exploits the fact that the non leptonic two-body decays of the B mesons can be described in the Standard Model using the *Operator Product Expansion* (**OPE**) and the renormalization group techniques [10]. In this formalism, the B decays are described with an effective hamiltonian and the amplitude for a B decaying into a final state f is expressed by:

$$\begin{aligned} A(B \to f) &= \langle f|H_{eff}|B\rangle = \\ &= \frac{G_F}{\sqrt{2}} \cdot \sum_i V_i^{CKM} C_i(\mu) \langle f|Q_i(\mu)|B\rangle \end{aligned}$$

where Q_i are local operators that have the right quantum numbers to describe the particular transition. Each operator contributes to the Hamiltonian with a weight given by the product

of the CKM factors V_i^{CKM} and Wilson coefficients $C_i(\mu)$. G_F is the Fermi constant, expressed by $\frac{G_F}{\sqrt{2}} = \frac{g_W}{8 \cdot M_W^2}$, and its value is $G_F = 1.16639(9) \cdot 10^{-5} GeV^{-2}$.

The scale μ marks the separation between *long distance* contributions (the ones arising from energies higher than the scale μ), contained in the Wilson coefficients $C_i(\mu)$ and *short distance* contributions (relative to energy scales lower than μ), described by the hadronic matrix elements $\langle f|Q_i(\mu)|B\rangle$. The μ scale is arbitrary, but its value is normally assumed to be of the order of the b quark mass ($\mu = 4.3\frac{GeV}{c^2}$). The dependence of the Wilson coefficients on this μ scale and on the renormalization scheme has to compensate the hadronic matrix elements one in such a way that the physical amplitudes do not show any dependence on the choice of the scale. This cancellation of the dependence is limited by the order at which the Wilson coefficients are calculated in perturbation theory.

Generally speaking, in order to describe the $B \to DK$ decays, eight operators are needed and the effective hamiltonian can be written as:

$$\begin{aligned} H_{eff} &= \frac{G_F}{\sqrt{2}} \cdot \{V_{ub}^* V_{cs} \cdot [C_1(\mu) Q_1^{scu}(\mu) + C_2(\mu) Q_2^{scu}(\mu)] + \\ &+ V_{cb}^* V_{us} \cdot [C_1(\mu) Q_1^{suc}(\mu) + C_2(\mu) Q_2^{suc}(\mu)] + \\ &+ V_{ub}^* V_{cd} \cdot [C_1(\mu) Q_1^{dcu}(\mu) + C_2(\mu) Q_2^{dcu}(\mu)] + \\ &+ V_{cb}^* V_{ud} \cdot [C_1(\mu) Q_1^{duc}(\mu) + C_2(\mu) Q_2^{duc}(\mu)]\} \end{aligned} \tag{2.1}$$

where the Q_1 and Q_2 operators are called *current-current operators* and are defined by:

$$\begin{aligned} Q_1^{d_i u_j u_k} &= (\bar{b} u_k)_{V-A} (\bar{u_j} d_i)_{V-A} \\ Q_2^{d_i u_j u_k} &= (\bar{b} d_i)_{V-A} (\bar{u_j} u_k)_{V-A}. \end{aligned}$$

The fact that, in the $B \to DK$ channels used to measure γ, there are no penguin contributions can be seen from the expression of the *current-current operators*, where the currents are never expressed by two quarks of the same flavor ($q\bar{q}$), since all the four quarks on the final state have different flavor.

The Wilson coefficients can be calculated with perturbative techniques, while there is not yet an agreement, within the theoretical community, on how to calculate the hadronic matrix elements and different approaches have been proposed. In the approach called factorization, the hadronic matrix elements are calculated as product of weak currents matrix elements, expressed in terms of form factors and decay constants of the interested mesons.

As an example, the matrix element

$$\langle D^- K^+ | (\bar{b} c)_{V-A} (\bar{u} s)_{V-A} | B^0 \rangle$$

is expressed in factorization as

$$\langle D^- K^+ | (\bar{b} c)_{V-A} (\bar{u} s)_{V-A} | B^0 \rangle = \langle D^- | (\bar{b} c)_{V-A} | B^0 \rangle \cdot \langle K^+ | (\bar{u} s)_{V-A} | 0 \rangle \tag{2.2}$$

where the process is split into two different subprocesses: the B meson decay into a D meson (described by the form factor $F^{B \to D}$), and a kaon created from the vacuum (described by the kaon decay constant f_K).

An intuitive way of explaining the factorization hypothesis is provided by the *color transparency* argument, proposed for the first time by Bjorken [22]. The emitted meson is defined as the one that does not contain the B spectator quark. In the hypothesis that the emitted meson is produced with large momentum, its two quarks (that have opposite colors) will have a large momentum along the meson flight direction and a relatively low momentum in the transverse direction. The exchange of soft gluons with other fermionic lines is hence suppressed because the gluon cannot discriminate the two quarks inside the meson that appears as a color singlet. In this assumption, the emitted meson creation can then be considered, to first approximation, a standalone process with respect to the rest of the decay.

Since this argument relies on the emitted meson having a large momentum, it is more plausible for light emitted mesons and cannot be valid in case the emitted meson is a D. Nonetheless, even in the cases of light emitted mesons, factorization cannot account for all the contributions to the amplitude and it is generally considered as insufficient. However it can be considered very useful for first approximation evaluations [21, 24].

As already stated, the amplitude for a B decaying to a final state $f = DK$ is given by $\langle f|H_{eff}|B\rangle$, where the effective Hamiltonian is expressed in eq. 2.1. Following the diagrammatic approach, presented in [23], the amplitudes are written as sums of the contributions from all the possible topologies resulting from the Wick contractions, between initial and final state, of the different effective Hamiltonian operators ($Q_{1,2}^{q_1 q_2 q_3}$ in expression 2.1). In this framework, the amplitudes for the decays can be expressed in terms of renormalization scheme and scale independent parameters, that are linear combinations of Wick contractions for different operators, weighted with their Wilson coefficients. Fig. 2.3 shows the topologies that are relevant for the $B \to DK$ decays: *Disconnected Emission* (**DE**), *Connected Emission* (**CE**), *Disconnected Annihilation* (**DA**) and *Connected Annihilation* (**CA**).

The following emission parameters can be defined as:

$$E_1 = C_1\langle Q_1\rangle_{DE} + C_2\langle Q_2\rangle_{CE} \; ;$$
$$E_2 = C_1\langle Q_1\rangle_{CE} + C_2\langle Q_2\rangle_{DE} \; ;$$

and similarly for the annihilation:

$$A_1 = C_1\langle Q_1\rangle_{DA} + C_2\langle Q_2\rangle_{CA} \; .$$

where $\langle Q_i\rangle_{DE,CE,DA,CA}$ $(i = 1, 2)$ indicates the insertion of the Q_i operator inside a topology of the kind of **DE**, **CE**, **DA**, **CA** respectively. More explicitly:

$$E_1(q_1, q_2, q_3, M_1, M_2) = C_1 DE(q_1, q_2, q_3, M_1, M_2) + C_2 CE(q_1, q_2, q_3, M_1, M_2) \; ;$$
$$E_2(q_1, q_2, q_3, M_1, M_2) = C_1 CE(q_1, q_2, q_3, M_1, M_2) + C_2 DE(q_1, q_2, q_3, M_1, M_2) \; ;$$
$$A_1(q_1, q_2, q_3, M_1, M_2) = C_1 DA(q_1, q_2, q_3, M_1, M_2) + C_2 CA(q_1, q_2, q_3, M_1, M_2) \; .$$

In the case of the **DE** topology, a sum can be performed on the color of the q_2 and q_3 quarks forming the emitted meson, on the contrary in the **CE** topology, the colors of the q_2 and q_1 quarks are determined by the colors of the q_3 quark and of the B spectator quark

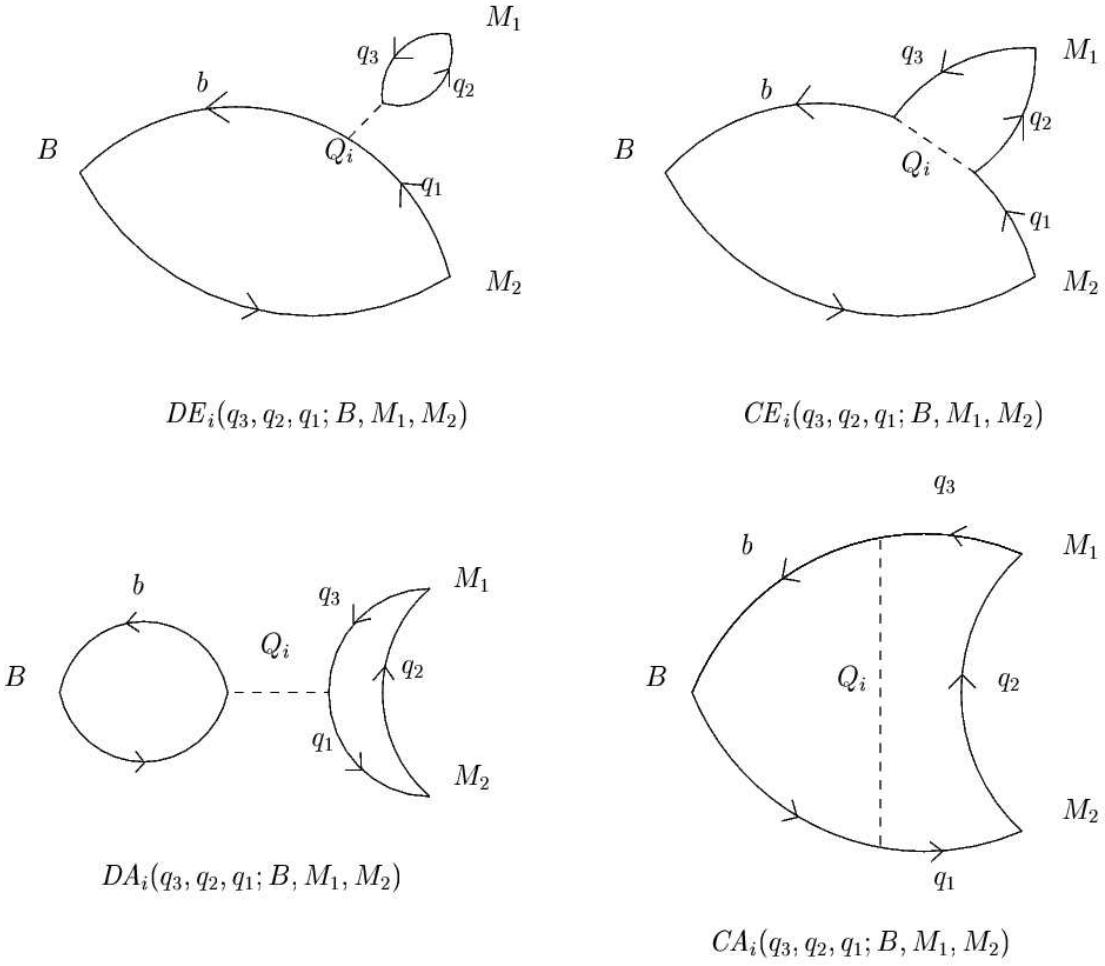

Figure 2.3: Relevant topologies for the $B \to DK$ decays amplitudes.

respectively (see Fig. 2.3). For this reason, the **CE** contribution is expected to be suppressed by a factor $1/N_C$ (where N_C is the number of colors) with respect to the contributions from **DE**. The contributions of the annihilation topologies are also expected to be suppressed with respect to **DE**.

The amplitudes for the $B \to DK$ decays of interest can be expressed as follows (with $l = u, d$):

$$
\begin{aligned}
&A\left(B^+ \to \bar{D}^0 K^+\right) = V_{us}\, V_{cb}^*(E_1\left(s,l,c,K,D\right) \,+\, E_2\left(c,l,s,D,K\right)) \,; \\
&A\left(B^0 \to \bar{D}^0 K^0\right) = V_{us}\, V_{cb}^*(E_2\left(c,l,s,D,K\right)) \,; \\
&A\left(B^+ \to D^0 K^+\right) = V_{cs}\, V_{ub}^*(E_2\left(l,c,s,D,K\right) \,+\, A_1\left(s,l,c,K,D\right)) \,; \\
&A\left(B^0 \to D^0 K^0\right) = V_{cs}\, V_{ub}^* E_2\left(l,c,s,D,K\right) \,.
\end{aligned}
$$

Due to the values of the Wilson coefficients, the E_1 and E_2 parameters are dominated by the **DE** and **CE** topologies respectively.

As already stressed, the values of those hadronic parameters cannot be calculated in a model-independent way. Moreover, these parameters are complex quantities and their actual contributions to the amplitudes depend on the relative strong phases that again cannot be predicted.

2.2 Measurements of the angle γ in $B \to DK$ decays

The idea of measuring a relative phase ϕ through the interference between two amplitudes A_1 and $A_2 e^{i\phi}$ connecting the same initial and final states is based on the fact that the decay rate between these two states is proportional to: $|A_1 + A_2 e^{i\phi}|^2 = A_1^2 + A_2^2 + 2A_1 A_2 \cos\phi$ and hence the interference term gives sensitivity to the relative phase ϕ (here A_1 and A_2 are real).

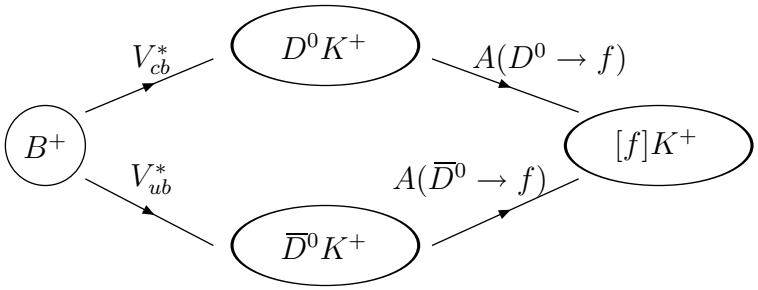

Figure 2.4: Interference scheme for $B^+ \to \overline{D}^0 K^+$ and $B^+ \to D^0 K^+$ decays .

In Fig. 2.4 we show an interference scheme for B^+ mesons decays giving sensitivity to γ. The B^+ can decay either to $\overline{D}^0 K^+$ through a $b \to c$ transition or to $D^0 K^+$ through a $b \to u$ transition. If both the D^0 and the $\overline{D}^0$ decay to the same final state f, the study of the decay $B^+ \to [f]K^+$ gives sensitivity to the relative phase between the two decay amplitudes.

The amplitude for $b \to c$ and $b \to u$ transitions can be written as $A(b \to u) \equiv |V_{ub}| e^{i\gamma} A_u e^{i\delta_u}$ and $A(b \to c) \equiv |V_{cb}| A_c e^{i\delta_c}$, where $A_{u(c)}$ and $\delta_{u(c)}$ are the absolute value and the phase of the strong interaction contribution to the amplitude. If the neutral D decay is also considered, a term $A_D e^{i\delta_D}$ (or $A_{\bar{D}} e^{i\delta_{\bar{D}}}$) has to be included. In the following we denote $\delta = \delta_D - \delta_{\bar{D}} + \delta_u - \delta_c$. In case of B^+, the interference term in the decay rate will be proportional to $\cos(\delta + \gamma)$. A similar diagram can be drawn for the CP conjugate decay ($B^- \to [f]K^-$), in this case the interference term will be proportional to $\cos(\delta - \gamma)$, since the strong interactions conserve CP.

The example shown in Fig. 2.4 refers to the $B^+ \to \overline{D}^0(D^0)K^+$, but equivalent arguments can be done for all the $B^+ \to \overline{D}^{(*)0}(D^{(*)0})K^+$ and $B^- \to D^{(*)0}(\overline{D}^{(*)0})K^-$ as well as for the $B^0 \to \overline{D}^{(*)0}(D^{(*)0})K^{(*)0}$ and $\overline{B}^0 \to D^{(*)0}(\overline{D}^{(*)0})\overline{K}^{(*)0}$ decays.

There are several methods that aim at the measurement of γ in $B \to DK$ decays, all based on the strategy sketched in Fig. 2.4, that differ because of the neutral D final states f they reconstruct and consequently because of different experimental analysis techniques they use.

A fundamental quantity in all these measurements is the parameter $r_B = \frac{|A(b\to u)|}{|A(b\to c)|}$. Being the absolute value of the ratio of the $b \to u$ to the $b \to c$ transition amplitudes, r_B drives the sensitivity to γ in each channel. The big challenge of measuring γ is related to the fact that r_B is small or, in other words, the $b \to u$ transitions are suppressed with respect to the $b \to c$ ones.

Looking at the possible diagrams in Fig. 2.1 and 2.2, r_B for charged $B \to DK$ channels can be written as:

$$r_B^{CH} \equiv r_B(D^0K^+) = \frac{|A(B^+ \to D^0K^+)|}{|A(B^+ \to \overline{D}^0K^+)|} = \frac{|V_{cs}V_{ub}^*|}{|V_{us}V_{cb}^*|}\frac{|\bar{C}+A|}{|T+C|}; \tag{2.3}$$

and, for neutral decays, as:

$$r_B^{NEUT} \equiv r_B(D^0K^0) = \frac{|A(B^0 \to D^0K^0)|}{|A(B^0 \to \overline{D}^0K^0)|} = \frac{|V_{cs}V_{ub}^*|}{|V_{us}V_{cb}^*|}\frac{|\bar{C}|}{|C|}. \tag{2.4}$$

In the expressions 2.3 and 2.4, the term $\frac{|V_{cs}V_{ub}^*|}{|V_{us}V_{cb}^*|}$ only depends on absolute values of CKM parameters and is known to be $\sqrt{\bar{\rho}^2+\bar{\eta}^2} = 0.372 \pm 0.012$ [25], while the terms depending on the hadronic parameters are not easily predictable, although one can make some argument for their evaluation, typically based on the fact that the *color-suppressed* and *annihilation* diagram contributions are suppressed with respect to the *tree* ones.

From simple arguments of this kind, one would expect $r_B^{CH} \approx 0.1$ for the charged $B \to DK$ channels and $r_B^{NEUT} \approx 0.4$ for the neutral $B \to DK$ ones. This assumes that the ratio between the two *color-suppressed* diagrams (C and $\bar{C}$) is ≈ 1 [23], $|C|/|T| \approx 0.3$ and $|A|/|T| \approx 0.5$ [26]. A more quantitative evaluation is given in sec. 2.4.

In conclusion, the measurements of γ are difficult because $b \to u$ transitions are strongly suppressed with respect to $b \to c$ ones, as described by r_B ratios [1], and each analysis aiming to determine γ has to simultaneously measure the r_B ratio (for the particular analyzed channel) or either make some assumption on it. More explicitly, see Fig. 2.4, the unknowns in any γ analysis are γ itself, the r_B ratio and a strong phase δ. These are usually called polar coordinates. Some analyses make use of the "cartesian coordinates", defined in terms of the polar coordinates as:

$$x_\pm = r_B\cos(\delta \pm \gamma)\ ;\ y_\pm = r_B\sin(\delta \pm \gamma) \tag{2.5}$$

The present knowledge on γ comes from the combination of measurements of several channels with different methods, described in section 2.2.1, 2.2.2 and 2.2.3. As we will see, some of the methods are more sensitive to γ itself, while some others are particularly powerful in measuring the r_B ratios. For the sake of simplicity, in sections 2.2.1, 2.2.2 and 2.2.3 the formulas and graphs will refer to the case of $B^+ \to \overline{D}^0(D^0)K^+$, while the methods are of course valid for all the $B^+ \to \overline{D}^{(*)0}(D^{(*)0})K^+$ and $B^- \to D^{(*)0}(\overline{D}^{(*)0})K^-$ decays as well as for the $B^0 \to \overline{D}^{(*)0}(D^{(*)0})K^{(*)0}$ and $\overline{B}^0 \to D^{(*)0}(\overline{D}^{(*)0})\overline{K}^{(*)0}$ decays.

[1] It has to be stressed that the parameters r_B are ratios between amplitudes, the ratio between number of events from $b \to u$ and $b \to c$ transitions will be proportional to r_B [2].

2.2.1 The GLW method

In the GLW method [28, 29], γ is measured from the study of B decays to $D^0_\pm K$ final states, where $D^0_\pm$ is a CP eigenstate with eigenvalues ± 1, defined as:

$$|D^0_\pm\rangle = \frac{1}{\sqrt{2}}(|D^0\rangle \pm |\bar{D^0}\rangle)$$

From the definition of $D^0_\pm$, it follows:

$$\sqrt{2}\cdot A(B^+ \to D^0_\pm K^+) = A(B^+ \to D^0 K^+) \pm A(B^+ \to \overline{D}^0 K^+)$$
$$\sqrt{2}\cdot A(B^- \to D^0_\pm K^-) = A(B^- \to D^0 K^-) \pm A(B^- \to \overline{D}^0 K^-).$$

The amplitudes can be written as follows:

$$A(B^+ \to D^0 K^+) = V^*_{ub}|A|e^{i\alpha} = |V_{ub}|e^{i\gamma}|A|e^{i\alpha};$$
$$A(B^- \to \overline{D}^0 K^-) = V_{ub}|A|e^{i\alpha} = |V_{ub}|e^{-i\gamma}|A|e^{i\alpha};$$

and the following relation, for the amplitudes of the $b \to u$ processes, holds:

$$A(B^+ \to D^0 K^+) = e^{2i\gamma} A(B^- \to \overline{D}^0 K^-).$$

The amplitudes for the $b \to c$ processes are related by the following expressions:

$$A(B^+ \to \overline{D}^0 K^+) = A(B^- \to D^0 K^-).$$

These relations can be represented in a complex plane as two triangles, as shown in Fig. 2.5, and the presence of CP violation is described by $|A(B^+ \to D^0_+ K^+)|$ being different from $|A(B^- \to D^0_+ K^-)|$. The following observables are measured:

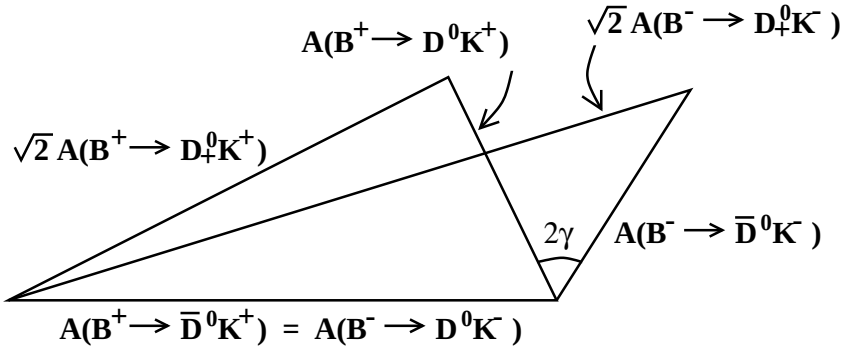

Figure 2.5: Representation, in a complex plane, of the amplitudes used in the GLW method.

$$R_{CP^\pm} = \frac{\Gamma(B^+ \to D^0_\pm K^+) + \Gamma(B^- \to D^0_\pm K^-)}{\Gamma(B^+ \to D^0 K^+) + \Gamma(B^- \to \bar{D}^0 K^-)} = 1 + {r_B}^2 \pm 2 r_B \cos\gamma \cos\delta_B$$
$$A_{CP^\pm} = \frac{\Gamma(B^+ \to D^0_\pm K^+) - \Gamma(B^- \to D^0_\pm K^-)}{\Gamma(B^+ \to D^0_\pm K^+) + \Gamma(B^- \to D^0_\pm K^-)} = \frac{\pm 2 r_B \sin\gamma \sin\delta_B}{R_{CP^\pm}}$$

where δ_B is the relative strong phase between the two B decay amplitudes, γ the weak phase, and r_B is the ratio $r_B = \frac{|A(b\to u)|}{|A(b\to c)|}$.

In the GLW method, four observables, $A_{CP\pm}$ and $R_{CP\pm}$, are measured to constrain three unknowns, γ, δ and r_B. It is instructive to see that $A_{CP\pm}$ and $R_{CP\pm}$ are invariant under the following operations:

- $S_{sign} : \gamma \leftrightarrow -\gamma$ and $\delta_B \leftrightarrow -\delta_B$;
- $S_{exchange} : \gamma \leftrightarrow \delta_B$;
- $S_{\pi} : \gamma \to \gamma + \pi$ and $\delta_B \to \delta_B + \pi$.

It follows that the GLW method suffers of an irreducible four-fold ambiguity on the determination of the phases. With the present available statistics, is very useful in measuring r_B, but has typically a low sensitivity to γ.

2.2.2 The ADS method

In the ADS method [30, 31], γ is measured from the study of $B \to DK$ decays, where D mesons decay into non CP eigenstate final states. In this method the suppression of $b \to u$ transition with respect to the $b \to c$ one is partly overcome by the study of decays of the B meson in final states which can proceed in two ways: either through a favored $b \to c$ B decay followed by a suppressed D decay ($D^0 \to f$, or $\bar{D}^0 \to \bar{f}$), or through a suppressed $b \to u$ B decay followed by a favored D decay ($D^0 \to \bar{f}$ or $\bar{D}^0 \to f$), as sketched in Fig. 2.6. In this way the two amplitudes are comparable and one can expect larger interference terms.

A typical final state f used in ADS analyses is $f = K^+\pi^-$ (hence $\bar{f} = K^-\pi^+$). The D^0 decay in this state is unfavoured with respect to the $\bar{D}^0$ decay because of the CKM elements in the amplitudes:

$$\frac{|A(D^0 \to f)|}{|A(D^0 \to \bar{f})|} \sim \frac{|V_{cd}^* V_{us}|}{|V_{ud}^* V_{cs}|} = \lambda^2 \tag{2.6}$$

with $\lambda = \sin\theta_C \sim 0.22$. For this reason, the decays $D^0 \to \bar{f}$ and $D^0 \to f$ are called Cabibbo-allowed (CA) and doubly-Cabibbo-suppressed (DCS) respectively.
In the ADS method, one measures the observables:

$$R_{ADS} = \frac{\Gamma(B^+ \to \bar{f}K^+) + \Gamma(B^- \to fK^-)}{\Gamma(B^+ \to fK^+) + \Gamma(B^- \to \bar{f}K^-)} \tag{2.7}$$

$$A_{ADS} = \frac{\Gamma(B^- \to fK^-) - \Gamma(B^+ \to \bar{f}K^+)}{\Gamma(B^- \to fK^-) + \Gamma(B^+ \to \bar{f}K^+)}. \tag{2.8}$$

In the following, we will assume that CP is conserved in D decays. We define:

$$\begin{aligned}
&A(B^+ \to \overline{D}^0 K^+) = A(B^- \to D^0 K^-) = A_B;\\
&A(B^+ \to D^0 K^+) = r_B A_B e^{i(\delta_B+\gamma)};\\
&A(B^- \to \overline{D}^0 K^-) = r_B A_B e^{i(\delta_B-\gamma)};\\
&A(D^0 \to \bar{f}) = A(\overline{D}^0 \to f) = A_D(CA) = A_D;\\
&A(D^0 \to f) = A(\overline{D}^0 \to \bar{f}) = A_D(DCS) = r_D A_D e^{i\delta_D}.
\end{aligned}$$

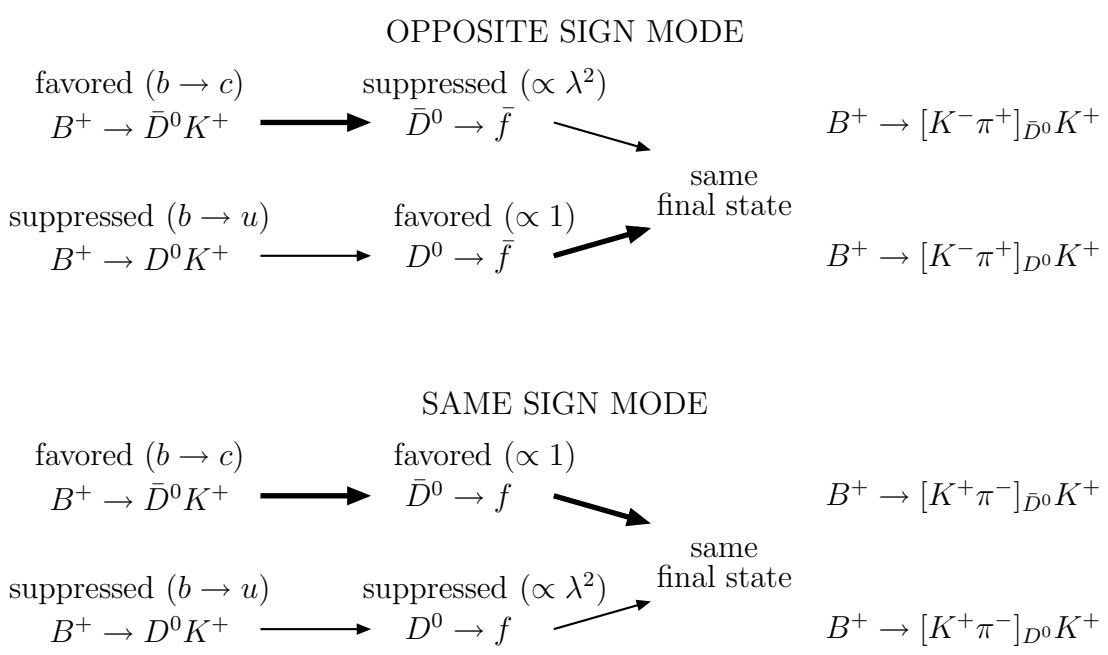

Figure 2.6: Scheme for the ADS method: B^+ mesons decaying to the same final state, through two different decay chains, for "opposite sign" events (top) and for "same sign" events (bottom). The scheme is shown for the D final state $f = K^+\pi^-$

Two new quantities have been introduced: δ_D, which is the relative strong phase between Cabibbo-allowed and doubly-Cabibbo-suppressed D decay amplitudes, and r_D, which is the ratio between the absolute values of the amplitudes, as in eq. 2.6, $r_D = |A_D(DCS)|/|A_D(CA)| \propto ||V_{cd}^* V_{us}|/|V_{ud}^* V_{cs}| = \lambda^2$.

The numerator of the ratio R_{ADS} is the sum of the contribution from B^+ decays:

$$|A_B A_D r_B e^{i(\delta_B+\gamma)} + A_B A_D r_D e^{i\delta_D}|^2 = \\ A_B^2 A_D^2 [r_B^2 + r_D^2 + 2 r_B r_D \cos(\delta+\gamma)],$$

where $\delta = \delta_B + \delta_D$ is the sum of the strong phase differences in the B and in the D amplitudes, and the contribution from B^- decays:

$$|A_B A_D r_B e^{i(\delta_B-\gamma)} + A_B A_D r_D e^{i\delta_D}|^2 = \\ A_B^2 A_D^2 [r_B^2 + r_D^2 + 2 r_B r_D \cos(\delta-\gamma)]$$

resulting in:

$$2A_B^2 A_D^2 [r_B^2 + r_D^2 + r_B r_D(\cos(\delta+\gamma) + \cos(\delta-\gamma))] = \\ 2A_B^2 A_D^2 [r_B^2 + r_D^2 + 2 r_B r_D \cos\gamma \cos\delta]$$

The denominator of R_{ADS} is the sum of the contribution from B^+ decays:

$$|A_B A_D + A_B A_D r_D r_B e^{i(\delta_B+\delta_D+\gamma)}|^2 = \\ A_B^2 A_D^2 [1 + r_B^2 r_D^2 + 2 r_B r_D \cos(\delta+\gamma)] = A_B^2 A_D^2 [1 + x_+] \approx A_B^2 A_D^2$$

and the contribution from B^- decays:

$$|A_B A_D + A_B A_D r_D r_B e^{i(\delta_B+\delta_D-\gamma)}|^2 =$$
$$A_B^2 A_D^2[1 + r_B^2 r_D^2 + 2 r_B r_D \cos(\delta-\gamma)] = A_B^2 A_D^2[1 + x_-] \approx A_B^2 A_D^2$$

resulting in:

$$A_B^2 A_D^2[2 + 2 r_B^2 r_D^2 + r_B r_D(\cos(\delta+\gamma) + \cos(\delta-\gamma))] =$$
$$A_B^2 A_D^2[2 + x_+ + x_-] \approx 2 A_B^2 A_D^2$$

where the terms x_+ and x_- are defined as:

$$x_+ = r_B^2 r_D^2 + 2 r_B r_D \cos(\delta+\gamma);$$
$$x_- = r_B^2 r_D^2 + 2 r_B r_D \cos(\delta-\gamma)].$$

The ratio R_{ADS} can hence be written as following:

$$R_{ADS} \simeq (r_D^2 + {r_B}^2 + 2 r_B r_D \cos\gamma \cos(\delta))[1 - \frac{x_+ - x_-}{2}].$$

The terms x_+ and x_- are small with respect to the leading contribution (which is of the order ~ 1), since they are proportional to $r_B r_D$ (of the order of a few percent) and can be neglected. Let's see the meaning of neglecting these terms. The decay amplitude for each channel contributing to the denominator of R_{ADS} is the sum of two amplitudes: $A_B(b \to c)A_D(CA) + A_B(b \to u)A_D(DCS)$, where the first is the leading one. Neglecting the terms x_+ and x_- corresponds to neglect the term $A_B(b \to u)A_D(DCS)$ (i.e. the amplitude for the $b \to u$ suppressed decay of the B, followed by a doubly Cabibbo suppressed decay of the D) and approximating the denominator with its leading term $A_B(b \to c)A_D(CA)$.

In a similar way, for A_{ADS} we obtain the following expression:

$$A_{ADS} \simeq r_B r_D[-\cos(\delta+\gamma) + \cos(\delta-\gamma)] \frac{1 - \frac{x_+ - x_-}{2}}{R_{ADS}}.$$

If we neglect the terms x_+ and x_- in R_{ADS}, the observables R_{ADS} and A_{ADS} can be written as follows:

$$\begin{aligned} R_{ADS} &= r_D^2 + {r_B}^2 + 2 r_B r_D \cos\gamma \cos(\delta_B + \delta_D) \\ A_{ADS} &= r_B r_D[-\cos(\delta+\gamma) + \cos(\delta-\gamma)]/R_{ADS} \\ &= 2 r_B r_D \sin\gamma \sin\delta / R_{ADS}. \end{aligned}$$

This method is very useful in measuring r_B, but normally it has very low sensitivity to γ. Even in the hypothesis of very high statistics, where both R_{ADS} and A_{ADS} can be measured with a good precision, the ADS method would suffer from having three unknowns (r_B,γ and δ, the r_D ratios being known) and only two observables (R_{ADS} and A_{ADS}). In this thesis, as for other ADS analyses, the ratio R_{ADS} is measured but not the asymmetry A_{ADS}. The observable A_{ADS} is the direct *CP* asymmetry built up using only the opposite sign events. With the statistics available for the studies presented in this thesis (~ 400 fb^{-1}), the error on A_{ADS} would be too large to allow to extract any useful information on r_B, γ and δ.

2.2.3 The GGSZ Dalitz method

In this method [32] γ is measured from the $B \to DK$ decays with the D decaying to multi-body CP eigenstate final states. Multi-body decays are usually described by the isobar model, in which the decay amplitude is written as a sum of amplitudes with quasi two-body intermediate states.

The amplitude for a three-body neutral D decay $D^0 \to M_1 M_2 M_3$ is written as a sum of amplitudes for decays of the kind $D^0 \to \mathcal{M}_r M_3$, where $\mathcal{M}_r$ are resonances that decay to M_1, M_2 final states. These decays are studied in the Dalitz plane (s_{12}, s_{13}) , where $s_{ij} = (p_i + p_j)^2$ is the invariant mass of the couple $M_i M_j$ of the D decay products.

The isobar model parametrizes the amplitude $A = A_k e^{i\delta_k}$, at each point k of the D Dalitz plane, as a sum of two-body decay matrix elements plus a non resonant part, according to the following expression:

$$A_k e^{i\delta_k} = \sum_j a_j e^{i\delta_j} BW_k^j(m, \Gamma, s) + a_{nr} e^{i\Phi_{nr}} \tag{2.9}$$

where $BW_k^j(m, \Gamma, s)$ is the expression for the relativistic Breit-Wigner describing the decay through an intermediate j^{th} resonance characterised by its spin s, its mass m and decay width Γ.

A typical Dalitz plane distribution can be seen in Fig. 2.7, where the Dalitz plot for a large sample of $D^0 \to K_S \pi^+ \pi^-$ events is shown, and the zones of higher density represent the contributions from different resonances.

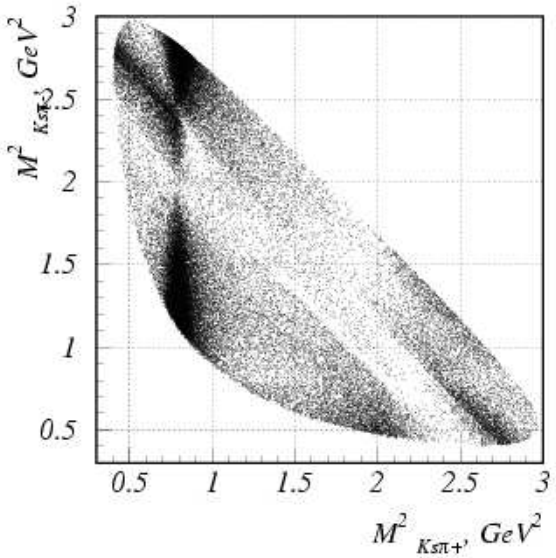

Figure 2.7: Dalitz plane distribution for a D^0 decaying to a final state $K_S \pi^+ \pi^-$.

Analyses of large tagged neutral D data samples (typically from decays of $D^{*+} \to D^0 \pi^+$ and $D^{*-} \to \overline{D}^0 \pi^-$) allow for a good determination of amplitudes and relative strong phases

of the different resonances contributing to the D Dalitz distributions. As explained, those samples are studied assuming an isobar model and writing the sum of amplitudes from the different quasi-two-body intermediate states with resonances as a sum of Breit-Wigner functions. Some components that are not easily explained with resonances are described by effective parametrizations, such as the K-matrix approach [62, 63], which will be discussed in more detail in chapter 6.

This information is used as input to the Dalitz analyses aiming to measure γ, where the complete and rich structure of the multi-body D decay is exploited and detectable interference terms are expected because of the presence of different strong phases. This method is indeed very powerful and it is so far the one that gives the best error on the weak phase γ.

Continuing on the example of the $K_s\pi^+\pi^-$ final state, we define

$$A_D(s_{12}, s_{13}) = A_{12,13}e^{i\delta_{12,13}} = A(D^0 \to K_S(p_1)\pi^-(p_2)\pi^+(p_3)) = \\ = A(\bar{D^0} \to K_S(p_1)\pi^+(p_2)\pi^-(p_3)) \; ;$$

where $s_{ij} = (p_i + p_j)^2$ and p_1, p_2, p_3 are the 4−momenta of K_s, π^- and π^+ respectively, $A_{12,13} > 0$ and $0 < \delta_{12,13} < 2\pi$.

We have, for the decay rates:

$$d\Gamma(B^- \to [K_s\pi^-\pi^+]K^-) \propto (A^2_{12,13} + r_B^2 A^2_{13,12} + \\ +2r_B\mathcal{R}e\,[\, A_D(s_{12}, s_{13})A^*_D(s_{13}, s_{12}))e^{i(\delta_B-\gamma)}\,]\,)ds_{12}ds_{13}\;; \tag{2.10}$$

$$d\Gamma(B^+ \to [K_s\pi^+\pi^-]K^+) \propto (A^2_{13,12} + r_B^2 A^2_{12,13} + \\ +2r_B\mathcal{R}e\,[\, A_D(s_{13}, s_{12})A^*_D(s_{12}, s_{13}))e^{i(\delta_B+\gamma)}\,]\,)ds_{12}ds_{13}\;. \tag{2.11}$$

From the study of these decays we are hence sensitive to r_B, γ and δ_B (the relative strong phase between the B amplitudes).

2.3 State-of-the-art for measurements of γ and r_B

As already stated, the knowledge on the angle γ comes from the combination of results obtained from many channels with different methods (listed in sec. 2.2.1, 2.2.2 and 2.2.3). So far these results are obtained using charged $B \to DK$ decays. The available experimental results are:

- GLW analyses of $B^\pm \to D^0_{CP\pm}K^\pm$, $B^\pm \to D^{*0}_{CP\pm}K^\pm$ and $B^\pm \to D^0_{CP\pm}K^{*\pm}$, performed both by *BABAR* [64] and Belle collaborations [65].

- ADS analyses of $B^\pm \to \overline{D}^0(D^0)K^\pm$ with the neutral D reconstructed in $K^\pm\pi^\mp$, performed both by *BABAR* [66] and Belle collaborations [68].

- *BABAR* also performed an ADS measurement in the channels $B^\pm \to \overline{D}^{*0}(D^{*0})K^\pm$ and $B^\pm \to \overline{D}^0(D^0)K^{*\pm}$, with the neutral D reconstructed in $K^\pm\pi^\mp$, and a measurement in the channel $B^\pm \to \overline{D}^0(D^0)K^\pm$ with the neutral D reconstructed into $K^\pm\pi^\mp\pi^0$ [66, 67].

- Dalitz measurement of the channels $B^{\pm} \to D^0_{CP\pm}K^{\pm}$, $B^{\pm} \to D^{*0}_{CP\pm}K^{\pm}$ and $B^{\pm} \to D^0_{CP\pm}K^{*\pm}$, with the neutral D reconstructed in $K_S\pi^+\pi^-$ final state by the Belle collaboration [70], and both in $K_S\pi^+\pi^-$ and in $K_SK^+K^-$ final states by the *BABAR* collaboration [69].

- *BABAR* also performed a Dalitz analysis of the channel $B^{\pm} \to D^0_{CP\pm}K^{\pm}$, with the neutral D reconstructed in $\pi^+\pi^-\pi^0$ [71].

The pdf for γ obtained from the combination of all these analyses (using all the available measurements presented at the 2008 winter conferences) is shown in Fig. 2.8, where the dark and light zones indicate the 68% and 95% probability regions. It results in $\gamma = (80 \pm 13)^o$.

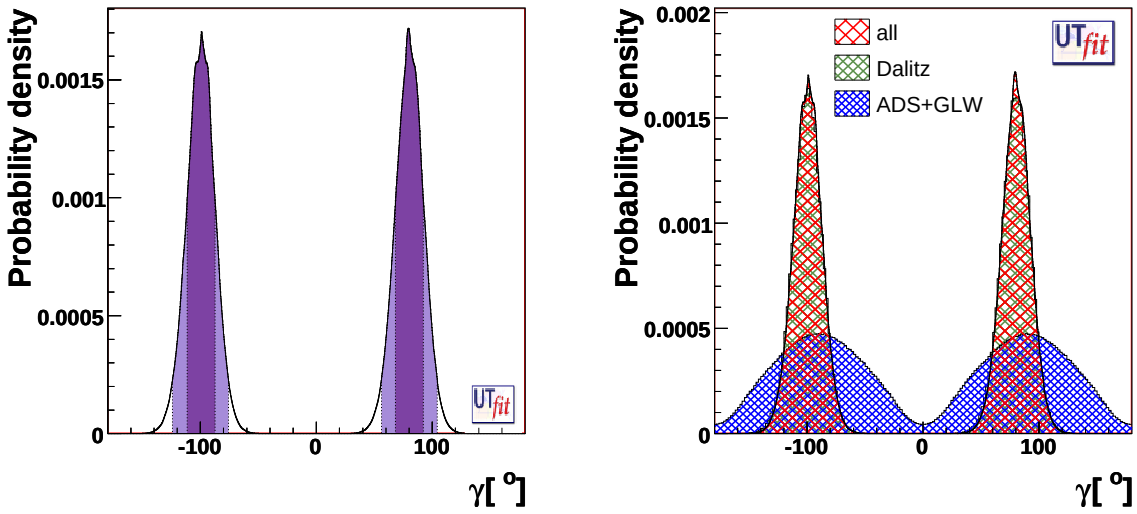

Figure 2.8: One-dimensional pdf for γ from the combination of all the analyses in the charged $B \to DK$ modes (left). The dark and light colored zones show the 68% and 95% probability regions respectively. In the right plot pdfs are shown separately for γ from GLW and ADS and from Dalitz analyses separately. The combination is also shown, but is barely visible since it is almost coinciding with the result from Dalitz analysis alone. These results are obtained using experimental data available for the 2008 winter conferences.

The pdf obtained for the r_B ratios, for the $B^{\pm} \to D^0_{CP\pm}K^{\pm}$, $B^{\pm} \to D^{*0}_{CP\pm}K^{\pm}$ and $B^{\pm} \to D^0_{CP\pm}K^{*\pm}$ channels, are shown in Fig. 2.9, where the dark and light zones represent the 68% and 95% probability regions respectively. The numerical results are:

$$\begin{aligned} r_B(D^0K^+) &= 0.10 \pm 0.02; \\ r_B(D^{*0}K^+) &= 0.09 \pm 0.04; \\ r_B(D^0K^{*+}) &= 0.13 \pm 0.09. \end{aligned} \tag{2.12}$$

In Fig. 2.9 we also show the pdf for the r_B ratios separately from GLW and ADS and from Dalitz analyses.

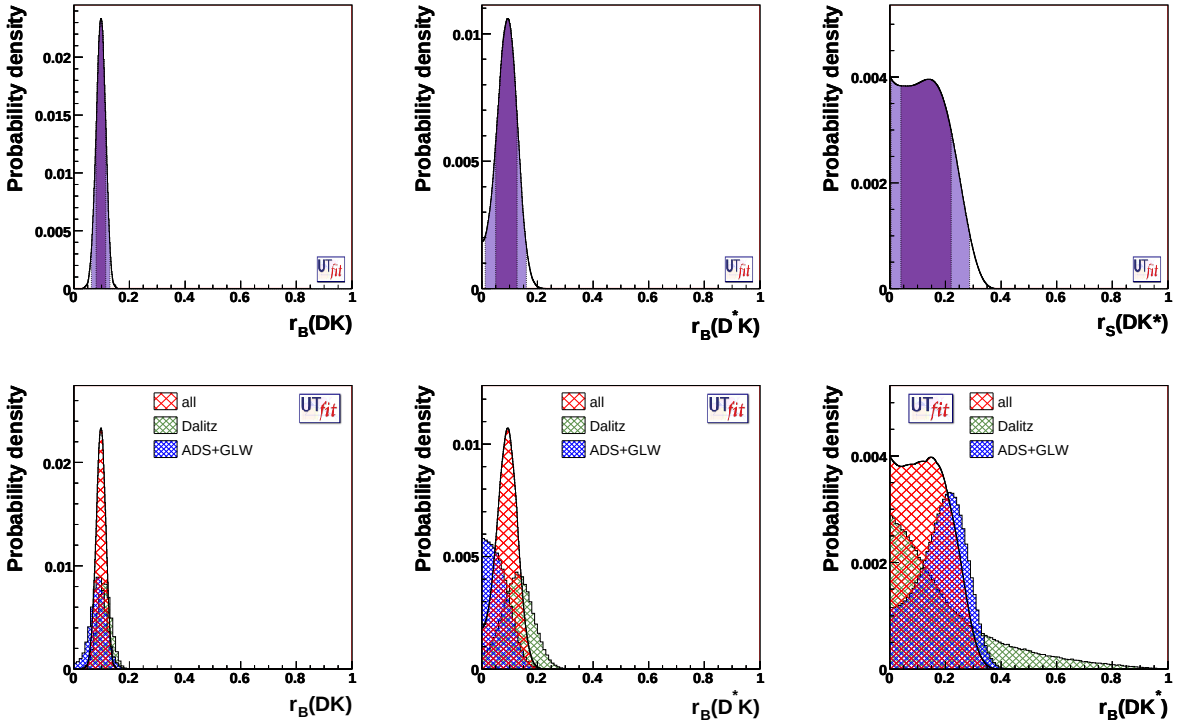

Figure 2.9: One-dimensional pdf of the r_B ratios for $B^{\pm} \to D^0_{CP\pm}K^{\pm}$, $B^{\pm} \to D^{*0}_{CP\pm}K^{\pm}$ and $B^{\pm} \to D^0_{CP\pm}K^{*\pm}$ channels from the combination of all the analyses in the charged $B \to DK$ modes. In the top row, the dark and light colored zones show the 68% and 95% probability regions respectively. In the bottom row, the pdf for these ratios obtained separately from GLW and ADS analyses and from Dalitz analyses separately and from their combination is also shown. These results are obtained using experimental data available for the 2008 winter conferences.

It is noteworthy that, while the Dalitz method gives the leading contribution in constraining γ, the GLW and ADS analyses have an important weight in the determination of the r_B ratios.

2.4 (Great) expectations for r_B in neutral $B \to DK$ decays

As shown in [27], we can give an evaluation of the r_B^{NEUT} ratios for neutral B channels, starting from the values of r_B^{CH}, exploiting the fact that the two ratios can be expressed in terms of some common parameters (eqs. 2.3 and 2.4). We first consider the case in which annihilation can be neglected (we thus make the hypothesis that $|A|$=0). In this case, the following relation holds:

$$r_j^{NEUT} = R_j r_j^{CH}$$

where $R_j = \frac{C+T}{C}$ and $j = DK$, D^*K or DK^*. The values for R_j can be obtained from the measurement of the following branching fractions: $Br_{C+T} = Br(B^+ \to \bar{D}^{(*)0}K^{(*)+}) \propto |C+T|^2$, and $Br_C = Br(B^0 \to \bar{D}^{(*)0}K^{(*)0}) \propto |C|^2$.

If annihilation process is not neglected, the previous relation becomes more complicated:

$$r_j^{NEUT} = R_j \frac{1}{\sqrt{1+x^2+2xcos\phi_{A\bar{C}}}} r_j^{CH}$$

where $x = |A|/|\bar{C}|$ and $cos\phi_{A\bar{C}}$ is the strong phase between the color-suppressed and the annihilation amplitudes in $b \to u$ processes. The term $|A|$ is constrained by the measurement of the branching fraction $Br_A = Br(B^+ \to D^+K^{*0})$. So far, only upper limits exist.

Using a bayesian toy Monte Carlo procedure, we have evaluated the ratios r^{NEUT}, using the branching fractions shown in Tab.2.1 and the values for r^{CH}, obtained combining all the available measurements presented at the winter conferences (see eq. 2.12).

System	$Br(B^+ \to \bar{D}^{(*)0}K^{(*)+})$	$Br(B^0 \to \bar{D}^{(*)0}K^{(*)0})$	$Br_A = Br(B^+ \to \bar{D}^{(*)+}K^{(*)0})$
DK	$(4.02 \pm 0.33) \times 10^{-4}$	$(5.2 \pm 0.7) \times 10^{-5}$	$< 5.0 \times 10^{-6}$ @ 90% probability
D^*K	$(4.16 \pm 0.33) \times 10^{-4}$	$(3.2 \pm 1.2) \times 10^{-5}$	$< 9.0 \times 10^{-6}$ @ 90% probability
DK^*	$(5.3 \pm 0.4) \times 10^{-4}$	$(4.2 \pm 0.6) \times 10^{-5}$	-

Table 2.1: Branching fractions (Br) for the $b \to c$ mediated processes used in the study, for the $B \to DK$, $B \to D^*K$ and $B \to DK^*$ channels [8].

The study has been performed both assuming the annihilations to be negligible and using for them the experimental information, when available. In the latter case, $\cos\phi_{A\bar{C}}$ is assumed to be flat within its full range. The results of the study are summarized in Tab. 2.2.

The evaluations we have shown make use of some SU(2) assumption and suffer from the fact that we cannot determine the strong phases of the hadronic parameters, but are very useful as first approximations. These results show that indeed the r_B^{NEUT} ratios are expected to be larger that the r_B^{CH} ratios. This feature overcomes the fact that these decays are less abundant, since it gives higher sensitivity to γ.

Of course, the final knowledge on the r_B ratios has to be extracted form data.

System	R	r_B^{CH}	r_B^{NEUT} $\|A\|$=0	r_B^{NEUT} $\|A\| \propto \sqrt{Br_A}$
DK	(2.8 ± 0.4)	(0.10 ± 0.02)	(0.25 ± 0.06)	(0.23 ± 0.08)
D^*K	(3.6 ± 1.4)	(0.09 ± 0.04)	(0.24 ± 0.13)	(0.23 ± 0.14)
DK^*	(3.6 ± 0.6)	(0.13 ± 0.09)	(0.42 ± 0.21)	-

Table 2.2: The first column gives the results for $R = \sqrt{\frac{Br_{T+C}}{Br_C}}$. In the second column we recall the values for r^{CH} (2.12) as obtained from the combination of all the available measurements presented at the 2008 winter conferences. In the third and fourth columns we give the result for r^{NEUT} in case $|A|$=0 and using for $|A|$ the experimental measurements respectively.

2.5 Comparison between different methods

In this paragraph we perform a study to compare the expected relative errors obtained on r_B with the different analysis techniques, GLW, ADS and Dalitz. To do that, we use a toy Monte Carlo bayesian procedure:

- a large number of experiments is generated, by extracting r_B, γ and δ within their definition ranges.
- For each extraction i, the values of the observables ($R^i_{CP\pm}$and $A^i_{CP\pm}$ for the GLW method, R^i_{ADS} for the ADS method, $x^i_\pm$ and $y^i_\pm$ for the Dalitz method) are calculated.
- To each extraction of (r_B,γ,δ) is assigned a weight w^i, depending on its agreement with the measured values (for example, if R_{ADS} is measured and found to be Gaussian $R_{ADS} = \mu \pm \sigma$, then the weight is $w^i = e^{-(R^i_{ADS}-\mu)^2/\sigma^2}$). All the measurements are assumed to be Gaussian in this study.
- The distribution of the values of the variables (r_B,γ,δ), reweighted with w^i for each extraction, is normalized to unit area, resulting in the a-posteriori pdf for the given variable.
- The error on r_B is calculated from the interval obtained by integrating the pdf for r_B, starting from the most probable value, until we get the 68% of the total area.

For this study we assume fake central values for the observables, calculated assuming $r_B = 0.1$, $\gamma = 60^o$ and $\delta_B = 40^o$. The errors are taken from the latest *BABAR* results for the $B^\pm \to D^0(\overline{D}^0)K^\pm$. In these measurements, the neutral D is reconstructed in $\pi^+\pi^-$, K^+K^- (CP-even) and $K_s\pi^0$, $K_s\omega$ (CP-odd) for the GLW method on 363 fb^{-1}; $K^\pm\pi^\mp$ and $K^\pm\pi^\mp\pi^0$ for the ADS method with 210 fb^{-1}; $K_s\pi^+\pi^-$ and $K_sK^+K^-$ for the Dalitz method on 363 fb^{-1}. The statistical errors are then rescaled to 450 fb^{-1} and 1 ab^{-1} assuming that they scale as $1/\sqrt{\text{Lumi}}$, while the systematic errors stay unchanged.

It is interesting to note that the ADS method gives the best determination of r_B at low statistics (300–400 fb^{-1}). However the evolution of the relative error on r_B from ADS tends to saturate at about 30%. We recall here the definition of R_{ADS}:

$$R_{ADS} = r_B^2 + r_D^2 + 2r_Br_D\cos\gamma\cos\delta = r_B^2 + r_D^2 + 2r_Br_DK \tag{2.13}$$

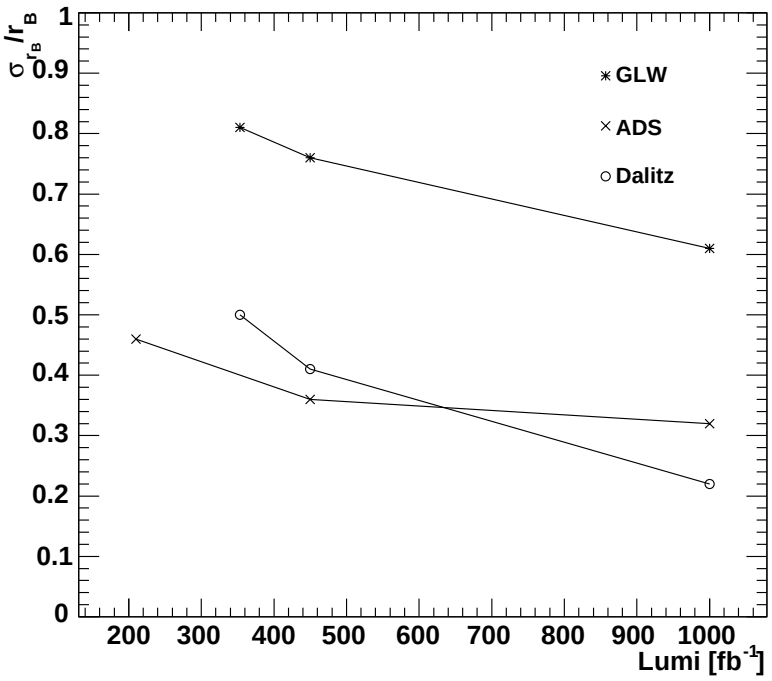

Figure 2.10: Expected relative errors on r_B from different experimental measurement techniques, assuming $r_B = 0.1$.

where $K = \cos\gamma\cos\delta \in [-1, 1]$. Solving the eq.2.13, the expression for r_B (keeping only the positive solution) is the following:

$$r_B = -r_D K + \sqrt{r_D^2 K^2 - r_D^2 - R_{ADS}}. \tag{2.14}$$

It follows that the error on r_B is:

$$\sigma(r_B) = (r_D + \frac{2r_D^2 K}{2\sqrt{r_D^2 K^2 - r_D^2 - R_{ADS}}})\sigma(K) \oplus \frac{\sigma(R_{ADS})}{2\sqrt{r_D^2 K^2 - r_D^2 - R_{ADS}}} \tag{2.15}$$

which, neglecting the terms proportional to r_D^2 and assuming the average of K to be zero, becomes:

$$\sigma(r_B) = r_D\sigma(K) \oplus \frac{\sigma(R_{ADS})}{2\sqrt{R_{ADS} - r_D^2}}. \tag{2.16}$$

with the hypothesis that r_D is known. This relation shows that, for very small $\sigma(R_{ADS})$, the error on r_B tends to an irreducible contribution from the term $\sigma_{\text{limit}} = r_D\sigma(K)$. Considering that K is flat distributed between -1 and 1, we have:

$$\sigma_{\text{limit}} = \frac{r_D}{\sqrt{3}} \sim [0.02, 0.04], \tag{2.17}$$

where the interval is due to different values of r_D for the three D channels. It follows that, for $r_B = 0.1$, $\sigma_{\rm limit}/r_B \sim 30\%$. The presence of this irreducible error is due to the fact that we use only one observable, R_{ADS}, to determine three unknowns (r_B, γ and δ). This problem is not present for GLW and Dalitz methods. It is noteworthy that for higher values of r_B ($r_B = 0.3$), as expected for neutral B decays (see sec. 2.4), the contribution of this irreducible error would be less important. The comparison of the relative errors on r_B from GLW, ADS and Dalitz methods with a statistics of 10 ab^{-1} is summarized in Tab. 2.3, for $r_B = 0.1$ and $r_B = 0.3$.

	GLW	ADS	Dalitz
$r_B = 0.1$	0.17	0.26	0.07
$r_B = 0.3$	0.07	0.08	0.06

Table 2.3: Relative error on r_B obtained with GLW, ADS and Dalitz method for fake measurements using 10 ab^{-1}, assuming $r_B = 0.1$ and $r_B = 0.3$.

For the extrapolation to $r_B = 0.3$ configuration, we make the hypothesis that we have the same number of $b \to u$ events as in the case of $r_B = 0.1$. Only statistical errors are taken into account in this study.

It should be finally stressed that, for 10 ab^{-1}, the Dalitz method would give an error of 4^o on γ with a two-fold ambiguity ($\gamma \leftrightarrow \gamma + \pi$). With the same statistics, the GLW method would allow for a determination of γ with 16^o error and a four-fold ambiguity. The ADS method, with R_{ADS} as only observable, cannot determine the angle γ.

2.6 Measuring γ using the $B^0 \to \overline{D}^0(D^0)K^{*0}$ and $\overline{B}^0 \to D^0(\overline{D}^0)\overline{K}^{*0}$ decays

As we have seen, the neutral $B \to DK$ decays amplitudes proceed both through $b \to c$ and $b \to u$ transitions, and are sensitive to γ through their interference.

However, in the case of B^0 decays, the phenomenon of $B^0 - \overline{B}^0$ mixing has to be considered. If both B^0 and $\overline{B}^0$ can decay to the same final state f, then it has to be taken into account that f can be reached from an initial B^0 state, by a $b \to c$ or $b \to u$ (technically, here we should write, $\bar{b} \to \bar{c}$ and $\bar{b} \to \bar{u}$, but we avoid doing that for simplicity and, by $b \to u$, we mean both $b \to u$ and $\bar{b} \to \bar{u}$ transitions) transition, but also from an initial B^0 state that mixed, followed by a $b \to c$ or $b \to u$ transition of the $\overline{B}^0$ meson.

CP violation studies of these decays will give sensitivity to γ (the weak phase of V_{ub}^*, $V_{ub}^* = |V_{ub}|e^{i\gamma}$) through the interference of the decay amplitudes and also to β (the weak phase of V_{td}, $V_{td} = |V_{td}|e^{i\beta}$) through the mixing process. These decays can be used to measure the combination of weak phases $2\beta + \gamma$ and, from the experimental point of view, a tagging procedure of the neutral B meson flavor and a time-dependent analysis are necessary to access this information.

The arising of a β phase and the need of a time-dependent analysis can be avoided if the final states contain a particle which allows to unambiguously identify if a B^0 or $\bar{B}^0$ has

decayed. This is the case of neutral B^0 mesons decaying into $\bar{D^0}K^{*0}[K^+\pi^-]$ final states through the sign of the electric charge of the K.

The work presented in this thesis, performed in the spirit of continuing to investigate several methods to constraint γ, consists of studying the decay modes $B^0 \to \overline{D}^0(D^0)K^{*0}$ and $\overline{B}^0 \to D^0(\overline{D}^0)\overline{K}^{*0}$, where the K^{*0} is reconstructed into $K^+\pi^-$ and the $\overline{K}^{*0}$ into $K^-\pi^+$. In this case, the presence of a K^+ in the final state will tag the neutral B that decayed as a B^0 while the presence of a K^- in the final state will tag the neutral B that decayed as a $\overline{B}^0$.

The two measurements here presented are:

- The Dalitz analysis, with neutral D reconstructed in the $K_S\pi^+\pi^-$ final state.
- The ADS analysis, with neutral D reconstructed in the $K^\pm\pi^\mp$, $K^\pm\pi^\mp\pi^0$ and $K^\pm\pi^\mp\pi^\mp\pi^\pm$ final states.

Now that almost all the possible analyses have been performed with the charged $B \to DK$ decays, the work presented here is a starting point for constraining γ from neutral $B \to DK$ decays. One thing that has to be kept in mind about neutral $B \to DK$ decays is that, despite the fact that the branching fraction are smaller than the ones for charged $B \to DK$ decays (by a factor of approximately $\frac{|C|^2}{|T|^2}$), the r_B ratio is expected to be larger (of the order ≈ 0.4 instead of ≈ 0.1, see eq. 2.3 and 2.4). This r_B ratio has never been measured for any neutral $B \to DK$ channel and *BABAR* , with low statistics, sets a limit on $r_B(D^0K^{*0}) < 0.4\,@\,90\%$ probability [73]. Depending on the value of r_B, the measurement of γ using neutral decays can be as precise (or better) than the one obtained from charged B decays. A large value of r_B in these decay modes can also be of interest for future experiments, as LHCb, since these channels involve only charged particles in the final state.

2.6.1 Introducing k, δ_S and r_S parameters

In contrast with $B^+ \to \overline{D}^0(D^0)K^+$, for $B^0 \to D^0K^{*0}$ decays, the natural width of the K^{*0} being not small ($\sim$50 MeV), the interference with other $B^0 \to \overline{D}^0(K\pi)^0_{\rm non-K^*}$ processes may not be negligible. This changes the relationships between the unitarity angle γ and the experimental observables. We follow here the formalism and the idea suggested in [33]. The amplitudes of the $\overline{B}^0 \to (D^0X_s^0)_p$ and $\overline{B}^0 \to (\overline{D}^0X_s^0)_p$ processes, can be expressed as:

$$A(\overline{B}^0 \to (D^0X_s^0)_p) = A_c(p)e^{i\delta_c(p)} \tag{2.18}$$
$$A(\overline{B}^0 \to (\overline{D}^0X_s^0)_p) = A_u(p)e^{i\delta_u(p)}e^{-i\gamma} \tag{2.19}$$
$$A(D^0 \to f) = A_f e^{i\delta_f} \tag{2.20}$$
$$A(D^0 \to \bar{f}) = A_{\bar{f}} e^{i\delta_{\bar{f}}}\,, \tag{2.21}$$

where $A_c(p)$, $A_u(p)$, A_f and $A_{\bar{f}}$ are real and positive, X_s^0 is a state with strangeness and p indicates a point in the phase space of the final state $D^0X_s^0$ (A_c, A_u, δ_c and δ_u vary as a function of p). The subscript c and u refer to the $b \to c$ and $b \to u$ transitions, respectively. The amplitudes $A_c(p)e^{i\delta_c(p)}$ and $A_{up}e^{i\delta_{up}}e^{-i\gamma}$ include both the resonant $\overline{B}^0 \to D^0/\overline{D}^0K^{*0}$ processes and the non-resonant contributions.

The amplitude of the process $\overline{B}^0 \to D[\to f]X_s^0$, where D indicates either a D^0 or a $\overline{D}^0$ decaying to the final state f, can be written as

$$A(\overline{B}^0 \to (D[\to f]X_s^0)_p) = A(\overline{B}^0 \to (D^0X_s^0)_p)A(D^0 \to f) + A(\overline{B}^0 \to (\overline{D}^0X_s^0)_p)A(\overline{D}^0 \to f) = A_c(p)A_f e^{i(\delta_c(p)+\delta_f)} + A_u(p)A_{\bar{f}}e^{i(\delta_u(p)+\delta_{\bar{f}}-\gamma)}\,. \tag{2.22}$$

and the rate of the process $\overline{B}^0 \to D[\to f]X_s^0$ is

$$\Gamma(\overline{B}^0 \to D[\to f]X_s^0) = \int dp\left(A_c^2(p)A_f^2 + A_u^2(p)A_{\bar{f}}^2 + 2A_c(p)A_fA_u(p)A_{\bar{f}}Re(e^{i(\delta(p)+\delta_D-\gamma)})\right)\,, \tag{2.23}$$

where $\delta(p) = \delta_u(p) - \delta_c(p)$ and $\delta_D = \delta_{\bar{f}} - \delta_f$. The rate for the charge-conjugated mode is the one in Eq. (2.23) with $\gamma \to -\gamma$.
From the expression for the amplitudes in 2.18 and 2.19, the partial rates $\Gamma(\overline{B}^0 \to D^0X_s^0)$ and $\Gamma(\overline{B}^0 \to \overline{D}^0X_s^0)$ are

$$\Gamma(\overline{B}^0 \to D^0X_s^0) = \int dp\,|A_c^2(p)|\,, \tag{2.24}$$

$$\Gamma(\overline{B}^0 \to \overline{D}^0X_s^0) = \int dp\,|A_u^2(p)|\,. \tag{2.25}$$

In case of a Dalitz analysis, the partial decay rate in eq. 2.11 becomes:

$$d\Gamma(\overline{B}^0 \to D[\to f]X_s^0) \propto A_f^2 + \frac{\int dpA_u^2(p)}{\int dpA_c^2(p)}A_{\bar{f}}^2 + 2\frac{\int dpA_c(p)A_u(p)Re(e^{i(\delta(p)+\delta_D-\gamma)})}{\int dpA_c^2(p)}A_fA_{\bar{f}} = A_f^2 + \frac{\int dpA_u^2(p)}{\int dpA_c^2(p)}A_{\bar{f}}^2 + 2\sqrt{\frac{\int dpA_u^2(p)}{\int dpA_c^2(p)}}\frac{\int dpA_c(p)A_u(p)Re(e^{i(\delta(p)+\delta_D-\gamma)})}{\sqrt{\int dpA_c^2(p)\int dpA_u^2(p)}}A_fA_{\bar{f}},$$

where p is the coordinate of the B Dalitz plane and the dependence of A_f and $A_{\bar{f}}$ on the D Dalitz plane point is not explicit (with respect to eq. 2.11, here $A_f \equiv A_{12,13}$ and $A_{\bar{f}} \equiv A_{13,12}$).

Following the same notation as in [33], we introduce the quantities r_S, k and δ_S:

$$r_S^2 = \frac{\Gamma(\overline{B}^0 \to \overline{D}^0X_S^0)}{\Gamma(\overline{B}^0 \to D^0X_S^0)} = \frac{\int dp\,|A_u^2(p)|}{\int dp\,|A_c^2(p)|} \tag{2.26}$$

$$ke^{i\delta_S} = \frac{\int dp\;A_c(p)A_u(p)e^{i\delta(p)}}{\sqrt{\int dp\,|A_c^2(p)|\;\int dp\,|A_u^2(p)|}}\,, \tag{2.27}$$

where $0 \le k \le 1$ for the Schwartz inequality and $\delta_S \in [0, 2\pi]$. The parameters k and r_S allow to write the observables for $B \to DK^*$ channels in a functional form similar to the two-body case, as it is shown below with two examples (the partial decay rate for a Dalitz analysis and R_{ADS}).

Substituting the definitions in eq. 2.26 and eq. 2.27, the expression for the partial decay rate is written:

$$d\Gamma(\overline{B}^0 \to D[\to f]X_S^0) \propto A_f^2 + r_S^2A_{\bar{f}}^2 + 2r_Sk\mathcal{R}e\left(A_fA_{\bar{f}}e^{i\delta_D}e^{i\delta_S+\gamma}\right). \tag{2.28}$$

In case of an ADS analysis, starting from the expression in eq. 2.7, R_{ADS} will be written as follows (neglecting the small term x, as discussed in sec. 2.2.2):

$$R_{ADS} = \frac{\Gamma(B^+ \to \bar{f}K^+) + \Gamma(B^- \to fK^-)}{\Gamma(B^+ \to fK^+) + \Gamma(B^- \to \bar{f}K^-)} =$$
$$\frac{2\int dpA_u^2(p)A_f^2 + 2\int dpA_c^2(p)A_{\bar{f}}^2 + 4\int dpA_c(p)A_u(p)\mathcal{R}ee^{i(\delta(p)+\delta_D)}\cos\gamma A_f A_{\bar{f}}}{2\int dpA_c^2(p)A_f^2} =$$
$$\frac{\int dpA_u^2(p)}{\int dpA_c^2(p)} + \frac{A_{\bar{f}}^2}{A_f^2} + 2\sqrt{\frac{\int dpA_u^2(p)}{\int dpA_c^2(p)}}\frac{A_{\bar{f}}}{A_f}\frac{\int dpA_c(p)A_u(p)A_{\bar{f}}Re(e^{i(\delta(p)+\delta_D)})}{\sqrt{\int dpA_c^2(p)\int dpA_u^2(p)}}\cos\gamma$$

which leads to:

$$R_{ADS} = r_S^2 + r_D^2 + 2kr_S r_D\cos(\delta_S + \delta_D)\cos\gamma$$

In the limit of a $B \to$2-body decay, such as $\overline{B}^0 \to D\bar{K}^0$, we have:

$$\begin{aligned} & r_S \to r_B \equiv \frac{|A(\overline{B}^0 \to \overline{D}^0\bar{K}^0)|}{|A(\overline{B}^0 \to D^0\bar{K}^0)|}\,, \\ & \delta_S \to \delta_B \equiv \text{strong phase of } \frac{\mathrm{A}(\overline{\mathrm{B}}^0 \to \overline{\mathrm{D}}^0\bar{\mathrm{K}}^0)}{\mathrm{A}(\overline{\mathrm{B}}^0 \to \mathrm{D}^0\bar{\mathrm{K}}^0)}\,, \\ & k \to 1\,. \end{aligned} \tag{2.29}$$

Although we show here only two examples (the partial decay rate for a Dalitz analysis and R_{ADS}), it is in general true that, in $B \to DK^*$ decays, the observables for the GLW, ADS and Dalitz method can be written in a functional form similar to the one used for the two-body $B \to DK$ decay, provided that the change of variables $r_B^2 \to r_S^2$, $\delta_B \to \delta_S$ and $r_B \to r_S k$ is performed. With respect to the two-body decay case, in presence of a K^{*0} the parameter k, that accounts for possible contributions from other $(K\pi)^0_{\mathrm{non-K^*}}$ processes, is an additional unknown of the system and should in principle be determined on data. In order to avoid this additional unknown, a study has been performed to evaluate the possible variations of k, as detailed in sec. 2.6.2.

2.6.2 Evaluation of k and r_S in $B^0 \to \overline{D}^0(D^0)[K^+\pi^-]$ and $\overline{B}^0 \to D^0(\overline{D}^0)[K^-\pi^+]$ decays

To evaluate the expected values for the parameters r_S and k we have built a hadronic model for the $B^0 \to \bar{D}^0K^+\pi^-$ decay. In fact we have seen in the previous section that these parameters are the result of an effective parametrization of the variation of r_B and of the strong phases over the B Dalitz plane and can be obtained by integrating over some portion of the B Dalitz plot, corresponding in our case to the K^{*0} region.

Resonance contributions

We discuss now the hadronic model for the $B^0 \to \bar{D}^0K^+\pi^-$ decay. Following the processes explained in the previous paragraph, the Dalitz plot can be modelled in terms of the following

resonances :

$$\begin{array}{lll} B \to \bar{D}^0 X & X \to K^+\pi^- & X = (K^*(892), K_0^*(1430), K_2^*(1430), K^*(1680)) \\ B \to K^+ Y & Y \to \bar{D}^0\pi^- & Y = (D_0^*(2308)^0, D_2^*(2460)^0) \\ B \to \pi^- Z & Z \to \bar{D}^0 K^+ & Z = (D_{s,2}(2573)^{\pm}) \end{array} \quad (2.30)$$

The model assumed for the decay parametrises the amplitude A at each point k of the Dalitz plot as a sum of two-body decay matrix elements and a non-resonant term according to the following expression :

$$A_{c_k(u_k)} e^{i\delta_{c_k(u_k)}} = \sum_j a_j e^{i\delta_j} BW_k^j(m, \Gamma, s) + a_{nr} e^{i\phi_{nr}} \quad (2.31)$$

where c_k (u_k) indicates the Cabibbo allowed (suppressed) decay in each point k of the Dalitz plot. Each term of the sum is parametrized with an amplitude (a_j or a_{nr}) and a phase (δ_j or ϕ_{nr}). The factor $BW_k^j(m^j, \Gamma^j, s^j)$ is the Lorentz invariant expression for the matrix element of a resonance j as a function of the position k in the B Dalitz plot; the functional dependence varies with the spin s^j of the resonance according to the isobar model [49]. The total phase and amplitude are arbitrary. For building the decay model we used, whenever available, experimental information. When this was missing, we made reasonable hypotheses, as detailed in the following.

The branching fraction $B^0 \to \bar{D}^0 K^{*0}$ has been measured [8]:

$$Br(\bar{B}^0 \to \bar{D}^0 K^{*0}) \times Br(K^{*0} \to K^+\pi^-) = (2.3 \pm 0.3) \times 10^{-5}. \quad (2.32)$$

The contribution from higher K^{**} resonances can be evaluated by using measurements performed in the B^0 sector with a final states containing a D^- meson ([50, 51]) :

$$\frac{B^0 \to D^- K^{*+}(892)(K_S\pi^+)}{B^0 \to D^- K_S\pi^+} = 0.66 \pm 0.08 \quad (2.33)$$

The use of this information is rather clean, since the processes which are contributing to the production of $D^- K_s\pi^+$ final states are largely dominated by the two body intermediate states containing K^{*0} and higher K^{**} resonances [52]. We make a SU(2) hypothesis, assuming that this relative contribution is not affected when exchanging $D^- \to D^0$ and $K^{*+} \to K^{*0}$.

A measurement is also available to partially define the D^{**} part of the Dalitz plot [8]:

$$Br(B^0 \to D_{J=2}^{**-} K^+) \times Br(D_{J=2}^{**-} \to \bar{D}^0\pi^-) = (1.8 \pm 0.4 \pm 0.3) \times 10^{-5} \quad (2.34)$$

The measurement on the D^{**} production from the above branching fractions involves only diagrams at the tree level (T). Nevertheless, only 2^+ final states have been measured so far. We can make the hypothesis that the 0^+ states decaying into Dπ modes are as abundant as the 2^+ states. The measurements presented so far are relative to $b \to c$ transitions, to account for $b \to u$ transition some hypothesis has to be made. For the nominal model the ratio between the $b \to u$ and the $b \to c$ amplitudes in case of K^{*0} and excited K mesons has been taken to be equal to 0.4. The phases have been taken arbitrarily.

The results are summarized in Tab. 2.4 and a corresponding Dalitz plot (with all the strong phases set to zero) is shown in Fig.2.11 for illustration.

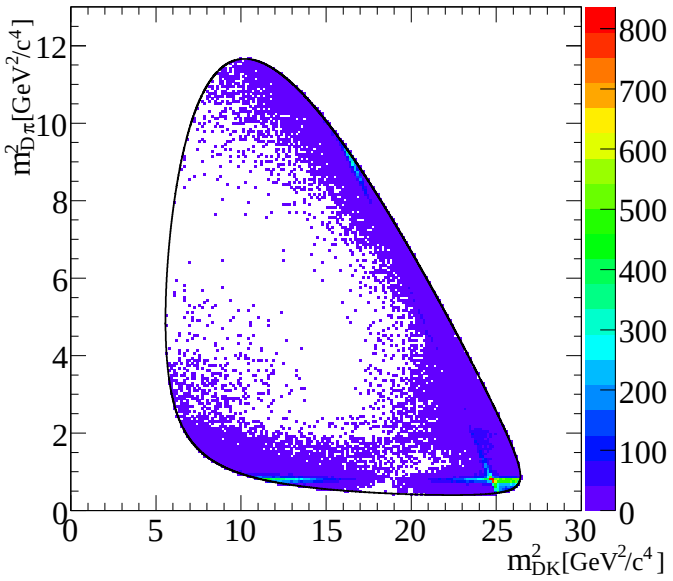

Figure 2.11: Dalitz plot for $B^0 \to \bar{D}^0 K^+ \pi^-$ using the values of the amplitudes given in Tab. 2.4. All strong phases have been all set to zero.

	$Mass(GeV/c^2)$	$Width(GeV/c^2)$	J^P	$a(b \to c)$	$a(b \to u)$
$D_{s,2}(2573)^{\pm}$	2.572	0.015	2^+	-	0.02
$D_2^*(2460)^{\pm}$	2.459	0.029	2^+	1.0	-
$D_0^*(2308)^{\pm}$	2.403	0.283	0^+	1.0	-
$D_0^*(2010)^{\pm}$	2.0100	0.000096	1^-	not included	-
$K^*(892)^0$	0.89610	0.0507	1^-	1.0	0.4
$K_0^*(1430)^0$	1.412	0.294	0^+	0.3	0.12
$K_2^*(1430)^0$	1.4324	0.109	2^+	0.15	0.06
$K^*(1680)^0$	1.717	0.322	1^-	0.2	0.08
Non resonant	-	-	-	not included	not included

Table 2.4: List of mass, widths and quantum numbers of the resonances considered in our model. The last two columns present the chosen values of the coefficients a_j in Eq. 2.31 for the $b \to c$ and $b \to u$ transitions respectively. Note that the phase δ_j are not indicated and their choice is arbitrary, since no experimental information is available. Fig. 2.11 corresponds to a Dalitz model obtained with the amplitudes given here and all the strong phases set to zero.

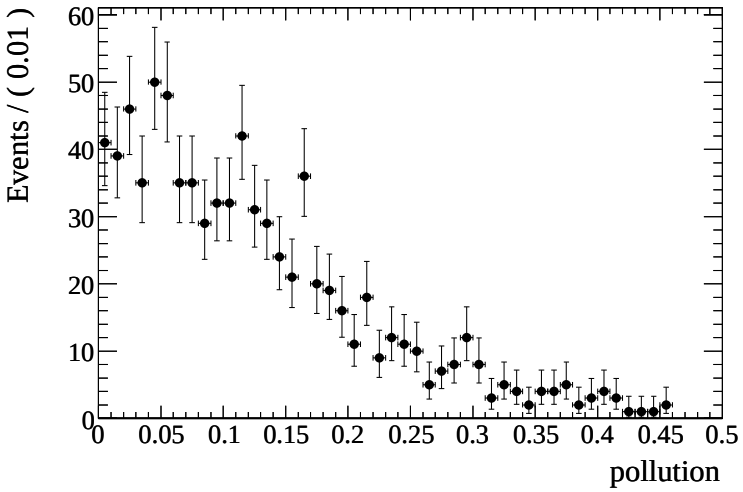

Figure 2.12: Pollution of non-K^{*0} events in the K^{*0} mass region ($\pm$50 MeV around its nominal mass), as defined in eq. 2.35,. The distribution is obtained by randomly varying all the strong phases and the amplitudes within $\pm$ 30% the nominal values given in Tab. 2.4.

Numerical analysis

To give an idea of the overlap of the different resonances in Fig. 2.12 we show the pollution of non-$K^{*0}(892)$ events in the mass region defined within ± 50 MeV/c^2 around its nominal mass. The pollution has been defined as the ratio of the integrals, in the K^{*0} mass region, of the K^{*0} amplitudes (V_{ub} and V_{cb}) over the total.

$$pollution = \frac{\int dp\ |A_p(K^*)|^2}{\int dp\ |A_p(total)|^2} \tag{2.35}$$

The distribution shown in Fig. 2.12 has been obtained by randomly varying all the strong phases (between [0-2π]) and amplitudes (between [0.7-1.3] of their nominal value given in Tab. 2.4). It can be noticed that the pollution of non-K^* events in the K^* mass region can be quite important and up to 40%. Finally, in Fig. 2.13 we show the variation of r_B along the Dalitz plot.

We have seen in the previous section that following the the formalism and the ideas suggested in [33] we can integrate over some portion of the B Dalitz plot and to use an effective parametrization of the variation of r_B and of the strong phases, resulting in the introduction of three new variables r_S, δ_S and k.

In the following we caracterize the B Dalitz plot in terms of the parameters k and r_s of the new parametrization.

We first consider a region within ± 50 MeV/c^2 of the nominal mass of the $K^{*0}(892)$ resonance. In Fig. 2.14 we show the distribution of r_S, k and kr_S obtained by randomly varying all the strong phases between 0 and 2π and the amplitudes between 0.7 and 1.3 of their nominal value. The amplitudes for $D_{s,2}(2573)^{\pm}$ are varied between 0 and twice their

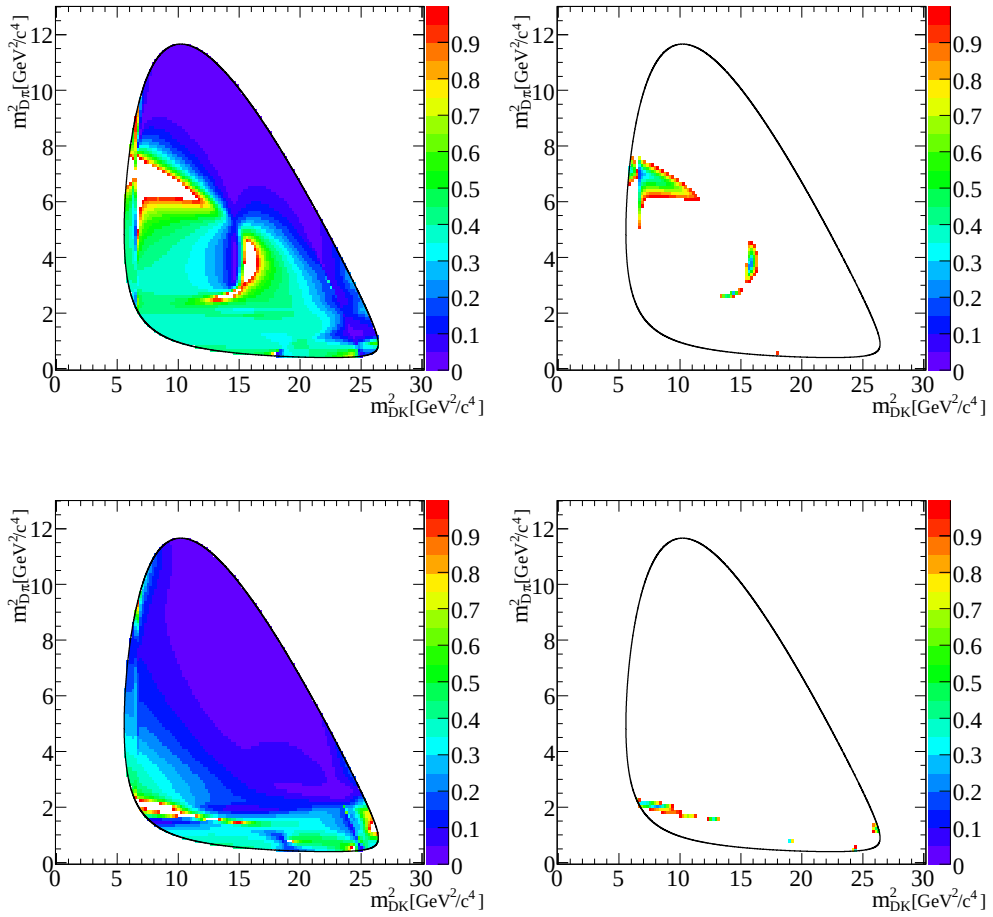

Figure 2.13: Variation of r_S along the Dalitz plot (plots on the left side). If the value of r_B is found to be larger than unity it is not displayed in the same plot but in a separate one (plots on the right side) as $1/r_B$. All the plots have been obtained with the amplitudes set to the nominal values of Table 2.4. For the plots on the top row all strong phases have been set to zero. For the plots on the bottom row a random set of strong phases has been taken.

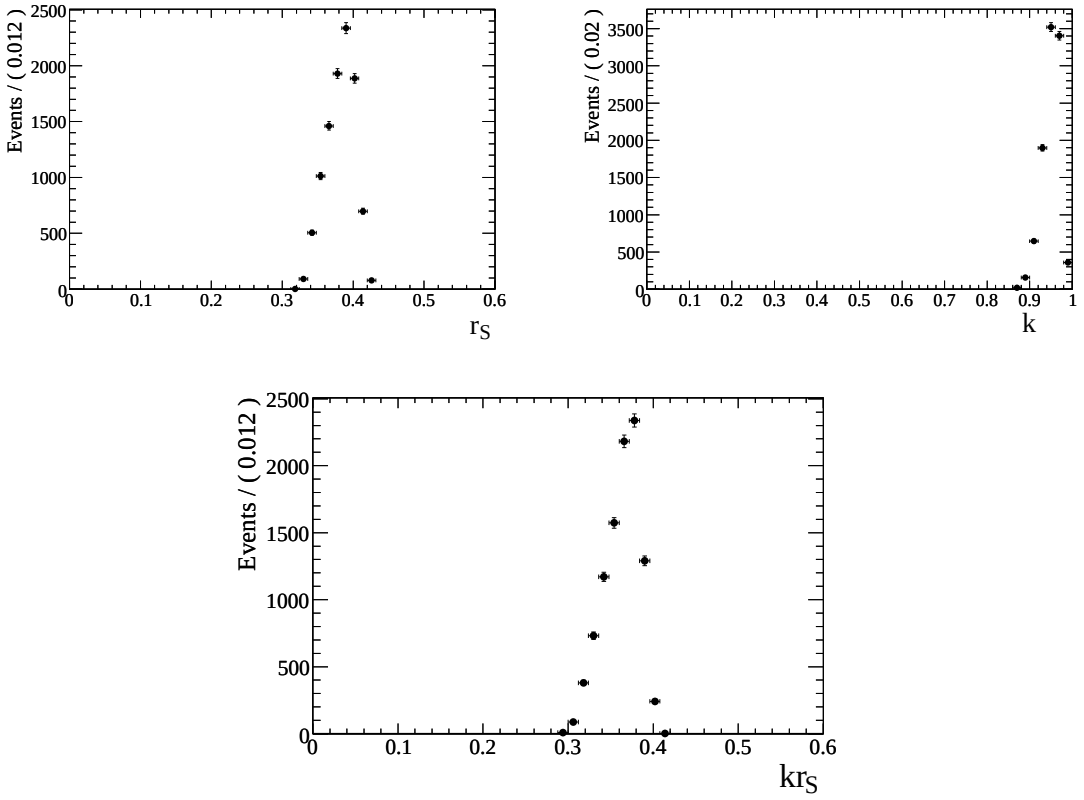

Figure 2.14: Distribution of r_S, k and kr_S in a region within $\pm$ 50 MeV the nominal mass of the $K^{*0}(892)$ resonance ($m_{K\pi}$ in the range [0.7159, 0.8951] GeV$^2/c^4$). These distributions have been obtained by randomly varying all the strong phases between 0 and 2π, the amplitudes between 0.7 and 1.3 of their nominal value. The relative $b \to u$ contribution for K^* has been fixed to 0.4 and he $b \to u$ amplitude of the $D_{s,2}(2573)^{\pm}$ has been varied between 0 and twice its nominal value. The nominal model is given in Tab. 2.4).

nominal value. The $b \to u$ contribution of K^{*0} has been fixed to 0.4. From these plots we can notice that, in $K^{*0}(892)$ mass region, r_S can vary between 0.3 and 0.45 depending upon the values of the phases and of the amplitudes contributing in the K^{*0} region. In the absence of pollution we would have expected $r_S = r_B = 0.4$. The distribution of k is quite narrow and the possible values are lower than unity ($k < 1$ by definition) by no more than 10%. We expect that, in the majority of the cases, the sensitivity (see the distribution of kr_S) of the analysis is reduced due to the presence of other resonances in the K^* region. However it should be noted that the reduction of the sensitivity is not dramatic. Because the distribution of k is rather peaked, the value of k can be assumed as a fixed value and varied in the systematics. This is important since, for example for the Dalitz analysis, where r_S is fitted on data, it reduces the number of free parameters in the final fit.

For the sake of completeness (not used for the analyses presented in this thesis), we repeat the same exercise in two different regions of the Dalitz plot. The corresponding distributions of r_S, k and kr_S are shown in Fig. 2.15. The distributions of r_S and k are quite broad and

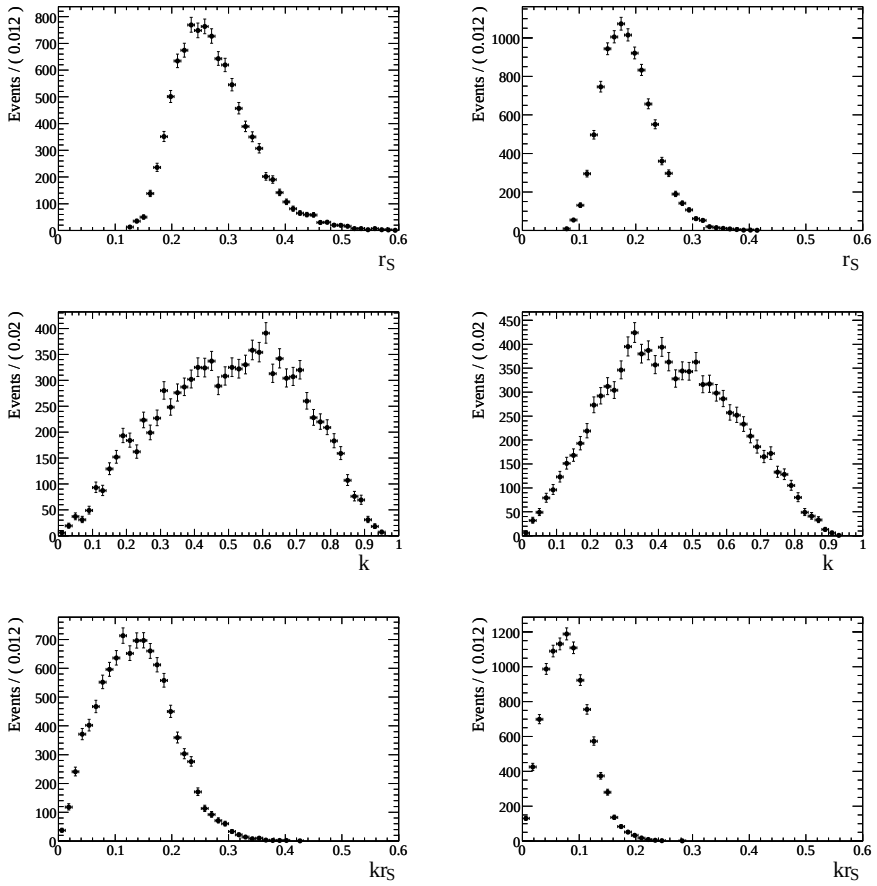

Figure 2.15: Distributions of r_s, k and kr_S in two different regions of the Dalitz plot. Left: within $\pm$ 80 MeV the nominal mass of the $K_0^*(1430)$ resonance ($m^2_{K\pi}$ in the range [1.8290, 2.2873] GeV$^2/c^4$. Right: in the region of $m^2_{K\pi}$ in the range [2.3, 3.5] GeV$^2/c^4$, this region is centered around the nominal $K^*(1680)^0$ mass.

they translate in a broad distribution for kr_s with a central value centered around 0.1. The sensitivity to γ is thus much reduced and it is strongly dependent upon the values of the amplitudes and of the strong phases which compose the Dalitz plot.

From these studies we conclude that only the region around the K^{*0} is interesting to measure the angle γ using a portion of the Dalitz space. To efficiently use the signal events in the other regions a complete Dalitz analysis (fitting the amplitudes and the strong phases) has to be performed.

Chapter 3

The *BABAR* Experiment

The *BABAR* experiment, located at the Stanford Linear Accelerator Center (SLAC) in California, has been optimized for the systematic study of *CP* violation in the B meson system. It involves a large international collaboration of more than 500 physicists. The experiment consists of a detector [35] built around the interactionregion of the high luminosity e^+e^- asymmetric collider PEP-II [36]. The geometry of the detector as well as the technical requirements of the main components have been designed in order to obtain the cleanest environment and the best efficiency to reconstruct the B meson decays.

In this chapter we describe the main features and performances of PEP-II and the *BABAR* detector.

3.1 The PEP-II accelerator

The PEP-II B-Factory is an asymmetric-energy e^+e^- collider designed to operate at a center of mass energy of $E_{CM} = 10.58\,\mathrm{GeV}$, corresponding to the mass of the $\Upsilon(4S)$ vector meson resonance. The $\Upsilon(4S)$ has a mass slightly above the $B\bar{B}$ threshold, and thus it decays almost exclusively into $B\overline{B}^0$ or B^+B^- pairs.

If the Υ is produced at rest, then the B mesons would have an average residual momentum of the order of $\sqrt{(M_{\Upsilon(4S)}/2)^2 - M_B^2} \sim 325\,\mathrm{MeV}/c$ [1]. With this momentum, the average distance covered by a B meson would be of the order of [2] $\beta\gamma c\tau_B \sim 30\mu m$ and it would be experimentally very difficult to measure the separation between the decay points of the two B mesons.

The PEP-II machine collides a 9.0 GeV electron beam head-on with a 3.1 GeV positron beam, in this way the Lorentz boost of the $\Upsilon(4S)$ is $\beta\gamma = \frac{E_{e^-} - E_{e^+}}{E_{CM}} \sim 0.56$, resulting in an average separation between the two B meson of the order of 250 μm, compatible with the *BABAR* vertex resolution, as it will be shown in the following.

An overview of the accelerator is shown in Fig. 3.1.

Electrons and positrons are accelerated in the 3.2 km long SLAC linac and accumulated into two 2.2 km long storage rings, called HER (high-energy ring, in which the electrons cir-

[1] We use $M_{\Upsilon(4S)}$ =10.58 GeV/c^2 and $M_B = 5.28$ GeV/c^2.

[2] The factor $\beta\gamma$ arising from a momentum of the B of 325 MeV/c is $\beta\gamma \sim 0.061$ and the B meson lifetime is $\tau_B = (1.530 \pm 0.009) \times 10^{-12} s$[8].

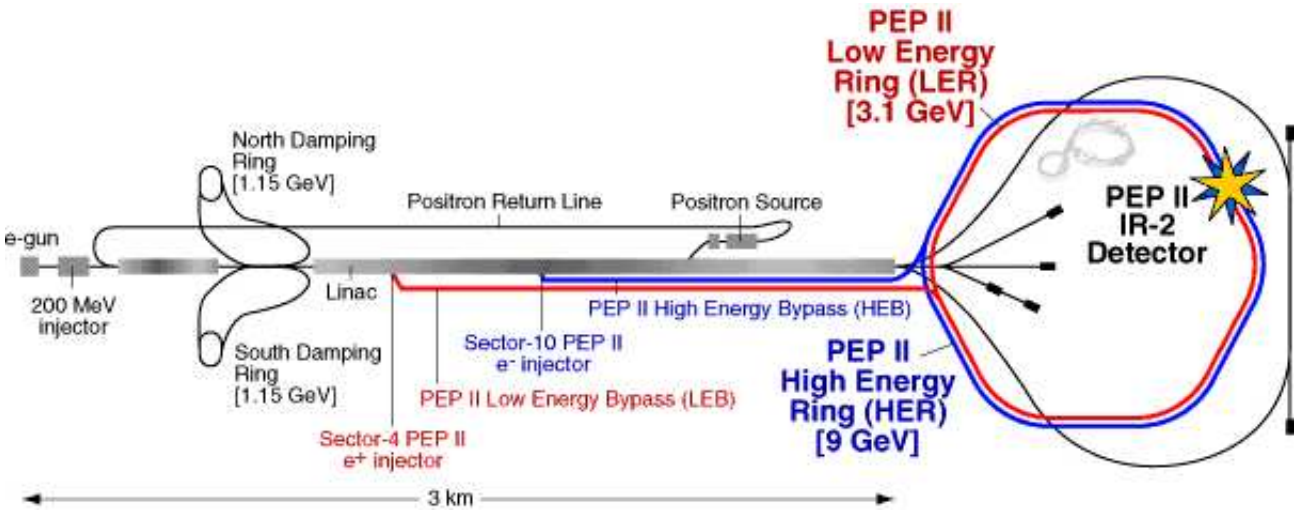

Figure 3.1: Overview of the PEP-II B-Factory.

culate) and LER (low-energy ring, in which the positrons, produced in the linac by collisions of 30 GeV electrons on a target, circulate).

In proximity of the interaction region the beams are focused by a series of offset quadrupoles (labelled Qx) and bent by means of a pair of dipole magnets, which allow the bunches to collide head-on and then to separate. The tapered B1 dipoles, located at $\pm$ 21 cm on either side of the interaction point (IP), and the Q1 quadrupoles operate inside the field of the *BABAR* superconducting solenoid, while Q2, Q4, and Q5, are located outside or in the fringe field of the solenoid (Fig. 3.3). The interaction region is enclosed in a water-cooled beam pipe consisting of two thin layers of beryllium with a water channel in between. Its outer radius is about 28 mm. The total thickness of the central beam pipe section at normal incidence corresponds to 1.06 % of a radiation length.

The beam pipe, the permanent magnets and the Silicon Vertex Tracker (SVT) are assembled, aligned and then enclosed in a 4.5 m long support tube. This rigid structure is inserted into the *BABAR* detector, spanning the IP.

The *BABAR* data taking, started with the first collissions in PEP-II at the end of 1999 and ended in the first days of April 2008. *BABAR* has recorded an integrated luminosity of about 531 fb^{-1}, including about 54 fb^{-1} just below the $\Upsilon(4S)$ resonance, 433 fb^{-1} recorded at the $\Upsilon(4S)$ and 44 fb^{-1} at other Υ resonances. The *BABAR* recorded luminosity until the end of data taking is shown in Fig. 3.2.

PEP-II surpassed its design performances, both in terms of the instantaneous luminosity and the daily integrated luminosity (see Tab. 3.1), achieving the peak value of $1.2 \times 10^{34}\ cm^{-2}\ s^{-1}$ during Run 6. A significant improvement to the integrated luminosity has been achieved between December 2003 and March 2004 with the implementation of a novel mode of operation of PEP-II, called "trickle injection". Until the end of 2003, PEP-II typically operated in a series of 40-minute fills during which the colliding beams coasted: at the end of each fill, it took about three to five minutes to replenish the beams for the next fill, and during this period the *BABAR* data acquisition system had to be turned off for

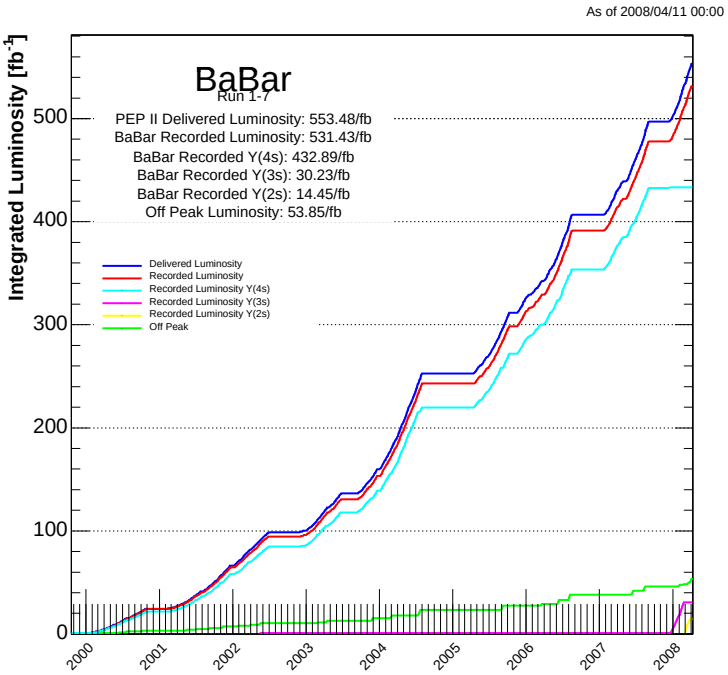

Figure 3.2: PEP-II delivered and *BABAR* recorded integrated luminosity in Run 1 to Run 7 (from October 1999 to April 2008).

Parameters	Design	2007
Energy HER/LER (GeV)	9.0/3.1	9.0/3.1
Current HER/LER (A)	0.75/2.15	1.9/2.9
# of bunches	1658	1722
Bunch length (mm)	15	11–12
Luminosity ($10^{33} cm^2/s$)	3	12
Integrated luminosity (pb^{-1}/day)	135	911

Table 3.1: PEP beam parameters. Values are given both for the design and for the records achieved during 2007.

detector safety. With the new technique, the *BABAR* detector can keep taking data virtually uninterrupted while the linac continuously injects electron and positron bunches (at a rate up to 10 Hz in the HER and 20Hz in the LER) into the two PEP-II storage rings. This novel mode of operation allows an increase of 20 to 30% of the integrated luminosity. Moreover, the continuous injection makes the storage of particles more stable, so that PEP-II rings are easier to operate and beam losses are far less frequent than with the previous operational mode. This result is very important since, after a loss of the stored beams, it takes approximately 15 minutes to refill the two beams during which obviously no data taking is allowed.

3.2 The *BABAR* detector

The design of the *BABAR* detector is optimized for *CP* violation studies, but it is also well suited to do precision measurements in other B and non B physics. To achieve the goal of performing accurate measurements there are many requirements:

- a large and uniform acceptance, in particular down to small polar angles relative to the boost direction, to avoid particle losses. Although the boost originated by the asymmetric beams is not a big one, optimizing the detector acceptance leads to an asymmetric detector;
- a good vertex resolution;
- an excellent detection efficiency and an excellent precision on the momentum measurement for charged particles with transverse momentum ranging between 60 MeV/c and 4 GeV/c;
- an excellent energy and angular resolution for photons and π^0 s with energy down to 20 MeV and up to 5 GeV;
- a good discrimination between e, μ, π, K, p over a wide kinematic range;
- neutral hadrons identification capability.

Since the average momentum of charged particles produced in B meson decays is below 1 GeV/c, the errors on the measured track parameters are dominated by multiple Coulomb scattering, rather than intrinsic spatial resolution of the detectors. Similarly, the detection efficiency and energy resolution of low energy photons are severely impacted by material in front of the calorimeter. Thus, special care has been given to keep the material in the active volume of the detector to a minimum. A schematic view of the *BABAR* detector is shown in Fig. 3.3. The *BABAR* superconducting solenoid, which produces a 1.5 T axial magnetic field, contains a set of nested detectors, which are – going from inside to outside – a five layers Silicon Vertex Tracker (SVT), a central Drift Chamber (DCH) for charged particles detection and momentum measurement, a fused-silica Cherenkov radiation detector (DIRC) for particle identification, and a CsI(Tl) crystal electromagnetic calorimeter for detection of photons and electrons. The calorimeter has a barrel and an end-cap which extends asymmetrically into the forward direction (e^- beam direction), where many of the collision products emerge. All the detectors located inside the magnet have practically full acceptance in azimuth (ϕ). The flux return outside the cryostat is composed of 18 layers of steel, which increase in thickness outwards, and are instrumented (the IFR) with 19 layers of planar resistive plate chambers (RPCs) or limited streamer tubes (LSTs) in the barrel and 18 in the end-caps. The IFR allows the muon identification, and also detects penetrating neutral hadrons. The right-handed coordinate system is indicated in Fig. 3.3. The z axis corresponds to the magnetic field axis and is offset relative to the beam axis by about 20 mrad in the horizontal plane. It is oriented in the direction of electrons. The positive y-axis points upward and the positive x-axis points away from the center of the PEP-II storage rings. A schematic view of the interaction region is shown in Fig. 3.4.

The next sections are dedicated to a description of each subsystem.

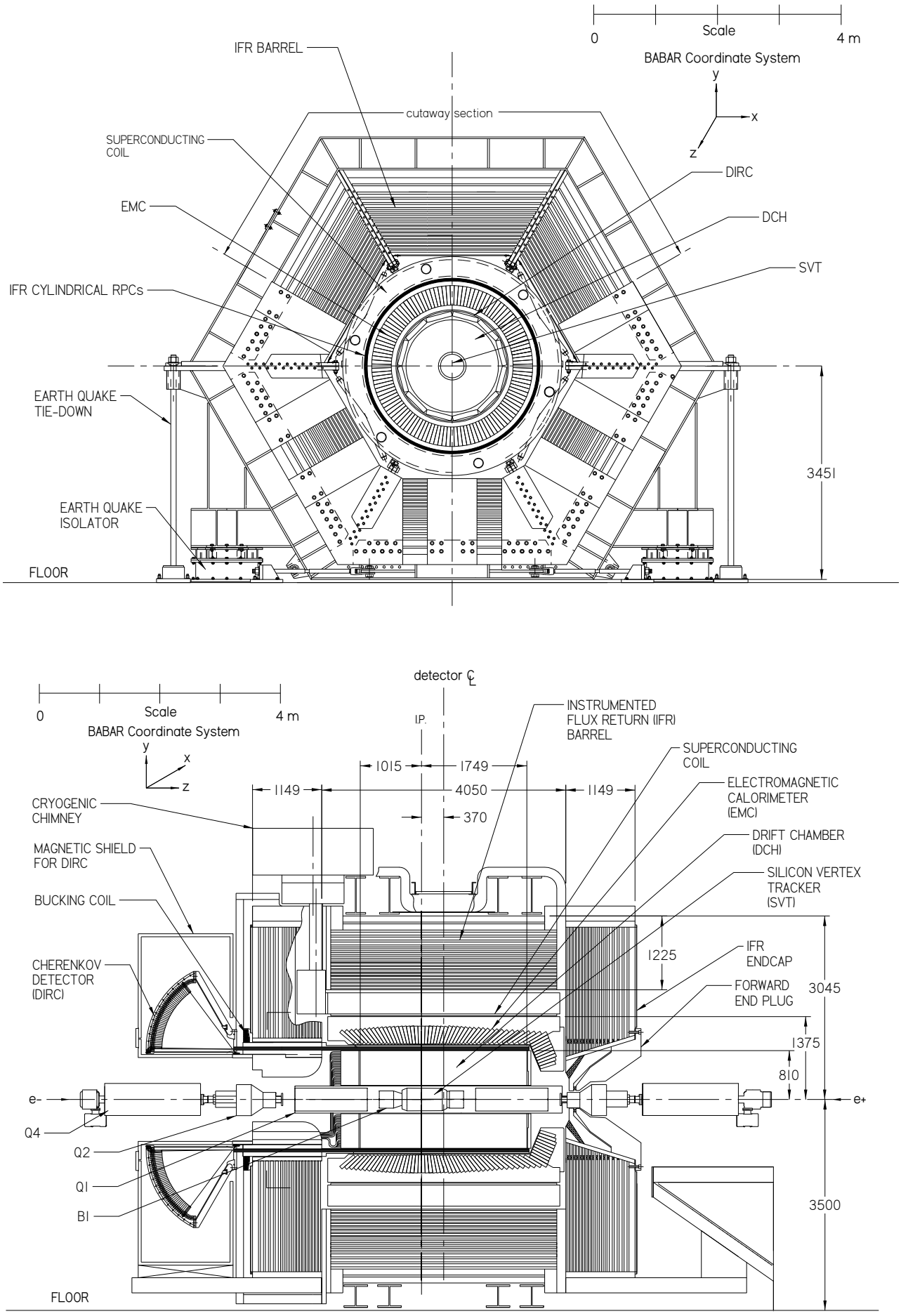

Figure 3.3: *BABAR* detector front view (top) and side view (bottom).

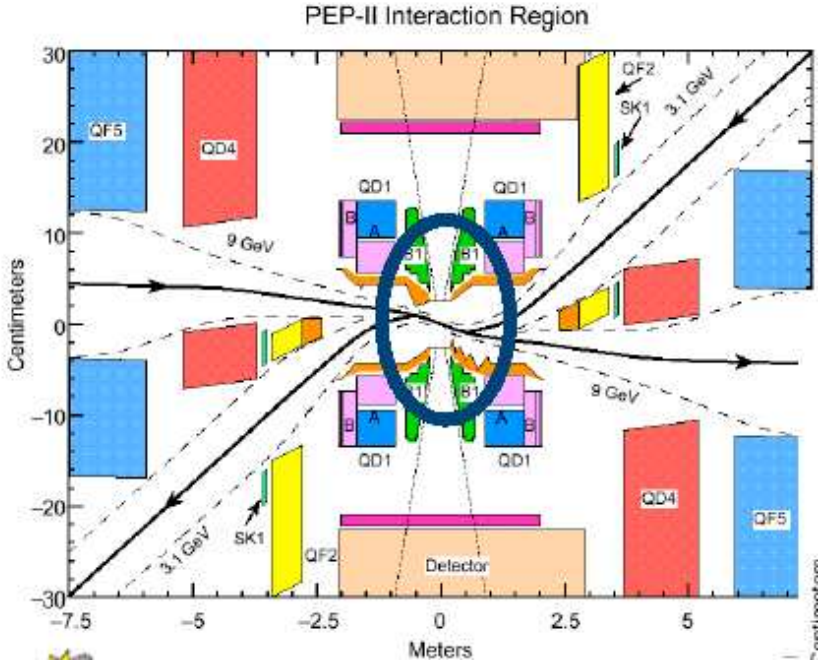

Figure 3.4: *Transverse view of the interaction region.*

3.2.1 The Silicon Vertex Tracker

The Silicon Vertex Tracker (SVT) provides a precise measurement of the decay vertices and of the charged particle trajectories near the interaction region. The mean vertex resolution along the z-axis for a fully reconstructed B decay must be better than 80 μm in order to avoid a significant impact on the time-dependent CP asymmetry measurement precision; a $100\mu m$ resolution in the $x - y$ transverse plane is necessary in reconstructing decays of bottom and charm mesons, as well as τ leptons. The SVT also provides standalone tracking for particles with transverse momentum too low to reach the drift chamber, like soft pions from D^* decays and many charged particles produced in multi-body B meson decays. Finally, the SVT supplies particle identification (PID) information both for low and high momentum tracks. For low momentum tracks the SVT dE/dx measurement is the only PID information available, for high momentum tracks the SVT provides the best measurement of the track angles, required to achieve the design resolution on the Cherenkov angle measured by the DIRC.

The design of the SVT is constrained by the components of the storage ring which have been arranged so as to allow maximum SVT coverage in the forward direction: the SVT extends down to 20° (30°) in polar angle from the beam line in the forward (backward) direction. Furthermore, it must have a small amount of material, so to reduce the multiple scattering which would affect the performance of the outer subdetectors. The solution which was adopted is a five-layer device with 340 double-sided silicon wafers mounted on a carbon-fiber frame (see Fig. 3.5). On the inner (outer) face of each wafer, strip sensors are located running orthogonal (parallel) to the beam direction, measuring the z (ϕ) coordinate of the

tracks. The wafers are organized in modules split into forward and backward sections: they are read out on their respective ends and the charge deposited by a particle is determined by the time over threshold of the signal on each strip. In total, 150,000 read-out channels are present. The inner three layers, containing six modules each, are placed close to the beam pipe (at 3.3, 4 and 5.9 cm from it) and dominate the determination of tracks position and angles. The outer two layers, containing 16 and 18 modules respectively, are arch-shaped, thus minimizing the amount of silicon needed to cover the solid angle, and placed close to the DCH (between 9.1 and 14.6 cm from the beam pipe) to help the track matching between the two detectors.

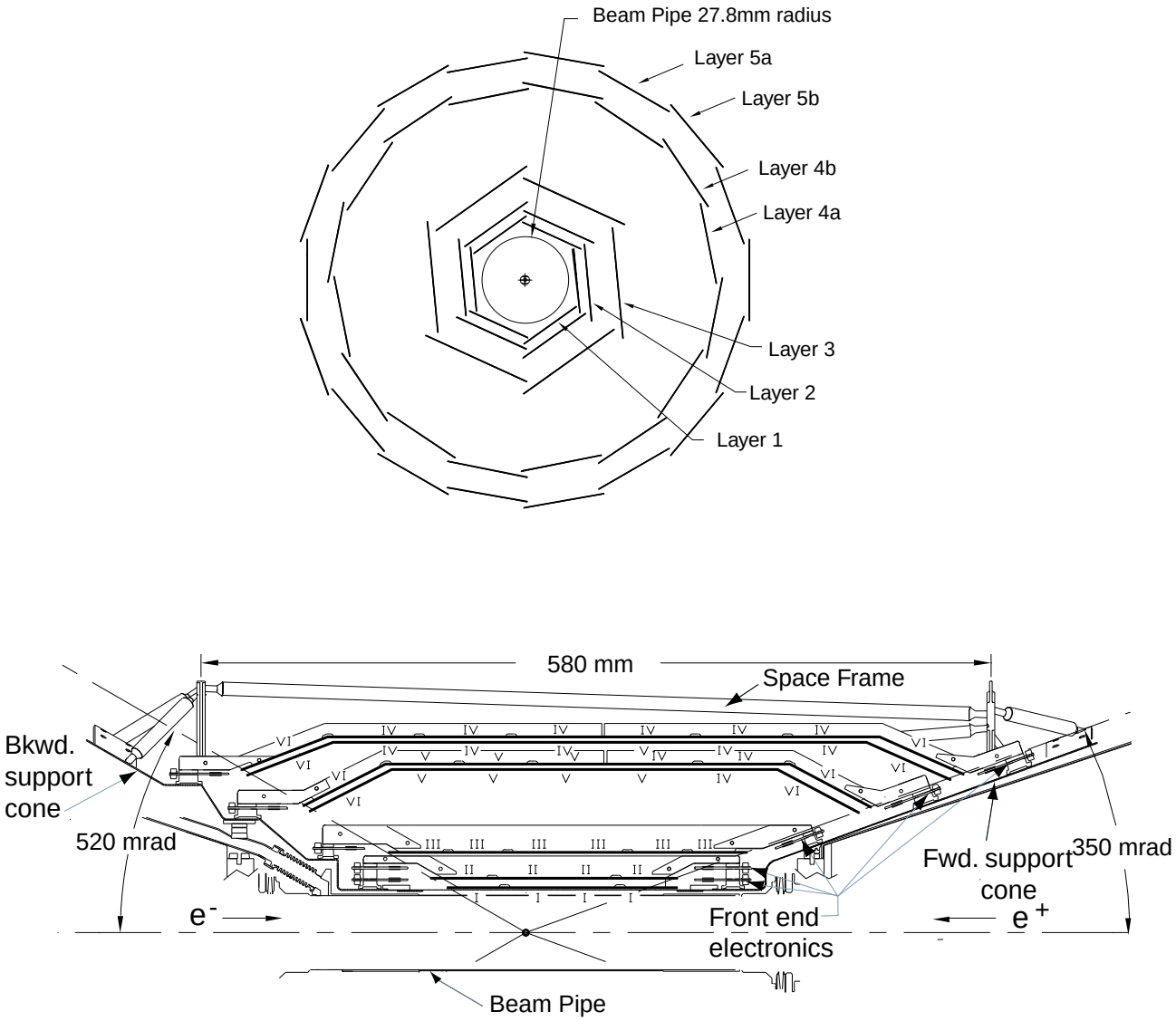

Figure 3.5: Schematic view of the SVT, transverse section (upper plot) and longitudinal section (bottom plot).

The total active silicon area is 0.96 m^2 and the geometrical acceptance is 90% of the solid

angle in the center-of-mass frame. The material traversed by particles corresponds to $\sim 4\%$ of a radiation length.

The SVT efficiency is calculated for each section of the modules by comparing the number of associated hits to the number of tracks crossing the active area of the module and is found to be 97%. The spatial resolution of SVT hits is determined by measuring the distance between the track trajectory and the hit for high-momentum tracks in two-prong events: it is generally better than $40\mu m$ in all layers for all track angles, allowing a precise determination of decay vertices to better than $70\mu m$ (see Fig. 3.6).

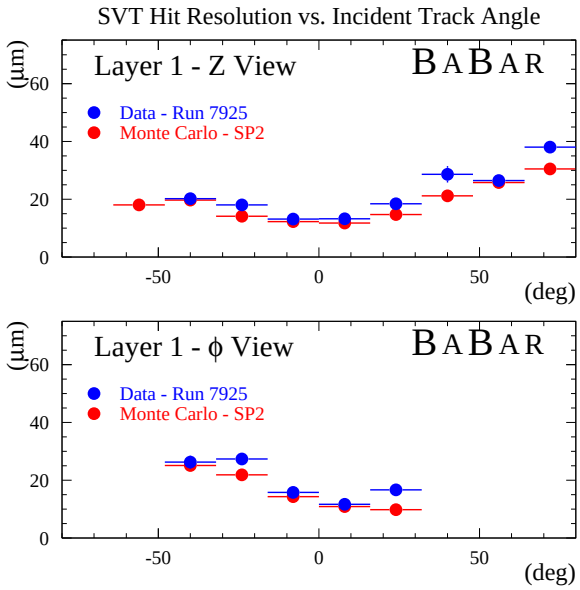

Figure 3.6: SVT resolution (layer 1) on the single hit, as a function of the track angle.

The SVT provides stand-alone tracking for low momentum particles that do not reach the drift chamber, with an efficiency estimated to be 20% for particles with transverse momenta of 50 MeV/c, rapidly increasing to over 80% at 70 MeV/c. Limited particle ID information for low momentum particles that do not reach the drift chamber and the Cherenkov detector is provided by the SVT through the measurement of the specific ionization loss, dE/dx, as derived from the total charge deposited in each silicon layer (see sec. 4.3).

3.2.2 The Drift Chamber

The Drift Chamber (DCH) is the main tracking device for charged particles with transverse momenta p_T above $\sim 120\,\mathrm{MeV}/c$, providing the measurement of p_T from the curvature of the particle's trajectory inside the 1.5 T solenoidal magnetic field. The DCH also allows the reconstruction of secondary vertices located outside the silicon detector volume, such as those from $K_S \to \pi^+\pi^-$ decays. For this purpose, the chamber is able to measure not only the transverse coordinate, but also the longitudinal (z) position of tracks with good resolution (about 1 mm). Good z resolution also aids in matching DCH and SVT tracks,

and in projecting tracks to the DIRC and the calorimeter. For low momentum particles the DCH provides particle identification by measurement of ionization loss (dE/dx), thus allowing for K/π separation up to $\approx 600\,\mathrm{MeV}/c$. This capability is complementary to that of the DIRC in the barrel region, while it is the only mean to discriminate between different particle hypotheses in the extreme backward and forward directions which fall outside of the geometric acceptance of the DIRC. Finally, the DCH provides real-time information used in the first level trigger system. The DCH is a 2.80 m long cylinder with an inner radius of 23.6 cm and an outer radius of 80.9 cm (Fig. 3.7). Given the asymmetry of the beam energies, the DCH center is displaced by about 37 cm with respect to the interaction point in the forward direction. The active volume provides charged particle tracking over the polar angle range $-0.92 < \cos\theta < 0.96$.

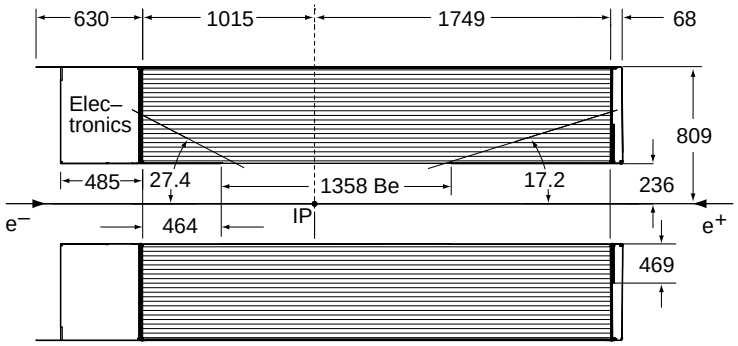

Figure 3.7: Schematic view of the DCH (longitudinal section).

The drift system consists of 7104 hexagonal cells, approximately 1.8 cm wide by 1.2 cm high, arranged in 10 superlayers of 4 layers each, for a total of 40 concentric layers (Fig. 3.8). Each cell consists of one sense wire surrounded by six field wires. The sense wires are 20 μm Rh-W gold-plated wires operating nominally in the range 1900-1960 V;

the field wires are 120 μm Al wires operating at 340 V. Within a given superlayer, the sense and field wires are organized with the same orientation. For measuring also the z coordinate, the superlayers alternate in orientation: first an axial view, then a pair of small angle stereo views (one with positive, one with negative angle), as indicated in Fig. 3.8.

The layers are housed between a 1 mm beryllium inner wall and a 9 mm carbonfiber outer wall (corresponding to 0.28% and 1.5% radiation lengths, respectively) both to facilitate the matching between the SVT and DCH tracks and to minimize the amount of material in front of the DIRC and the calorimeter. The counting gas is a 80:20 mixture of helium: isobutane, which again satisfies the requirement of keeping the multiple scattering at minimum. Overall, the multiple scattering inside the DCH is limited by less than 0.2% radiation lengths of material.

The drift chamber reconstruction efficiency has been measured on data in selected samples of multi-track events by exploiting the fact that tracks can be reconstructed independently in the SVT and the DCH. The absolute drift chamber tracking efficiency is determined as the fraction of all tracks detected in the SVT which are also reconstructed by the DCH when they fall within its acceptance. Its dependency on the transverse momentum and polar angle

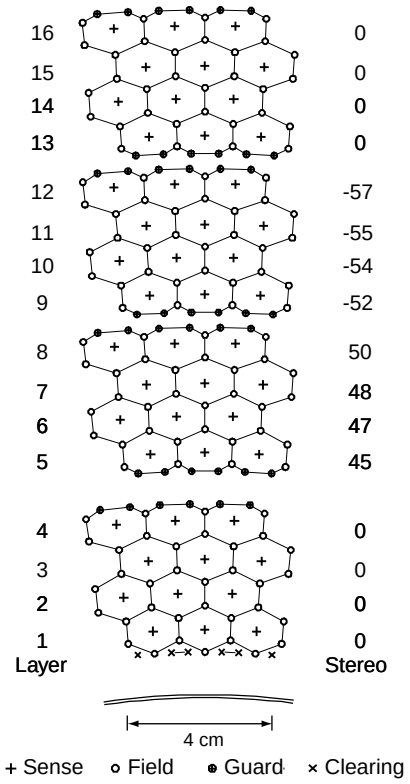

Figure 3.8: Schematic layout of the drift cells for the four innermost superlayers. The numbers on the right side give the stereo angles (mrad) of sense wires in each layer.

is shown in Fig. 3.9 [35]. At the design voltage of 1960V the reconstruction efficiency of the drift chamber averages $98 \pm 1\%$ for tracks above 200 MeV/c and polar angle $\theta > 500$ mrad (29°).

The p_T resolution is measured as a function of p_T in cosmic ray studies:

$$\frac{\sigma_{p_T}}{p_T} = (0.13 \pm 0.01)\% \cdot p_T + (0.45 \pm 0.03)\%, \tag{3.1}$$

where p_T is expressed in GeV/c. The first contribution, dominating at high p_T, comes from the curvature error due to finite spatial measurement resolution; the second contribution, dominating at low momenta, is due to multiple Coulomb scattering. The specific ionization loss dE/dx for charged particles traversing the drift chamber is derived from the total charge deposited in each drift cell. The resolution achieved to date is typically about 7.5% (as shown in Fig. 3.10 for $e^{\pm}$ from Bhabha scattering). A 3σ separation between kaons and pions can be achieved up to momenta of about 700 MeV/c [44].

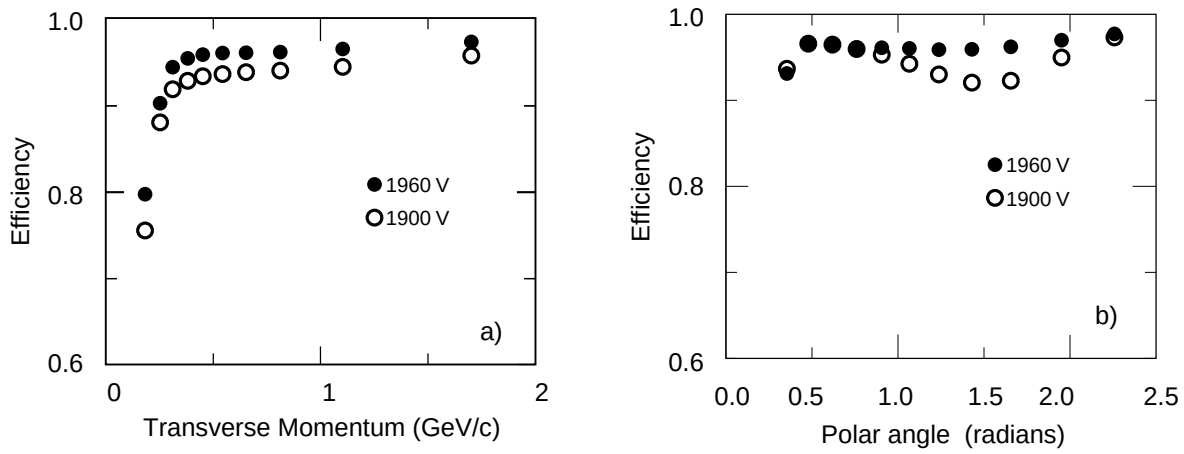

Figure 3.9: Track reconstruction efficiency in the drift chamber at operating voltages of 1900 V and 1960 V, as a function of transverse momentum (a) and polar angle (b).

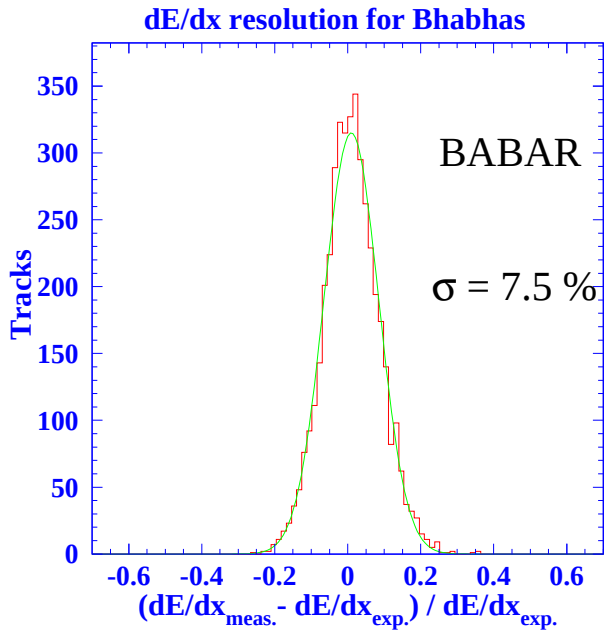

Figure 3.10: Resolution on dE/dx for $e^{\pm}$ from Bhabha scattering.

3.2.3 The Cherenkov detector

The particle identification (PID) at low momenta exploits primarily the dE/dx measurements in the DCH and SVT. However, above the threshold of 700 MeV/c, the dE/dx information does not allow to separate pions and kaons. The Detector of Internally Reflected Cherenkov radiation (DIRC) is employed primarily for the separation of pions and kaons from about 500 MeV/c to the kinematic limit of 4 GeV/c reached in rare B decays like $B \to \pi^+\pi^-/K^+K^-$. The principle of the DIRC is based on the detection of Cherenkov light generated by a charged particle in a medium of refractive index n, when its velocity v is greater than c/n. The photons are emitted on a cone of half-angle θ_c with respect to the particle direction, where $cos\theta_c = 1/\beta n,\ \beta = v/c$. Knowing the particle momentum thanks to the SVT and the DCH, the measurement of θ_c allows the mass measurement, so the particle identification, with the relation:

$$m^2c^2 = \frac{1-\beta^2}{\beta^2}p^2 \tag{3.2}$$

Fig. 3.11 illustrates the principles of light production, transport, and imaging.

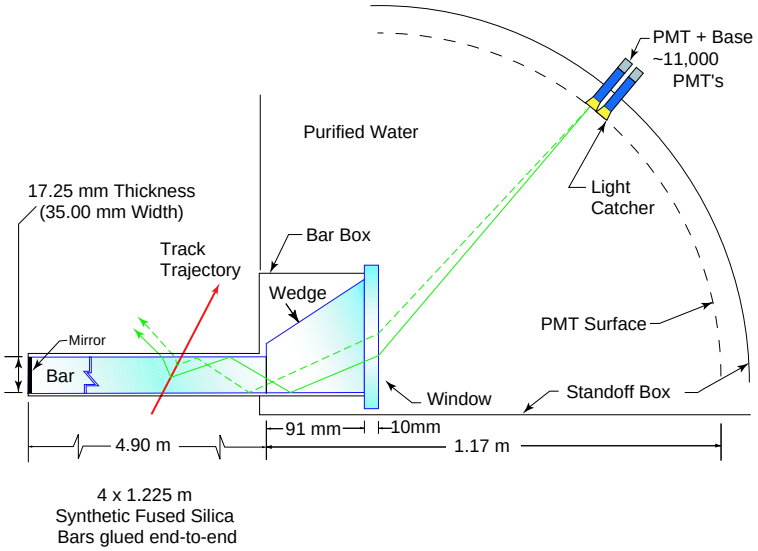

Figure 3.11: Schematics of the DIRC fused silica radiator bar and imaging region.

The radiator material of the DIRC is synthetic fused silica (refraction index $n = 1.473$) in the form of 144 long, thin bars with regular rectangular cross section. The bars, which are 17 mm thick, 35 mm wide and 4.9 m long, are arranged in a 12-sided polygonal barrel, each side being composed of 12 adjacent bars placed into sealed containers called bar boxes. Dry nitrogen gas flows through each bar box, and humidity levels are measured to monitor that the bar box to water interface remains sealed. The solid angle subtended by the radiator bars corresponds to 94% of the azimuth and 83% of the cosine of the polar angle in the center-of-mass system. The bars serve both as radiators and as light pipes for the portion of the light trapped in the radiator by total internal reflection. For particles with $\beta \approx 1$, some photons will always lie within the total internal reflection limit, and will be transported to

either one or both ends of the bar, depending on the particle incident angle. To avoid having to instrument both bar ends with photon detectors, a mirror is placed at the forward end, perpendicular to the bar axis, to reflect incident photons to the backward (instrumented) bar end.

Once photons arrive at the instrumented end, most of them emerge into an expansion region filled with 6000 litres of purified water ($n = 1.346$), called the stand-off box (see Fig. 3.12). A fused silica wedge at the exit of the bar reflects photons at large angles and thereby reduces the size of the required detection surface. The photons are detected by an array of densely packed photo-multiplier tubes (PMTs), each surrounded by reflecting "light catcher" cones to capture light which would otherwise miss the PMT active area. The PMTs, arranged in 12 sectors of 896 phototubes each, have a diameter of 29 mm and are placed at a distance of about 1.2 m from the bar end. The expected Cherenkov light pattern at this surface is essentially a conic section, whose cone opening-angle is the Cherenkov production angle modified by refraction at the exit from the fused silica window. By knowing the location of the PMT that observes a Cherenkov photon and the charged particle direction from the tracking system, the Cherenkov angle can be determined. In addition, the time taken for the photon to travel from its point of origin to the PMT is used to effectively suppress hits from beam-generated background and from other tracks in the same event, and also to resolve some ambiguities in the association between the PMT hits and the track (for instance, the forward-backward ambiguity between photons that have or haven't been reflected by the mirror at the forward end of the bars).

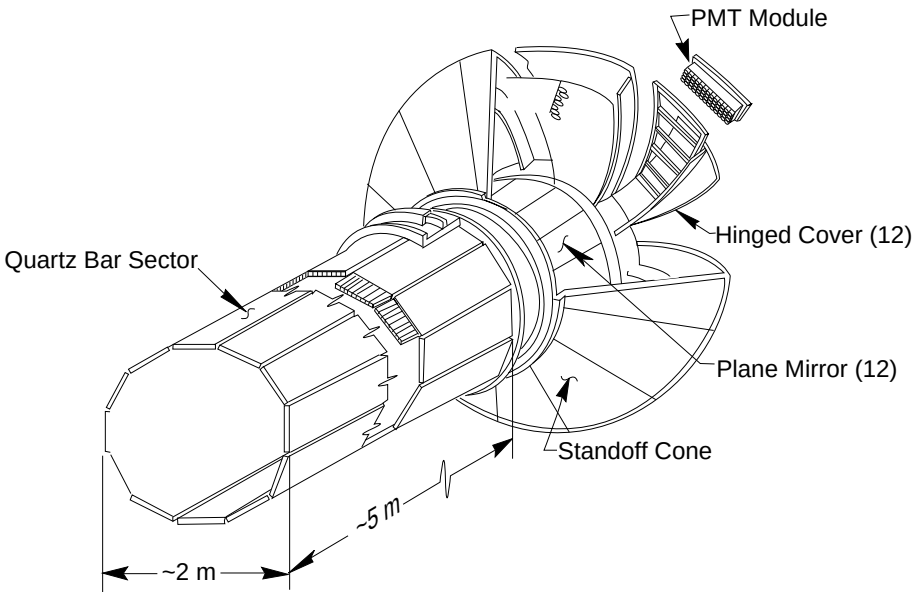

Figure 3.12: Schematic view of the DIRC.

The relevant observable to distinguish between signal and background photons is the difference between the measured and expected photon time, δt_γ. It is calculated for each photon using the track time-of-flight, the measured time of the candidate signal in the PMT and the photon propagation time within the bar and the water filled standoff box. The resolution on this quantity, as measured in dimuon events is 1.7 ns, close to the intrinsic 1.5

ns transit time spread of the photoelectrons in the PMTs. Applying the time information substantially improves the correct matching of photons with tracks and reduces the number of accelerator induced background hits by approximately a factor 40, as can be seen in Fig. 3.13 [46]. The reconstruction routine provides a likelihood value for each of the five stable particle types ($e,\ \mu,\ \pi,\ K,\ p$) if the track passes through the active volume of the DIRC. These likelihoods are calculated in an iterative process by maximising the likelihood value for the entire event while testing different hypotheses for each track. If enough photons are found, a fit of θ_c and the number of observed signal and background photons are calculated for each track.

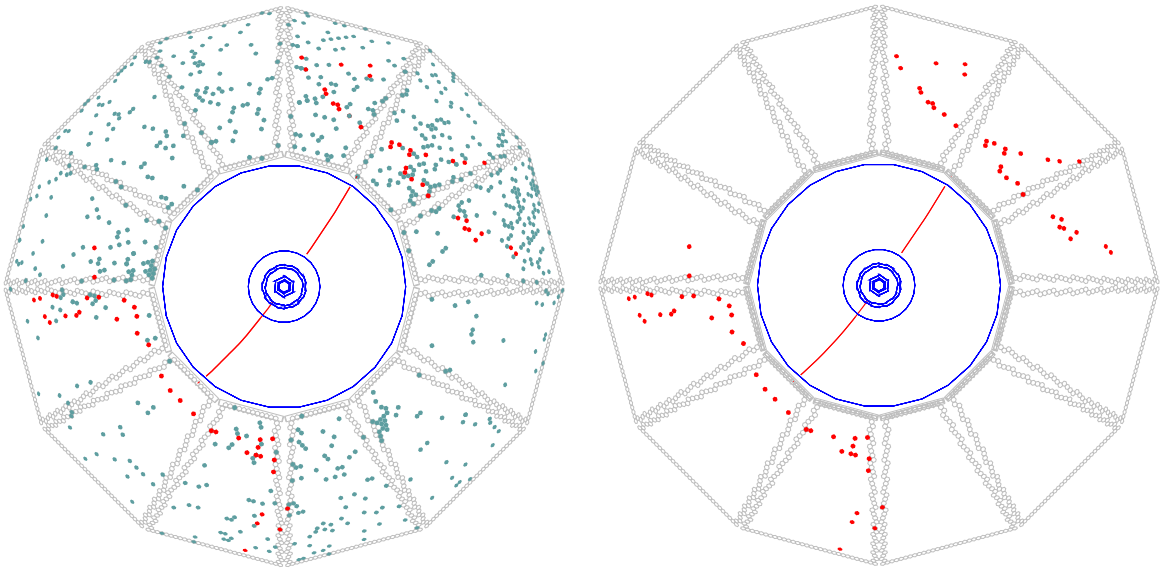

Figure 3.13: Display of one $e^+e^- \to \mu^+\mu^-$ event reconstructed in *BABAR* with two different time cuts. On the left, all DIRC PMTs that were hit within the ± 300 ns trigger window are shown. On the right, only those PMTs that were hit within 8 ns of the expected Cherenkov photon arrival time are displayed.

The DIRC uses two independent approaches for a calibration of the unknown PMT time response and the delays introduced by the electronic and the fast control system. The first one is a conventional pulser calibration: 1 ns duration light pulses are emitted from 12 blue LEDs (one per sector), with a rate of 2 kHz. A calibration run requires a few minutes and is taken about three times a week. The second calibration system uses reconstructed tracks from the collision data ("rolling calibration"). It performs a calibration of the global time delay, and the time delay sector by sector.

Fig. 3.14 shows the number of photons detected as a function of the polar angle in di-muons events. It increases from a minimum of about 20 at the center of the barrel ($\theta \approx 90°$) to well over 50 in the forward and backward directions, corresponding to the fact that the path-length in the radiator is longer for tracks emitted at large dip angles (therefore the number of Cherenkov photons produced in the bars is greater) and the fraction of photons trapped by total internal reflection rises. This feature is very useful in the *BABAR* environment, where, due to the boost of the center-of-mass, particles are emitted preferentially in the forward

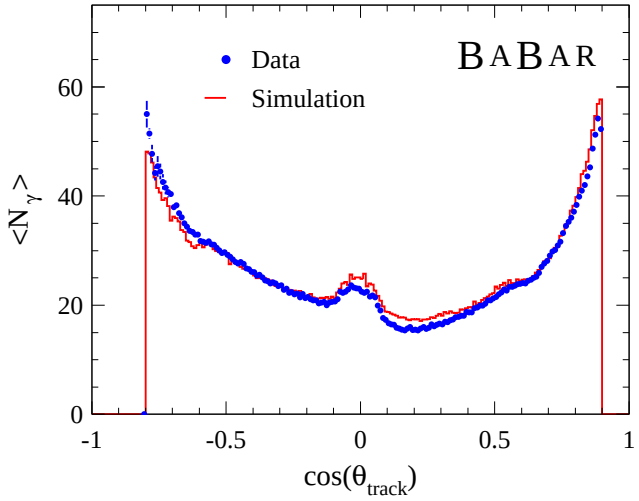

Figure 3.14: Number of detected photoelectrons versus track polar angle for reconstructed di-muon events in data and simulation.

direction. The bump at $\cos\theta = 0$ is a result of the fact that for tracks at small angles internal reflection of the Cherenkov photons occurs in both the forward and backward direction. The small decrease of the number of photons from the backward direction to the forward one is a consequence of the photon absorption along the bar before reaching the stand-off box in the backward end. The combination of the single photon Cherenkov angle resolution, the distribution of the number of detected photons versus polar angle and the polar angle distribution of charged tracks yields a typical track Cherenkov angle resolution which is about 2.5 *mrad* in di-muon events.

The pion-kaon separation power is defined as the difference of the mean Cherenkov angles for pions and kaons assuming a Gaussian-like distribution, divided by the measured track Cherenkov angle resolution. As shown in Fig. 3.15, left, the separation between kaons and pions at 3 GeV/c is about 4.3 σ. The efficiency for correctly identifying a charged kaon hitting a radiator bar and the probability of wrongly identifying a pion as a kaon are determined using D^0 decays kinematically selected from inclusive D^* meson production (Fig. 3.15): the kaon identification efficiency and pion mis-identification probability are about 96% and 2%, respectively.

3.2.4 The Electromagnetic Calorimeter

The *BABAR* electromagnetic calorimeter (EMC) is designed to detect and measure electromagnetic showers with high efficiency and very good energy and angular resolution over a wide energy range between 20 MeV and 9 GeV. This allows the reconstruction of $\pi^0 \to \gamma\gamma$ and $\eta \to \gamma\gamma$ decays where the photons can have very low energy, as well as the reconstruction of Bhabha events and processes like $e^+e^- \to \gamma\gamma$, important for luminosity monitoring and calibration, where the electron and photon energies can be as large as 9 GeV. The EMC also provides the primary information for electron identification and electron-hadron separation.

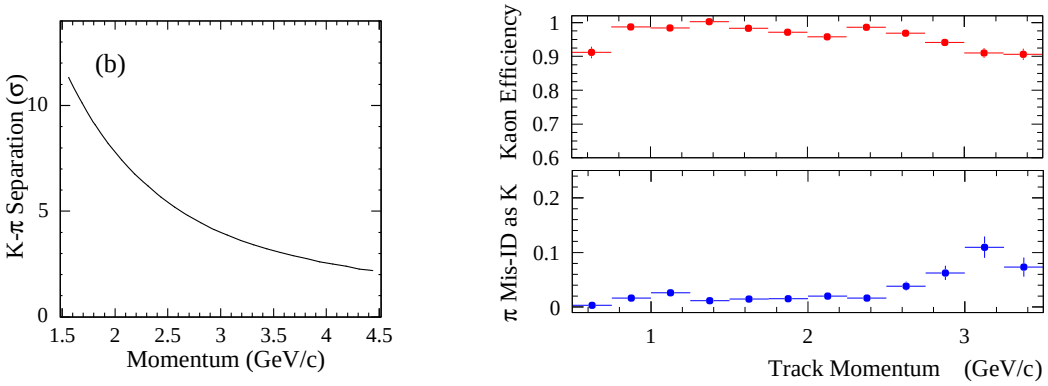

Figure 3.15: Left plot: average difference between the expected value of θ_C for kaons and pions, divided by the uncertainty, as a function of momentum. Right plot: efficiency and misidentification probability for the selection of charged kaons as a function of track momentum.

Energy deposit clusters in the EMC with lateral shape consistent with the expected pattern from an electromagnetic shower are identified as photons when they are not associated to any charged tracks extrapolated from the SVT and the drift chamber, and as electrons if they are matched to a charged track and if the ratio between the energy E measured in the EMC and the momentum p measured by the tracking system is $E/p \approx 1$.

The EMC contains 6580 CsI crystals doped with Tl (Fig. 3.16). CsI(Tl) has a high light yield (50,000 photons/ MeV) and a small Molière radius (3.8 cm), which provide the required energy and angular resolution; its radiation length of 1.86 cm guarantees complete shower containment at the *BABAR* energies.

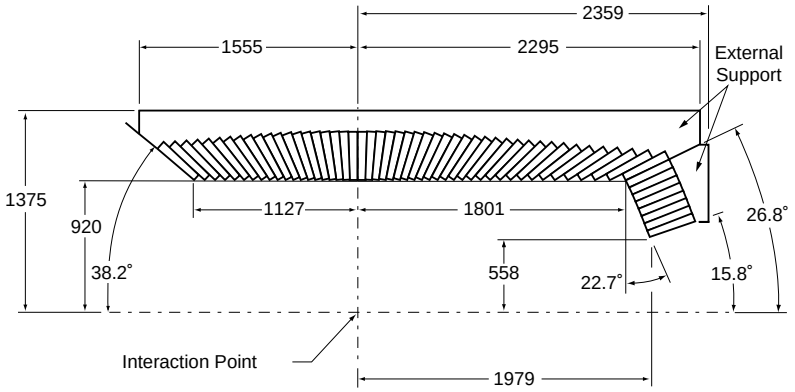

Figure 3.16: Longitudinal section of the top half of the EMC. Dimensions are in mm.

Each crystal is a truncated trapezoidal pyramid and ranges from 16 to 17.5 radiation lengths in thickness. The front faces are typically about 5 cm in each dimension. The crystals are arranged to form a barrel and a forward endcap giving a 90% solid-angle coverage in the center-of-mass frame. The barrel has 48 rows of crystals in θ and 120 in ϕ; the forward

endcap contains 8 rings in θ. Overall the EMC extends from an inner radius of 91 cm to an outer radius of 136 cm and is displaced asymmetrically with respect to the interaction point.

The crystals are read out by two independent 1 cm^2 PIN photodiodes, glued to their rear faces, which are connected to low-noise preamplifiers that shape the signal with a short shaping time (400 ns) so to reduce soft beam-related photon backgrounds.

For the purpose of precise calibration and monitoring, use is made of a neutron activated fluorocarbon fluid, which produces a radioactive source (^{16}N) originating a 6.1 MeV photon peak in each crystal. A light pulser system injecting light into the rear of each crystal is also used. In addition, signals from data, including π^0 decays and $e^+e^- \to e^+e^-/\gamma\gamma/\mu^+\mu^-$ events, provide an energy calibration and resolution determination.

The efficiency of the EMC exceeds 96% for the detection of photons with energy above 20 MeV. The energy resolution is usually parameterized by

$$\frac{\sigma_E}{E} = \frac{\sigma_1}{E^{1/4}(\text{ GeV})} \oplus \sigma_2, \tag{3.3}$$

where $\sigma_1 = 2.32 \pm 0.30\%$ and $\sigma_2 = 1.85 \pm 0.12\%$, as determined using the above mentioned sources. The first term in Eq. 3.3 arises from fluctuations in photon statistics and is dominant for energies below about 2.5 GeV, while the constant term takes into account several effects, such as fluctuations in shower containment, non-uniformities, calibration uncertainties and electronic noise.

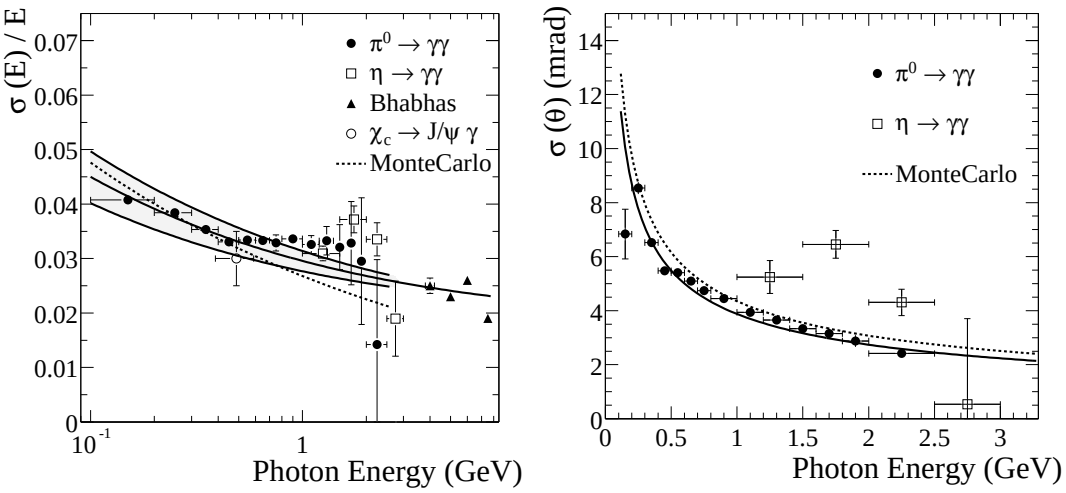

Figure 3.17: Energy (left) and angular (right) resolutions measured using a variety of data. The solid curves represent a fit to the data using Equation 3.3 and 3.4 respectively.

The decays of π^0 and η candidates in which the two photons have approximately equal energy are used to infer angular resolution. It varies between about 12 mrad at low energies and 3 mrad at high energy. The data fit the empirical parameterization:

$$\sigma_{\theta,\phi} \;=\; \left(\frac{(3.87 \pm 0.07)}{\sqrt{E(\text{ GeV})}} + (0.00 \pm 0.04) \right) mrad \tag{3.4}$$

Fig. 3.17 [47] shows the energy and angular resolution measured as a function of the photon energy.

3.2.5 The Instrumented Flux Return

The Instrumented Flux Return (IFR) is designed to identify muons and neutral hadrons (primarily K_L and neutrons). Muons are important for tagging the flavor of neutral B mesons via semi-leptonic decays, for the reconstruction of vector mesons, like the J/ψ, and the study of semi-leptonic and rare decays involving leptons from B and D mesons and τ leptons. K_L detection allows for the study of exclusive B decays, in particular CP eigenstates. The principal requirements for IFR are large solid angle coverage, good efficiency and high background rejection for muons down to momenta below 1 GeV/c. For neutral hadrons, high efficiency and good angular resolution are most important. The IFR uses the steel flux return of the magnet as muon filter and hadron absorber, limiting pion contamination in the muon identification. Originally single gap resistive plate chambers (RPC) with two-coordinate readout, operated in limited streamer mode constituted the active part of the detector [48], with 19 layers in the barrel and 18 in each endcap. The RPC were installed in the gaps of the finely segmented steel of the six barrel sectors and the two end-doors of the flux return, as illustrated in Fig. 3.18. The steel segmentation has been optimized on the basis of Monte Carlo studies of muon penetration and charged and neutral hadron interactions. In addition, two layers of cylindrical RPCs were installed between the EMC and the magnet cryostat to detect particles exiting the EMC. RPCs contain a 2 mm Bakelite gap with ~ 8 kV across it. Ionizing particles which cross the gap create streamers of ions and electrons in the gas mixture (Argon, freon and isobutane), which in turn creates signals via capacitive coupling on the strips mounted on each side of the RPC. Soon after the installation (which took place

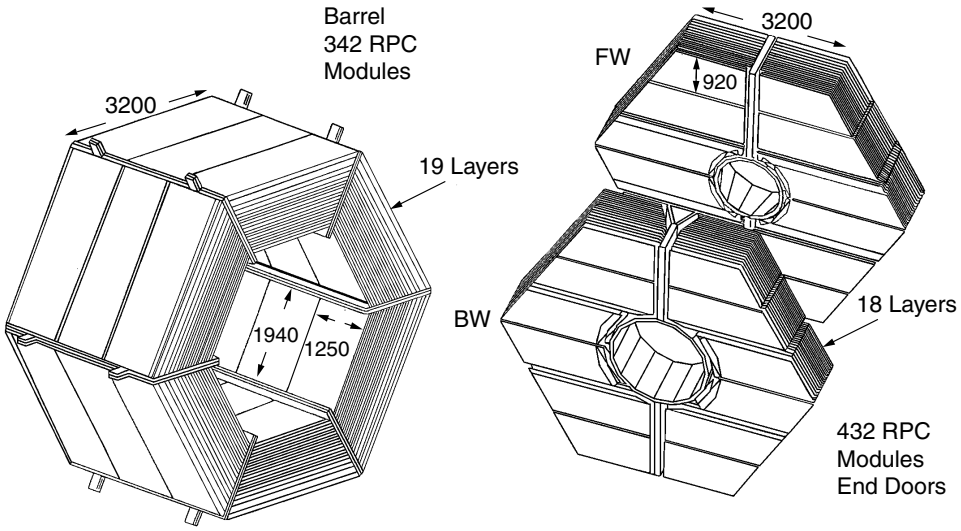

Figure 3.18: Overview of the IFR Barrel sectors and forward and backward end-doors; the shape of the RPC modules and the way they are stratified is shown.

in Summer 1999), the efficiency of a significant fraction of the chambers (initially greater then 90%) has started to deteriorate at a rate of 0.5-1%/month. In order to solve some of the inefficiency problems, an extensive improvement program has been developed. The forward endcap was retrofitted with new improved RPCs in 2002, their efficiency has not significatly decreased since then. In the barrel, the RPCs have been replaced in 2004 and 2006 by 12 layers of limited streamer tube (LST) detectors and 6 layers of brass have been added to improve hadron absorption. The tubes have performed well since their installation with an efficiency of all layers at the geometrically expected level of 90%. The pion rejection versus muon efficiency is shown in Fig. 3.19 for the LSTs and RPCs. The LSTs efficiency is better than the efficiency that the RPCs had, even during the Run1.

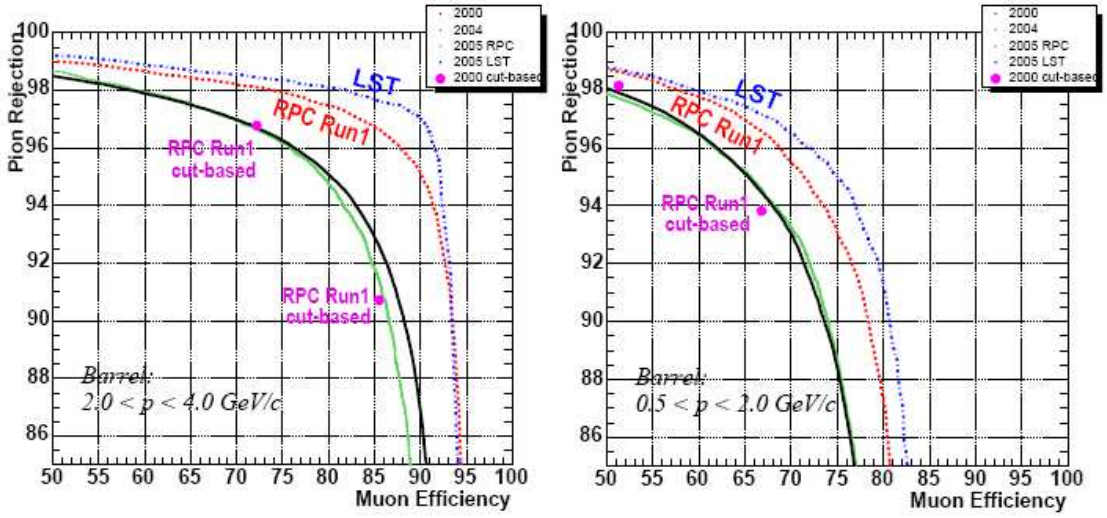

Figure 3.19: Pion rejection versus muon efficiency for two different momentum ranges (left: $2 < p < 4$ GeV/c, right $0.5 < p < 2$ GeV/c). The LST efficiency (blue) is compared with the RPC one for different Runs. We see the deterioration of the RPC performance between 2000 (red) and 2005 (green).

3.2.6 Trigger

The *BABAR* trigger is designed to select a large variety of physics processes (efficiency greater than 99% for $B\bar{B}$ events) while keeping the output rate below 400 Hz to satisfy computing limitations of the offline processing farms (beam induced background rates with at least one track with $p_t > 120$ MeV/c or at least one EMC cluster with $E > 100$ MeV are typically 20 kHz). The trigger accepts also 95 % of continuum hadronic events and more than 90 % of $\tau^+\tau^-$ events. It is implemented as a two level hierarchy, the hardware Level 1 (L1) followed by the software Level 3 (L3).

The L1 trigger has an output rate of the order of 1 kHz to 3 kHz, depending on the luminosity and background conditions. It is based on charged tracks in the DCH above a preset transverse momentum, showers in the EMC, and track detected in the IFR. L3

L3 Trigger	$\epsilon_{b\bar{b}}$	$\epsilon_{B\to\pi^0\pi^0}$	$\epsilon_{B\to\tau\nu}$	$\epsilon_{c\bar{c}}$	ϵ_{uds}	$\epsilon_{\tau\tau}$
Combined DCH filters	99.4	89.1	96.6	97.1	95.4	95.5
Combined EMC filters	93.5	95.7	62.3	87.4	85.6	46.3
Combined DCH+EMC filters	>99.9	99.3	98.1	99.0	97.6	97.3
Combined L1+L3	>99.9	99.1	97.8	98.9	95.8	92.0

Table 3.2: L3 trigger efficiency (%) for various physics processes, derived from Monte Carlo simulation.

operates by refining and augmenting the selection methods used in L1. Based on both the complete event and L1 trigger information, the L3 software algorithm selects events of interest allowing them to be transferred to mass storage data for further analysis. It uses an algorithm based on the drift chamber tracking, which rejects beam-induced charged particle background produced in the material close to the IP, and a second algorithm based on the calorimeter clustering. Then, based on the L3 tracks and clusters, a variety of filters perform event classification and background reduction. Tab. 3.2 shows the L3 and L1+L3 trigger efficiency for some relevant physics processes, derived from simulated events.

3.3 Data acquisition and Online system

The *BABAR* online data acquisition collects the data from all the *BABAR* subdetectors and the information of the Level1 trigger and merges them into raw data, that are then the object of reconstruction and production processes. The online data acquisition system also allows for real-time data quality monitoring during data taking.

The *BABAR* Online Data Flow system communicates with the front-end electronics of the detector components through read out modules, which are organized in crates, each including a master read out module. Each master read out module builds part of the event collecting data from the other modules of the crate and send them to the nodes of the Online Event Processing farm (OEP). The Data Flow system also contains a Fast Control and Timing module, which phases *BABAR* ans PEP-II timing.

The farm nodes in OEP apply the Level3 trigger algorithm and perform first data quality monitoring functions; events that pass the Level3 trigger are then sent to a logging manager process that writes them to disk. The data quality monitoring results, collected from all OEP nodes, are merged and displayed to the *BABAR* operators, who check and compare the data against references constantly during the data taking.

The online computing system includes other additional components, such as the Online Detector Control, and the Online Run Control. The Detector Control provides environmental monitoring and control (low and high voltages, temperatures, gas flow etc..together with some parameter of the collider) and is responsible of the communication between *BABAR* and PEP-II. The Run Control allows the *BABAR* operators to manage the data taking, and interlocks data acquisition with safe detector conditions.

3.4 Babar and PEP-II backgrounds

The PEP-II high luminosity environment implies different background sources that have to be monitored since they can affect *BABAR* data taking and damage the detector, limiting its lifetime. For this reason, the backgrounds generated by PEP-II have been studied in detail and the interaction region has been carefully designed. In addition, *BABAR* background monitoring provides an important feedback to PEP-II operators allowing for an improvement of the running conditions.

For these reasons, the background conditions are constantly monitored in *BABAR* , using information from all the subdetectors and from a dedicated Radiation Monitoring and Protection System of the SVT detector, called SVTRAD, that will be briefly described in the following.
The main sources of background are the following [39]:

- synchrotron radiation, generated by the bending dipoles B1 and final focusing quadrupoles near the interaction point (see fig. 3.4). This background is not an issue in PEP-II due to an attentive design of the interaction region.

- *beam-gas* background, arising from the interaction (bremsstrahlung or Compton scattering) of incoming electrons and positrons with residual gas in the beam pipes. These interactions reduce the particle energy. The separating dipoles B1 (see fig. 3.4) bend some of these off-energy or off-angle electrons and positrons to hit the detector along the horizontal plane. Primary source of radiation damage and particularly worrying for the SVT, this background is monitored by the SVTRAD system, which, in case of too high radiation dose, can abort the beams to prevent damages to the detector.

- *luminosity* background, generated from off-energy outgoing electrons and positrons from radiative Bhabha reactions, $e^+e^- \rightarrow e^+e^-\gamma$, that are bent by the B1 dipole magnets (see fig. 3.4) and strike against vacuum components within a few meters from the interaction point. This background source is strictly linear with the luminosity. For geometrical reasons, it is not seen by the SVT system, but affects the DCH and DIRC.

- *beam-beam* background arising from instabilities created by the interactions between the two beams. These effects are characterized thanks to data collected in single-beam runs. The occupancies in the different subdetectors are studied in single-beam runs (when either only positrons or only electrons are circulated in the rings) and during running with both the beams filled, allowing for a disentanglement of the HER and LER contribution. In these studies, the effect of the interaction between the two beams is observed in all the subdetectors.

- trickle injection (see sec. 3.1) background, arising from bad quality or bad orbit of the beam that has been injected. This background is monitored by the study of the average radiation dose per injected bunch recorded by the SVTRAD system and by the number of triggers generated in the DCH and EMC per injection pulse.

As already said, the risks of damage to the detector, and especially to its inner part, the SVT, depend on the radiation dose near the interaction point, which is measured by SVTRAD. The SVTRAD system consists of 12 PIN diodes grouped into four modules: two of them in the forward region (on the east and west side of the beamline respectively [1]) and the other two in the backward region (on the east and west side respectively). Each module contains three diodes, one located in the bending plane of the magnet (and which, for this reason, receive higher radiation doses) and the other two located respectively above and below this plane. A schematic overview of the SVTRAD system is shown in figure 3.20.

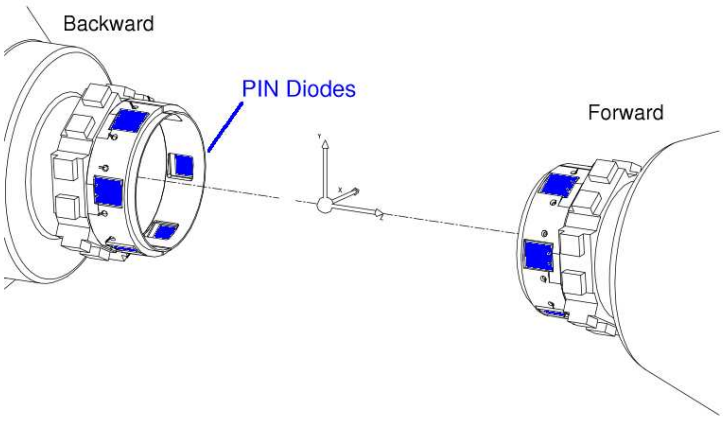

Figure 3.20: Schematic overview of the SVTRAD system. The east and west sides correspond to positive and negative x coordinates respectively

The temperature of each diode is measured by 2 surrounding thermistors. The output current from a PIN diode, apart from a pedestal current that has to be subtracted, is proportional to the instantaneous radiation dose. In 2002, two diamond detectors of roughly the same size as the PIN diodes were installed in the backward end of the support tube. For those diodes the pedestal currents are lower and are almost independent from the temperature. The reading of the radiation dose by means of sensors in different positions along the beamline allows to correlate the background with one beam or the other (due to the design of the interaction point, the east side of the detector is more sensitive to effects from the positrons low energy ring and the west side is more sensitive to effects from the electrons high energy ring). The radiation dose evolution over time can be correlated with the status of the vacuum inside the PEP-II beam pipes, which is constantly monitored along the rings. The SVTRAD is the only subsystem that can abort the beams. This can happen in two different ways:

[1]Where the east and west sides correspond to positive and negative x coordinates respectively, in the *BABAR* right-handed coordinate system, defined in sec. 3.2

- Soft aborts: an abort timer starts whenever the radiation rises above 100 mRad/s and the *BABAR* shifters and PEP-II operators are notified. After 10 minutes continuously over threshold, the SVTRAD causes a beam abort.

- Fast aborts: they occur when there are very high and rapid spikes of radiation. Fast aborts can occur when the radiation dose exceeds 1.25 Rad/s and 5 Rad are integrated or when the radiation dose exceeds 400 Rad/s (radiation occurrences of this kind can happen on a time scale of the order of ms).

Other quantities used to monitor the background conditions in *BABAR* are the occupancies in each subdetectors and the current in the Drift Chamber wires: when this current is too high in one of them, the corresponding HV group is ramped off and the voltage of the other groups is lowered, waiting for the conditions to improve. During this period, the data acquisition is paused. For each one of the twelve sectors of the DIRC, one phototube is used as a scaler, i.e. it simply counts the number of hits it receives. The average rate read by the DIRC scalers is also monitored.

The presence of background can cause high deadtime and hence affect the *BABAR* data taking efficiency. The total deadtime is the sum of three components: busy deadtime, full deadtime and inhibit deadtime, defined as follows:

- The *busy deadtime*, proportional to the L1 trigger rate. *BABAR* data acquisition system structure implies a 2.7 μs irreducible deadtime each time there is an output of the L1 trigger (*L1accept*). For example, for a L1 trigger rate of 3 kHz, the busy deadtime would be 0.8%.

- The *full deadtime*, which occurs when the data acquisition system is unable to keep up with the rate of L1 trigger output. This contribution to the deadtime is not linear with the L1 trigger rate (it is negligible under a threshold and can increase rapidly above it) and is for this reason critical for the data acquisition.

- The *inhibit deadtime*, due to the L1accept that are inhibited because of the trickle injection. The trickle injection procedure allows to refill single bunches inside one beam. The injected bunches are noisy after the injection and for that reason the data acquisition from collisions involving these particular bunches and their neighbours is inhibited for a given interval of time right after injection. The hardware inhibited L1accept correspond to a deadtime of 0.055% for each kHz in the L1 trigger rate for each beam. A further cut is applied at reconstruction level, corresponding, respectively for the LER and the HER, to 0.19% and 0.28% for each kHz in the L1 trigger rate.

At the end of Run6 (August 2007), the average deadtime was around 1.5%-2%, with a relative contribution of 50% from busy deadtime, 30% from full deadtime and 20% from inhibit deadtime. In fig. 3.21, we show the Level1 trigger rate as a function of the luminosity, for two different periods of running, corresponding to a part of the Run5 and the Run6 *BABAR* data taking (from January until August 2006 and from March until June 2007 respectively). For the same luminosity, a higher Level1 trigger rate, that implies a higher deadtime, is a symptom of degraded background conditions. The behaviour of the deadtime as a function of the L1 trigger rate is linear for the Run5 and not for the Run6, sign of worst background conditions.

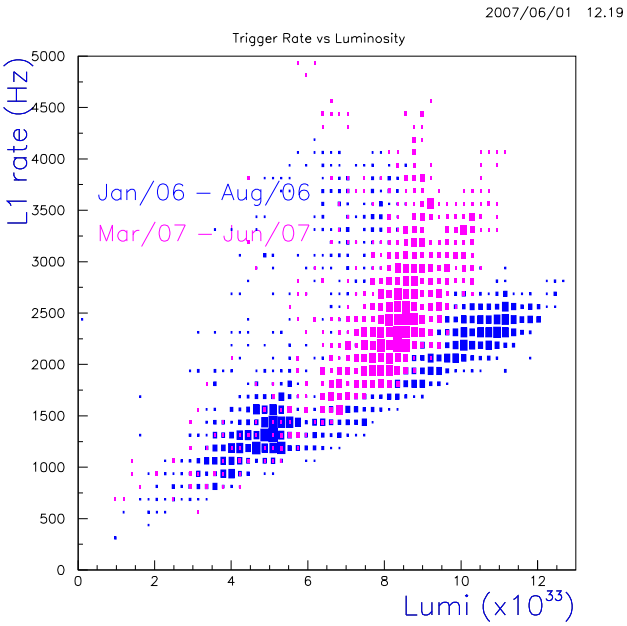

Figure 3.21: Level 1 trigger rate (in Hz) as a function of the luminosity, for two different periods of data taking: January-August 2006 (during Run5 data taking period) and March-June 2007 (during Run6 data taking period)

Chapter 4

Event reconstruction and background rejection

The events from B decays we are interested in are selected starting from the full data sample produced in e^+e^- collisions at a center-of-mass energy corresponding to the $\Upsilon(4S)$ resonance. Only a fraction of the e^+e^- collisions actually produces an $\Upsilon(4S)$ and hence a pair of B mesons ($e^+e^- \to \Upsilon(4S) \to B\bar{B}$). The other events are of the kind $e^+e^- \to u\bar{u}, d\bar{d}, s\bar{s}, c\bar{c}$ (so called continuum events) or $e^+e^- \to l\bar{l}$ and $e^+e^- \to \gamma\gamma$. In Tab. 4.1 the cross sections for the main processes are shown [37]. While the QED processes can be easily distinguished from the $e^+e^- \to q\bar{q}$ looking at the tracks multiplicity and at the visible energy in each event, the $e^+e^- \to c\bar{c}, u\bar{u}, d\bar{d}, s\bar{s}$ are more similar to $e^+e^- \to b\bar{b}$ and normally represent a background to analyses of B decays. In order to caracterize this kind of events, a fraction of the *BABAR* data (tipically 10%) are collected from e^+e^- collisions at a center-of-mass energy 40 MeV below the $\Upsilon(4S)$ resonance, where the production of $B\bar{B}$ meson pairs is kinematically forbidden. This sample is called off-resonance data and is very useful for background studies.

Cross section	Value [nb]
$\sigma(bb)$	1.05
$\sigma(c\bar{c})$	1.30
$\sigma(u\bar{u}, dd, s\bar{s})$	2.09
$\sigma(\tau^+\tau^-)$	0.94
$\sigma(\mu^+\mu^-)$	1.16
$\sigma(e^+e^-)$	40

Table 4.1: Cross section for different processes for e^+e^- collisions at a center-of-mass energy $\sqrt{s} = M(\Upsilon(4S))$. The Bhabha cross section value takes into account the detector acceptance.

4.1 From raw data to B meson reconstruction: a typical analysis structure

In this chapter we describe how the B-meson candidates are reconstructed starting from their decay products, using the information measured by the *BABAR* experimental apparatus, that allows to detect charged tracks and neutral energy deposits. For each event, photons and charged tracks (sec. 4.3) are reconstructed and dedicated "selectors" are applied to determine if the track is an electron, muon, charged pion or charged kaon. The charged particles, π^0 and K_S candidates (described in sec.4.4 and sec.4.5 respectively) are combined to reconstruct the neutral D in the given decay channel (sec. 4.7), and finally the B candidates are reconstructed (sec 4.8).

All the quantities are measured in the laboratory frame, but often studied in the $\Upsilon(4S)$ rest frame, also called the center-of-mass (CM) frame. The detector response, reconstruction and selection procedures are test on Monte Carlo simulated events (MC), generated using GEANT-based software.

In sec. 4.3, the charged particle reconstruction and identification are described. In sec. 4.4 we describe the π^0 reconstruction. The variables and procedures described in these two first sections are directly taken from *BABAR* reconstruction software and are used in many *BABAR* analyses. The reconstructions of K_S, neutral D (in different decay modes) and finally neutral B mesons, described in sec. 4.5 and following, are specific to the analyses presented in this thesis.

The procedures described in this chapter result in a reconstructed sample of B candidates (in some cases, more than one candidate per event). For each candidate, several variables caracterizing the B meson and its decay products (the candidate particles used to reconstruct the particular B candidate) are stored. In addition, some global information on the event containing the candidate is also stored. In a typical event in *BABAR* , many tracks and neutral clusters are present, and the reconstruction procedure can results in B candidates from events in which no real B meson actually decayed in the reconstructed channel. These candidates belong to the category of background events. The sources of background to the analyses presented in this thesis are of two kinds:

- **$B\bar{B}$ background**
  These are $B\bar{B}$ non-signal events that pass the selection. Most of them can be rejected using selection criteria. Dedicated studies have to be devoted, within the $B\bar{B}$ background, to particular channels that could lead to the same final state as the signal. For these events, also called *peaking background* events, some crucial variable has a distribution similar to that of the signal.

- **Continuum background**
  This is defined as $e^+e^- \rightarrow q\bar{q}$ ($q = u, d, s, c$) events that pass the selection. It is a common fact that in exclusive B decays analyses (like the analyses shown in this thesis) the main source of background are continuum events. These events are abundant, but can be discriminated from the signal using several global variables, which are described in sec. 4.9.

A selection procedure, in which some of the stored variables are requested to fulfill specific conditions, is applied to the reconstructed sample. Whenever, after the selection, more than one B candidate is present in a given event, the best one is chosen, according to some criteria. Finally, a maximum likelihood fit is performed on the selected sample, in order to distinguish between signal and background events and to extract the quantities of interest. These last steps, selection, best candidate choice and maximum likelihood fit, will be described separately for the two analyses in chapters 5 and 6.

4.2 Decay vertex reconstruction and kinematic fits

Since the vertexing procedure is used in the reconstruction of all the particles described below, it is introduced here once for all. The four-momentum of a charged particle or π^0 is calculated starting from the available information on its momentum or energy, making an assumption on its mass. Depending on the studied channel, the tracks and clusters are associated to a decay vertex and used to determine the position and the four-momentum of the decaying particle. In the vertex determination procedure, also the four-momenta of the decay products are readjusted, as briefly explained in the following

The decay point of a particle is determined by finding the best intersection of the tracks using a χ^2 minimization. Since the tracks trajectories are bent by the magnetic field, the problem is not linear and we make use of an iterative search for local solutions until the χ^2 between one iteration and the next one is below 0.01. The maximum number of possible iterations is six.

The χ^2 is minimized by varying the position and four-momentum components of the decay products. In addition, the energy and momentum conservation is applied by use of the Lagrange multipliers and the mass of the decaying particle can be fixed to its nominal mass.

4.3 Charged track identification

Charged tracks are identified using *selectors* that combine different information from all the *BABAR* subdetectors. These selectors provide various working points, ranked in terms of purity and efficiency.

Most of the tracks produced in an event are pions. The tracks are basically requested to have at least five hits (either in the SVT or in the DCH), to have a maximum distance of closest approach in the $x - y$ plane of 1.5 cm and their θ angle has to be in the interval $0.4 \text{ rad} < \theta < 2.54 \text{ rad}$

In the channels we are interested in, we reconstruct, toghether with pions, also charged kaons. In sec. 4.3.1 the kaons selection criteria are described. Electrons and muons, described in sec. 4.3.2 and 4.3.3, are mainly used to reconstruct the second B in the event.

4.3.1 Charged kaon identification

Kaons and pions are produced in B decays in a ratio of about one to seven. The selectors discriminating between charged kaons and pions make use of the loss of energy, dE/dx, as

measured by the SVT and DCH, and the Cerenkov angle, θ_C, as measured by the DIRC. Coming from different detectors, these measurements can be considered as uncorrelated and their combination improves the discriminating power.

As can be seen in Fig. 4.1, the dE/dx variable has a good discriminating power for track momenta up to ∼700 MeV/c for the DCH and up to ∼600 MeV/c for the SVT. For momenta higher than ∼700 MeV/c, the Cerenkov angle θ_C information from the DIRC is necessary, as shown in Fig. 4.2.

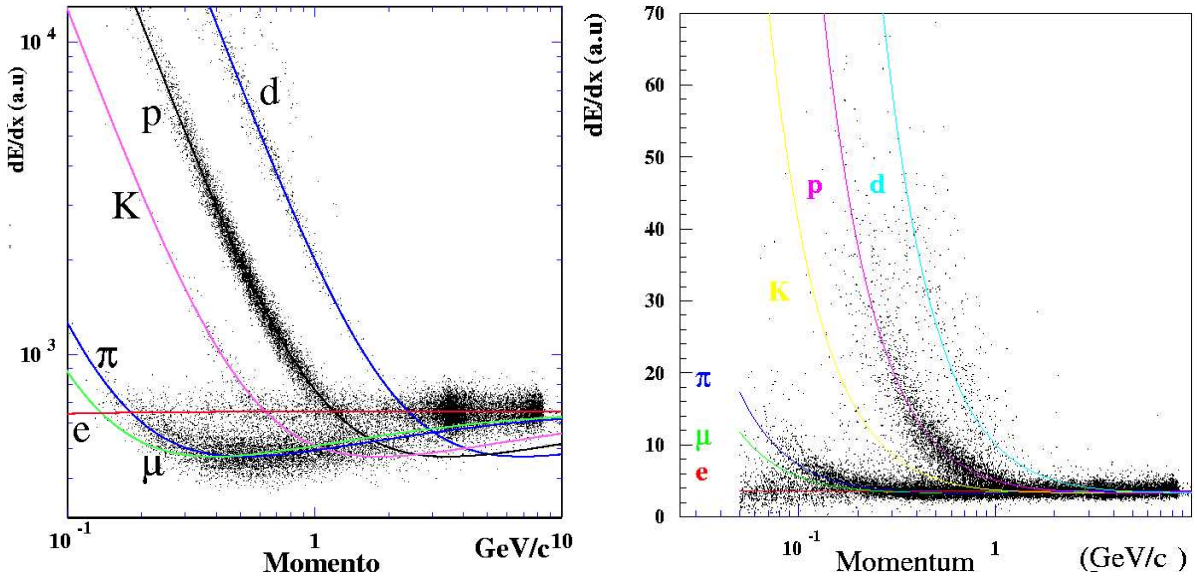

Figure 4.1: Energy loss dE/dx (in arbitrary units), as a function of the track momentum, in the DCH (left) and in the SVT (right) for different types of particles. The curves are the theoretical behaviours following the Bethe-Bloch formula.

Both analyses presented here do not use directly the information on dE/dx and θ_C, but make use of selection criteria developed in *BABAR* during the years. In order to identify a track, a pdf for each particle hypothesis (e, μ, π, p, K) is constructed. These pdf are then combined to construct a likelihood for the electron hypothesis, $\mathcal{L}_e$, a likelihood for the kaon hypothesis, $\mathcal{L}_K$, and so on... The selectors are then defined by different cuts on the ratios $\mathcal{L}_K/\mathcal{L}_p$, $\mathcal{L}_K/\mathcal{L}_\pi$ and they differ in efficiency and purity. The following information is used:

- for track momenta $p < 500$ MeV/c, dE/dx measurements from SVT and DCH are combined;
- for track momenta 500 MeV/c $< p <$ 600 MeV/c, dE/dx measurement from DCH only is used;
- for track momenta $p > 600$ MeV/c, the θ_C measurement from DIRC is used.

In both analyses presented in this thesis, the charged kaon from the K^{*0} decay is requested to pass the *KLHTight* selector criteria, which has a average efficiency on kaons of about 85% and an efficiency of reconstructing a pion as a kaon of about 1%. In the ADS analysis,

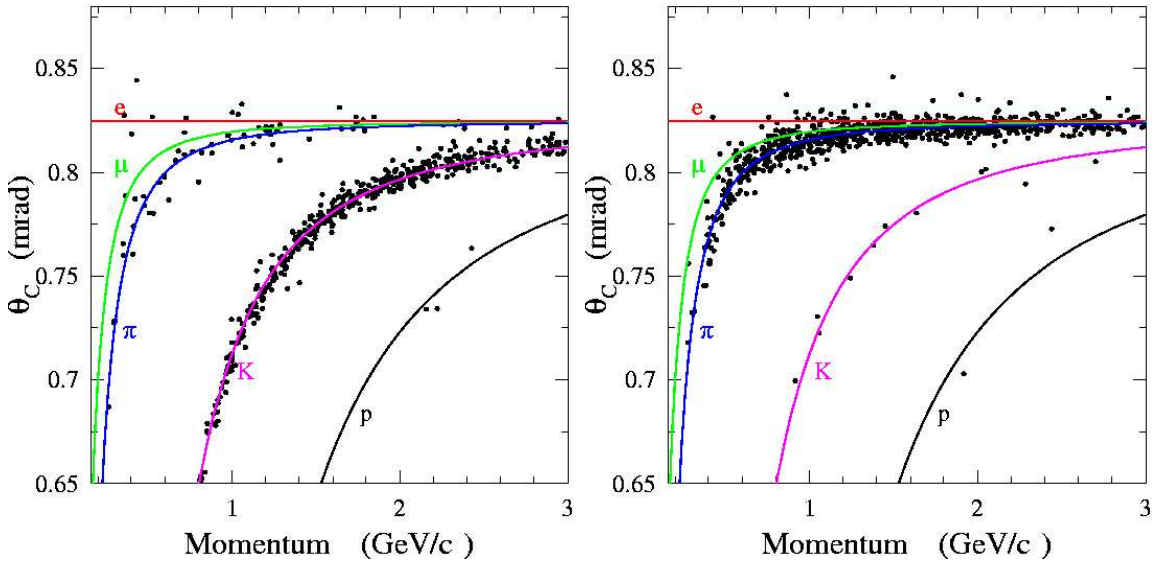

Figure 4.2: Cerenkov angle θ_C, as a function of the track momentum, for samples of identified kaons (left) and pions (right). The curves describe the typical functional behaviours for different charged particles.

for the charged kaons produced in the neutral D decays, we use the $KLHLoose$ selector, which has a average efficiency on kaons of about 90% and an efficiency of reconstructing a pion as a kaon of about 2%. The efficiency of reconstructing electrons, muons or protons as kaons are normally lower than the efficiency of reconstructing a pion as a kaon, for both the selectors. In Fig. 4.3, we show the efficiency using the $KLHTight$ and $KLHLoose$ criteria for kaons. In Fig. 4.4 we show the probability of reconstructing a pion as a kaon, for the two selectors. The efficiency of the selectors obtained on data and on simulated events are in good agreement.

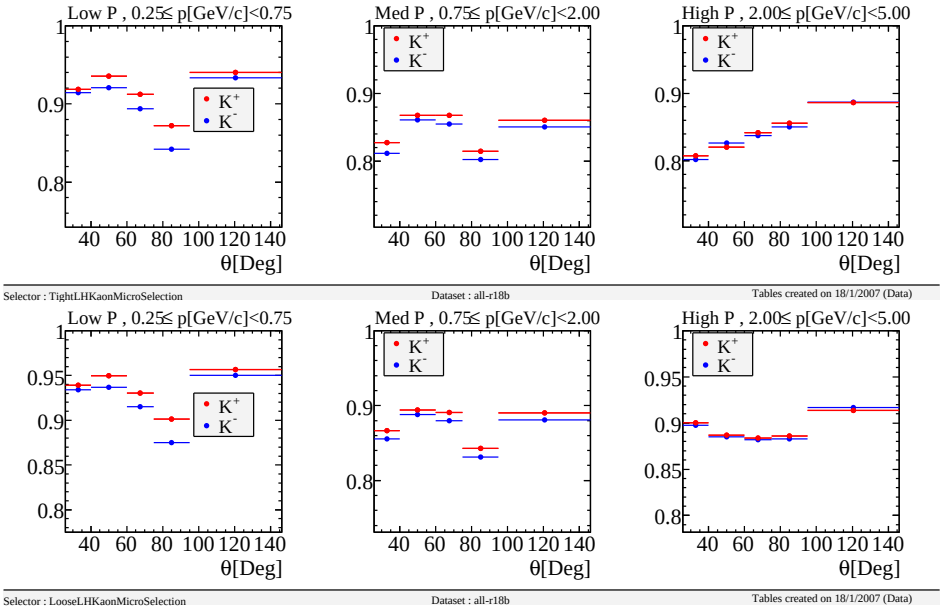

Figure 4.3: Efficiency on kaons (i.e. probability of reconstruncting kaons as kaons) using the $KLHTight$ and the $KLHLoose$ selectors (upper and lower plots respectively), as a function of the polar angle θ for different track momentum intervals (from left to right: $0.25 \leq p[\mathrm{GeV}/c] < 0.75$; $0.75 \leq p[\mathrm{GeV}/c] < 2.00$; $2.00 \leq p[\mathrm{GeV}/c] < 5.00$).

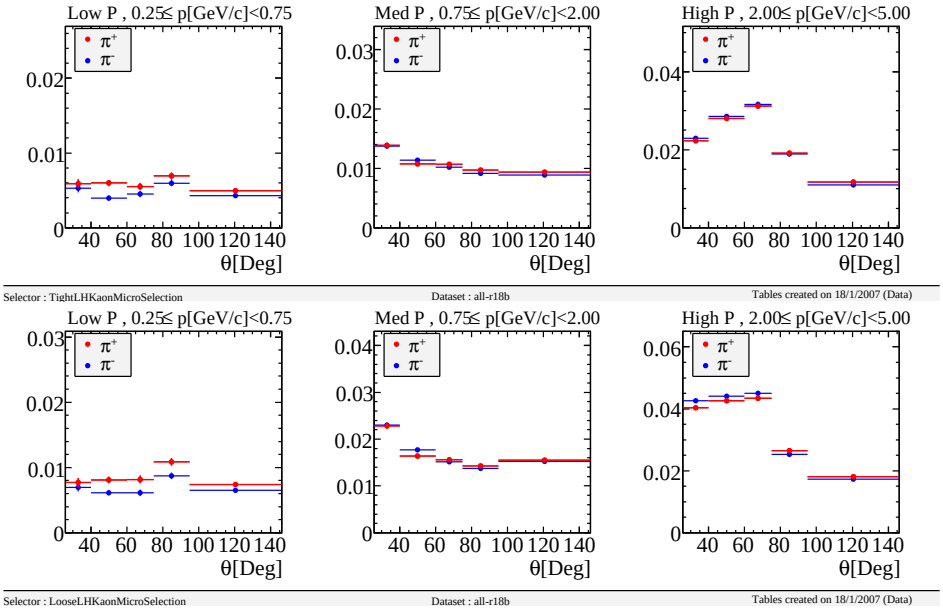

Figure 4.4: Probability of reconstructing a pion as a kaon using the $KLHTight$ selector, as a function of the polar angle θ for different track momentum intervals (from left to right: $0.25 \leq p[\mathrm{GeV}/c] < 0.75$; $0.75 \leq p[\mathrm{GeV}/c] < 2.00$; $2.00 \leq p[\mathrm{GeV}/c] < 5.00$).

4.3.2 Electron identification

Electron identification is based on EMC information, since the electrons that reach the calorimeter produce electromagnetic showers depositing their energy in the crystals.

Also hadrons that reach the EMC interact and start to produce a shower. However an electromagnetic shower has a symmetric shape around the particle flight direction, while an hadronic shower has an irregular distribution. In addition, the hadronic interaction length of the EMC being much larger than the electromagnetic one, the hadrons deposit only part of their energy in the EMC, while the electrons deposit all their energy. The electron candidates are identified from energy deposits in a fiducial volume, defined by 0.36 rad $< \theta <$ 2.372 rad. More details on the electromagnetic showers are given in sec. 4.4, while describing the photon reconstruction.

4.3.3 Muon identification

The detector dedicated to the muon identification in *BABAR* is the IFR. In order to associate the DCH information to each energy deposit in the IFR, all the charged tracks reconstructed in the DCH are extrapolated to the IFR, taking into account the bending due to the magnetic field. Only tracks that intersect the layers close to a hit are associated with a charged cluster.

4.4 Reconstruction of π^0 mesons

The π^0 mesons, used in the ADS analysis (see chapter 5) to reconstruct the neutral D decaying to $K^{\pm}\pi^{\mp}\pi^0$ final state, are reconstructed from pairs of photons detected in the EMC. Each photon produces an electromagnetic shower in the EMC, distinguishable from an hadronic shower because of the different shape. In order to select photons the following condition is required on the lateral energy distribution:

$$LAT < 0.8 \;\text{ where }\; LAT = \frac{\sum_{i=3}^{N} E_i r_i^2}{\sum_{i=3}^{N} E_i r_i^2 + E_1 r_0^2 + E_2 r_0^2};$$

where N is the number of crystals touched by the shower, E_i the energy of the i-th crystal (with $E_i > E_{i+1}$), r_i the distance between the i-th crystal and the shower axis, as shown in Fig. 4.5 and r_0 is the average distance between the two most energetic crystals (typically, $r_0 = 5$ cm). The distribution of the LAT variable for reconstructed photons is shown in Fig. 4.5.

To ensure that the electromagnetic shower was generated by a photon and not by an electron, photon candidates for which the DCH has detected a charged track pointing to the direction of the energy deposit in the EMC are rejected.

Any pair of two photons, each one with energy higher that 30 MeV and with a total energy sum larger than 200 MeV makes a candidate π^0, provided that its invariant mass is in the interval 110 MeV/c^2 $< m_{\gamma\gamma} <$ 160 MeV (the π^0 nominal mass being $m_{\pi^0} = 135$ MeV/c^2 [8]). The π^0 four-momentum is determined from a fit to the two photons, in which the π^0 reconstructed mass is constrained to be equal to the nominal π^0 mass (see sec. 4.2).

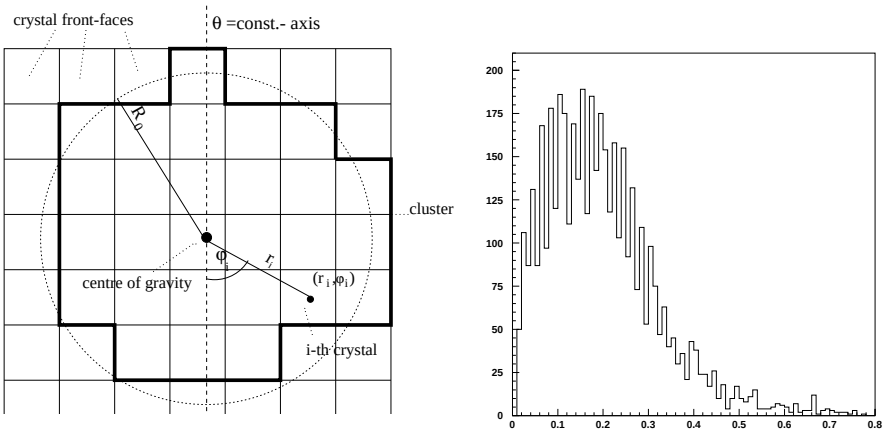

Figure 4.5: Graphical representation of the variables caracterizing an energy deposit in the EMC (left) and LAT distribution for reconstructed photons (right).

4.5 Reconstruction of K_S mesons

In the Dalitz analysis presented in chapter 6, we reconstruct K_S produced in neutral D decays to $K_S\pi^+\pi^-$ final states. The K_S candidates are reconstructed from pairs of oppositely charged pions ($BR(K_S \to \pi^+\pi^-) = (69.2 \pm 0.05)10^{-2}$) originating from a common vertex. The K_S four-momentum is obtained from its decay products through a fit in which the K_S reconstructed mass is constrained to be equal to the nominal K_S mass (see sec. 4.2).

4.6 Reconstruction of the neutral K^* mesons

In both analyses presented in this thesis, for the reasons explained in 2.6, the neutral K^* candidates are reconstructed in the final state $K^\pm\pi^\mp$. In the following, unless not specified otherwise, K^{*0} refers to $K^{*0}(892)$.

The charged kaon is required to pass the $KLHTight$ selection while no particular requirements are asked for the pion. The K^* four-momentum is determined by a fit to its decay products, and we require the fit to have converged (referred to as "$P[\chi^2(K^{*0})_{vtx}, ndof] > 0$" in the following, with $ndof$ the number of degrees of freedom).

K^{*0} candidates are selected using the invariant mass of the K^{*0} and the cosine of the helicity angle of the K^{*0} decay products, $\cos\theta_{Hel}$. The helicity angle θ_{Hel} is defined as the angle in the K^* rest frame between the direction of flight of a K^* decay product with respect to the direction of flight of the K^* in the B rest frame. The K^* has spin 1, therefore the angular distribution is a function of the helicity angle, $\frac{dN}{d(\cos\theta_{Hel})} \propto \cos^2\theta_{Hel}$. The distribution for background events is expected to be flat. It has to be stressed here that the selection of the K^* candidates has an effect on the numerical evaluation of the factor k. The knowledge of the parameter k is important, as explained in sec. 2.6 and 2.6.2, since it modifies the relations between the observables we measure and the quantities we want to determine (γ, r_S and δ_S). Thus, it is important that both the ADS and Dalitz analyses apply the same

cuts on the K^{*0} mass and helicity. To define the optimal selection criteria on the invariant mass of the K^{*0} and on $\cos\theta_{Hel}$, we use the statistical significance $S/\sqrt{S+B}$, where S and B are the expected numbers of signal and background events respectively. For the evaluation of the number of signal events S, we assume $r_S = 0.3$ and $R_{ADS} \sim r_S^2 = 0.09$. In Fig. 4.6 we show the distribution of the invariant mass of the K^{*0} and on $\cos\theta_{K^{*0}Hel}$ for signal and the variation of the statistical significance as a function of the value of the cuts on the two variables. The shown distributions has been obtained on one particular channel (the $K\pi$ mode) studied in the ADS analysis (following a procedure that will be explained in more detail in sec. 5.2.3), however tests have been made to see that the chosen cuts are suitable for all the analyzed modes. We apply the following cuts: $|m_{K^*} - m_{K^*}(nominal)| < 48$ MeV/c^2 and $|\cos\theta_{Hel}| > 0.3$.

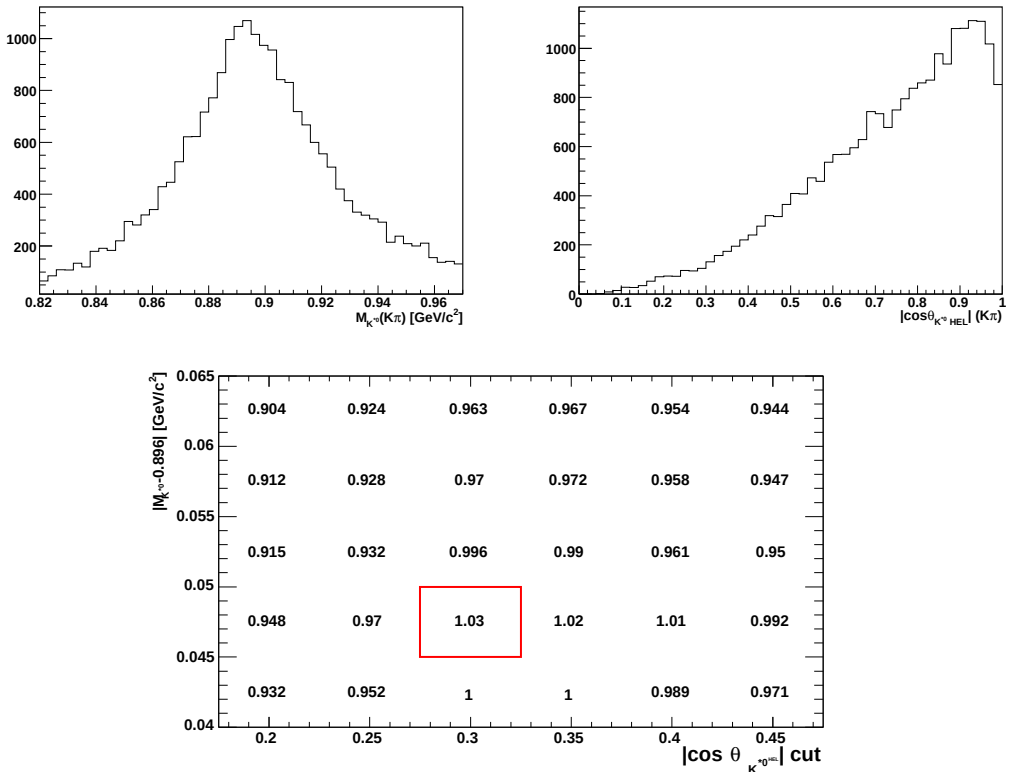

Figure 4.6: Variation of the statistical significance $S/\sqrt{S+B}$ (where S and B are the number of signal and background events respectively) for different values of the cuts on the invariant mass of the K^* and on the cosine of the helicity angle of the K^* decay products. The distribution has been obtained on simulated events and the bin marked with a (red) box corresponds to the highest significance.

4.7 Reconstruction of the neutral D mesons

In the two analyses presented in this thesis, the neutral D mesons are reconstructed in:

- $K^{\pm}\pi^{\mp}$, $K^{\pm}\pi^{\mp}\pi^{0}$ **and** $K^{\pm}\pi^{\mp}\pi^{\mp}\pi^{\pm}$**, for the ADS analysis**
  The charged kaon is requested to pass the *KLHLoose* selector (see sec. 4.3.1) in all the three modes. The neutral D four-momentum is determined from a fit to its decay products in which the D reconstructed mass is constrained to be equal to the nominal D^0 mass. We require this fit to have converged ($P[\chi^2(D^0)_{vtx}, ndof] > 0$) for the $K^{\pm}\pi^{\mp}$ and $K^{\pm}\pi^{\mp}\pi^{0}$ modes, while for the $K^{\pm}\pi^{\mp}\pi^{\mp}\pi^{\pm}$ mode the requirement on the χ^2 probability of the fit is tighter ($P[\chi^2(D^0)_{vtx}, ndof] > 0.001$), because of the presence of abundant combinatorial background.

- $K_S\pi^{+}\pi^{-}$ **final state, for the Dalitz analysis**
  The neutral D is reconstructed from K_S candidates and a couple of oppositely charged pions. The neutral D four-momentum is determined from a fit to its decay products in which the D reconstructed mass is constrained to be equal to the nominal D^0 mass, we require this fit to have converged ($P[\chi^2(D^0)_{vtx}, ndof] > 0$).

The D candidate invariant mass distributions, for all the four decays analyzed in this thesis, are shown in fig 4.7 and the corresponding resolutions are listed in Tab. 4.2. These results are obtained on dedicated samples of simulated signal events.

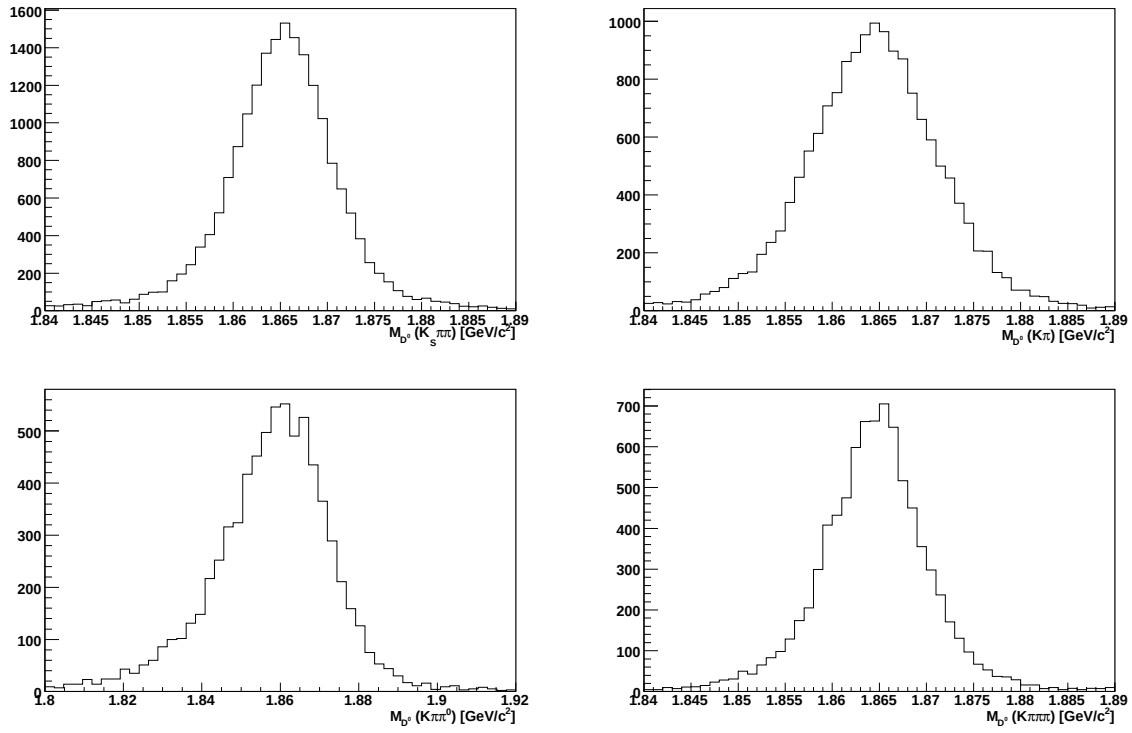

Figure 4.7: D^0 mass distribution for $B^0 \to D^0 K^{*0}$ MC generated signal events with D^0 decaying to $K_s\pi^{+}\pi^{-}$ (up left), $K^{\pm}\pi^{\mp}$ (up right), $K^{\pm}\pi^{\mp}\pi^{0}$ (down left), $K^{\pm}\pi^{\mp}\pi^{\mp}\pi^{\pm}$ (down right).

	$K_S\pi\pi$	$K\pi$	$K\pi\pi^0$	$K\pi\pi\pi$
$\sigma_{M_{D^0}}$ [MeV/c^2]	6.0	7.2	13.5	5.7

Table 4.2: M_{D^0} distribution resolutions for the different decay modes analyzed in this thesis.

4.8 Reconstruction of the neutral B mesons

The neutral B meson is reconstructed from a (mass constrained) D and a K^*. A kinematic fit, in which the D and the K^* are constrained to originate from the interaction point (*beamspot constraint*), is applied to the B. In the *beamspot constrained* fit, the error on the determination of the interaction point, which is about 10 μm in y, 200 μm in x and 8 mm in z, is taken into account.

4.8.1 The m_{ES} and ΔE variables

The B mesons are caracterized by two almost independent kinematic variables: the beam-energy substituted mass

$$m_{ES} \equiv \sqrt{(E_0^{*2}/2 + \vec{p_0} \cdot \vec{p_B})^2/E_0^2 - {p_B}^2} \tag{4.1}$$

and the energy difference

$$\Delta E \equiv E_B^* - E_0^*/2\,, \tag{4.2}$$

where E and p are the energy and the momentum respectively, the subscripts B and 0 refer to the candidate B and to the e^+e^- system respectively and the asterisk denotes the e^+e^- CM frame. The two variables are not correlated, as can be seen in Fig. 4.8, where a distribution of m_{ES} as a function of ΔE is shown on signal MC events and on off-resonance data.

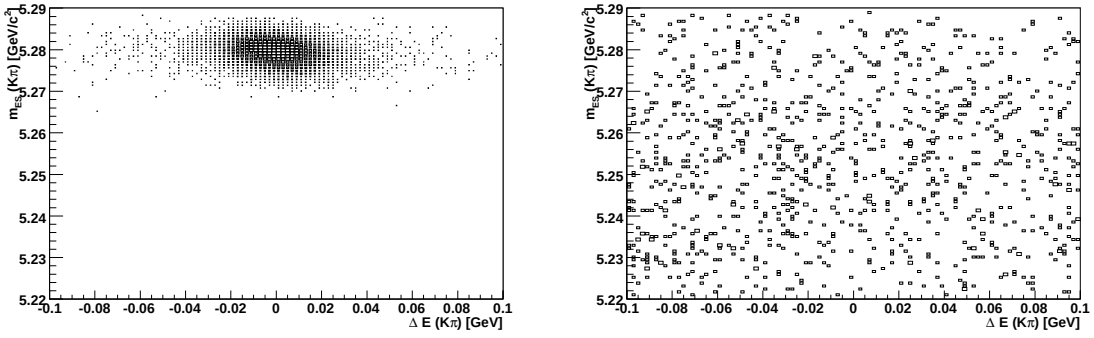

Figure 4.8: Distribution of m_{ES} as a function of ΔE on $B^0 \to D^0 K^{*0}$ MC generated signal events (left) and on off-resonance events (right). The D^0 mesons are reconstructed in $K^{\pm}\pi^{\mp}$ final state.

A typical m_{ES} distribution for MC signal events, as shown in Fig. 4.9, is described by a Gaussian distribution centered at the B mass value. The width of the m_{ES} distribution does

not depend on the reconstructed channel. Indeed, if we look at the simplified expression in the center-of-mass frame ($m_{ES}{}^2 = E_0^{*2} - p_B^{*2}$), we can see that :

$$\Delta m_{ES} \propto \sqrt{|\frac{E_0^*}{m_{ES}}|^2 \Delta E_0^* + |\frac{p_B^*}{m_{ES}}|^2 \Delta p_B^*}$$

and the contribution coming from the B momentum resolution is suppressed by the factor $|\frac{p_B^*}{m_{ES}}|^2 \approx |\frac{0.3}{5.28}|^2$. The m_{ES} resolution only depends on the error on the energy of the beams, which is known with a very high precision. The m_{ES} distribution is usually fitted with a Gaussian with a typical resolution is 2.6 MeV/c^2.

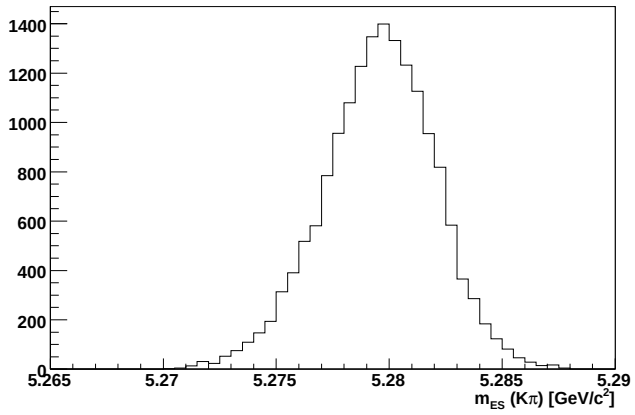

Figure 4.9: Distribution of m_{ES} on $B^0 \to D^0 K^{*0}$ MC generated signal events. The D^0 meson is reconstructed into $K^{\pm}\pi^{\mp}$ final state.

Continuum and $B\bar{B}$ background events have a different m_{ES} distribution. A typical distribution for continuum events, obtained on off-resonance data, is shown in Fig. 4.10. Similar distributions are obtained for $B\bar{B}$ background events.

This distribution is normally fitted using an Argus function $A(x)$, defined as follows:

$$A(x) = x\sqrt{1 - (\frac{x}{x_0})^2} \cdot e^{c\,(1-(\frac{x}{x_0})^2)}\,, \tag{4.3}$$

where the x_0 parameter represents the maximum allowed value for the variable x described by $A(x)$ and c accounts for the shape of the distribution.

On the other hand, the ΔE distribution is centered at zero for signal events and its resolution depends on the reconstructed channel through E_B^*. The ΔE distributions, for all the decays analyzed in this thesis, are shown in fig 4.11. These distributions are fitted with a Gaussian and the corresponding resolutions are listed in Tab. 4.3.

A typical ΔE distribution for continuum background, obtained on off-resonance events, is shown in Fig. 4.12. ΔE distributions are usually fitted with a polynomial function. Similar distributions are obtained for $B\bar{B}$ background events.

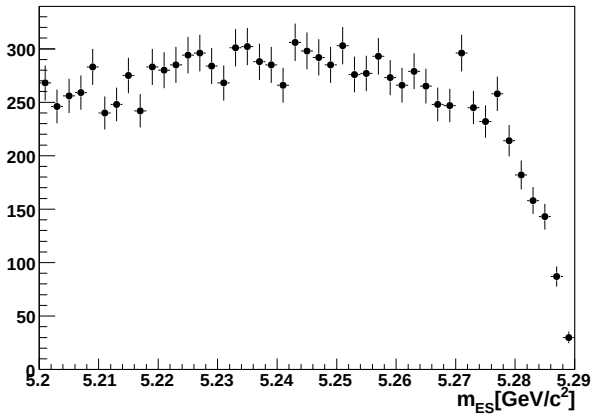

Figure 4.10: Distribution of m_{ES} for off-resonance continuum events.

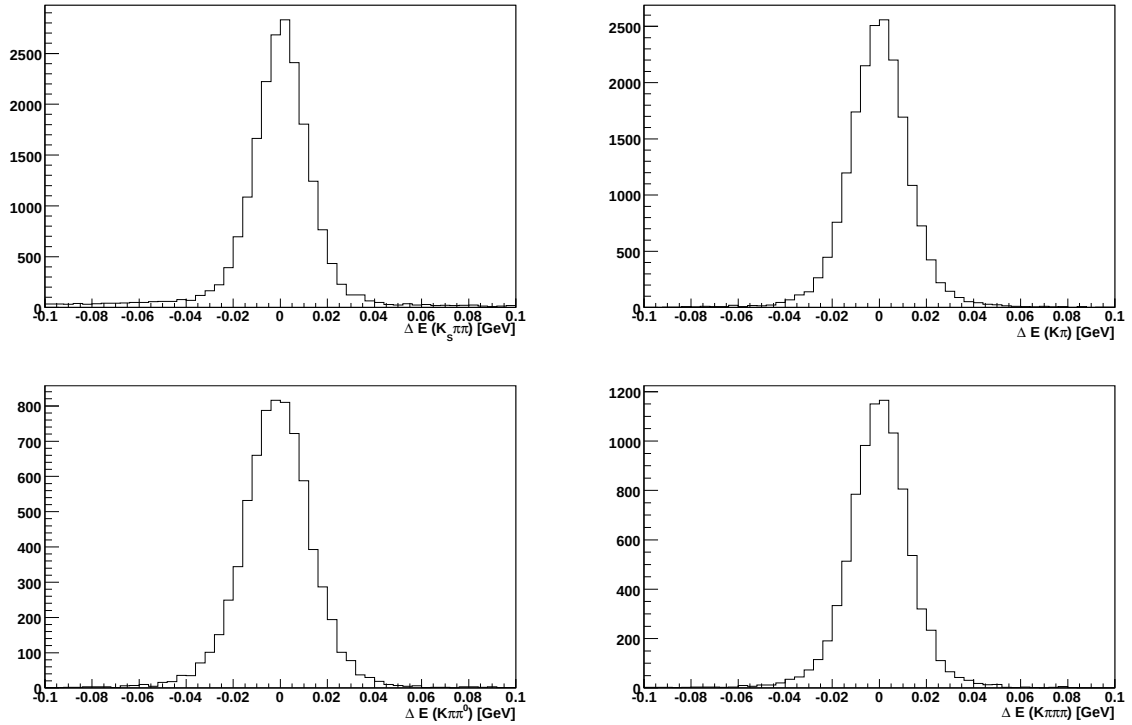

Figure 4.11: ΔE distribution of $B^0 \to D^0 K^{*0}$ MC-generated signal events with D^0 decaying to $K_S\pi^+\pi^-$ (top left), $K^\pm\pi^\mp$ (top right), $K^\pm\pi^\mp\pi^0$ (bottom left), $K^\pm\pi^\mp\pi^\mp\pi^\pm$ (bottom right).

4.8.2 Best candidate choice

If more than one B candidate is reconstructed in the same event (the fraction of events in which this happens is of the order of 1%), we choose the one with smallest $(M_{D^0} - M_{D^0}^{\rm nominal})/\sigma(M_{D^0})^2$ (where $M_{D^0}^{\rm nominal}$ is the nominal D^0 mass). In case of two B candidates

	$K_S\pi\pi$	$K\pi$	$K\pi\pi^0$	$K\pi\pi\pi$
$\sigma_{\Delta E}$ [MeV]	12.5	12.5	13.5	13.5

Table 4.3: ΔE distribution resolutions for the different decay modes analyzed in this thesis.

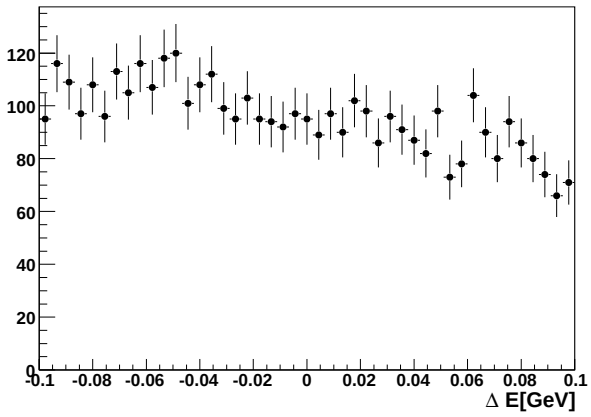

Figure 4.12: Distribution of ΔE for off-resonance continuum events.

reconstructed from the same D meson, we choose the one that has the largest absolute value of the cosine of the K^{*0} helicity angle, in the Dalitz analysis, and the one with smallest absolute value of ΔE for the ADS analysis.

4.9 Event shape variables

Since e^+e^- collide at $\sqrt{s} = M(\Upsilon(4S))$, the $\Upsilon(4S)$ resonance is produced almost at rest. Given the mass of the $\Upsilon(4S)$, $M_{\Upsilon(4S)} = 10.58$ GeV/c^2, and the mass of the B, $M_B = 5.279$ GeV/c^2, the B mesons have a very low momentum (of the order of 330 MeV/c) in the CM frame. On the other hand, $q\bar{q}$ pairs are produced with large momenta because the quark q is lighter than the quark b; the two quarks fly in opposite directions and hadronize independently. For this reason, $q\bar{q}$ events have a jet-like spatial shape, different from the spherically distributed shape of $B\bar{B}$ events.

This shape difference is reflected in several variables that can be used to distinguish continuum events from $B\bar{B}$ ones. These variables contain global information on the event shape and normally use all the tracks and energy clusters in the event, not only the ones used to reconstruct the B candidates. The variables used in the analysis presented in this thesis are (other variables have been tried, but are not used because they don't give significant gain in sensitivity):

- $|\cos(\theta_{thrust})|$, the absolute value of the cosine of the angle between the B direction and the rest of the event thrust axis (where the thrust axis is defined as the direction that maximizes the sum of the longitudinal momenta of all the particles), in the e^+e^-

center-of-mass frame. Since continuum events have a jet-like topology, the $|\cos(\theta_{thrust})|$ distribution is peaked at 1, while for $B\overline{B}$ events (that are spherically distributed in the space) it is uniform.

- **Legendre Moments**, L_{10} and L_{12}, defined as follows:

$$\begin{aligned} L_{10} &= \sum_{i=0}^{roe} p_i \ , \\ L_{12} &= \sum_{i=0}^{roe} p_i \cdot \frac{1}{2} \cdot (3\cos^2(\theta_i) - 1) \ , \end{aligned}$$

  where p_i and θ_i are the momentum and the polar angle of the particle i, in the e^+e^- center-of-mass frame. The index i runs on all the charged tracks and neutrals coming from the rest of the events (i.e. that do not belong to the reconstructed B).

- $|\Delta t|$, the absolute value of the proper time interval between the two B decays. This is calculated from the measured separation, Δz, between the decay points of the reconstructed B ($B_{\rm rec}$) and the other B ($B_{\rm oth}$) along the beam direction. The $B_{\rm rec}$ decay point is the common vertex of the two B decay products. The $B_{\rm oth}$ decay point is obtained using tracks which do not belong to $B_{\rm rec}$ and imposing constraints from the beam energy and the beam-spot location on the $B_{\rm rec}$ momentum and decay point. For events in which the B has been correctly reconstructed, the $|\Delta t|$ distribution is the convolution of a decreasing exponential function (with B lifetime τ_B) with the resolution on Δz from the detector reconstruction. The distribution is then wider than in the case of continuum events, in which just the resolution effect is observed.

These variables can be either used separately or, as it is often done, can be combined in a Fisher discriminant.

The Fisher discriminant [53] is a technique allowing to discriminate between two classes of events. Starting from a set of discriminating variables, an iterative procedure (*training*) computes the linear combination of these variables that maximizes the separation between the two classes. We consider a sample of n_{var} variables x_k, their mean values $\overline{x}_k$, their mean values when considering only the signal or only the background samples $\overline{x}_{S(B),k}$, and the total covariance matrix C of these variables. The covariance matrix can be decomposed into the sum of a within-class matrix (W) and a between-class matrix (B). They respectively describe the dispersion of events relative to the means of their own class, and relative to the overall sample means:

$$W_{kl} = \sum_{U=S,B} \langle x_{U,k} - \overline{x}_{U,k} \rangle \langle x_{U,l} - \overline{x}_{U,l} \rangle$$

$$B_{kl} = \frac{1}{2} \sum_{U=S,B} (\overline{x}_{U,k} - \overline{x}_k) (\overline{x}_{U,l} - \overline{x}_l)$$

The Fisher coefficients, F_k, are then given by:

$$F_k = \frac{\sqrt{N_S N_B}}{N_S + N_B} \sum_{l=1}^{n_{var}} W_{kl}^{-1} (\overline{x}_{S,l} - \overline{x}_{B,l})$$

where $N_{S,(B)}$ are the number of signal (background) events in the sample. The Fisher discriminant $y(i)$ for event i is given by

$$y(i) = F_0 + \sum_{k=1}^{n_{var}} F_k x_k(i);$$

where the offset F_0 centers the sample mean $\overline{y}$ of all $N_S + N_B$ events at zero.

Chapter 5

ADS analysis of $B^0 \to D^0 K^{*0}$ decay channel

In this chapter we report on the study of $B^0 \to [D^0/\bar{D}^0]K^{*0}$ decays through the ADS method, performed on 433 fb^{-1} (444×10^6 $B\bar{B}$ pairs) of data collected with the *BABAR* detector, corresponding to the full data sample collected by *BABAR* at the $\Upsilon(4S)$ center of mass energy.
The reconstructed D final states (see Fig. 5.1) are $f = K^+\pi^-$, $f = K^+\pi^-\pi^0$ and $f = K^+\pi^-\pi^+\pi^-$.

As already presented in sec. 2.2.2, the ADS method aims at bypassing the problem of the magnitude difference between the amplitudes $A(B^0 \to D^0K^{*0})$ and $A(B^0 \to \bar{D}^0K^{*0})$ by considering decays of the neutral B meson to final states that can be reached in two ways: either through a favoured B decay ($B^0 \to \bar{D}^0K^{*0}$) followed by a doubly Cabibbo suppressed D^0 decay ($\bar{D}^0 \to \bar{f}$), or through a suppressed B decay ($B^0 \to D^0K^{*0}$) followed by a favoured (not Cabibbo suppressed) D^0 decay ($D^0 \to \bar{f}$).

As shown in Fig. 5.1, there are two classes of events, which can be distinguished experimentally because of the sign of the electric charge of the two kaons in the final state. Either the two kaons have opposite electric charge (these events will be denoted as "opposite sign" in the following), or same electric charge (these events will be denoted as "same sign" in the following).

The measured observables are R_{ADS}, which is the ratio between the opposite sign and same sign events, and A_{ADS}, defined as follows:

$$R_{ADS} = \frac{\Gamma(B^0 \to \bar{f}K^{*0}) + \Gamma(\overline{B}^0 \to f\overline{K}^{*0})}{\Gamma(B^0 \to fK^{*0}) + \Gamma(\overline{B}^0 \to \bar{f}\overline{K}^{*0})}. \tag{5.1}$$

$$A_{ADS} = \frac{\Gamma(\overline{B}^0 \to f\overline{K}^{*0}) - \Gamma(B^0 \to \bar{f}K^{*0})}{\Gamma(\overline{B}^0 \to f\overline{K}^{*0}) + \Gamma(B^0 \to \bar{f}K^{*0})}. \tag{5.2}$$

In our analysis, as in other ADS studies, the A_{ADS} is not measured, as explained in sec. 2.2.2.

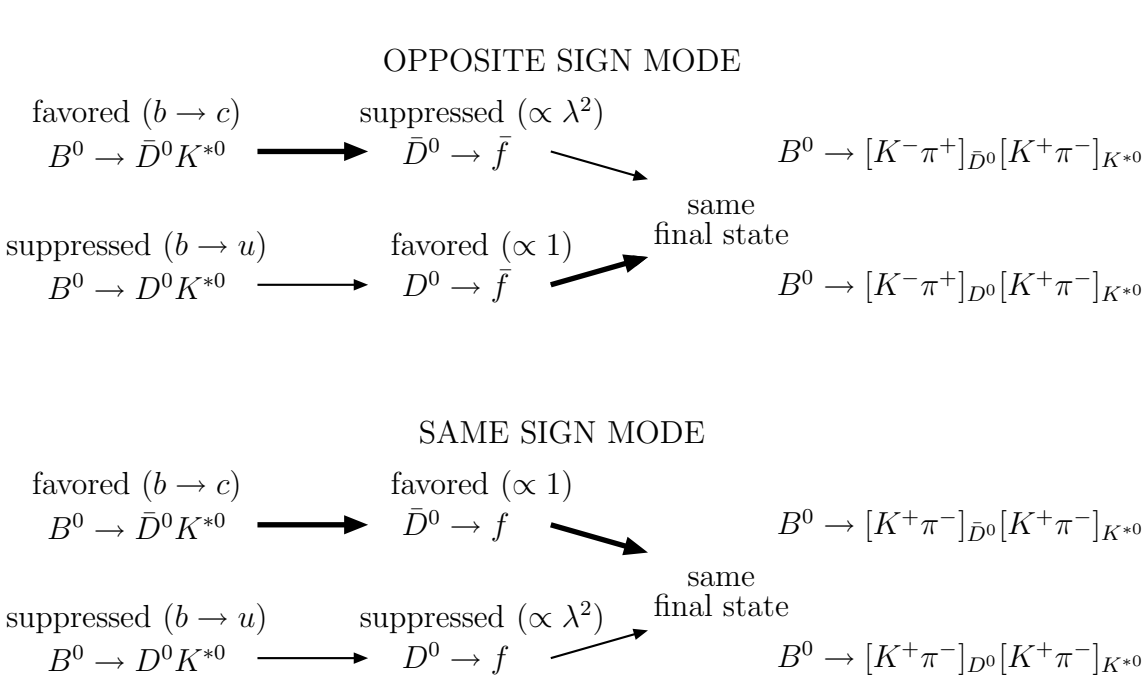

Figure 5.1: Scheme for the ADS method: B^0 mesons decaying to the same final state, through two different decay chains, for "opposite sign" events and for "same sign" events. The scheme is shown for the D final state $f \equiv K^+\pi^-$

5.1 Analysis overview: ADS method at work

5.1.1 Neutral D decays into two-body final states ($D^0 \to K^+\pi^-$)

For a D^0 decay to a two-body final state f (for example $f \equiv K^+\pi^-$) we can write:

$$A(D^0 \to f) = r_D |A(D^0 \to \bar{f})| e^{i\delta_D} \tag{5.3}$$

where δ_D is the relative strong phase between $D^0 \to f$ and $D^0 \to \bar{f}$ decay amplitudes, and r_D is the ratio between the absolute values of the two amplitudes, defined as:

$$r_D = \frac{|A(D^0 \to f)|}{|A(D^0 \to \bar{f})|}. \tag{5.4}$$

The measured value of r_D^2 for the $D^0 \to K^+\pi^-$ mode, is $r_D^2 = (3.76 \pm 0.09) \times 10^{-3}$ [8]. As shown in sec. 2.2.2 and 2.6.1, the following relations can be obtained:

$$\begin{aligned} R_{ADS} &= \frac{\Gamma(\bar{B}^0 \to [f]_D \bar{K}^{*0}) + \Gamma(B^0 \to [\overline{f}]_D K^{*0})}{\Gamma(\bar{B}^0 \to [\overline{f}]_D \bar{K}^{*0}) + \Gamma(B^0 \to [f]_D K^{*0})} \\ &= r_D^2 + r_S^2 + 2 r_S k r_D \cos\gamma \cos(\delta_S + \delta_D) \end{aligned} \tag{5.5}$$

$$\begin{aligned} A_{ADS} &= \frac{\Gamma(\bar{B}^0 \to [f]_D \bar{K}^{*0}) - \Gamma(B^0 \to [\overline{f}]_D K^{*0})}{\Gamma(\bar{B}^0 \to [f]_D \bar{K}^{*0}) + \Gamma(B^0 \to [\overline{f}]_D K^{*0})} \\ &= 2 k r_S r_D \sin\gamma \sin(\delta_S + \delta_D)/R_{ADS} \end{aligned} \tag{5.6}$$

The factor $\cos\gamma\cos(\delta_S+\delta_D)$ can vary in the range $[-1,1]$, which implies that R_{ADS} can vary in the range $[r_D^2+r_S^2-2kr_Sr_D, r_D^2+r_S^2+2kr_Sr_D]$. Taking into account the error on r_D, the range of variation of $R_{ADS}^{K\pi}$ as a function of r_S is shown in Fig. 5.2.

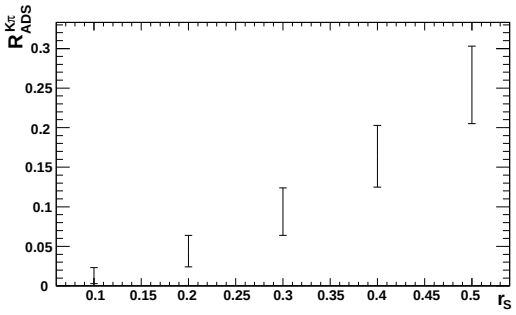

Figure 5.2: Ranges of variation of $R_{ADS}^{K\pi}$ for different values of r_S.

Eventually, the strong phase δ_D can be measured in quantum correlated $D\bar{D}$ decays by CLEO-c.

5.1.2 Neutral D decays to multi-body final states ($D^0\to K^+\pi^-\pi^0$, $D^0\to K^+\pi^-\pi^+\pi^-$)

We now consider the multi-body final states $f=K^+\pi^-\pi^0$ ($\bar{f}=K^-\pi^+\pi^0$) and $f=K^+\pi^-\pi^-\pi^+$ ($\bar{f}=K^-\pi^+\pi^+\pi^-$). Since we are dealing with a three (or four) body D^0 decay, the decay amplitude is a function of the point represented by the D^0 decay final state in the 3-body (4-body) phase space. The amplitude for the $D^0\to K\pi\pi^0$ decay will be written as a function of $m^2_{K\pi}$ and $m^2_{K\pi^0}$ and for the amplitude of $D^0\to K\pi\pi\pi$ the Cabibbo-Maksymowicz variables [54] can be used: $m^2_{K\pi}$, $m^2_{\pi\pi}$, $\theta_{K^-\pi^-}$, $\theta_{\pi^+\pi^+}$ and ϕ. These variables are defined as follows:

- m^2_{ab} is the squared invariant mass of the couple of particles a and b.
- θ_{ab} is the angle between the momentum of the particle a in the rest frame of the ab system and the momentum of the ab system in the D rest frame.
- for $D^0\to K\pi\pi\pi$ decays, ϕ is the angle between the $K^\mp\pi^\mp$ and the $\pi^\pm\pi^\pm$ decay planes.

More explicitly, if the considered D final state is $f=K^+\pi^-\pi^0$ or $K^+\pi^-\pi^+\pi^-$, then $m^2_{K\pi}=m^2_{K^+\pi^-}$, $m^2_{K\pi^0}=m^2_{K^+\pi^0}$, $m^2_{\pi\pi}=m^2_{\pi^+\pi^-}$, $\theta_{K\pi}=\theta_{K^+\pi^+}$, $\theta_{\pi\pi}=\theta_{\pi^-\pi^-}$ and ϕ is the angle between the $K^+\pi^+$ decay plane and the $\pi^-\pi^-$ decay plane in the rest frame of the D meson. On the other hand, if the D considered final state is $\bar{f}$, then $m^2_{K\pi}=m^2_{K^-\pi^+}$, $m^2_{K\pi^0}=m^2_{K^-\pi^0}$, $m^2_{\pi\pi}=m^2_{\pi^-\pi^+}$, $\theta_{K\pi}=\theta_{K^-\pi^-}$, $\theta_{\pi\pi}=\theta_{\pi^+\pi^+}$ and ϕ is the angle between the $K^-\pi^-$ decay plane and the $\pi^+\pi^+$ decay plane in the rest frame of the D meson.

The following definitions are used, where m indicates the generic point in the Dalitz plane ($m=m_{K\pi}, m_{K\pi^0}$ for the $D\to K\pi\pi^0$ decay and $m=m^2_{K\pi}, m^2_{\pi\pi}, \theta_{K\pi}, \theta_{\pi\pi}, \phi$):

$$\mathcal{B}_B = \mathcal{BR}(B^0 \to \bar{D}^0 K^{*0}) \tag{5.7}$$
$$\mathcal{B}_D = \mathcal{BR}(D^0 \to \overline{f}) \tag{5.8}$$
$$\mathcal{A}_D(m)e^{i\delta(m)} = \mathcal{A}(D^0 \to f) = \mathcal{A}(\bar{D}^0 \to \bar{f}) \tag{5.9}$$
$$\overline{\mathcal{A}}_D(m)e^{i\overline{\delta}(m)} = \mathcal{A}(D^0 \to \bar{f}) = \mathcal{A}(\bar{D}^0 \to f) \tag{5.10}$$
$$r_S e^{i(\gamma+\delta_S)} = \frac{\mathcal{A}(B^0 \to D^0 K^{*0})}{\mathcal{A}(B^0 \to \bar{D}^0 K^{*0})} \tag{5.11}$$
$$r_D = \sqrt{\frac{\int |\mathcal{A}_D|^2 dm}{\int |\overline{\mathcal{A}}_D|^2 dm}} \tag{5.12}$$

Equation 5.9 is a formulation of the CP conservation in D decays and more specifically we can write:

$$A(D^0 \to K^+(p_1)\pi^-(p_2)\pi^0(p_3)) = A(\bar{D}^0 \to K^-(p_1')\pi^+(p_2')\pi^0(p_3')) \tag{5.13}$$

or, for the $K\pi\pi\pi$ mode,

$$A(D^0 \to K^+(p_1)\pi^-(p_2)\pi^-(p_3)\pi^+(p_4)) = A(\bar{D}^0 \to K^-(p_1')\pi^+(p_2')\pi^+(p_3')\pi^-(p_4')) \tag{5.14}$$

where the primed 4-momenta have the spatial components with opposite sign and therefore $|p_i + p_j|^2 = |p_i' + p_j'|^2$.

In the following, we calculate R_{ADS} and A_{ADS} in case of multibody D decays. The branching fractions have to be expressed as integrals over the Dalitz plane:

$$\begin{aligned}
\mathcal{BR}(B^0 \to \overline{f}K^{*0}) &= \mathcal{B}_B \int |r_S e^{i(\gamma+\delta_S)}\overline{\mathcal{A}}_D(m)e^{i\overline{\delta}(m)} + \mathcal{A}_D(m)e^{i\delta(m)}|^2 dm = \\
&= \mathcal{B}_B \int [|r_S\overline{\mathcal{A}}_D|^2 + |\mathcal{A}_D|^2 + 2r_S\mathcal{A}_D\overline{\mathcal{A}}_D\cos(\gamma + \delta_S + \overline{\delta} - \delta)]dm = \\
&= \mathcal{B}_B\mathcal{B}_D \cdot [r_S^2 + r_D^2 + \frac{2r_S}{\mathcal{B}_D}\int \mathcal{A}_D\overline{\mathcal{A}}_D(\cos\Delta\cos\gamma - \sin\Delta\sin\gamma)dm] = \\
&= \mathcal{B}_B\mathcal{B}_D \cdot [r_S^2 + r_D^2 + 2r_S r_D(C\cos\gamma - S\sin\gamma)]
\end{aligned} \tag{5.15}$$

where $\Delta = \delta_S + \overline{\delta} - \delta$ and

$$C = \frac{1}{\mathcal{B}_D r_D}\int \mathcal{A}_D(m)\overline{\mathcal{A}}_D(m)\cos\Delta dm\,, \tag{5.16}$$
$$S = \frac{1}{\mathcal{B}_D r_D}\int \mathcal{A}_D(m)\overline{\mathcal{A}}_D(m)\sin\Delta dm\,. \tag{5.17}$$

The terms $\mathcal{B}_D r_D$ can be written as:

$$\mathcal{B}_D r_D = \int |\overline{\mathcal{A}}_D(m)|^2 dm \cdot \sqrt{\frac{\int |\mathcal{A}_D(m)|^2 dm}{\int |\overline{\mathcal{A}}_D(m)|^2 dm}} = \sqrt{\int |\overline{\mathcal{A}}_D(m)|^2 dm \cdot \int |\mathcal{A}_D(m)|^2 dm} \tag{5.18}$$

and C and S as:

$$C \equiv \frac{\int \mathcal{A}_D(m)\overline{\mathcal{A}}_D(m)\cos\Delta dm}{\sqrt{\int |\overline{\mathcal{A}}_D(m)|^2 dm \cdot \int |\mathcal{A}_D(m)|^2 dm}} \tag{5.19}$$

$$S \equiv \frac{\int \mathcal{A}_D(m)\overline{\mathcal{A}}_D(m)\sin\Delta dm}{\sqrt{\int |\overline{\mathcal{A}}_D(m)|^2 dm \cdot \int |\mathcal{A}_D(m)|^2 dm}}\,. \tag{5.20}$$

The expression of the branching ratios for opposite sign events, that enter in the definition of the numerator of R_{ADS}, is the following:

$$\begin{aligned}
\mathcal{BR}(B^0 \to \overline{f}K^{*0}) &= \mathcal{B}_B\mathcal{B}_D(r_S^2 + r_D^2 \\
&+ 2r_S r_D(C\cos\gamma - S\sin\gamma)); &(5.21)\\
\mathcal{BR}(\bar{B}^0 \to f\bar{K}^{*0}) &= \mathcal{B}_B\mathcal{B}_D(r_S^2 + r_D^2 \\
&+ 2r_S r_D(C\cos\gamma + S\sin\gamma)). &(5.22)\\
& &(5.23)
\end{aligned}$$

The expression of the branching ratios of same sign events, that enter in the definition of the denominator of R_{ADS}, making the same approximation as in sec. 2.2.2, is the following

$$\begin{aligned}
\mathcal{BR}(B^0 \to fK^{*0}) &= \mathcal{B}_B\mathcal{B}_D(1 + r_S^2 r_D^2 \\
&+ 2r_S r_D(C\cos\gamma - S\sin\gamma)) \sim \mathcal{B}_B\mathcal{B}_D &(5.24)\\
\mathcal{BR}(\bar{B}^0 \to \overline{f}\bar{K}^{*0}) &= \mathcal{B}_B\mathcal{B}_D(1 + r_S^2 r_D^2 \\
&+ 2r_S r_D(C\cos\gamma + S\sin\gamma)) \sim \mathcal{B}_B\mathcal{B}_D &(5.25)\\
& &(5.26)
\end{aligned}$$

where the quantities C and S are the same for the B^0 and the $\bar{B}^0$ if no CP violation is assumed in D decays since the CP transformation of the D decay amplitudes does not change the Dalitz variables $m_{K\pi}$ and $m_{K\pi^0}$ (see Eq. 5.14 and related comment). The expression for R_{ADS} and A_{ADS} are the following:

$$\begin{aligned}
R_{ADS} &= r_S^2 + r_D^2 + 2r_S r_D C\cos\gamma &(5.27)\\
A_{ADS} &= 2r_S r_D S\sin\gamma / R_{ADS}. &(5.28)
\end{aligned}$$

We now consider the expression for C in eq. 5.19. The following inequality holds:

$$\begin{aligned}
&\int dmdm'[\mathcal{A}_D(m)^2\overline{\mathcal{A}}_D(m')^2 - \mathcal{A}_D(m)\overline{\mathcal{A}}_D(m)\mathcal{A}_D(m')\overline{\mathcal{A}}_D(m')] = \\
&\qquad = \frac{1}{2}\int dmdm'[\mathcal{A}_D(m)\overline{\mathcal{A}}_D(m') - \mathcal{A}_D(m')\overline{\mathcal{A}}_D(m)]^2 \geq 0. &(5.29)
\end{aligned}$$

from which it follows that:

$$\int |\mathcal{A}_D|^2 dm \cdot \int |\overline{\mathcal{A}_D}|^2 dm - [\int \mathcal{A}_D(m)\overline{\mathcal{A}_D}(m)dm]^2 \geq 0,$$

and since the following relations are valid:

$$\begin{aligned} -\int \mathcal{A}_D\overline{\mathcal{A}}_D dm \leq \int \mathcal{A}_D\overline{\mathcal{A}}_D \cos\Delta dm &\leq \int \mathcal{A}_D\overline{\mathcal{A}}_D dm; \\ -\int \mathcal{A}_D\overline{\mathcal{A}}_D dm \leq \int \mathcal{A}_D\overline{\mathcal{A}}_D \sin\Delta dm &\leq \int \mathcal{A}_D\overline{\mathcal{A}}_D dm; \end{aligned} \tag{5.30}$$

hence the following inequalities hold:

$$\begin{aligned} -\sqrt{\int |\overline{\mathcal{A}}_D|^2 dm \cdot \int |\mathcal{A}_D|^2 dm} \leq \int \mathcal{A}_D\overline{\mathcal{A}}_D \cos\Delta dm &\leq \sqrt{\int |\overline{\mathcal{A}}_D|^2 dm \cdot \int |\mathcal{A}_D|^2 dm}; \\ -\sqrt{\int |\overline{\mathcal{A}}_D|^2 dm \cdot \int |\mathcal{A}_D|^2 dm} \leq \int \mathcal{A}_D\overline{\mathcal{A}}_D \sin\Delta dm &\leq \sqrt{\int |\overline{\mathcal{A}}_D|^2 dm \cdot \int |\mathcal{A}_D|^2 dm}; \end{aligned}$$

which imply

$$-1 \leq C \leq 1; \tag{5.31}$$

$$-1 \leq S \leq 1; \tag{5.32}$$

and therefore:

$$r_S^2 + r_D^2 - 2r_S r_D \cos\gamma \leq R_{ADS} \leq r_S^2 + r_D^2 + 2r_S r_D \cos\gamma. \tag{5.33}$$

$$-2r_S r_D \sin\gamma / R_{ADS} \leq A_{ADS} \leq 2r_S r_D \sin\gamma / R_{ADS}. \tag{5.34}$$

The experimental values for the ratios r_D^2, integrated over the whole Dalitz plane, for the $K\pi\pi^0$ and $K\pi\pi\pi$ modes, are [8]:

$$r_D^2(K\pi\pi^0) = (2.18 \pm 0.10)10^{-3}, \tag{5.35}$$

$$r_D^2(K\pi\pi\pi) = (3.23 \pm 0.24)10^{-3}. \tag{5.36}$$

$$\tag{5.37}$$

Taking into account the variation of C and S in their full range ($[-1, 1]$) and the experimental error on r_D, we give in Fig. 5.3 the variation for $R_{ADS}^{K\pi\pi^0}$ and $R_{ADS}^{K\pi\pi\pi}$ as a function of r_S.

It can be seen that the C and S parameters can be determined from a measurements of the Dalitz structure of the allowed and suppressed multibody D decays. Singling out the B decay strong phase, one can indeed write:

$$\begin{aligned} C &= P_c cos\delta_S - P_s sin\delta_S \\ S &= P_c sin\delta_S + P_s cos\delta_S \end{aligned} \tag{5.38}$$

where

$$\begin{aligned} P_c &= \frac{\int \mathcal{A}_D\overline{\mathcal{A}}_D \cos(\overline{\delta}(m) - \delta(m))dm}{\sqrt{\int |\overline{\mathcal{A}}_D|^2 dm \cdot \int |\mathcal{A}_D|^2 dm}} \\ P_s &= \frac{\int \mathcal{A}_D\overline{\mathcal{A}}_D \sin(\overline{\delta}(m) - \delta(m))dm}{\sqrt{\int |\overline{\mathcal{A}}_D|^2 dm \cdot \int |\mathcal{A}_D|^2 dm}} \end{aligned} \tag{5.39}$$

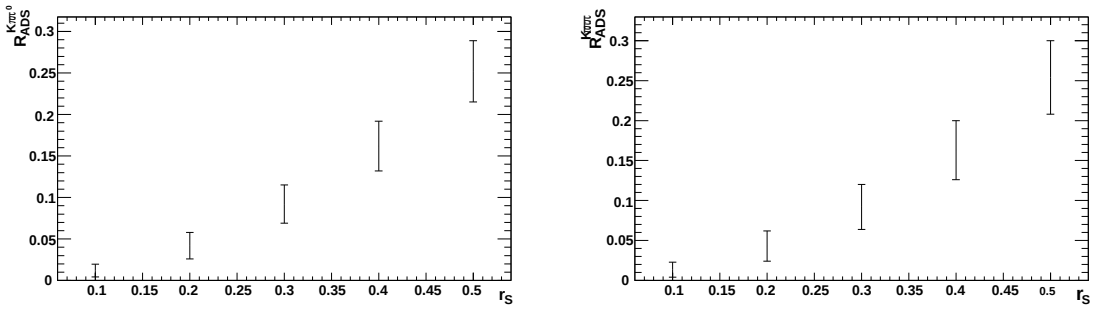

Figure 5.3: Ranges of variation of $R^{K\pi\pi^0}_{ADS}$ and $R^{K\pi\pi\pi}_{ADS}$ for different values of r_S.

which can be derived knowing the Dalitz structure.

An alternative formalism, formally identical to the one presented in [33] (that we use for describing $B \to DK^*$ decays, see sec. 2.6.1), is obtained starting from the following definition:

$$k_d e^{i\delta^D_S} = \frac{\int \mathcal{A}_D \overline{\mathcal{A}}_D e^{i(\overline{\delta}(m)-\delta(m))} dm}{\sqrt{\int |\overline{\mathcal{A}}_D|^2 dm \cdot \int |\mathcal{A}_D|^2 dm}}. \tag{5.40}$$

The quantities introduced in eq. 5.39 are simply related to the ones introduced in eq. 5.40 by:

$$P_c = k_D \cos\delta^D_S;$$
$$P_s = k_D \sin\delta^D_S;$$

and consequently:

$$C = k_D \cos(\delta^D_S + \delta_S);$$
$$S = k_D \sin(\delta^D_S + \delta_S).$$

The use of the definitions in eq. 5.40, that makes the expressions for multi-body decay formally identical to the ones for two-body decays (except for the k_D parameter), is adopted by the CLEO-c collaboration, where these parameters can be measured exploiting the quantum correlation in $D\bar{D}$ decays. The general expression for R_{ADS} and A_{ADS} in this formalism are the following:

$$R_{ADS} = r_S^2 + r_D^2 + 2 r_S r_D k k_D \cos\gamma \cos(\delta^D_S + \delta_S); \tag{5.41}$$
$$A_{ADS} = 2 r_S r_D k k_D \sin\gamma \sin(\delta^D_S + \delta_S)/R_{ADS}; \tag{5.42}$$

where k_D and δ^D_S result from integrals over the D Dalitz plane and depend on the D decay mode. The case of a two-body decay is obtained with $k_D \to 1$, $\delta^D_S \to \delta_D$.

5.1.3 Combination of the three channels

Recently, a measurement of the relative strong phase δ_D has been perfomed by the CLEO-c collaboration [55] and preliminary results for the coherence factor k_D and the strong phase δ_S^D for the $K\pi\pi\pi$ channel have been presented at the conference on "Flavour physics and CP violation" in Taipei, Taiwan (May 2008).

As a general fact, the knowledge of the strong phase for the $K\pi$ mode and of k_D and δ_S^D for $K\pi\pi^0$ and $K\pi\pi\pi$ would reduce the unknowns of the system to γ, r_S and δ_S. Also measuring only the ratios R_{ADS} in the three channels would then allow to close the system, since there would be three unknowns and three measured observables.

As a matter of fact, the preliminary results presented by CLEO-c on the $K\pi\pi\pi$ mode seem to prefer a value for $k_D^{K\pi\pi\pi}$ significantly smaller than unity. This would reduce the sensitivity to the phases, but improve the sensitivity to r_S.

5.2 Selection and background caracterization

The selection criteria are chosen, separately for each channel, in order to maximize the sensitivity to R_{ADS}. Assuming $r_S = 0.3$ and $r_D \ll r_S$ the ratios R_{ADS} are expected to be roughly of the order of 0.1 (see Fig. 5.2 and 5.3). We then expect to have ten times more "same sign" than "opposite sign" events and the error on the R_{ADS} ratios will mainly depend on the error on the latter. Moreover, as it will be shown in the following, we expect more background in the opposite sign sample than in the same sign. For these reasons, the selection criteria have been optimized in order to minimize the error on the number of "opposite sign" signal events, which leads the sensitivity to R_{ADS}.

The selection studies are based on MC generated events for the signal modes and for the different backgrounds and, whenever possible, directly on data. The agreement of the relevant variables distribution between data and MC has also been checked. To allow us to properly reweight the events according to different Dalitz structures, the same and opposite sign signal Monte Carlo samples are generated with the neutral D decaying isotropically (phase space), without assuming any resonance model. The MC samples for the background have been instead generated according to the measured Dalitz model for the favored D^0 decay. The data and MC samples used for the ADS analysis are summarized in Tab. 5.1.

5.2.1 Preselection criteria

The first step of the analysis consists of some loose preselection cuts, described below. The main reason for this step is to reduce the size of the initial sample without losing almost any signal efficiency. The optimization of the final selection cuts is made on events that pass these first loose cuts.

The described preselection criteria are summarized below:

- $m_{ES} \in [5.2,5.3]\,\mathrm{GeV}/c^2$;
- $|\Delta E| < 0.06\mathrm{GeV}$ ($\sim 4.8\sigma$ for $K\pi$ and $K\pi\pi\pi$ and $\sim 4.4\sigma$ for $K\pi\pi^0$);
- $0.105\ \mathrm{GeV/c^2} < \mathrm{M_{\pi^0}} < 0.155\ \mathrm{GeV/c^2}$;

Sample	# of events	cross section - BR	$\mathcal{L}_{eq}$
On-resonance data	-	-	423fb^{-1}
Off-resonance data	-	-	41.3fb^{-1}
Same Sign signal ($K\pi$)	60 k	1.68 fb	36ab^{-1}
Opposite Sign signal ($K\pi$)	60 k	0.27 fb	400ab^{-1}
Same Sign signal ($K\pi\pi^0$)	60 k	5.95 fb	10ab^{-1}
Opposite Sign signal ($K\pi\pi^0$)	60 k	0.95 fb	111ab^{-1}
Same Sign signal ($K\pi\pi\pi$)	60 k	3.40 fb	18ab^{-1}
Opposite Sign signal ($K\pi\pi\pi$)	60 k	0.54 fb	200ab^{-1}
Generic B^+B^-	685 M	0.55 nb	1245fb^{-1}
Generic $B^0\bar{B}^0$	686 M	0.55 nb	1247fb^{-1}
Generic $c\overline{c}$	1100 M	1.30 nb	837fb^{-1}
Generic uds	906 M	2.09 nb	433fb^{-1}

Table 5.1: Data and MC samples used in the analysis in terms of number of events and of equivalent integrated luminosity ($\mathcal{L}_{eq}$). The cross section of each process is also shown. The value of the branching fraction (BR) for the signal modes are estimated assuming $r_S = 0.3$.

- $K(D^0)$ KLHLoose;
- $K(K^{*0})$ KLHVeryLoose;
- $|M_{D^0} - M_{D^0}^{nominal}| < 0.036(K\pi)$, $0.068(K\pi\pi^0)$, $0.029(K\pi\pi\pi)$ GeV/c^2 (5σ);
- $|M_{K^{*0}} - M_{K^{*0}}^{nominal}| < 0.065$ GeV/c^2;

5.2.2 Continuum background caracterization and Fisher discriminant

As already discussed in sec. 4.9, in the center of mass frame, continuum events have a jet-like spatial distribution, while $B\bar{B}$ events are spherically distributed. Several variables account for this difference, allowing for a discrimination of the two kinds of events. In this analysis, the variables $|\cos(\theta_{thrust})|$, Δt, L_{10} and L_{12}, defined in sec. 4.9, are combined into a linear combination, the *Fisher discriminant* (introduced in sec. 4.9), that is used in the final maximum likelihood fit. The expression for the Fisher is:

$$Fisher = 0.9402 - 0.1706|\cos(\theta_{thrust})| + 0.3067L_{10} - 1.2224L_{12} + 0.2730|\Delta t|.$$

The distributions of the four variables of interest, for simulated signal events, off-resonance data and simulated $B\overline{B}$ background events, are shown in Fig. 5.5. In addition to the preselection, the following cuts are also applied:

- $m_{ES} > 5.27$ GeV/c^2.
- $|\Delta E| < 0.025$ GeV/c for $K\pi$ and $|\Delta E| < 0.02$ GeV/c for $K\pi\pi^0$ and $K\pi\pi\pi$.

- $|M_{D^0} - M_{D^0}^{nominal}| < 2\sigma_{M_{D^0}}\,\mathrm{GeV}/c^2$ for each channel.
- $|M_{K^{0*}} - M_{K^{*0}}^{nominal}| < 0.048\,\mathrm{GeV}/c^2$.
- $|\cos\theta_{HEL}^{K^{*0}}| > 0.29$.
- $\mathrm{Prob}(\chi^2_{B^0}) > 0.001$, $\mathrm{Prob}(\chi^2_{D^0}) > 0.001$, $\mathrm{Prob}(\chi^2_{K^{*0}}) > 0.001$.
- $0.120\,\mathrm{GeV}/c^2 < |M_{\pi^0} - 0.135| < 0.143\,\mathrm{GeV}/c^2$

These additional selection criteria have been applied in order to perform the continuum rejection studies on a sample similar to the final selected sample of this analysis. It should be stressed that the final cuts on the above listed variables are different and result from an optimization procedure as will be explained in sec. 5.2.3. The Fisher discriminant is used for the final cut optimization and for this reason we introduce it here.

Fig. 5.6 shows the agreement between off-resonance and simulated events for the different variables used for building the Fisher discriminant. The agreement is satisfactory and for this reason the simulated events have been used to train the Fisher discriminant (see sec. 4.9). In Fig. 5.7, the top plots show the agreement between off-resonance and simulated events for the Fisher distribution and the distributions for simulated signal and continuum events. In Fig. 5.7 the bottom plot shows the efficiency on the signal as a function of the efficiency on the background, for different cuts on the Fisher discriminant. The Fisher distributions shown in Fig. 5.7 are obtained using the three D^0 decay modes together. Tests performed building the Fisher discriminant using the three D modes separately give compatible results.

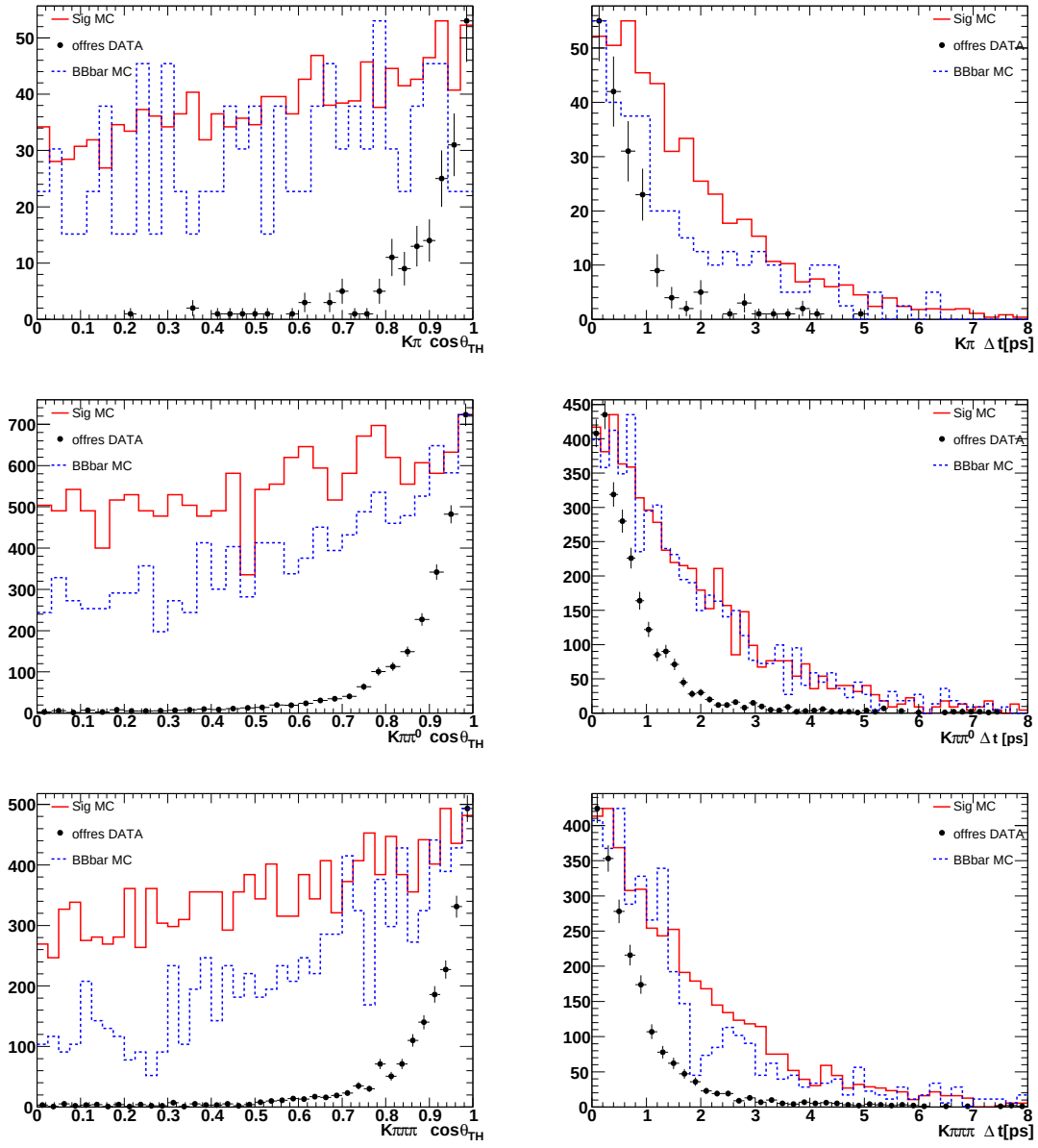

Figure 5.4: Distributions of $|cos(\theta_{thrust})|$ (left) and $|\Delta t|$ for simulated signal events, off-resonance data and simulated $B\overline{B}$ background events for $K\pi$ (top plots), $K\pi\pi^0$ (middle plots) and $K\pi\pi\pi$ events (bottom plots).

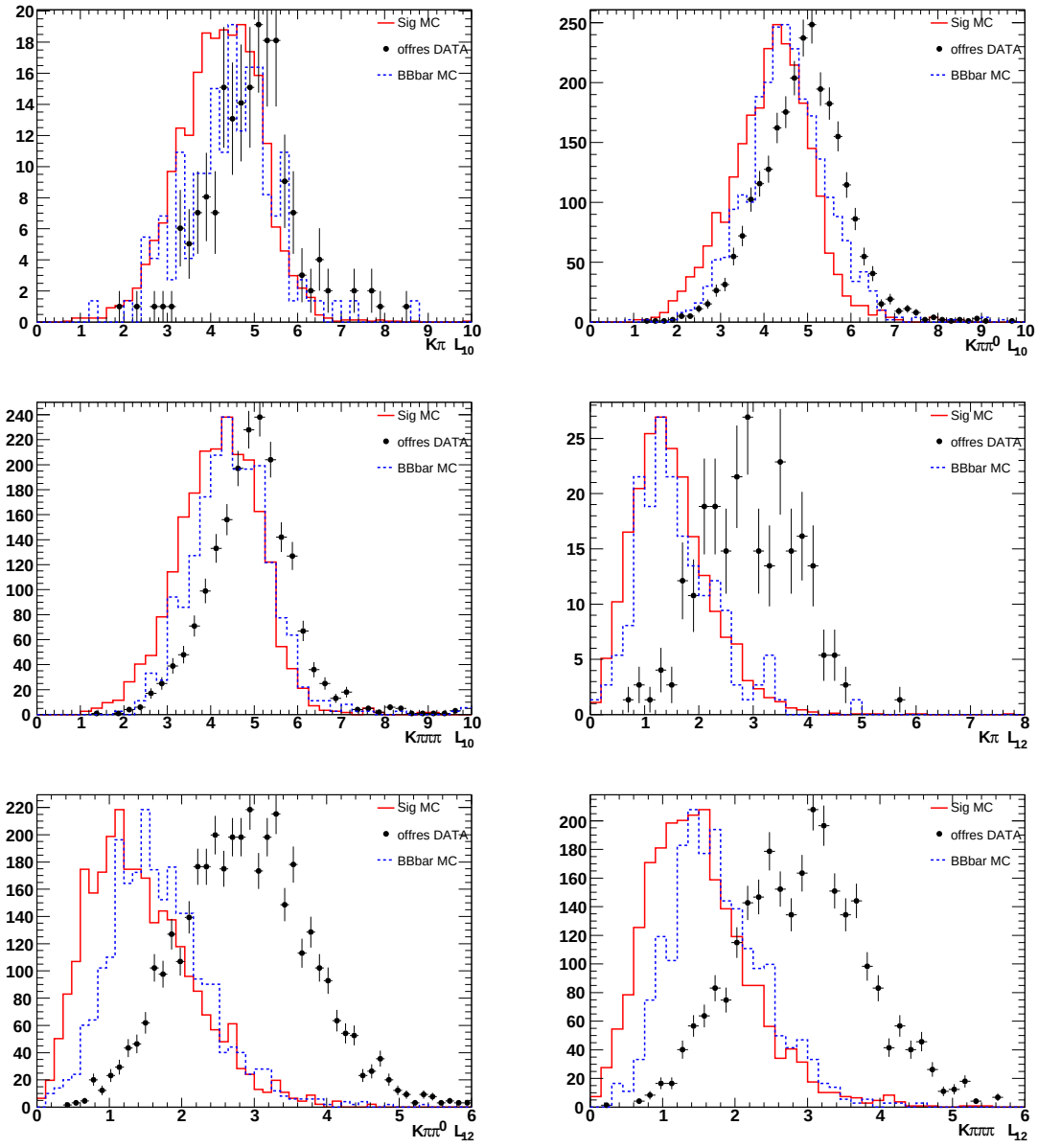

Figure 5.5: Distributions of L_{10} and L_{12} for simulated signal events, off-resonance data and simulated $B\overline{B}$ background events for $K\pi$ (top plots), $K\pi\pi^0$ (middle plots) and $K\pi\pi\pi$ events (bottom plots).

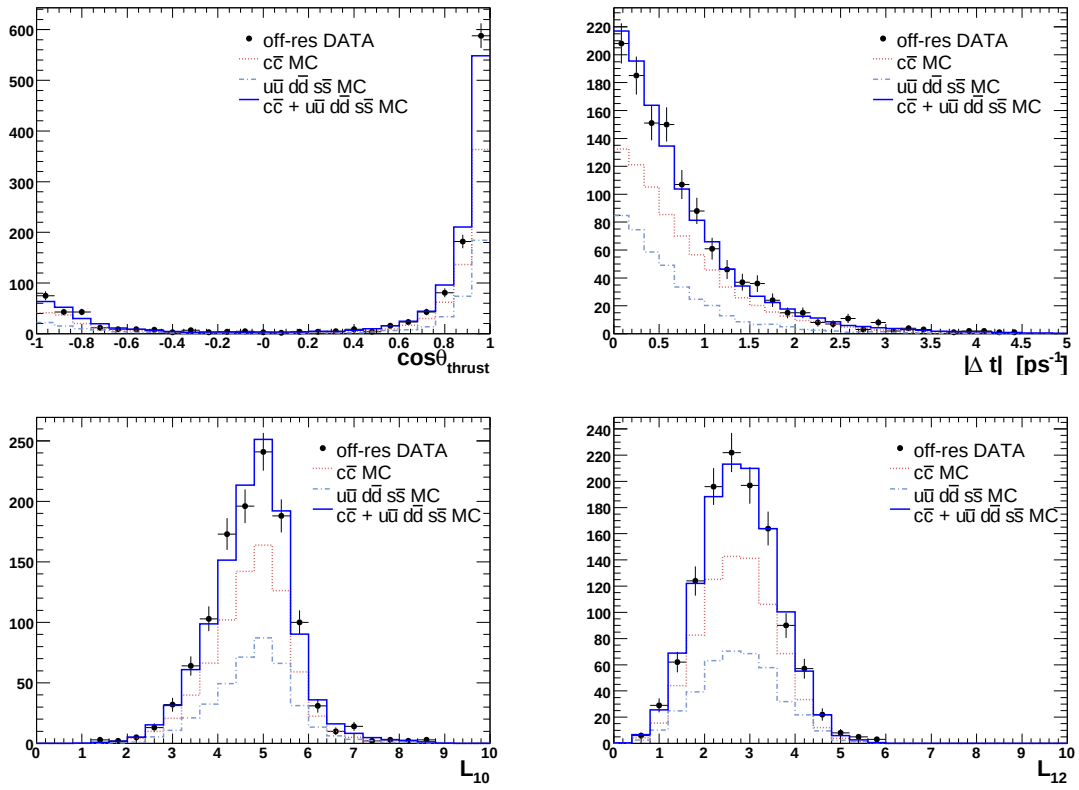

Figure 5.6: Distributions of the variables $|\cos(\theta_{thrust})|$ (top left), $|\Delta t|$ (top right), L_{10} (bottom left) and L_{12} (bottom right) obtained using simulated uds and $c\bar{c}$ events, a weighted sum of te two (according to their cross sections) and off-resonance data. All the distributions are normalized to the off-resonance data luminosity (41.3 fb^{-1}).

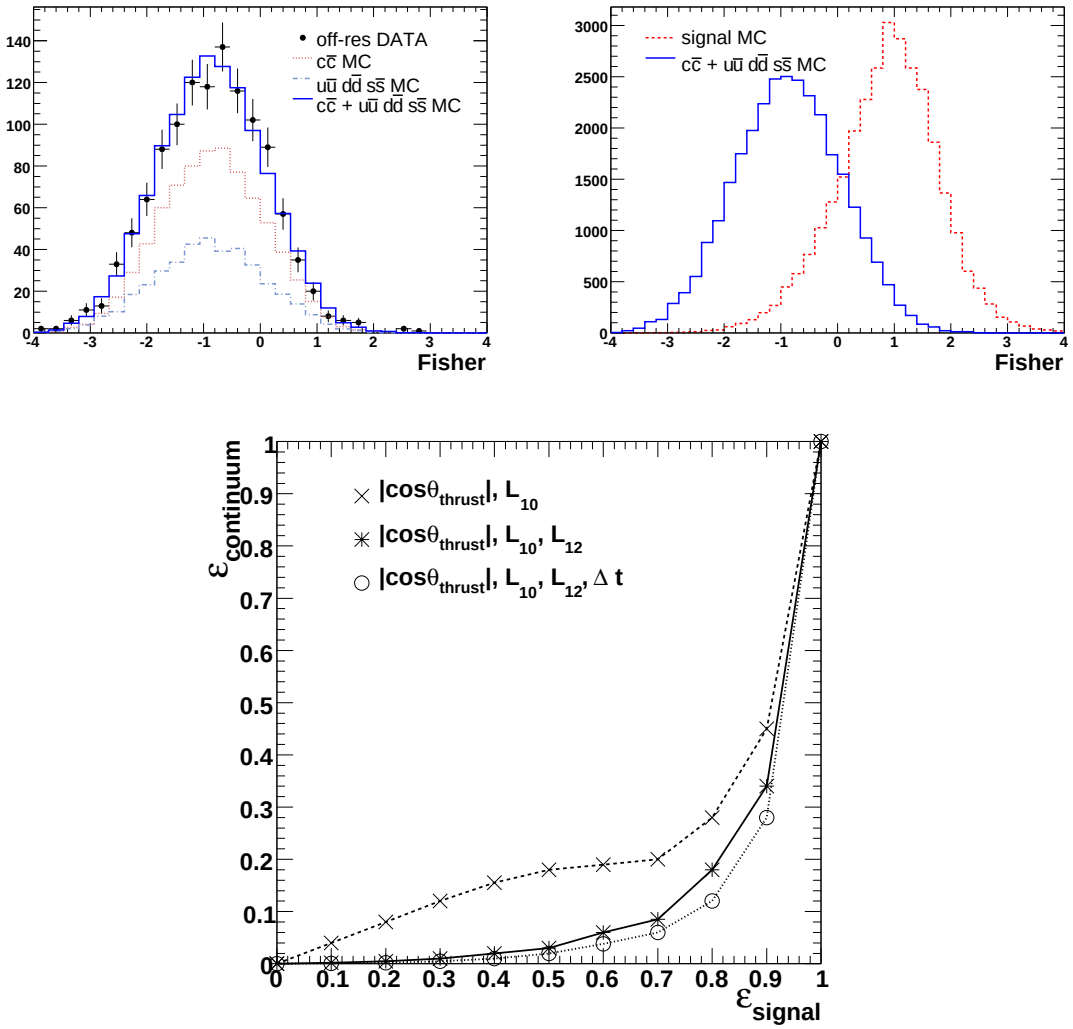

Figure 5.7: Top left: Fisher distribution obtained using simulated *uds* and $c\bar{c}$ events, a weighted sum of the two (according to their cross sections) and off-resonance data (all the distributions are normalized to the off-resonance data luminosity, 41.3 fb^{-1}). Top right: Fisher distribution for simulated signal and continuum events. Bottom plot: efficiency on simulated continuum events as a function of the efficiency on simulated signal events. The different curves are obtained using $|\cos(\theta_{thrust})|$ and L_{10}, $|\cos(\theta_{thrust})|$, L_{10} and L_{12}, $|\cos(\theta_{thrust})|$, L_{10}, L_{12} and $|\Delta t|$.

5.2.3 Selection cut optimization

An optimization procedure has been used to find the optimal cuts for the following variables: ΔE, M_{D^0}, probability of the χ^2 of the vertex fit for B, D and K^*, particle identification of the kaons produced in the K^* and D decays, M_{π^0} and the π^0 momentum in the e^+e^- center of mass frame $p^{CM}_{\pi^0}$ (the latter two variables only refer to the $K\pi\pi^0$ decay mode). The optimization procedure consists in finding the cuts that maximize the variable $S/\sqrt{S+B}$, where S and B are the numbers of selected events in simulated signal and background samples respectively. The choice of the cuts on $M_{K^{*0}}$ and $\cos\theta^{K^{*0}}_{HEL}$ is common to the two analyses presented in this thesis and was described in sec. 4.6.

The optimization is made using only opposite sign events. This choice is motivated by the fact that we want to suppress the background mainly in the opposite sign sample, which drives the error on R_{ADS} and hence the sensitivity to r_S. We then apply the same cuts to all the events because we are interested in having the same efficiency on same sign and opposite sign samples.

Since the extraction of signal and background is performed through a maximum likelihood fit to the variables m_{ES} and Fisher, the quantities $S/\sqrt{S+B}$ and $S/\sqrt{B}$ are evaluated for events that satisfy the additional criteria $m_{ES} > 5.27\,\mathrm{GeV}/c^2$ and Fisher>0. The variation of $S/\sqrt{S+B}$ and $S/\sqrt{B}$, for different choices of the cuts on M_{D^0}, ΔE and M_{π^0} are shown in Figs. 5.8–5.11.

The variation of $S/\sqrt{S+B}$ for different cuts on the kaon particle identification, on the probability of the χ^2 of the vertex fit for B, D and K^{*0} and on the momentum of the π^0 in the center of mass frame (for the $K\pi\pi^0$ mode) are shown in Tabs. 5.2 and 5.3. From these studies we decided to use the additional selection criteria: Prob $\chi^2_{BVtx} > 0.001$ and $|p^{CM}_{\pi^0}| > 0.3$ GeV/c.

The calculation of $S/\sqrt{S+B}$ depends on the assumed branching fraction for the signal, i.e. what assumption is made on r_S. This dependence is not present when the quantity $S/\sqrt{B}$ is maximized instead. It has been checked that very similar results are obtained when using $S/\sqrt{S+B}$ or $S/\sqrt{B}$ (as shown in Fig. 5.8–5.10). In the following, $S/\sqrt{S+B}$ is used.

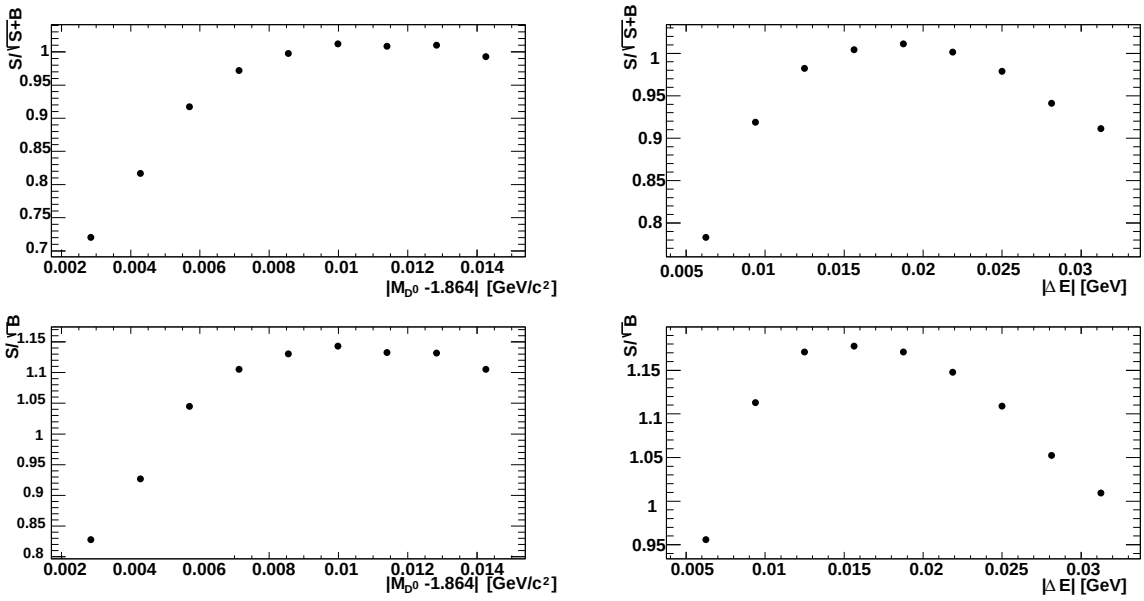

Figure 5.8: [$K\pi$ mode - selection cuts optimization]. Variation of $S/\sqrt{S+B}$ (top plots) and $S/\sqrt{B}$ (bottom plots) as a function of the cut on $|M_{D^0} - M_{D^0}^{\rm nominal}|$ (left) and ΔE (right). The optimization has been made on opposite sign events only, assuming $r_S = 0.3$, using preselection cuts, with the addition of $m_{ES} > 5.27$ GeV/c^2 and Fisher> 0.

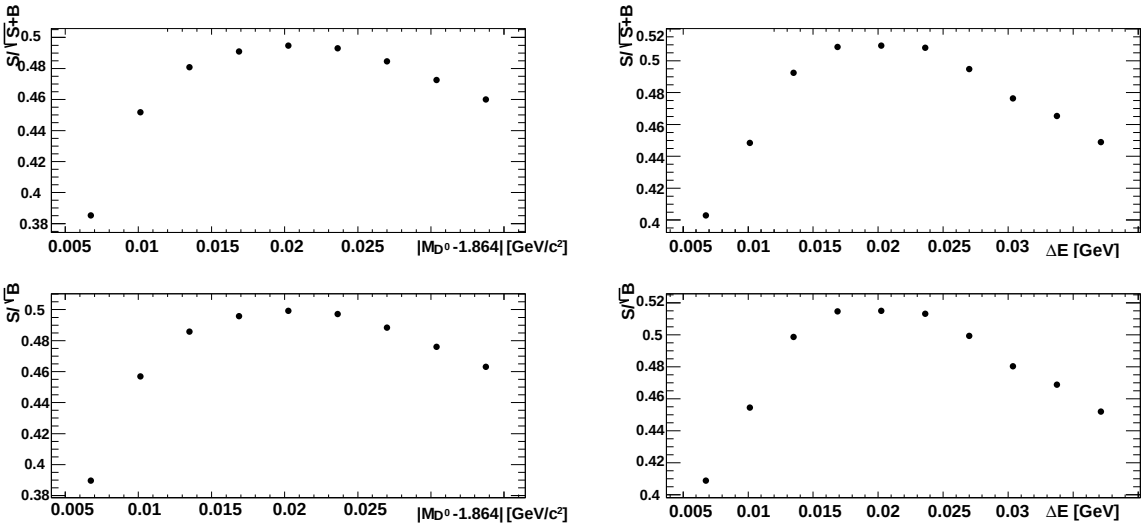

Figure 5.9: [$K\pi\pi^0$ mode - selection cuts optimization]. Variation of $S/\sqrt{S+B}$ (top plots) and $S/\sqrt{B}$ (bottom plots) as a function of the cut on $|M_{D^0} M_{D^0}^{\rm nominal}|$ (left) and ΔE (right). The optimization has been made on opposite sign events only, assuming $r_S = 0.3$, using preselection cuts, with the addition of $m_{ES} > 5.27$ GeV/c^2 and Fisher> 0.

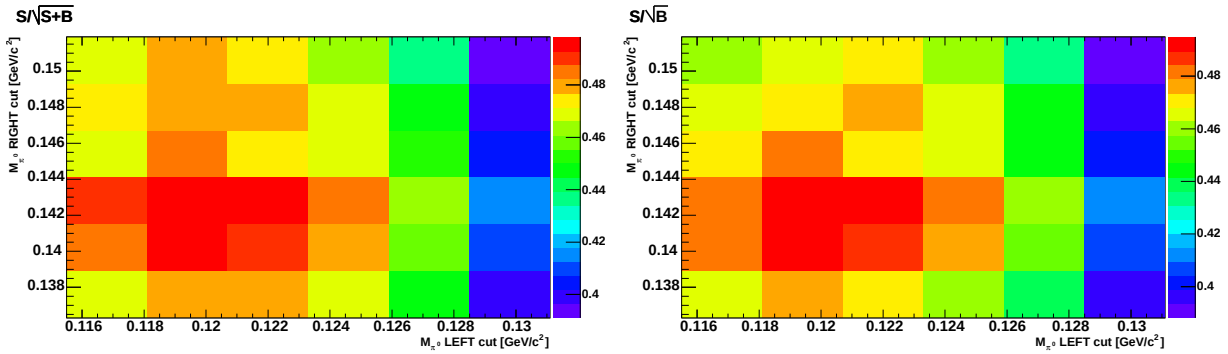

Figure 5.10: [$K\pi\pi^0$ mode - selection cuts optimization]. Variation of $S/\sqrt{S+B}$ (left plot) and $S/\sqrt{B}$ (right plot) as a function of the cut on $M_{\pi^0} - M_{\pi^0}^{\rm nominal}$ and $M_{\pi^0}^{\rm nominal} - M_{\pi^0}$. The optimization has been made on opposite sign events only, assuming $r_S = 0.3$, using preselection cuts, with the addition of $m_{ES} > 5.27$ GeV/c^2 and Fisher> 0.

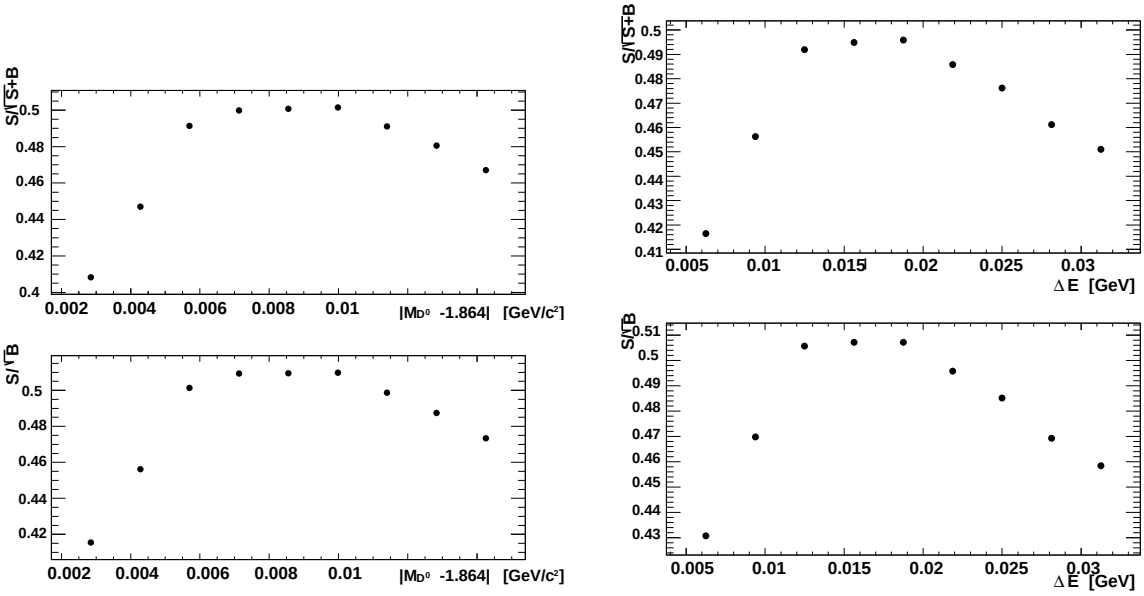

Figure 5.11: [$K\pi\pi\pi$ mode - selection cuts optimization]. Variation of $S/\sqrt{S+B}$ (top plots) and $S/\sqrt{B}$ (bottom plots) as a function of the cut on $|M_{D^0} - M_{D^0}^{\rm nominal}|$ (left) and ΔE (right). The optimization has been made on opposite sign events only, assuming $r_S = 0.3$, using preselection cuts, with the addition of $m_{ES} > 5.27$ GeV/c^2 and Fisher> 0.

Cut	$S/\sqrt{S+B}(K\pi)$	$S/\sqrt{S+B}(K\pi\pi^0)$	$S/\sqrt{S+B}(K\pi\pi\pi)$
Default value	1.038	0.517	0.459
Prob $\chi^2_{BVtx} > 0.001$	1.071	0.527	0.476
Prob $\chi^2_{DVtx} > 0.001$	1.037	0.516	0.467
Prob $\chi^2_{K^*Vtx} > 0.001$	1.03	0.515	0.461
K from K^{*0} PID KLHTight	1.020	0.510	0.455
K from D^0 PID KLHTight	1.017	0.516	0.458

Table 5.2: [selection cuts optimization]. Values of $S/\sqrt{S+B}$ for different cuts for the three D decay modes, obtained using opposite sign events. The first row corresponds to the optimized selection cuts for $|\Delta E|$, M_{D^0}, $M_{K^{*0}}$, $cos\theta^{K*0}_{HEL}$ and M_{π^0} (for the $K\pi\pi^0$ mode), with the addition of $m_{ES} > 5.27$ GeV/c^2 and Fisher> 0. The value of $S/\sqrt{S+B}$ in each row is the consequence of the addition of the indicated cut. We decided to use a cut if its application gives an improvement on $S/\sqrt{S+B}$, with respect to the value quoted in the first row.

Cut	$S/\sqrt{S+B}$
Default value	0.49
$p^{CM}_{\pi^0} > 0.1$ GeV/c	0.49
$p^{CM}_{\pi^0} > 0.2$ GeV/c	0.51
$p^{CM}_{\pi^0} > 0.3$ GeV/c	0.53
$p^{CM}_{\pi^0} > 0.4$ GeV/c	0.52
$p^{CM}_{\pi^0} > 0.5$ GeV/c	0.51

Table 5.3: [selection cuts optimization]. Values of $S/\sqrt{S+B}$ for different cuts on on $p^{CM}_{\pi^0}$, obtained using opposite sign $K\pi\pi^0$ decay mode events. The first row corresponds to the optimized selection cuts on $|\Delta E|$, M_{D^0}, $M_{K^{*0}}$, $cos\theta^{K*0}_{HEL}$ and M_{π^0}, with the addition of $m_{ES} > 5.27$ GeV/c^2 and Fisher> 0. The value of $S/\sqrt{S+B}$ in each row is the consequence of the addition of the indicated cut. We decided to use a cut if its application gives an improvement on $S/\sqrt{S+B}$, with respect to the value quoted in the first row.

5.2.4 Studies of peaking background events

A special attention has been put, within the $B\bar{B}$ background, on possible sources of peaking background. Peaking background consists of processes that lead to the same final state as for the reconstructed signal. Indeed the m_{ES} and Fisher distributions of these events are rather similar to the ones of the reconstructed signal.

The possible peaking background contributions have been identified from a study of $B\bar{B}$ simulated events. The contributing modes are listed in Tab. 5.4, where it is also indicated for which reconstructed D mode they are a background and if they are reconstructed as same sign (SameS) or opposite sign (OppS). In order to reconstruct some of the modes listed in Tab. 5.4 as signal, a misidentification of a $\pi^{\pm}$ as a $K^{\pm}$ is necessary (marked "wrong PID" in the table). To precisely evaluate the contribution of all these possible sources of peaking background, dedicated simulated samples have been generated, the equivalent luminosity of these samples is shown in Tab. 5.4. The most worrying backgrounds are those contributing to the opposite sign category: the decay modes $B^0 \to D^-[K^{*0}K^-]\pi^+$ for the $K\pi$ reconstructed channel, $B^0 \to D^-[K^{*0}K^-]\rho^+[\pi^+\pi^0]$ for the $K\pi\pi^0$ reconstructed channel, and $B^0 \to D^-[K^{*0}K^-]a_1^+[\pi^+\pi^+\pi^-]$ for the $K\pi\pi\pi$ reconstructed channel.

B decay mode	background for	category	gen. lumi [ab^{-1}]
$B^0 \to D^-[K^+\pi^-\pi^-]K^+$	$K\pi$ mode	SameS	1.0
$B^0 \to D^-[K^{*0}K^-]\pi^+$	$K\pi$ mode	OppS	1.9
$B^0 \to D^-[K^{*0}K^-]\rho^+[\pi^+\pi^0]$	$K\pi\pi^0$ mode	OppS	0.8
$B^0 \to D^-[K^{*0}K^-]a_1^+[\pi^+\pi^-\pi^-]$	$K\pi\pi\pi$ mode	OppS	1.1
$B^0 \to D^0\rho^0$ ($D^0 \to K\pi$)	$K\pi$ mode (wrong PID)	SameS	6.8
$B^0 \to D^0\rho^0$ ($D^0 \to K\pi\pi^0$)	$K\pi\pi^0$ mode (wrong PID)	SameS	1.9
$B^0 \to D^0\rho^0$ ($D^0 \to K\pi\pi\pi$)	$K\pi\pi\pi$ mode (wrong PID)	SameS	3.4
$B^0 \to D^{*-}[D^0\pi^-]\pi^+$ ($D^0 \to K\pi$)	$K\pi$ mode (wrong PID)	SameS	8.0
$B^0 \to D^{*-}[D^0\pi^-]\pi^+$ ($D^0 \to K\pi\pi^0$)	$K\pi\pi^0$ mode (wrong PID)	SameS	2.3
$B^0 \to D^{*-}[D^0\pi^-]\pi^+$ ($D^0 \to K\pi\pi\pi$)	$K\pi\pi\pi$ mode (wrong PID)	SameS	4.0

Table 5.4: Equivalent luminosity of dedicated MC generated samples for peaking background studies and equivalent luminosities (calculated assuming the nominal values for the different branching fractions).

To suppress the $B^0 \to D^-[K^{*0}K^-]\pi^+$(or ρ^+, or a_1^+) background that could simulate opposite-sign signal events, we veto all the candidates for which the invariant mass of the K^{*0} and the K^- from the D^0 is within ± 6 MeV from the nominal D^- mass (the efficiencies of these vetoes on signal are $\epsilon_{K\pi} = (99.84 \pm 0.01)\%$, $\epsilon_{K\pi\pi^0} = (98.89 \pm 0.03)\%$ and $\epsilon_{K\pi\pi\pi} = (99.97 \pm 0.01)\%$). The distribution of the invariant mass for signal $K\pi$, $K\pi\pi^0$ and $K\pi\pi\pi$ events can be seen in Fig. 5.12.

The effect of the cut on the invariant mass of the K^{*0} and the K^- from the D^0 can be observed in Tab. 5.5, where the number of expected events in the opposite sign mode, for $K\pi$, $K\pi\pi^0$ and $K\pi\pi\pi$ decay modes is shown. The cut on the invariant mass is very effective and it has been added to the final selection.

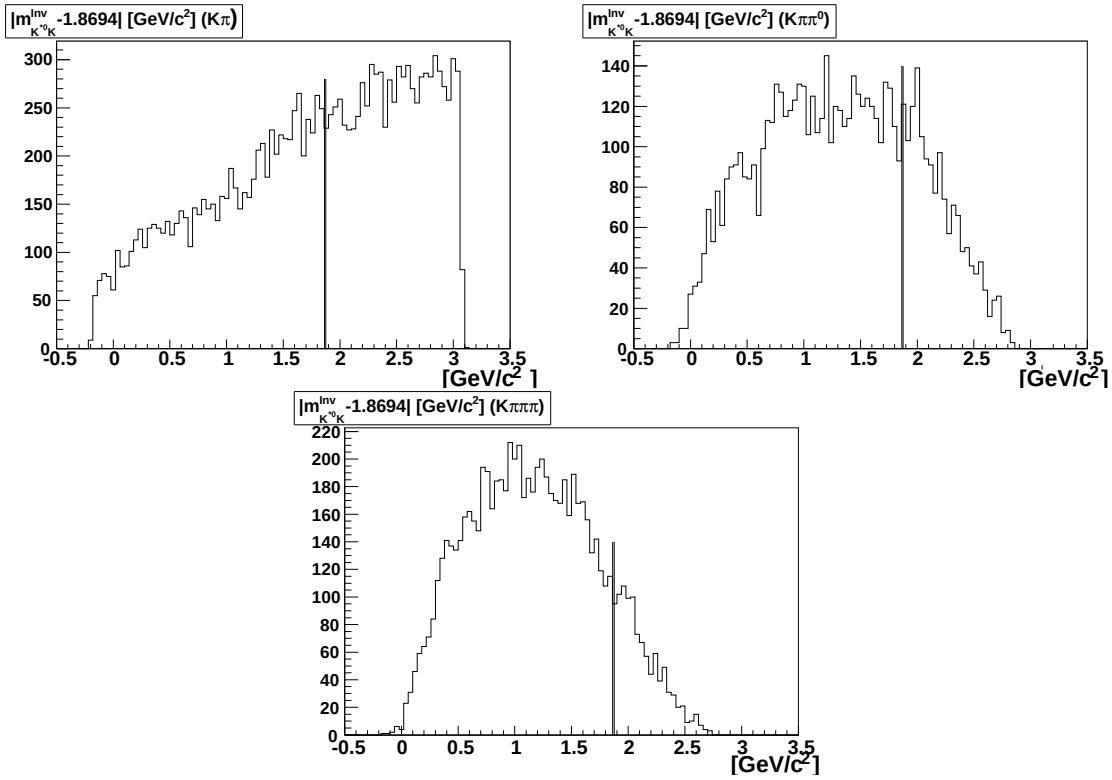

Figure 5.12: Invariant mass of the K^{*0} and the K^- from the D^0 for $K\pi$ (left) and $K\pi\pi^0$ (center), $K\pi\pi\pi$ (right) simulated signal events.

All the possible peaking sources have been studied and a cut on the particle identification (KLHTight) of the kaon from the K^{*0} has been found useful to reject peaking background from $D^0\rho^0$ modes. A summary of these studies is shown in tb. 5.6.

With the addition, presented in sec. 5.2.3, to the optimized selection cuts, of the cuts on the particle identification (KLHTight) of the kaon from the K^{*0} and on the invariant mass of the K^{*0} and the K^- from the D^0 all the possible sources of peaking background give a negligible contribution, as listed in Tab. 5.7.

Cut	$D^-[K^{*0}K^-]\pi^+$ ($K\pi$ OS)	$D^-[K^{*0}K^-]\rho^+$ ($K\pi\pi^0$ OS)	$D^-[K^{*0}K^-]a_1^+$ ($K\pi\pi\pi$ OS)
-	3.1 ± 0.9	3.0 ± 0.4	0.39 ± 0.30
$\lvert m_{K^{*0}K} - M_{D^+}\rvert > 6$ MeV/c^2	<0.07 @ 95%	<0.05 @ 95%	<0.12 @ 95%

Table 5.5: Number of expected peaking background events, in 423 fb^{-1} of on-resonance data, for the indicated modes. The first row corresponds to the number of events selected after the cuts on $|\Delta E|$, $|\cos\theta^B_{CM}|$, M_{D^0}, $M_{K^{*0}}$ and $|\cos\theta^{K^{*0}}_{HEL}|$.

	$D^0[K\pi]\rho^0$	$D^0[K\pi\pi^0]\rho^0$	$D^0[K\pi\pi\pi]\rho^0$
Cut	($K\pi$ SS)	($K\pi\pi^0$ SS)	($K\pi\pi\pi$ SS)
-	0.24 ±0.14	0.85±0.61	1.1±0.4
K^{*0} KLHTight	0.16 ± 0.12	0.43 ± 0.43	0.6 ± 0.3
Cut	($K\pi$ OS)	($K\pi\pi^0$ OS)	($K\pi\pi\pi$ OS)
-	$(1.0 \pm 0.6)\ 10^{-4}$	$(3.4 \pm 2.4)\ 10^{-4}$	$(4.4 \pm 1.5)\ 10^{-4}$
K^{*0} KLHTight	$(0.6 \pm 0.5)\ 10^{-4}$	$(1.7 \pm 1.7)\ 10^{-4}$	$(2.4 \pm 1.1)\ 10^{-4}$

Table 5.6: Number of expected peaking background events, in 423 fb^{-1} on-resonance data, for the indicated modes. The first row corresponds to the number of events selected after the cuts on $|\Delta E|$, $|cos\theta^B_{CM}|$, M_{D^0}, $M_{K^{*0}}$ and $|cos\theta^{K^{*0}}_{HEL}|$.

mode	$K\pi$ SS	$K\pi\pi^0$ SS	$K\pi\pi\pi$ SS
$B^0 \to D^-[K^+\pi^-\pi^-]K^+$	< 0.12 @95%	-	-
$B^0 \to D^0\rho^0$	< 0.09 @95%	$(0.6 \pm 0.6)10^{-4}$	$(0.6 \pm 0.6)10^{-4}$
$B^0 \to D^{*-}[D^0\pi^-]\pi^+$	< 0.05 @95%	< 0.16 @95%	< 0.09 @95%
mode	$K\pi$ OS	$K\pi\pi^0$ OS	$K\pi\pi\pi$ OS
$B^0 \to D^0\rho^0$	$(1.0 \pm 0.6)10^{-4}$	$(1.0 \pm 0.6)10^{-4}$	$(1.0 \pm 1.0)10^{-4}$
$B^0 \to D^{*-}[D^0\pi^-]\pi^+$	< 0.05 @95%	< 0.16 @95%	< 0.09 @95%
$B^0 \to D^-[K^{*0}K^-]\pi^+$	< 0.07 @95%	-	-
$B^0 \to D^-[K^{*0}K^-]\pi^+$	-	< 0.05 @95%	-
$B^0 \to D^-[K^{*0}K^-]\rho^+$	-	-	< 0.12 @95%

Table 5.7: Summary of the expected number of events from all the peaking background categories, after all the selection criteria have been applied, with the addition of the cuts on the particle identification (KLHTight) of the kaon from the K^{*0} and on the invariant mass of the K^{*0} and the K^- from the D^0 (see Tab. 5.5).

A further possible source of peaking background comes from charmless event (i.e. events with no real neutral D) of the kind $B^0 \to K^{*0}K\pi$. For these events, the branching fractions are not very well known and not all the decay modes are included in the simulated events. Thus, the possible sources of background from charmless events have been evaluated on data with a fit to the m_{ES} variable using the M_{D^0} sidebands (i.e. using only events for which the reconstructed D mass is more than 5σ away form the nominal D^0 mass), after all the selection cuts (with the exception of the cut on M_{D^0}) and after a cut on $Fisher > -1$. The resulting m_{ES} distribution has two components, a Gaussian distribution, as for the signal events (the peaking contribution) and an Argus distribution (defined in eq. 4.3). The parameters of the Argus function have been left free in the fit on data. The results obtained in the three samples ($K\pi$, $K\pi\pi^0$ and $K\pi\pi\pi$) are shown in Fig. 5.13 and summarized in Tab. 5.8. The number of fitted events have to be rescaled according to the M_{D^0} range in the selected sample. The rescaled number of events are given in Tab. 5.8.

All these studies are consistent with the hypothesis of negligible peaking contributions from charmless events, although in some cases the errors on the number of peaking events is rather large, considering that we expect order of 10 events in each opposite sign sample. Under the assumption that the charmless contributions are not sensibly different in the three D decay mode channels, the number of rescaled events can be combined. In this case, the contributions from charmless peaking events are found to be compatible with zero with a precision of ± 0.5 and ± 1.2 events for the same sign and opposite sign samples respectively. The peaking contributions will be assumed to be negligible in the final fit and these precisions will be used for the evaluation of the systematic uncertainty arising from this assumption.

	$K\pi$ SS	$K\pi\pi^0$ SS	$K\pi\pi\pi$ SS	$K\pi$ OS	$K\pi\pi^0$ OS	$K\pi\pi\pi$ OS
N_{peak}	-3.5 ± 4.6	0.5 ± 14.9	3.2 ± 9.7	2.7 ± 6.5	-31 ± 22	0.8 ± 13.8
N_{Nopeak}	300 ± 17	2173 ± 49	877 ± 31	394 ± 21	5150 ± 75	1929 ± 46
N_{peak} rescaled	0.8 ± 1.2	0.1 ± 3.2	0.5 ± 2.4	0.7 ± 1.6	-6 ± 5	0.1 ± 2.0
N_{peak} combined	0.5 ± 0.5			0.06 ± 1.21		

Table 5.8: Results of a fit to m_{ES} on 423 fb^{-1} of on resonance data in the M_{D^0} sidebands ($|M_{D^0} - M_{D^0}^{\rm nominal}| > 5\sigma$) for the three modes, $K\pi$, $K\pi\pi^0$ and $K\pi\pi\pi$, for same and opposite sign events separately. The number of peaking and non peaking events is shown, together with the number of peaking events rescaled according to the M_{D^0} range in the selected sample. Finally, we give the number of peaking events obtained when the results obtained on the three samples are combined.

5.2.5 Final selection criteria

The final selection cuts are summarized in table 5.9, for the three D decay modes. Some additional cuts (namely the cut on the particle identification of the charged kaon from the K^* and the cut on $m^{Inv}_{K^{*0}K}$) have been added to the final selection. Though they do not improve the statistical significance, they are very effective in rejecting specific background categories, as it was shown in sec. 5.2.4.

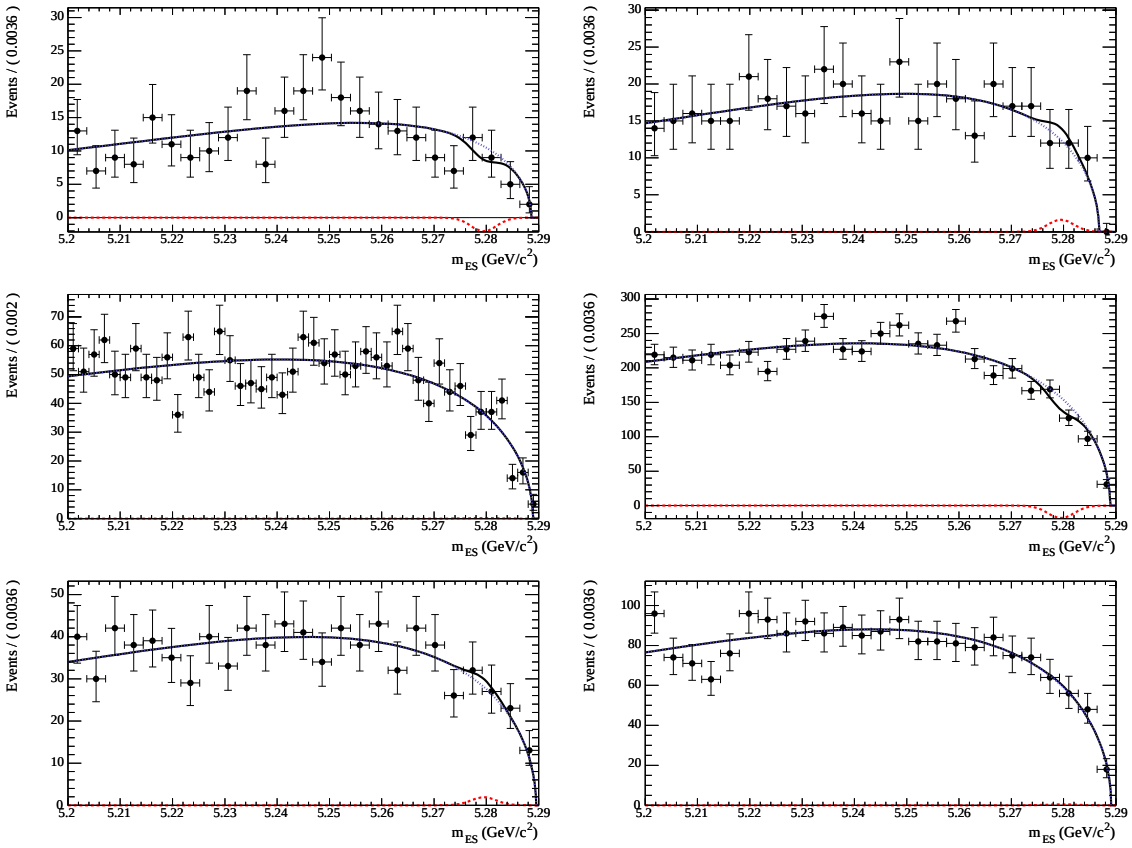

Figure 5.13: Fit to the m_{ES} distribution of data events in the M_{D^0} sidebands ($|M_{D^0} - M_{D^0}^{\rm nominal}| > 5\sigma$) for same sign (left plot) and opposite sign (right plot) events for the three modes, $K\pi$ (top plots), $K\pi\pi^0$ (middle plots) and $K\pi\pi\pi$ (bottom plots).

Cut	$K\pi$	$K\pi\pi^0$	$K\pi\pi\pi$
m_{ES}[GeV/c^2]	$5.2 < - < 5.29$	$5.2 < - < 5.29$	$5.2 < - < 5.29$
$\lvert\Delta E\rvert$[GeV]	< 0.016 (1.3σ)	< 0.020 (1.5σ)	< 0.019 (1.5σ)
$\lvert\cos\theta^B_{CM}\rvert$	< 0.9	< 0.9	< 0.9
K from K^{*0} PID	KLHTight	KLHTight	KLHTight
Prob χ^2_{BVtx}	> 0.001	> 0.001	> 0.001
Prob χ^2_{DVtx}	–	–	> 0.001
$\lvert M_{D^0} - 1.8641\rvert$[GeV/c^2]	$0.014(2.0\sigma)$	$0.020(1.5\sigma)$	$0.009(1.6\sigma)$
$\lvert M_{\pi^0} - 0.135\rvert$[GeV/c^2]	–	$(2.8\sigma)0.120 < - < 0.143(1.5\sigma)$	–
$\lvert p^{CM}_{\pi^0}\rvert$[GeV/$c$]	–	> 0.3	–
$\lvert M_{K^{*0}} - 0.8961\rvert$[GeV/c^2]	< 0.048	< 0.048	< 0.048
$\lvert\cos\theta^{K*0}_{HEL}\rvert$	> 0.29	> 0.29	> 0.29
$\lvert m^{Inv}_{K^{*0}K} - 1.8694\rvert$[GeV/c^2]	> 0.006	> 0.006	-

Table 5.9: Summary of the selection criteria for the three D decay modes.

5.2.6 Selection efficiencies and background composition

The efficiencies on the signal and background events for the three neutral D decay modes are listed in Tab. 5.10.

Same sign $K\pi$

Cut	B^0B^0	B^+B^-	signal	ϵ_{SIG}	uds	$c\bar{c}$
Selection	11	29	91	(13.2±0.1)%	142	270
$m_{ES} > 5.27\text{GeV/c}^2$	4	13	91	(13.2±0.1)%	17	46
$Fisher > 0.$	3	9	79	(11.5±0.1)%	3	10

Opposite sign $K\pi$

Cut	B^0B^0	B^+B^-	signal	ϵ_{SIG}	uds	$c\bar{c}$
Selection	21	27	10	(13.2±0.1)%	273	1433
$m_{ES} > 5.27\text{GeV/c}^2$	6	6	10	(13.2±0.1)%	46	254
$Fisher > 0.$	4	5	8	(11.5±0.1)%	5	38

Same sign $K\pi\pi^0$

Cut	B^0B^0	B^+B^-	signal	ϵ_{SIG}	uds	$c\bar{c}$
Selection	84	99	128	(5.2±0.1)%	1120	1540
$m_{ES} > 5.27\text{GeV/c}^2$	23	29	127	(5.2±0.1)%	173	230
$Fisher > 0.$	18	22	110	(4.5±0.1)%	3	10

Opposite sign $K\pi\pi^0$

Cut	B^0B^0	B^+B^-	signal	ϵ_{SIG}	uds	$c\bar{c}$
Selection	113	139	11	(5.2±0.1)%	2260	5878
$m_{ES} > 5.27\text{GeV/c}^2$	27	24	11	(5.2±0.1)%	368	942
$Fisher > 0.$	19	17	9	(4.5±0.1)%	59	194

Same sign $K\pi\pi\pi$

Cut	B^0B^0	B^+B^-	signal	ϵ_{SIG}	uds	$c\bar{c}$
Selection	82	104	90	(6.5±0.1)%	638	1211
$m_{ES} > 5.27\text{GeV/c}^2$	24	35	89	(6.5±0.1)%	101	187
$Fisher > 0.$	19	29	74	(5.4±0.1)%	10	36

Opposite sign $K\pi\pi\pi$

Cut	B^0B^0	B^+B^-	signal	ϵ_{SIG}	uds	$c\bar{c}$
Selection	113	110	8	(6.5±0.1)%	1250	4644
$m_{ES} > 5.27\text{GeV/c}^2$	24	16	8	(6.5±0.1)%	231	761
$Fisher > 0.$	19	11	7	(4.5±0.1)%	39	143

Table 5.10: Number of expected signal and background events, same and opposite sign, for the three D modes, $K\pi$, $K\pi\pi^0$ and $K\pi\pi\pi$. All the numbers of events are rescaled to a 423 fb^{-1} luminosity. For the signal, we also show the efficiencies.

5.2.7 Cross-feed between same sign and opposite sign events

The efficiency of reconstructing a same sign event as an opposite sign one or vice versa (by exchanging the charged kaon with a charged pion in the final state for the D decay) has been checked on simulated events. The values are summarized in Tab. 5.11.

	Cross-feed efficiency (%)
$\epsilon^{CF}_{K\pi}$	0.035 ± 0.005
$\epsilon^{CF}_{K\pi\pi^0}$	0.046 ± 0.006
$\epsilon^{CF}_{K\pi\pi\pi}$	0.019 ± 0.004

Table 5.11: Efficiency of reconstructing a same sign event as an opposite sign one or vice versa for the three D channels, using the default selection.

These efficiencies are small, however we have considered the possibility of vetoing neutral D candidates for which the invariant mass constructed from the D decay products, exchanging the kaon with a charged pion, is within $18\,\mathrm{MeV}/c^2$ of the nominal D^0 mass, as done in other similar analyses [66, 67]. The cross-feed efficiencies for the three neutral D channels, after the use of this criterium, as summarized in Tab. 5.12, do not decrease significantly. On the other hand, the reconstruction efficiencies drop by 1% as a consequence of the veto. For these reasons, the veto has not been applied. The effects of cross-feed are taken into account in the systematic uncertainties evaluation.

	Cross-feed efficiency (%)
$\epsilon^{CF}_{K\pi}$	0.014 ± 0.003
$\epsilon^{CF}_{K\pi\pi^0}$	0.041 ± 0.006
$\epsilon^{CF}_{K\pi\pi\pi}$	0.014 ± 0.003

Table 5.12: Efficiency of reconstructing a same sign event as an opposite sign one or vice versa for the three D channels, after D^0 veto criterium is applied, as described in the text.

5.2.8 Opposite sign to same sign efficiency ratio for $K\pi\pi^0$ and $K\pi\pi\pi$ mode

In the $K\pi\pi^0$ and $K\pi\pi\pi$ decay modes, the efficiencies in selecting the signal is evaluated using events generated with a flat Dalitz distribution. However the same sign sample is mainly constituted of $b \to c$ transition events with the neutral D decaying through Cabibbo-allowed mode, while the opposite sign sample is composed of $b \to c$ transition events with the neutral D decaying through doubly-Cabibbo-suppressed Cabibbo mode and $b \to u$ transition events with the neutral D decaying through Cabibbo-allowed mode (see Fig. 5.1). Due to the fact that the Cabibbo-allowed and doubly-Cabibbo-suppressed neutral D decays are kinematically different, and hence have different distributions over the Dalitz plane, the selection efficiencies in same sign and opposite sign samples could be different.

- **$K\pi\pi^0$ decay mode**
  We reweight the simulated events according to the Dalitz distributions of Cabibbo-allowed or the one of doubly-Cabibbo-suppressed events, obtained on data by *BABAR* [57]. We calculate the efficiencies of the selection criteria on Cabibbo-allowed or doubly-Cabibbo-suppressed reweighted events ($\epsilon_{D^0_{CA}}$ and $\epsilon_{D^0_{DCS}}$) and the efficiency evaluated on the simulated events, generated with a flat Dalitz distribution ($\epsilon_{D^0_{PHSP}}$). The reweighted efficiencies for the two modes are found to be compatible with $\epsilon_{D^0_{PHSP}}$. We thus calculate $\epsilon_{D^0_{CA}}/\epsilon_{D^0_{DCS}}$ to be 1.002 ± 0.03. We can hence assume that the efficiencies on Cabibbo-allowed and doubly-Cabibbo-suppressed event is the same within a precision of 3%. An uncertainty of 3% on the ratio of the efficiency on same sign and opposite sign events will be taken into account in the systematic evaluation.

- $K\pi\pi\pi$

  For the $K\pi\pi\pi$, the Cabibbo-allowed decay Dalitz distribution has been studied but we do not have Dalitz distributions obtained for doubly-Cabibbo-suppressed events.

  In order to evaluate how much the efficiency could change using different Dalitz models, we assume a resonance structure consistent with the measurements. We use the nominal branching fractions for neutral D decaying to the different intermediate states, obtained on the Cabibbo-allowed mode [8], which are shown in Tab. 5.13 thus we generate $D^0 \to K\pi\pi\pi$ events in 10 different configurations by varying the fractions of events in each resonance by $\pm 10\%$. The ratio of the efficiency computed using the Cabibbo-allowed Dalitz model (see Tab. 5.13) over the efficiency obtained using the flat Dalitz distribution for the Cabibbo allowed decay is found to be $r_{CA} = \epsilon_{D^0_{CA}}/\epsilon_{D^0_{PHSP}} = 1.02 \pm 0.04$. The values of this ratio, when assuming the 10 different configurations for the D^0 Dalitz structure are distributed as can be seen in Fig. 5.14.

decay modes	BR
$D^0 \to K^-\pi^+\rho^0$ tot.	$(6.4 \pm 0.4)\%$
$D^0 \to \bar{K^{*0}}\rho^0$	$(1.00 \pm 0.22)\%$
$D^0 \to K^- a_1^+$	$(3.6 \pm 0.6)\%$
$D^0 \to \bar{K^{*0}}\pi^+\pi^-$ tot	$(1.5 \pm 0.4)\%$
$D^0 \to K_1^-\pi^+$	$(0.29 \pm 0.3)\%$
$D^0 \to K^-\pi^+\pi^+\pi^-$ N.R.	$(1.80 \pm 0.25)\%$

Table 5.13: Branching ratios for D^0 decaying to the different intermediate states considered in the study. The values are taken from [8].

  The maximum deviation from unity is of 5% and the RMS of the distribution is 3%. By varying the amplitudes in this way, we think we account for the possible differences between the Cabibbo-allowed and doubly-Cabibbo-suppressed $K\pi\pi\pi$ mode. We conclude that these eventual differences would have a small impact on the efficiency of our selection. An uncertainty of 3% on the ratio of the efficiency on same sign and opposite sign events will be taken into account in the systematic evaluation.

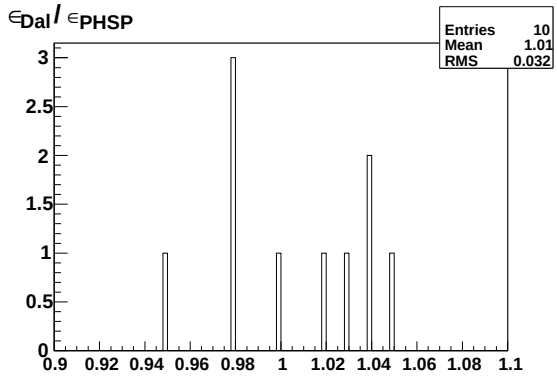

Figure 5.14: Values of the ratio $r = \epsilon_{D^0_{Dal}}/\epsilon_{D^0_{PHSP}}$ using 10 different Dalitz distributions for the neutral D decay mode into $K\pi\pi\pi$ final states.

5.3 Comparison between data and simulated events

In Fig. 5.15-5.18, we show the distributions of m_{ES} and Fisher in the m_{ES} sidebands ($m_{ES} < 5.27\ GeV/c^2$) as obtained for data and simulated events. We notice we found more simulated events with respect to data for the $K3\pi$ mode and viceversa for the $K\pi\pi^0$ mode. Nevertheless, it can be noted that the shapes of all the distributions are in good agreement. The latter is important, because the number of signal and background events (hence the overall normalization and the relative contributions) are left free in the fit on data.

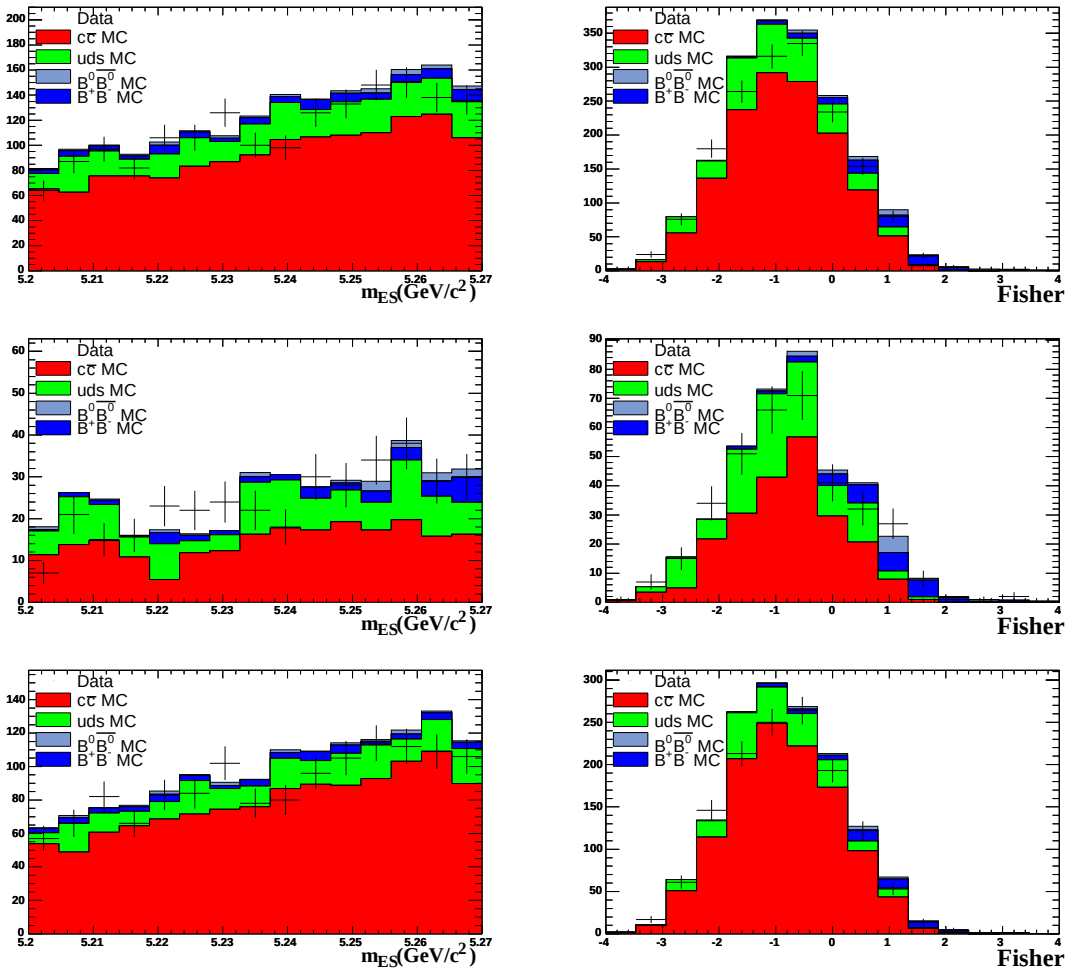

Figure 5.15: [$K\pi$ mode] Data-MC comparison of the m_{ES} (left) and Fisher (right) distributions, for $m_{ES} < 5.27 GeV/c^2$. The distributions are shown for $K\pi$ events (top plots), $K\pi$ same sign events (middle plots) and $K\pi$ opposite sign events (bottom plots). All the distributions are rescaled to the data luminosity (423 fb^{-1}).

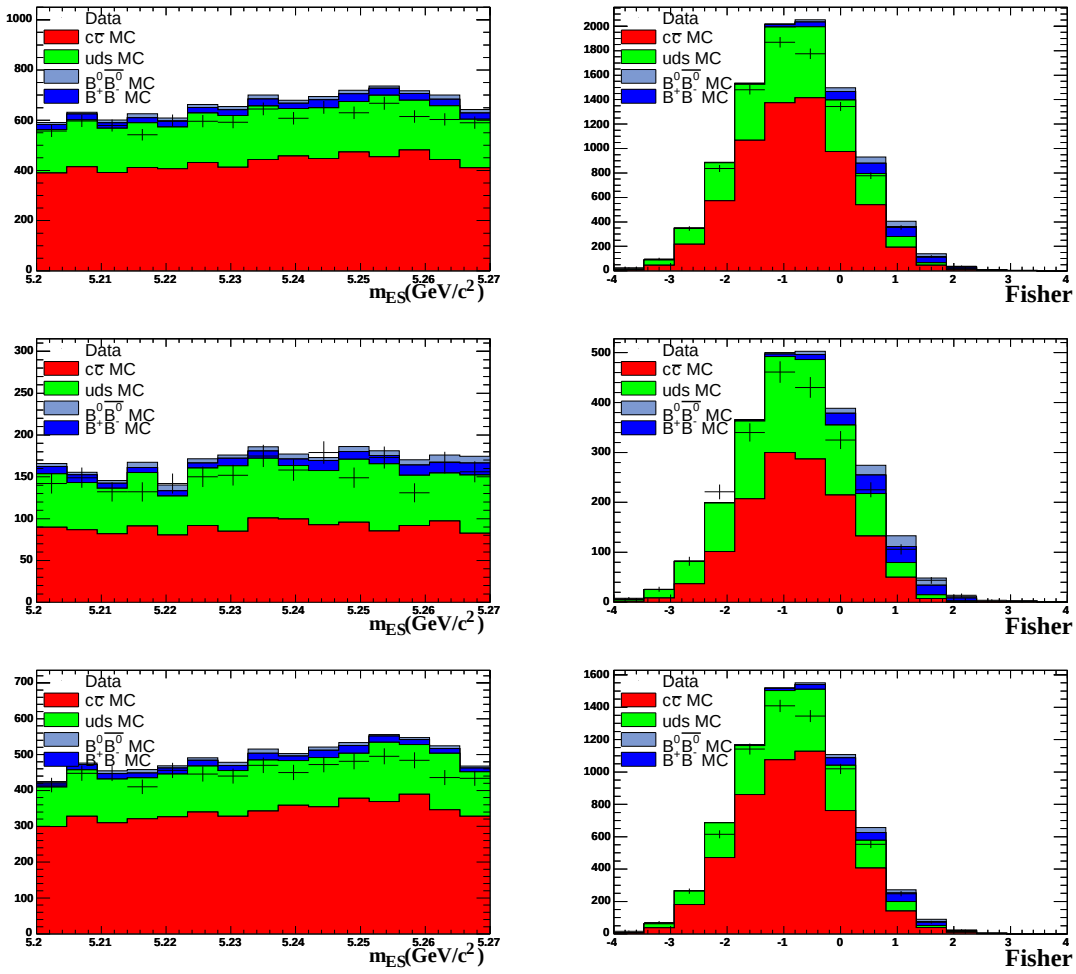

Figure 5.16: [$K\pi\pi^0$ mode] Data-MC comparison of the m_{ES} (left) and Fisher (right) distributions, for $m_{ES} < 5.27 GeV/c^2$. The distributions are shown for $K\pi\pi^0$ events (top plots), $K\pi\pi^0$ same sign events (middle plots) and $K\pi\pi^0$ opposite sign events (bottom plots). All the distributions are rescaled to the data luminosity (423 fb^{-1}).

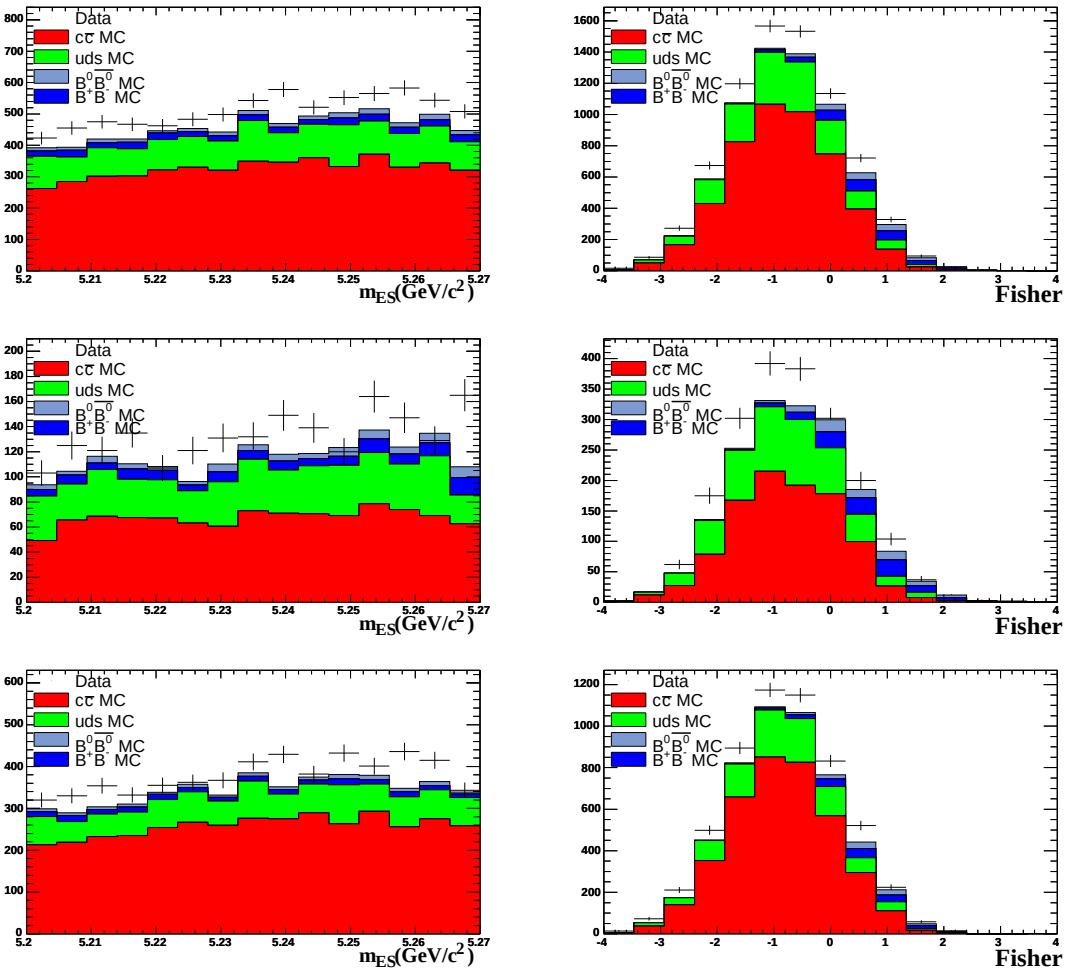

Figure 5.17: [$K\pi\pi\pi$ mode] Data-MC comparison of the m_{ES} (left) and Fisher (right) distributions, for $m_{ES} < 5.27 GeV/c^2$. The distributions are shown for $K\pi\pi\pi$ events (top plot), $K\pi\pi\pi$ same sign events (middle plot) and $K\pi\pi\pi$ opposite sign events (bottom plots). All the distributions are rescaled to the data luminosity (423 fb^{-1}).

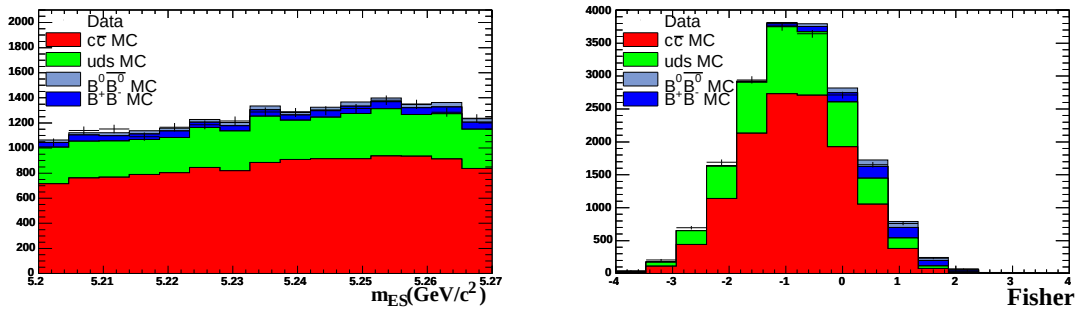

Figure 5.18: [All D modes] Data-MC comparison of the m_{ES} (left) and Fisher (right) distributions (for $m_{ES} < 5.27\ GeV/c^2$), for all the modes together. All the distributions are rescaled to the data luminosity (423 fb^{-1}).

5.4 Maximum likelihood fit

5.4.1 Structure of the fit model

To extract R_{ADS} we perform an extended maximum likelihood fit to the set of variables: $\{m_{ES}, \text{Fisher}, sgnK\}$, where $sgnK$ is a discrete variable equal to -1 for opposite sign events and equal to $+1$ for same sign events. We write the extended likelihood $\mathcal{L}$ as:

$$\mathcal{L} = \frac{e^{-N'}}{N!} N'^N \prod_{j=1}^{N} f(\mathbf{x}_j \mid \theta, N') \,,$$
$$\text{with} \;\; f(\mathbf{x} \mid \theta, N') = \frac{N_S f_S(\mathbf{x}|\theta) + \sum_i N_{B_i} f_{B_i}(\mathbf{x}|\theta)}{N'} \,,$$

where $f_S(\mathbf{x}|\theta)$ and $f_{B_i}(\mathbf{x}|\theta)$ are the probability density functions (pdfs) of the hypothesis that the event is a signal or a background event (B_i are the different background categories used in the fit). The variables are indicated by the vector $\mathbf{x}$ and θ indicates a set of parameters. The total pdf ($f(\mathbf{x} \mid \theta, N')$) is a linear combination of the pfds for the signal and background categories, with coefficients equal to the number of signal and background events, normalized by N' (and not $N = N_S + \sum_i N_{B_i}$), where N' is the expectation value for the total number of events.

There are two signal categories in the fit: one for the opposite sign "N_{SIG}^{OppS}" and one for the same sign "N_{SIG}^{SameS}" mode, so we can write:

$$\begin{aligned} f(\mathbf{x} \mid \theta, N') &= \frac{1}{N'}\{\frac{R_{ADS} N_{DK^*}}{1+R_{ADS}} f_{SIG}^{OppS}(\mathbf{x}|\theta_{SIG}^{OppS}) + \frac{N_{DK^*}}{1+R_{ADS}} f_{SIG}^{SameS}(\mathbf{x}|\theta_{SIG}^{SameS}) + \\ &+ N_{cont}^{OppS} f_{cont}^{OppS}(\mathbf{x}|\theta_{cont}^{OppS}) + N_{cont}^{SameS} f_{cont}^{SameS}(\mathbf{x}|\theta_{cont}^{SameS}) + \\ &+ N_{B\bar{B}}^{OppS} f_{B\bar{B}}^{OppS}(\mathbf{x}|\theta_{B\bar{B}}^{OppS}) + N_{B\bar{B}}^{SameS} f_{B\bar{B}}^{SameS}(\mathbf{x}|\theta_{B\bar{B}}^{SameS})\} \end{aligned}$$

where N_{DK^*} is the sum of the number of opposite sign and same sign signal events:

$$N_{DK^*} = N_{SIG}^{OppS} + N_{SIG}^{SameS};$$
$$R_{ADS} = \frac{N_{SIG}^{OppS}}{N_{SIG}^{SameS}}.$$

N_{cont}^{SameS}, N_{cont}^{OppS}, $N_{B\bar{B}}^{SameS}$ and $N_{B\bar{B}}^{OppS}$ are the number of same and opposite sign events for continuum and $B\bar{B}$ background. Each pdf (for a given category) is a function of all the variables. Since the correlations among the variables are negligible, we write the pdf as the product of the one-dimensional pdfs for the single variables.

The variable $sgnK$ is always parametrized with a two bin step function [1]: one bin for the value $sgnK = -1$ and one for $sgnK = +1$. For the opposite sign mode $f_{sgnK}(sgnK = -1) = 1$ and $f_{sgnK}(sgnK = +1) = 0$, while for the same sign mode $f_{sgnK}(sgnK = -1) = 0$ and $f_{sgnK}(sgnK = +1) = 1$.

[1] A function that has a constant value in each one of the intervals in which its domain is divided.

5.4.2 Parametrizations of the distributions used in the fit: m_{ES}, Fisher

In this section we show the parametrizations of the pdf for m_{ES} and Fisher for signal and background events. The parametrizations have been obtained on simulated events.

Signal

For both m_{ES} and Fisher distributions, the same sign and opposite sign signal events have been parametrized using the same probability density functions (pdf). The distribution of m_{ES} is parametrized with a Gaussian function, while the Fisher discriminant is parametrized with a double Gaussian distribution. The parametrizations are shown in Fig. 5.19. Details on the fitted parameters are given in appendix A.

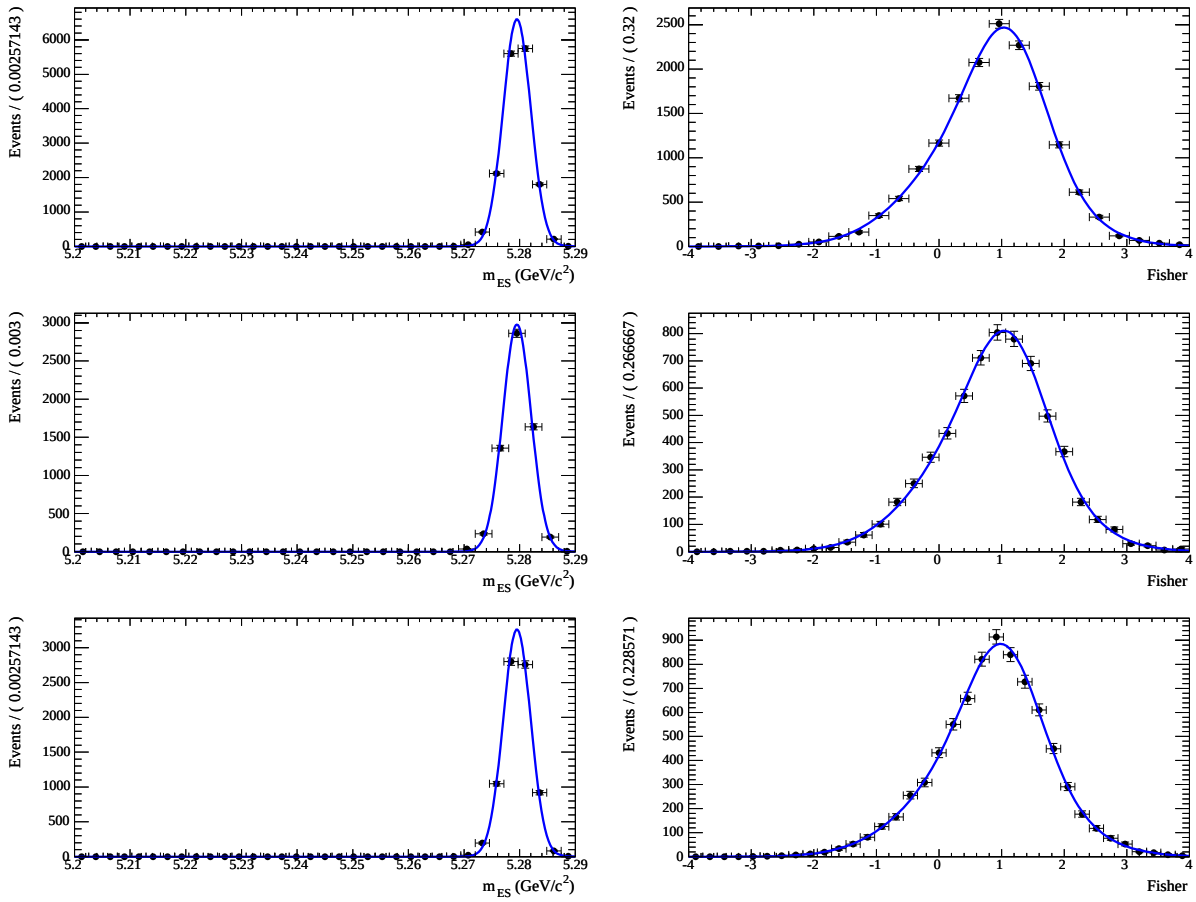

Figure 5.19: m_{ES} (left) and Fisher (right) distributions for simulated signal events for $K\pi$ (top plots), $K\pi\pi^0$ (middle plots) and $K\pi\pi\pi$ (bottom plots) modes. The superimposed curve is the result of a fit with a Gaussian function for m_{ES}, and the result of a fit with a double Gaussian function for the Fisher discriminant.

$B\overline{B}$ background

For the $B\overline{B}$ background, the variable m_{ES} is parametrized with an Argus function and the Fisher is parametrized using a double Gaussian distribution. For this category of background, we observed that the m_{ES} distribution has a different shape for same sign ($sgnK = 1$) and opposite sign ($sgnK = -1$) events, so the parameters of the pdfs are evaluated separately in the two categories. The results of the parametrizations are shown in Fig. 5.20 for m_{ES} and in Fig. 5.21 for Fisher discriminant. Details on the fitted parameters are given in appendix A.

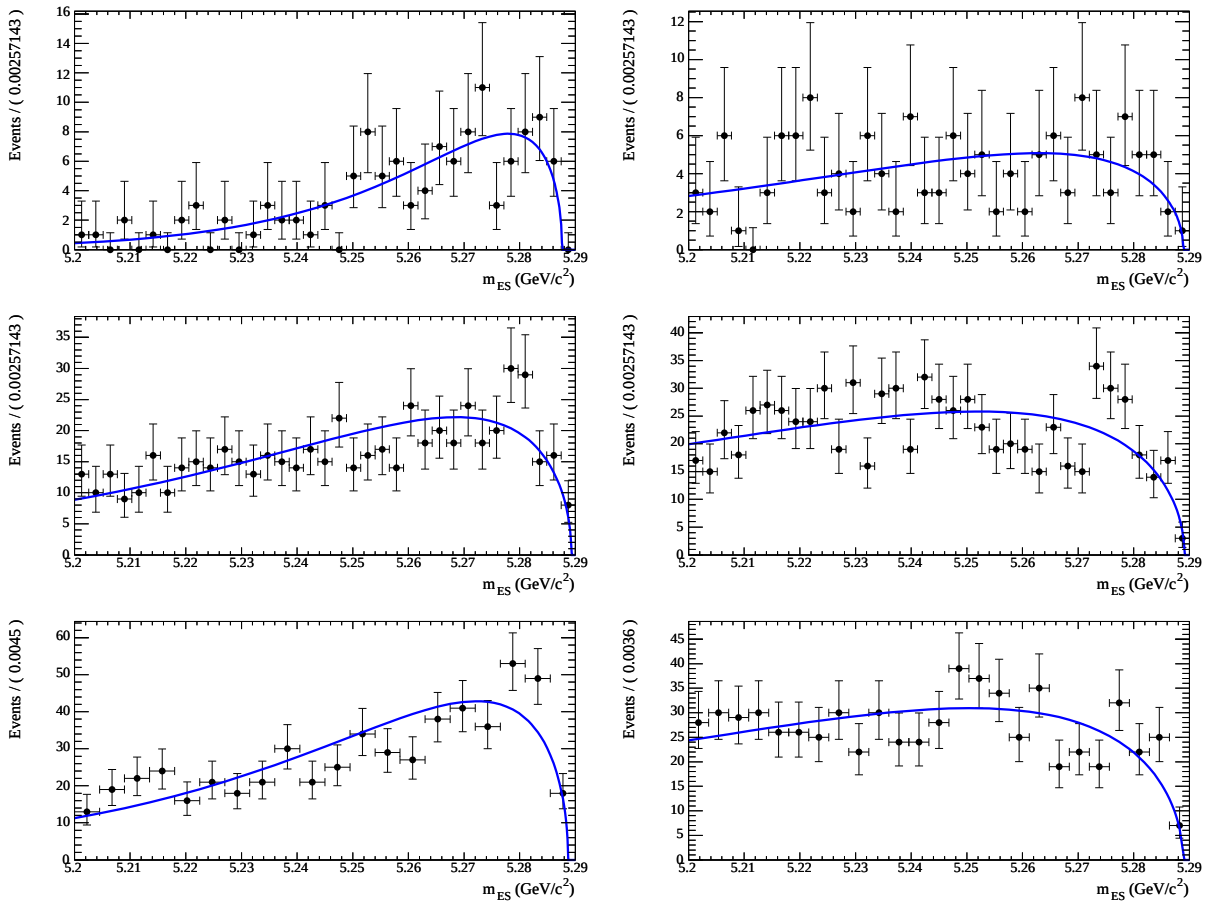

Figure 5.20: m_{ES} distribution for $B\overline{B}$ simulated events for $K\pi$ (top plots), $K\pi\pi^0$ (middle plots) and $K\pi\pi\pi$ (bottom plots) modes. The distributions for same and opposite sign events are shown on the left and on the right respectively. The superimposed curves are the result of a fit with an Argus function.

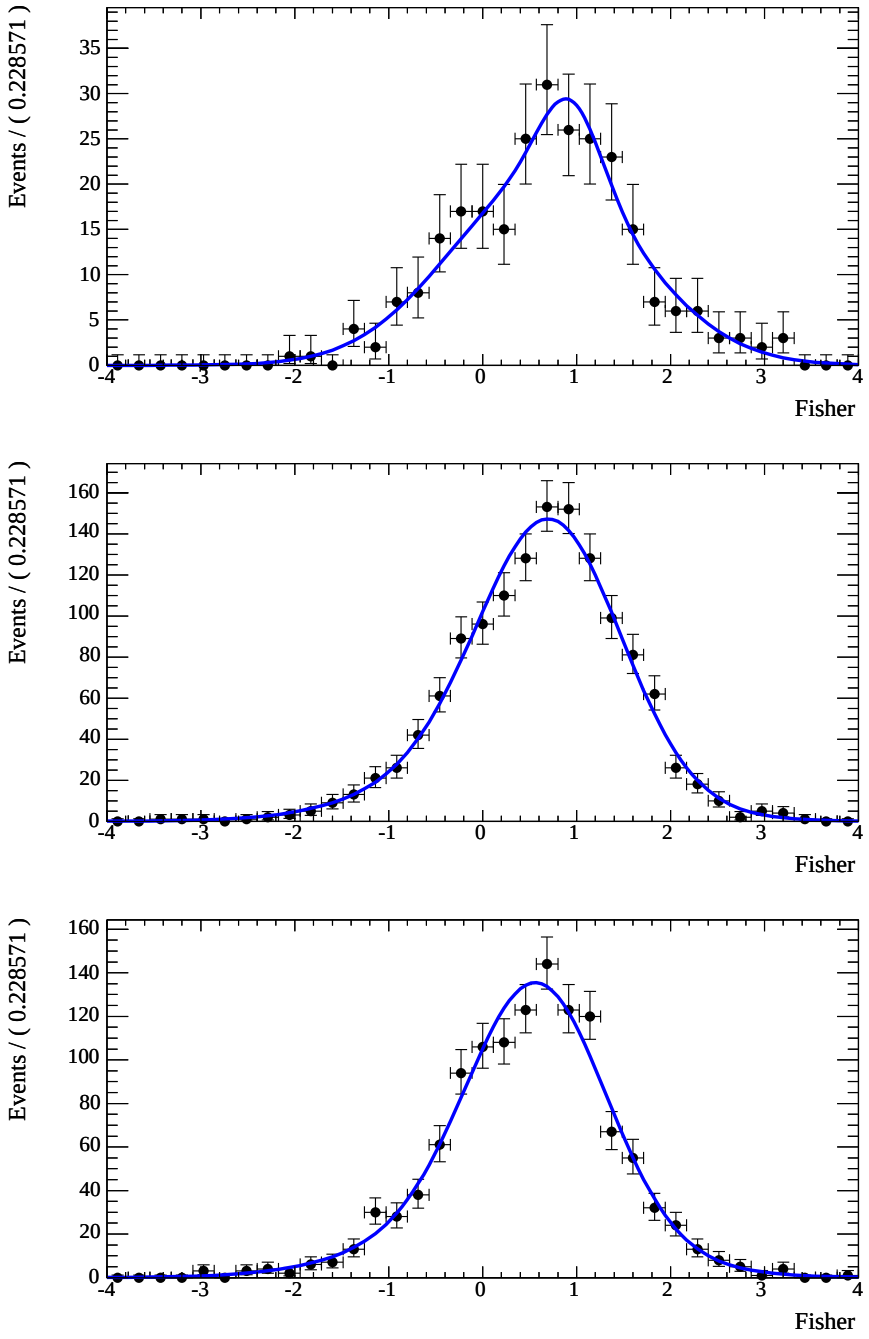

Figure 5.21: Fisher distribution for $B\overline{B}$ simulated events for $K\pi$ (top plots), $K\pi\pi^0$ (middle plots) and $K\pi\pi\pi$ (bottom plots) modes. The superimposed curve is the result of a fit with a sum of two Gaussian functions.

Continuum background

For the continuum background, the variable m_{ES} is parametrized with an Argus function and the Fisher is parametrized using a Gaussian distribution. For this category of background, we observed that the m_{ES} distribution has a different shape for same sign ($sgnK = 1$) and opposite sign ($sgnK = -1$) events, so the parameters of the pdfs are evaluated separately for the two categories. The results of the parametrizations are shown in Fig. 5.22 for m_{ES} and in Fig. 5.23 for Fisher discriminant. Details on the fitted parameters are given in appendix A.

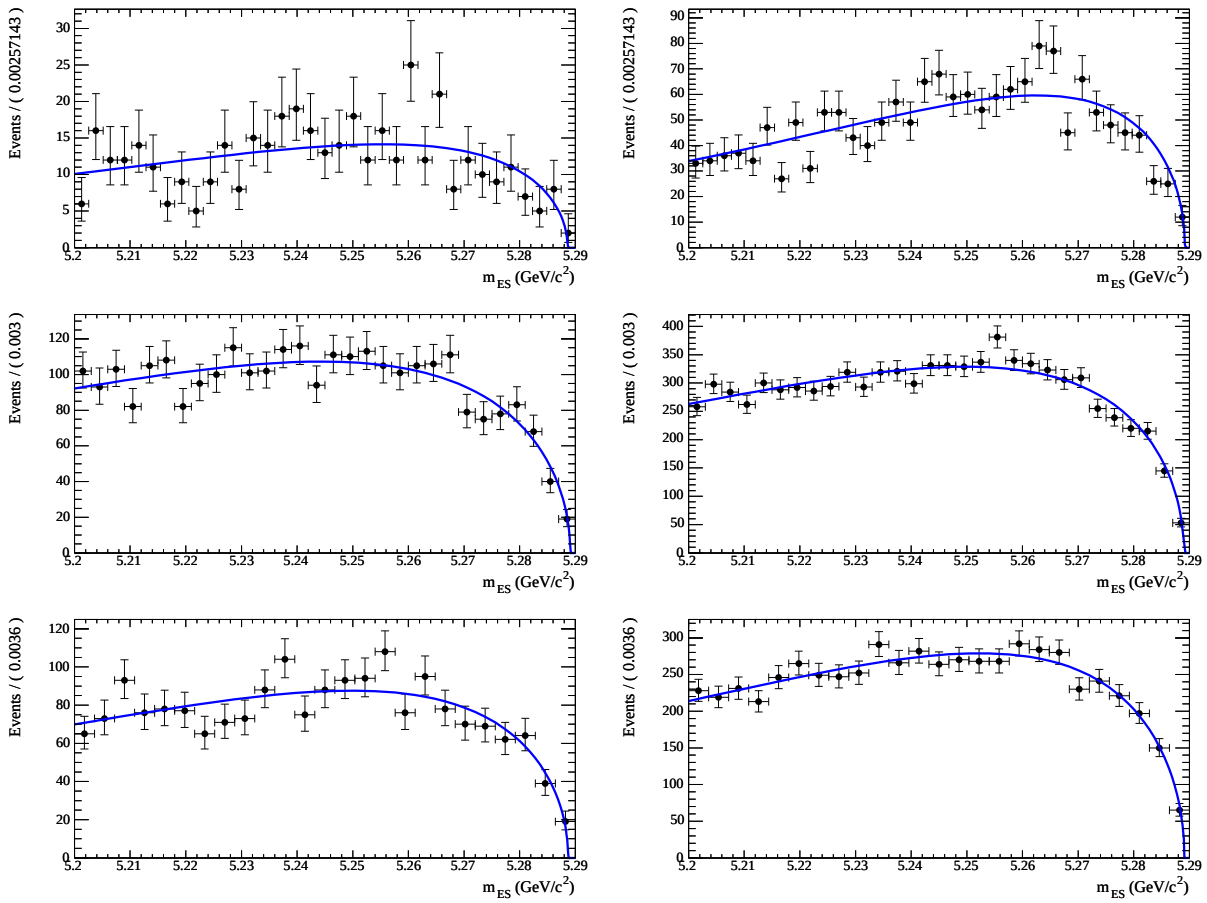

Figure 5.22: m_{ES} distribution for continuum simulated events for $K\pi$ (top plots), $K\pi\pi^0$ (middle plots) and $K\pi\pi\pi$ (bottom plots) modes. The distributions for same and opposite sign events are shown on the left and on the right respectively. The superimposed curves are the result of a fit with an Argus function.

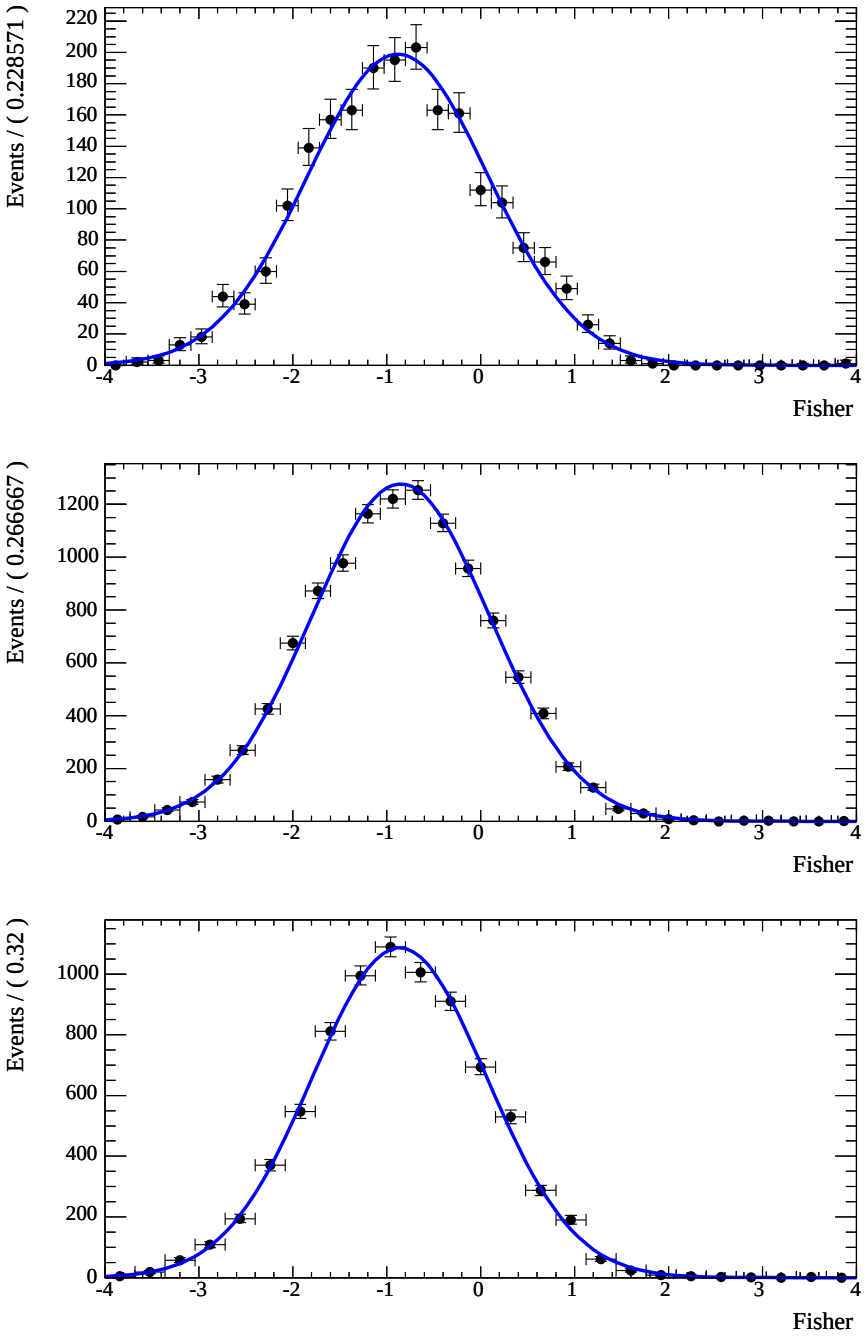

Figure 5.23: Fisher distribution for continuum simulated events for $K\pi$ (up), $K\pi\pi^0$ (middle) and $K\pi\pi\pi$ (down) modes. The superimposed curve is the result of a fit with a Gaussian function.

5.4.3 Fit validation using a Toy Monte Carlo procedure

The fit procedure has been validated by means of a toy Monte Carlo (toy MC) technique: 1000 samples for each one of the three decay channels are generated from the fit model, according to the distributions of m_{ES} and Fisher and using the parameters values listed in Tab. A.1, A.2 and A.3 in appendix A. The number of generated events are chosen following Poisson distributions with expected values equal to the expected number of events, as estimated on simulated events and reported in the Tab. 5.10. The fit is then performed on every generated sample.

In all the tests shown in the following the parameters left free to vary in the fit procedure are:

- the sum of the number of opposite sign and same sign signal events, N_{DK^*}, and R_{ADS};
- the number of same and opposite sign events for the backgrounds (N_{cont}^{SameS}, N_{cont}^{OppS}, N_{BB}^{SameS} and N_{BB}^{OppS});
- the mean value for the Gaussian describing m_{ES} for signal events;
- the parameters of the Argus function describing m_{ES} for continuum events.

We define the pull for a variable x as the difference between the fitted and the generated value, divided by its error: $x_{pull} = (x_{fit} - x_{gen})/x_{err}$. We look at the distribution of the pull variable for the quantities of interest (mainly N_{DK^*} and R_{ADS}) for all the generated toy-MC samples. If the likelihood of the fitted variable x is well described by a Gaussian, we expect the mean value of its pull distribution (x_{pull}) to be consistent with zero and its resolution to be consistent with unity.

In Fig. 5.24, we show the pull of N_{DK^*}, for the three D^0 channels. In Figs. 5.25, 5.26 and 5.27, we show the distribution of R_{ADS}, its error and its pull for the three D^0 channels. More details on the toy Monte Carlo results are shown in appendix B.

We also show the negative and positive errors we get for R_{ADS} when we fit for it with asymmetric errors and the corresponding pull distributions. When calculating the pull with asymmetric errors the negative error is used for fitted values that are smaller than the generated one, while the positive error is used for fitted values that are higher than the generated one. For all the three channels, the likelihood for R_{ADS} from the toy-MC experiments is not Gaussian and hence the pull for R_{ADS}, calculated using Gaussian errors, does not have a mean consistent with zero nor an RMS consistent with unity. On the other hand, the asymmetric pull distributions show a good behaviour, which means that the result for R_{ADS} is well described by a bifurcated Gaussian. The final outcome of the analysis will be a likelihood scan for the variables R_{ADS} for the three channels, thus independent from any Gaussian assumption.

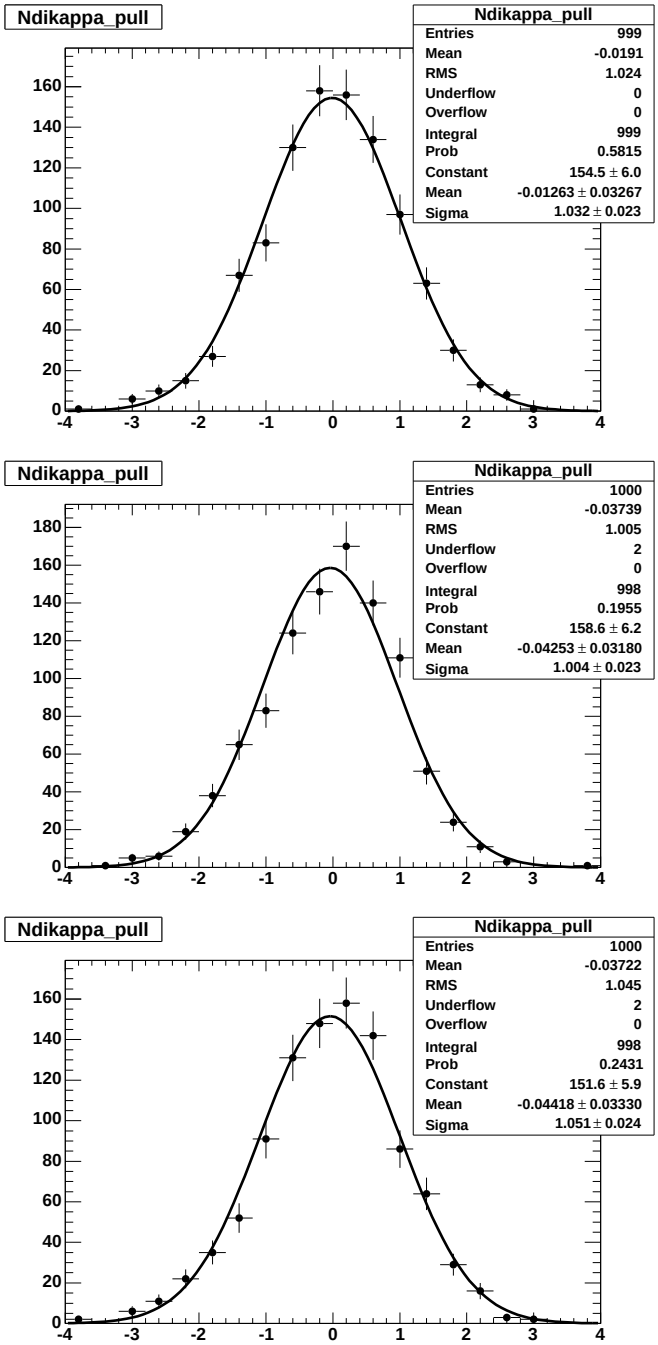

Figure 5.24: [toy Monte Carlo]. Pull distributions for N_{DK^*} (the sum of the number of opposite- and same sign signal events) obtained from the toy MC described in the text for the $K\pi$ (top), $K\pi\pi^0$ and $K\pi\pi\pi$ (bottom) channels.

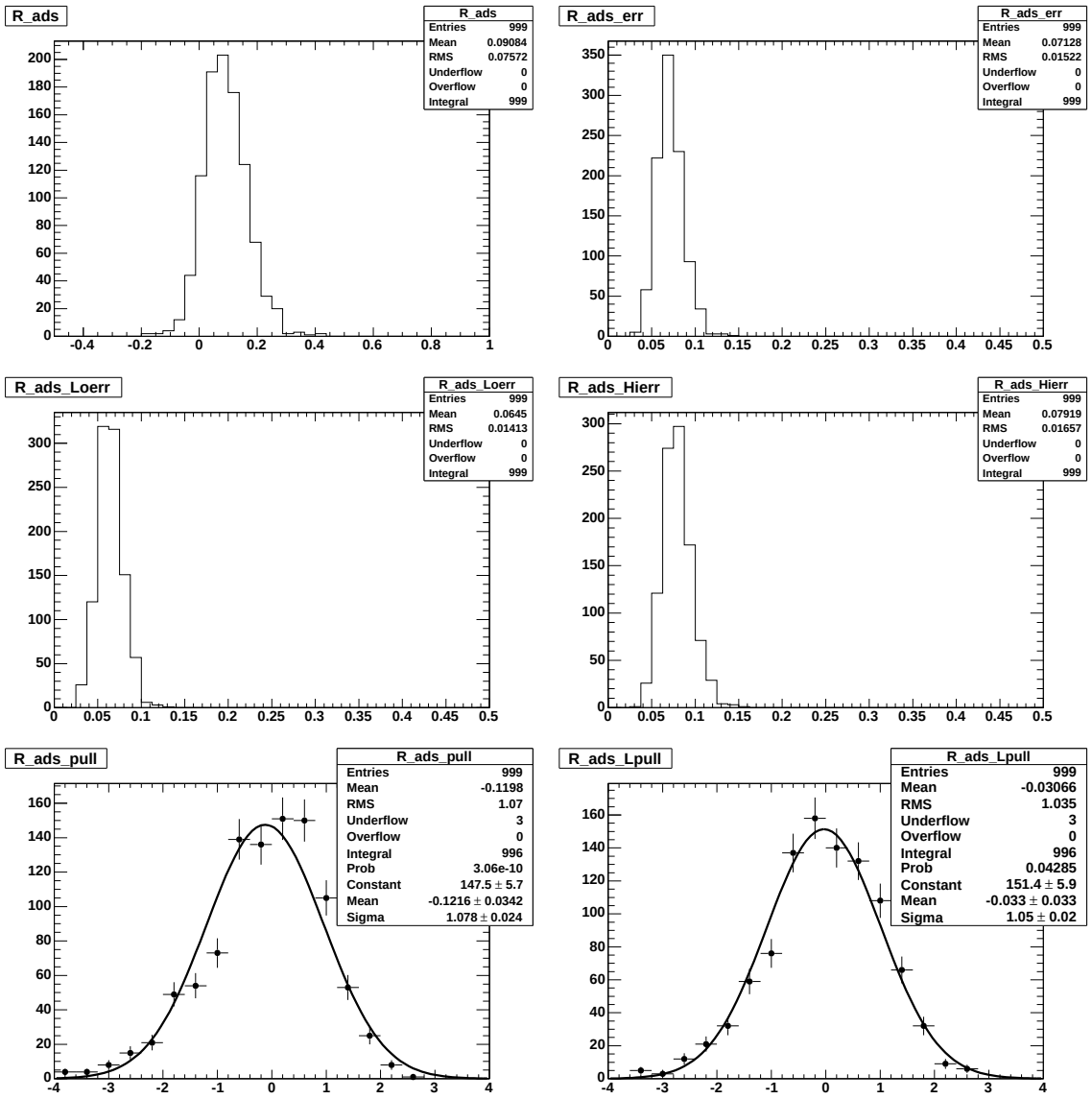

Figure 5.25: [toy Monte Carlo $K\pi$ mode]. Distributions of the fitted value for R_{ADS} and its (symmetric error) (top plots), its negative and positive errors (middle plots) and the symmetric and asymmetric pulls (bottom plots) obtained from the toy MC described in the text. The generated value is $R_{ADS} = 0.09$.

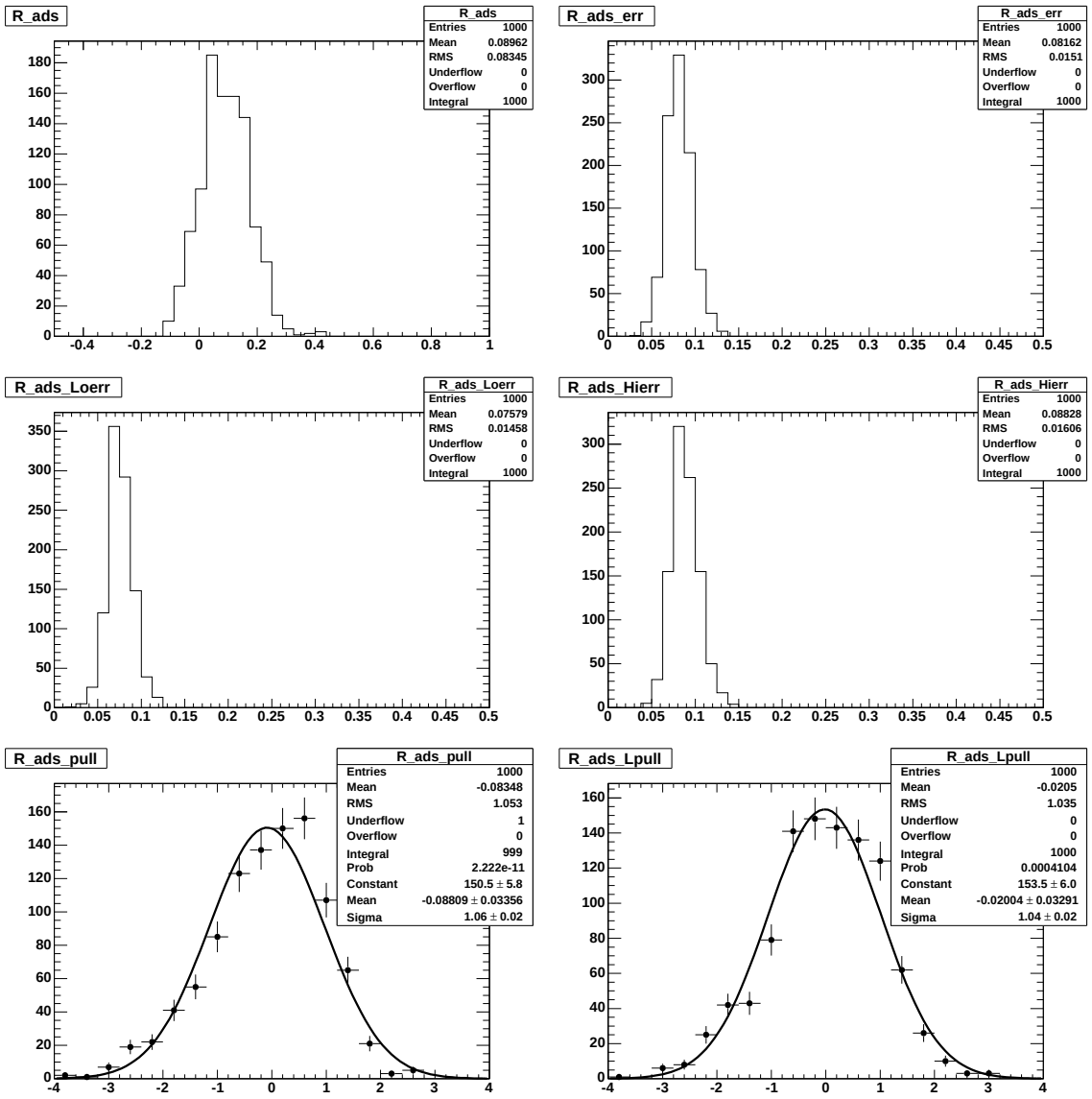

Figure 5.26: [toy Monte Carlo $K\pi\pi^0$ mode]. Distributions of the fitted value for R_{ADS} and its (symmetric error) (top plots), its negative and positive errors (middle plots) and the symmetric and asymmetric pulls (bottom plots) obtained from the toy MC described in the text. The generated value is $R_{ADS} = 0.09$.

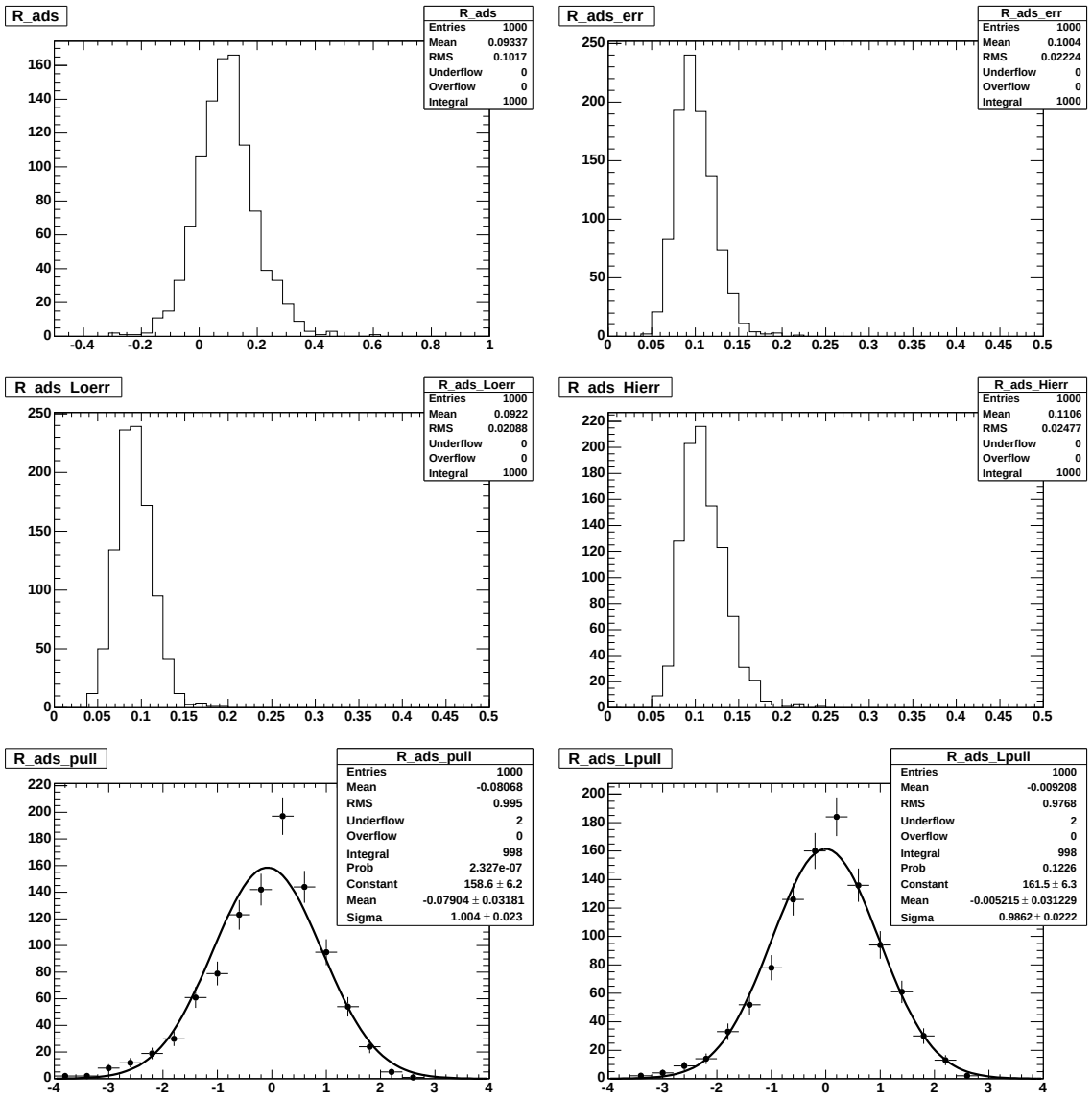

Figure 5.27: [toy Monte Carlo $K\pi\pi\pi$ mode]. Distributions of the fitted value for R_{ADS} and its (symmetric error) (top plots), its negative and positive errors (middle plots) and the symmetric and asymmetric pulls (bottom plots) obtained from the toy MC described in the text. The generated value is $R_{ADS} = 0.09$.

5.4.4 Fit validation on a fully simulated sample

As a further test of the fit procedure, the fit has been performed on three MC samples, one for each neutral D decay mode. The samples are constructed merging fully simulated signal and background events according to the expected number of events listed in Tab. 5.10. This check is useful to see the impact on the fit of possible correlations between the variables which have been assumed uncorrelated. On the other hand, the simulated events are enough to construct just one completely statistically independent sample, while the toy MC allows for more extensive tests and for this reason both validation procedures have been followed. The results of the fit on the three samples, for the $K\pi$, $K\pi\pi^0$ and $K\pi\pi\pi$ modes respectively, are shown in the Tabs. 5.14, 5.15 and 5.16. The fit results are compatible with the generated values, for all the three neutral D decay modes. The projections of the fit over the variables m_{ES} and Fisher are shown in Fig. 5.28 to Fig. 5.30.

Parameter	value $\pm$ error	generated value
N_{BB}^{SameS}	34 ± 13	40
N_{BB}^{OppS}	47 ± 20	48
N_{cont}^{SameS}	415 ± 22	412
N_{cont}^{OppS}	1712 ± 45	1706
N_{DK^*}	95 ± 12	101
R_{ADS}	0.040 ± 0.050	0.09
SameS cont m_{ES} cutoff $[GeV/c^2]$	5.28883 ± 0.00034	5.2886
SameS cont m_{ES} shape	-41.5 ± 6.0	-39.5
OppS cont m_{ES} cutoff $[GeV/c^2]$	5.28911 ± 0.00006	5.2892
OppS cont m_{ES} shape	-45.4 ± 2.7	-49.3
Sig m_{ES} μ $[GeV/c^2]$	5.27949 ± 0.00032	5.2795

Table 5.14: [Simulated $K\pi$ sample]. Results of the fit performed on a simulated sample.

Parameter	value ± error	generated value
N_{BB}^{SameS}	170 ± 42	183
N_{BB}^{OppS}	248 ± 31	252
N_{cont}^{SameS}	2591 ± 56	2660
N_{cont}^{OppS}	8219 ± 100	8138
N_{DK^*}	148 ± 18	139
R_{ADS}	0.134 ± 0.058	0.09
SameS cont m_{ES} cutoff $[GeV/c^2]$	5.28911 ± 0.00014	5.2891
SameS cont m_{ES} shape	-26.3 ± 2.3	-29.3
OppS cont m_{ES} cutoff $[GeV/c^2]$	5.28892 ± 0.00008	5.2890
OppS cont m_{ES} shape	-33.5 ± 1.3	-33.4
Sig m_{ES} μ $[GeV/c^2]$	5.27969 ± 0.00031	5.2795

Table 5.15: [Simulated $K\pi\pi^0$ sample]. Results of the fit performed on a simulated sample.

Parameter	value ± error	generated value
N_{BB}^{SameS}	258 ± 33	186
N_{BB}^{OppS}	202 ± 42	223
N_{cont}^{SameS}	1773 ± 50	1849
N_{cont}^{OppS}	5808 ± 85	5894
N_{DK^*}	102 ± 16	98
R_{ADS}	0.125 ± 0.102	0.09
SameS cont m_{ES} cutoff $[GeV/c^2]$	5.28920 ± 0.00022	5.2887
SameS cont m_{ES} shape	-30.9 ± 2.9	-34.0
OppS cont m_{ES} cutoff $[GeV/c^2]$	5.28910 ± 0.00012	5.2888
OppS cont m_{ES} shape	-35.0 ± 1.5	-34.3
Sig m_{ES} μ $[GeV/c^2]$	5.28028 ± 0.00041	5.2795

Table 5.16: [Simulated $K\pi\pi\pi$ sample]. Results of the fit performed on a simulated sample.

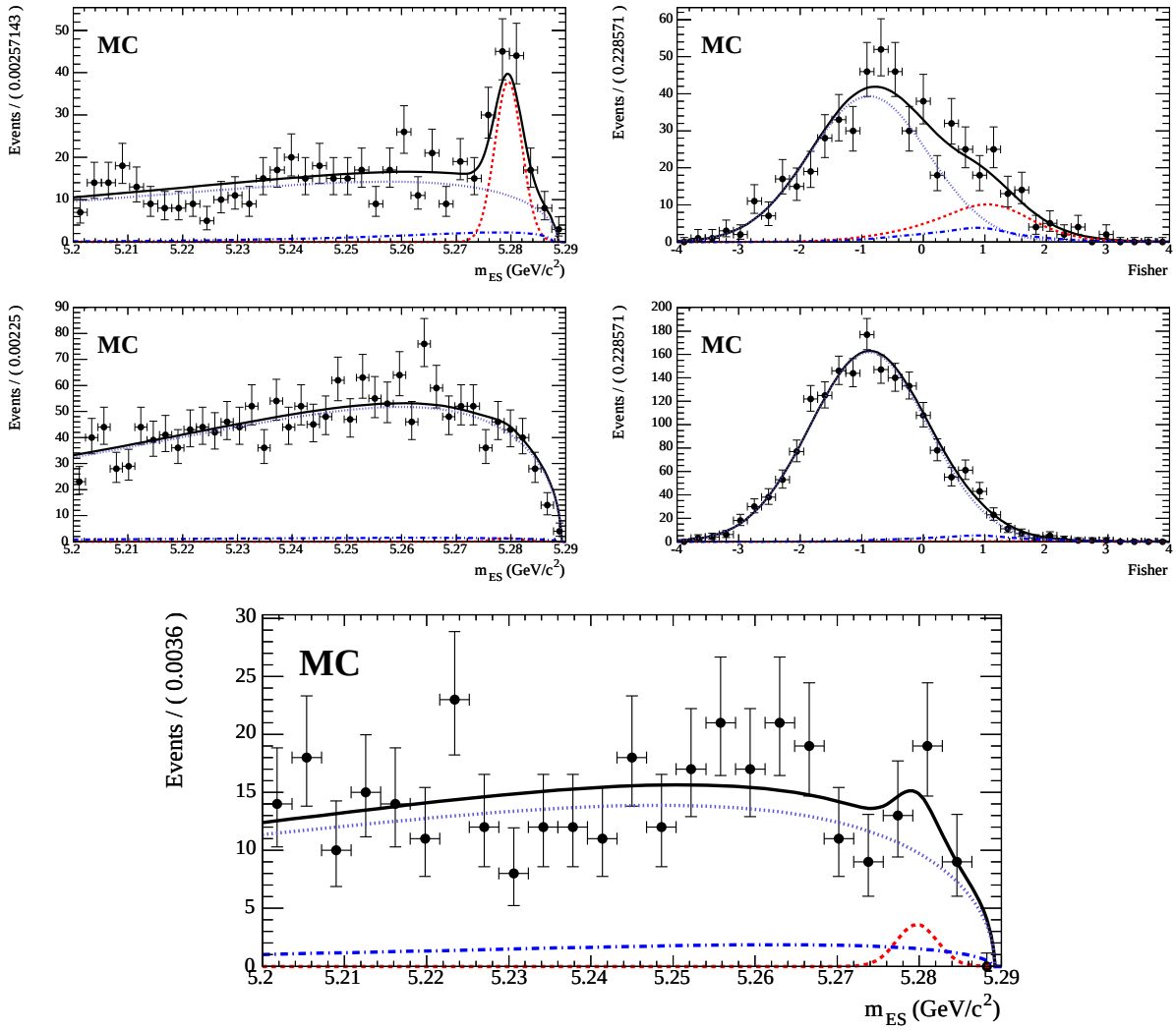

Figure 5.28: [Simulated $K\pi$ events]. Projections of the fit over the variables m_{ES} and Fisher for the same sign (top plots) and opposite sign (middle plots) $K\pi$ events. In the bottom plot, the projection of the fit over the variables m_{ES} after a cut on Fisher> 0, in order to enhance the signal, is shown for opposite sign $K\pi$ events. The point with error bars are simulated events and the superimposed curves are the result of the fit procedure as described in sec. 5.4. The dashed, dotted and dash-dotted lines represent the signal, continuum background and $B\bar{B}$ background contributions respectively.

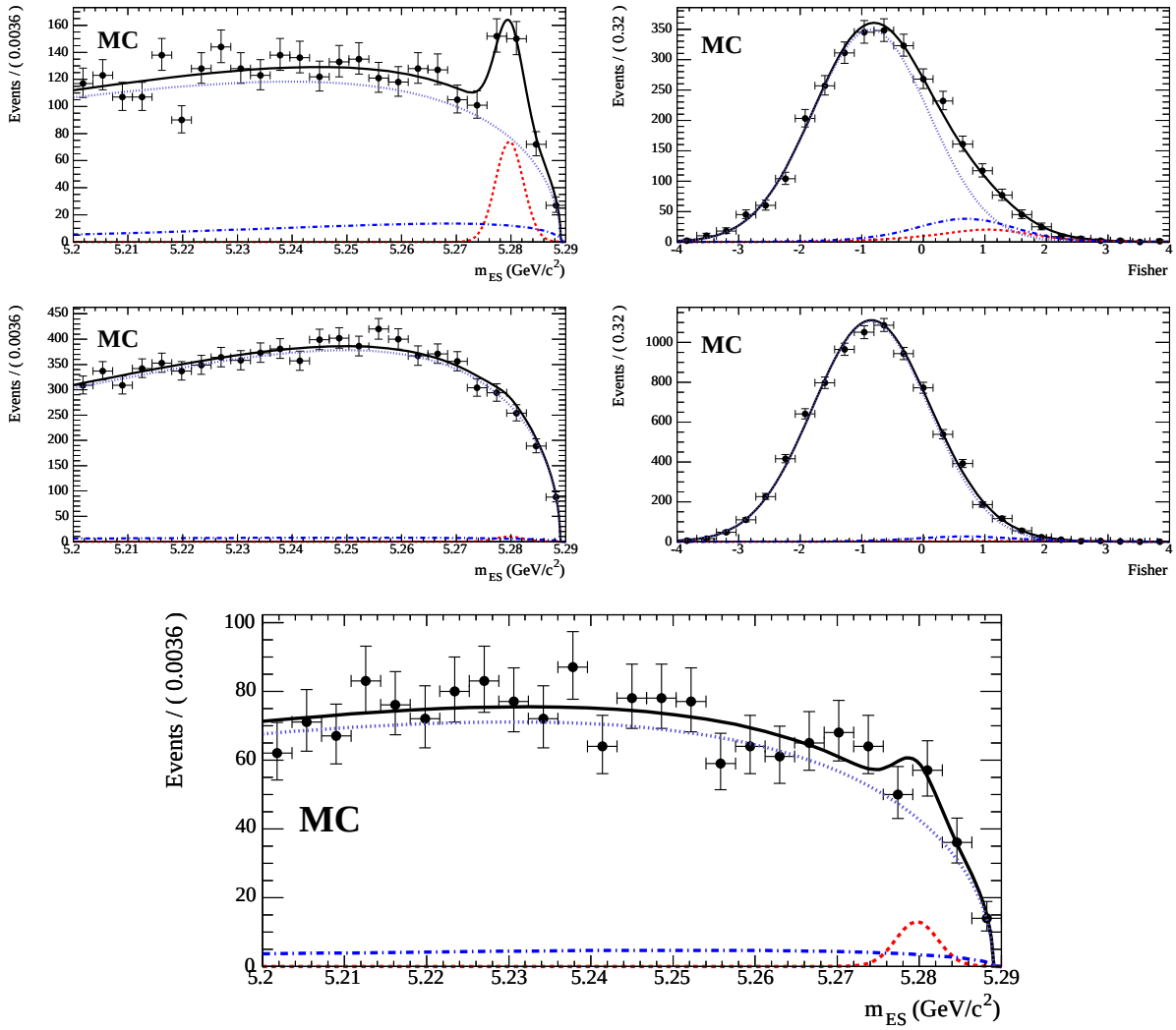

Figure 5.29: [Simulated $K\pi\pi^0$ events]. Projections of the fit over the variables m_{ES} and Fisher for the same sign (top plots) and opposite sign (middle plots) $K\pi\pi^0$ events. In the bottom plot, the projection of the fit over the variables m_{ES} after a cut on Fisher$>$ 0, in order to enhance the signal, is shown for opposite sign $K\pi\pi^0$ events. The points with error bars are simulated events and the superimposed curves are the result of the fit procedure as described in sec. 5.4. The dashed, dotted and dash-dotted lines represent the signal, continuum background and $B\bar{B}$ background contributions respectively.

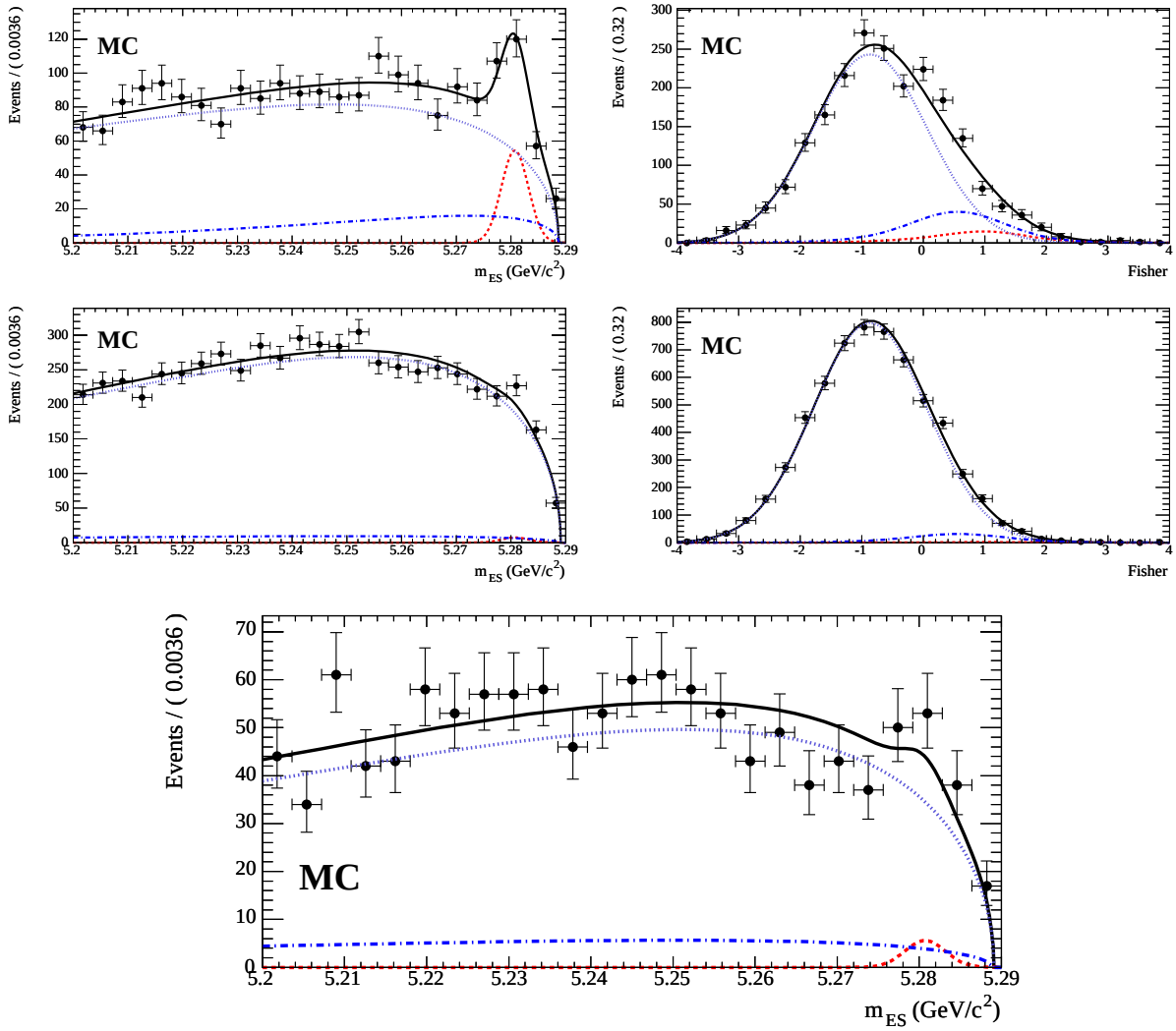

Figure 5.30: [Simulated $K\pi\pi\pi$ events]. Projections of the fit over the variables m_{ES} and Fisher for the same sign (top plots) and opposite sign (middle plots) $K\pi\pi\pi$ events. In the bottom plot, the projection of the fit over the variables m_{ES} after a cut on Fisher>0, in order to enhance the signal, is shown for opposite sign $K\pi\pi\pi$ events. The points with error bars are simulated events and the superimposed curves are the result of the fit procedure as described in sec. 5.4. The dashed, dotted and dash-dotted lines represent the signal, continuum background and $B\bar{B}$ background contributions respectively.

5.5 Results on data

In this chapter we present the results of the ADS analysis of $B^0 \to D^0(\overline{D}^0)K^{*0}$ decays, with neutral D reconstructed into $K\pi$, $K\pi\pi^0$ and $K\pi\pi\pi$ final states, obtained using a data sample of 423 fb^{-1}. In sec. 5.5.1 we show the results of the fit on data and the values for the R_{ADS} ratios and in sec. 5.5.4, we discuss the systematic uncertainties.

5.5.1 Fit on real data

The fit has been performed on a data sample of 423 fb^{-1} collected at the $\Upsilon(4S)$ peak. The results of the fit are shown in the Tabs. 5.17, 5.18 and 5.19, for the $K\pi$, $K\pi\pi^0$ and $K\pi\pi\pi$ respectively. From toy-MC studies it has been proved that the likelihood for R_{ADS} can be described by asymmetric Gaussians and for this reason the fit on data is performed with asymmetric errors. In the end, a likelihood scan for the R_{ADS} ratios will be performed. The projections of the fit over the variables m_{ES} and Fisher are shown in Fig. 5.31 and 5.32 for $K\pi$ same and opposite sign events, in Fig. .5.37 and 5.38 for $K\pi\pi^0$ same and opposite sign events, and in Fig. 5.35 and 5.36 for $K\pi\pi\pi$ same and opposite sign events. Projections of the fit over the variables m_{ES} after a cut on Fisher is applied, in order to visually enhance the signal contribution, are shown in Fig. 5.38 for the opposite sign samples and in Fig. 5.37 for the same sign samples.

Parameter	value $\pm$ error
N_{BB}^{SameS}	75 ± 16
N_{BB}^{OppS}	40 ± 17
N_{cont}^{SameS}	387 ± 22
N_{cont}^{OppS}	1602 ± 41
N_{DK^*}	74 ± 12
R_{ADS}	$0.062^{+0.067}_{-0.059}$
SameS cont m_{ES} cutoff $[GeV/c^2]$	5.28856 ± 0.00040
SameS cont m_{ES} shape	-54.1 ± 6.4
OppS cont m_{ES} cutoff $[GeV/c^2]$	5.28841 ± 0.00020
OppS cont m_{ES} shape	-49.1 ± 2.9
Sig m_{ES} μ $[GeV/c^2]$	5.28030 ± 0.00041

Table 5.17: [Data $K\pi$ mode] Results, for the $K\pi$ mode, of the fit on a data sample with an integrated luminosity of 423 fb^{-1}.

Parameter	value ± error
N_{BB}^{SameS}	265 ± 33
N_{BB}^{OppS}	215 ± 41
N_{cont}^{SameS}	2497 ± 56
N_{cont}^{OppS}	7793 ± 96
N_{DK^*}	146 ± 17
R_{ADS}	$0.057^{+0.046}_{-0.037}$
SameS cont m_{ES} cutoff $[GeV/c^2]$	5.28860 ± 0.00013
SameS cont m_{ES} shape	-32.7 ± 2.4
OppS cont m_{ES} cutoff $[GeV/c^2]$	5.28848 ± 0.00009
OppS cont m_{ES} shape	-31.0 ± 1.3
Sig m_{ES} μ $[GeV/c^2]$	5.27961 ± 0.00032

Table 5.18: [Data $K\pi\pi^0$ mode] Results, for the $K\pi\pi^0$ mode, of the fit on a data sample with an integrated luminosity of 423 fb^{-1}.

Parameter	value ± error
N_{BB}^{SameS}	345 ± 35
N_{BB}^{OppS}	327 ± 48
N_{cont}^{SameS}	2058 ± 53
N_{cont}^{OppS}	6372 ± 91
N_{DK^*}	101 ± 17
R_{ADS}	$0.136^{+0.107}_{-0.098}$
SameS cont m_{ES} cutoff $[GeV/c^2]$	5.28891 ± 0.00014
SameS cont m_{ES} shape	-32.8 ± 2.7
OppS cont m_{ES} cutoff $[GeV/c^2]$	5.28907 ± 0.00004
OppS cont m_{ES} shape	-33.4 ± 1.4
Sig m_{ES} μ $[GeV/c^2]$	5.27999 ± 0.00043

Table 5.19: [Data $K\pi\pi\pi$ mode] Results, for the $K\pi\pi\pi$ mode, of the fit on a data sample with an integrated luminosity of 423 fb^{-1}.

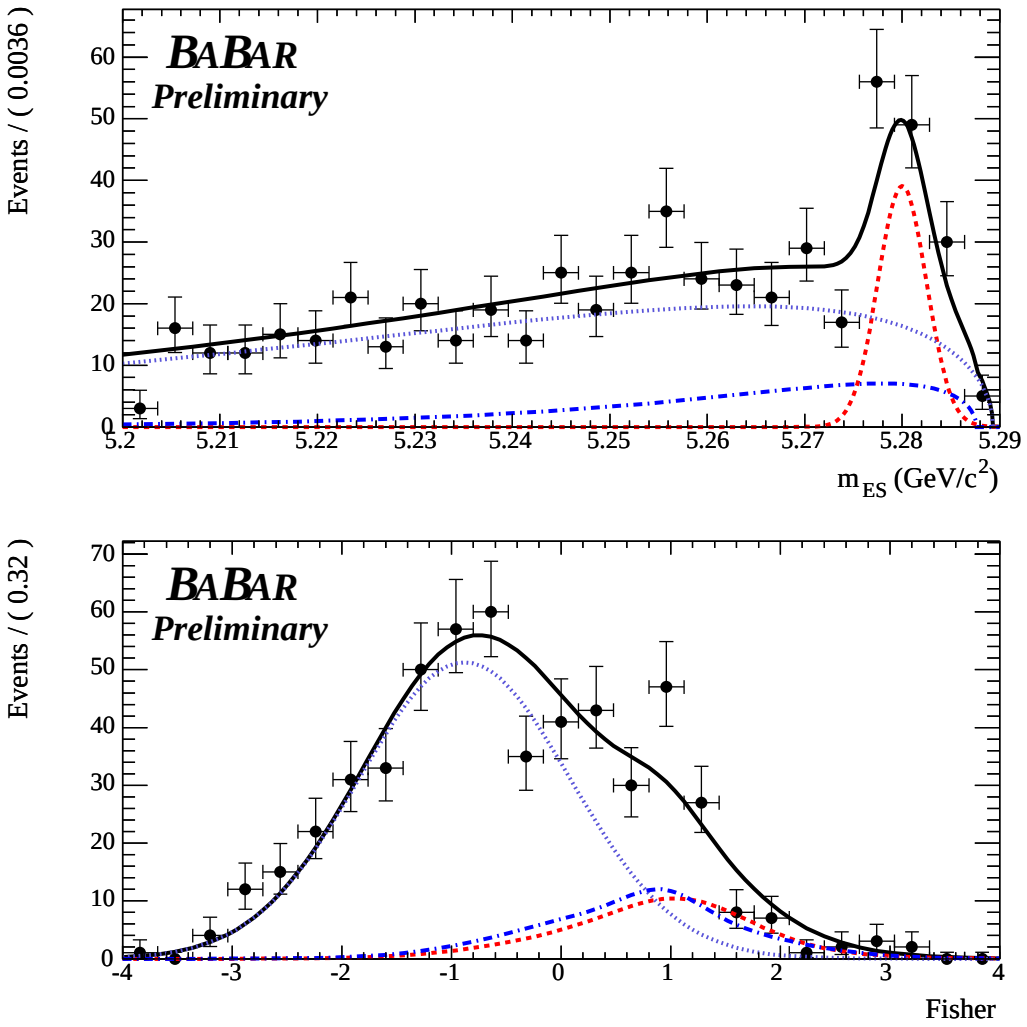

Figure 5.31: [Data $K\pi$ mode - same sign] Projections of the fit over the variables m_{ES} and Fisher for same sign $K\pi$ events. The points with error bars are data, and the superimposed curves are the result of the fit procedure as described in sec. 5.4. The dashed, dotted and dash-dotted lines represent the signal, continuum background and $B\bar{B}$ background contributions respectively.

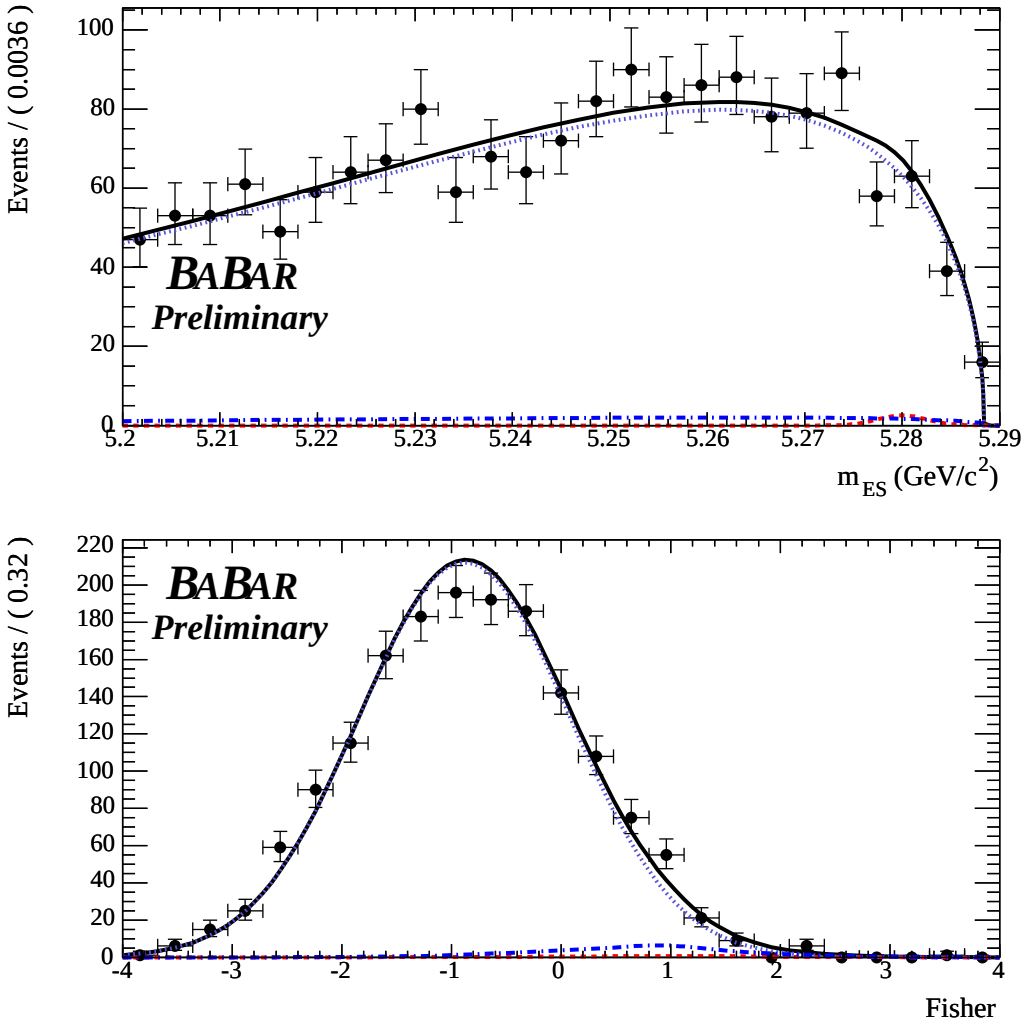

Figure 5.32: [Data $K\pi$ mode - opposite sign] Projections of the fit over the variables m_{ES} and Fisher for opposite sign $K\pi$ events. The points with error bars are data, and the superimposed curves are the result of the fit procedure as described in sec. 5.4. The dashed, dotted and dash-dotted lines represent the signal, continuum background and $B\bar{B}$ background contributions respectively.

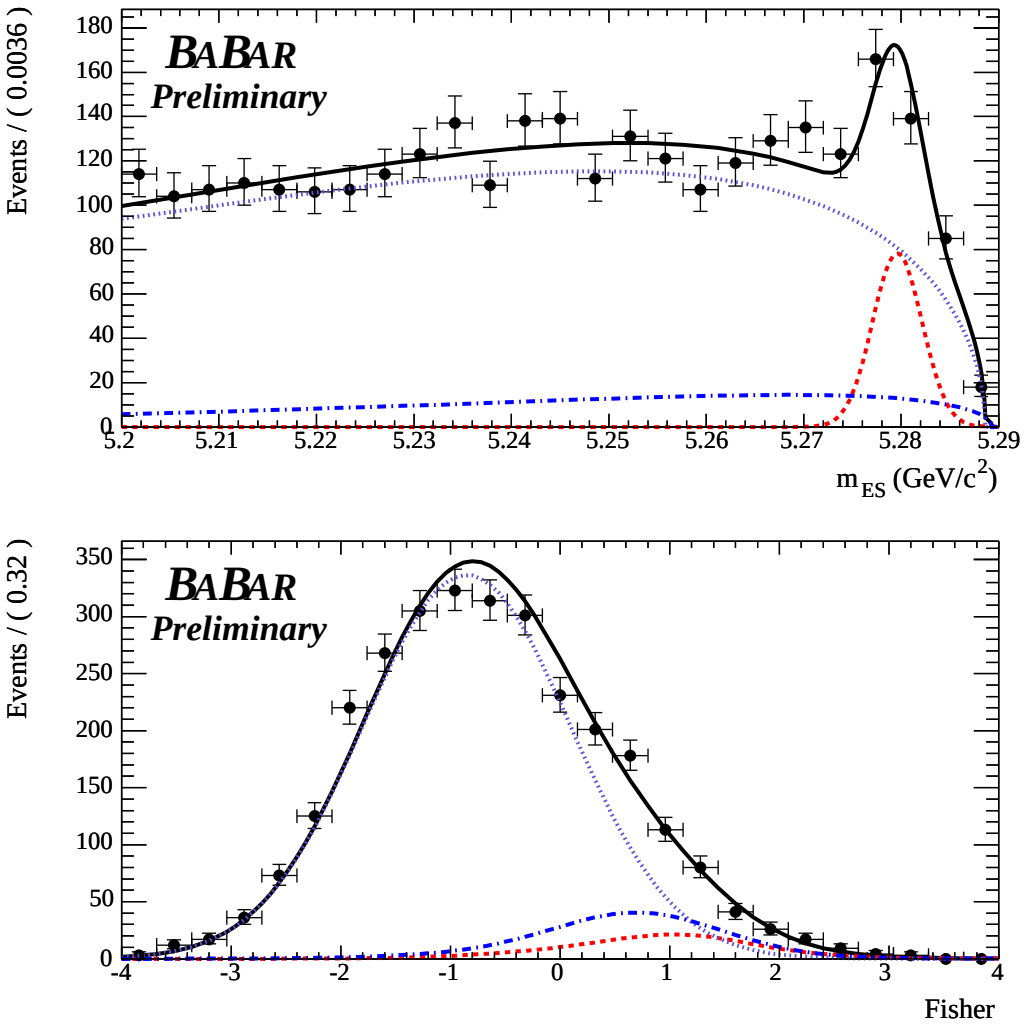

Figure 5.33: [Data $K\pi\pi^0$ mode - same sign] Projections of the fit over the variables m_{ES} and Fisher for same sign $K\pi\pi^0$ events. The points with error bars are data, and the superimposed curves are the result of the fit procedure as described in sec. 5.4. The dashed, dotted and dash-dotted lines represent the signal, continuum background and $B\bar{B}$ background contributions respectively.

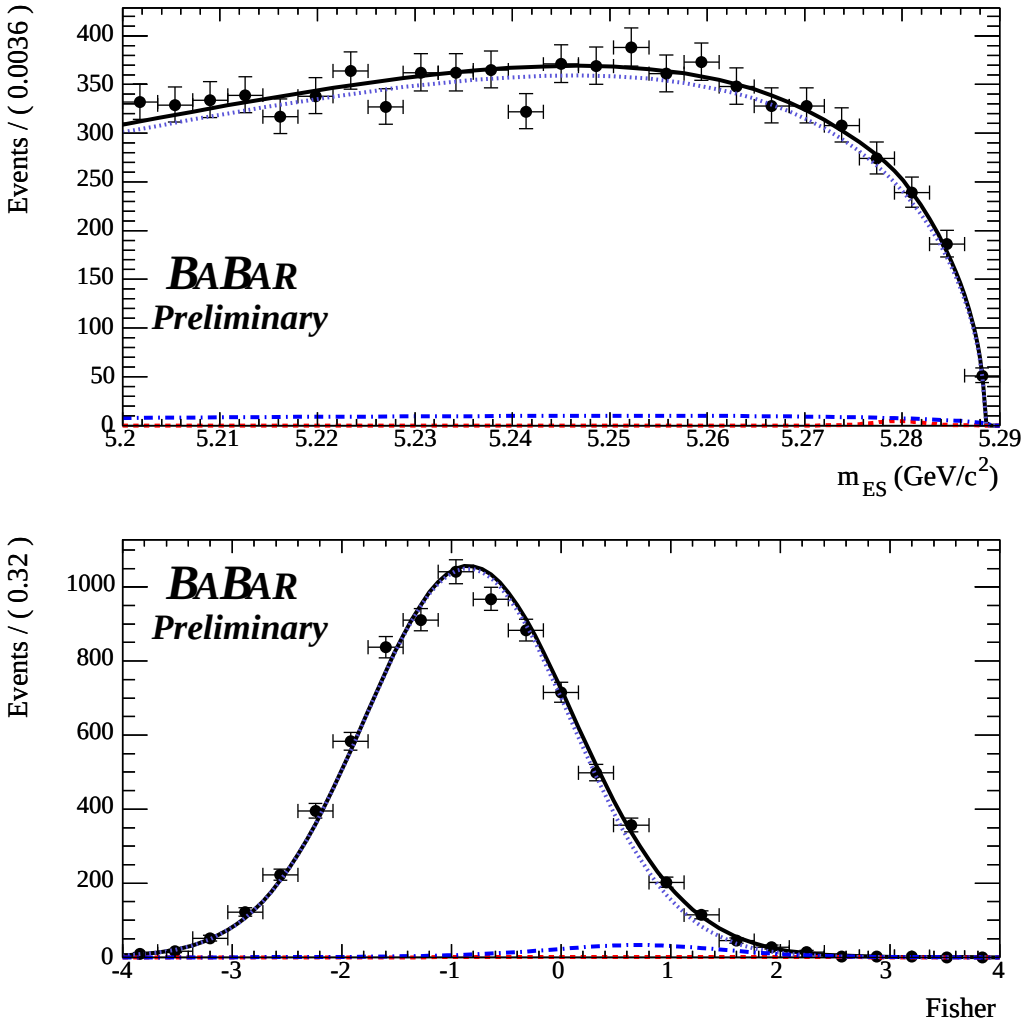

Figure 5.34: [Data $K\pi\pi^0$ mode - opposite sign] Projections of the fit over the variables m_{ES} and Fisher for opposite sign $K\pi\pi^0$ events. The points with error bars are data, and the superimposed curves are the result of the fit procedure as described in sec. 5.4. The dashed, dotted and dash-dotted lines represent the signal, continuum background and $B\bar{B}$ background contributions respectively.

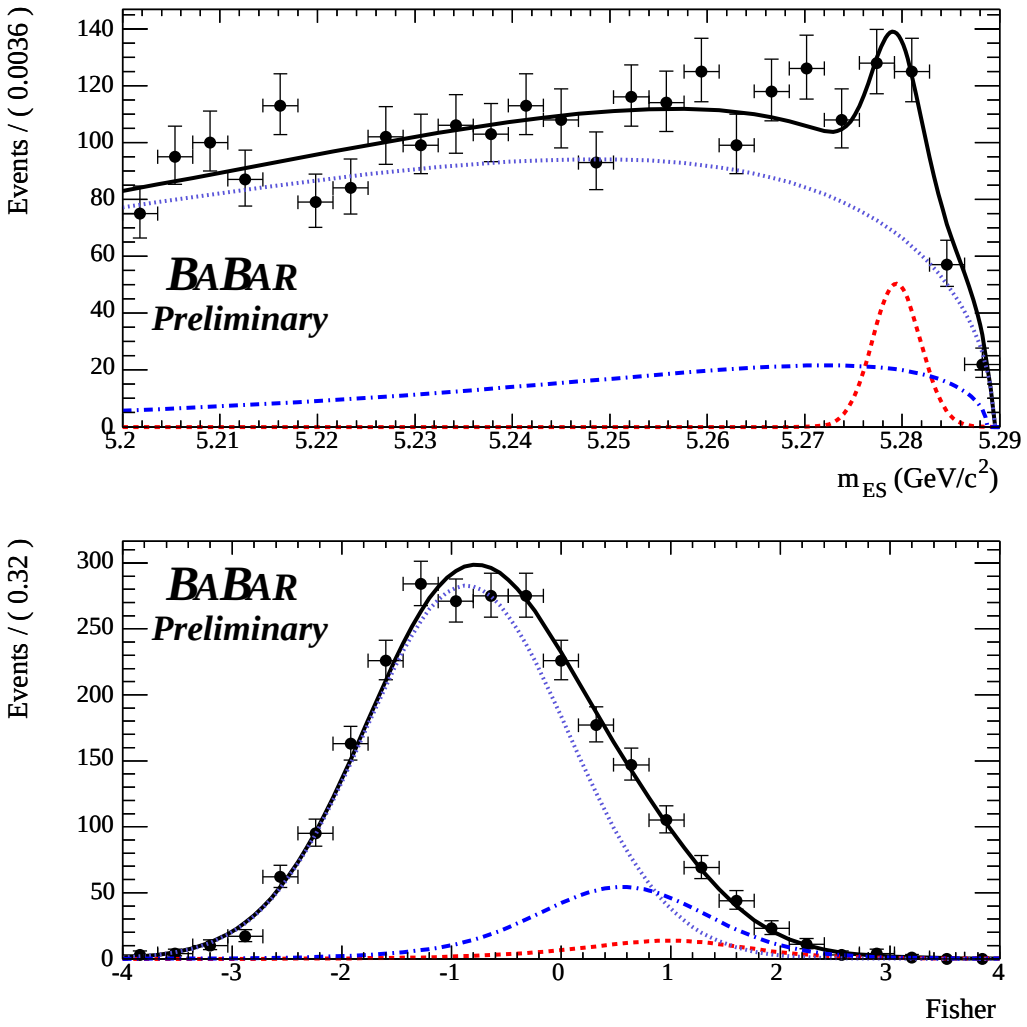

Figure 5.35: [Data $K\pi\pi\pi$ mode - same sign] Projections of the fit over the variables m_{ES} and Fisher for same sign $K\pi\pi\pi$ events. The points with error bars are data, and the superimposed curves are the result of the fit procedure as described in sec. 5.4. The dashed, dotted and dash-dotted lines represent the signal, continuum background and $B\bar{B}$ background contributions respectively.

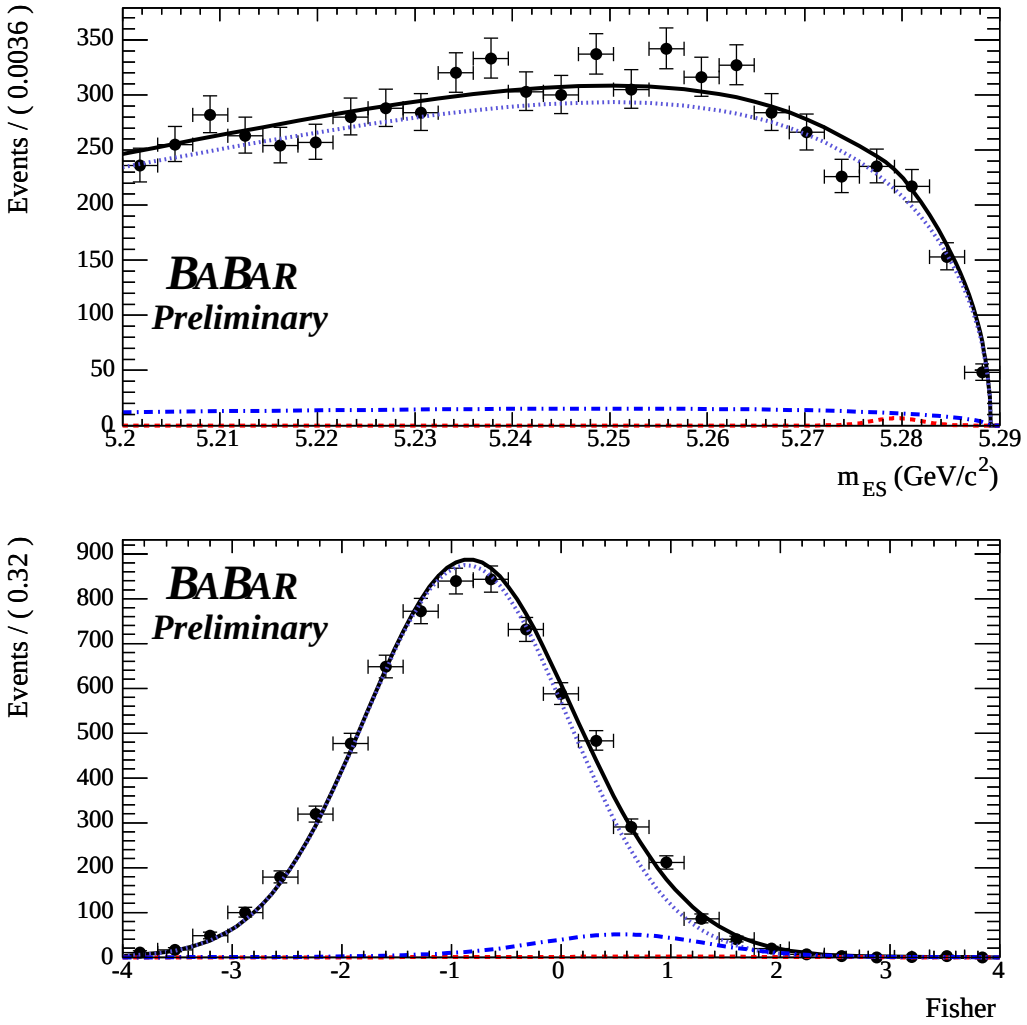

Figure 5.36: [Data $K\pi\pi\pi$ mode - opposite sign] Projections of the fit over the variables m_{ES} and Fisher for opposite sign $K\pi\pi\pi$ events. The points with error bars are data, and the superimposed curves are the result of the fit procedure as described in sec. 5.4. The dashed, dotted and dash-dotted lines represent the signal, continuum background and $B\bar{B}$ background contributions respectively.

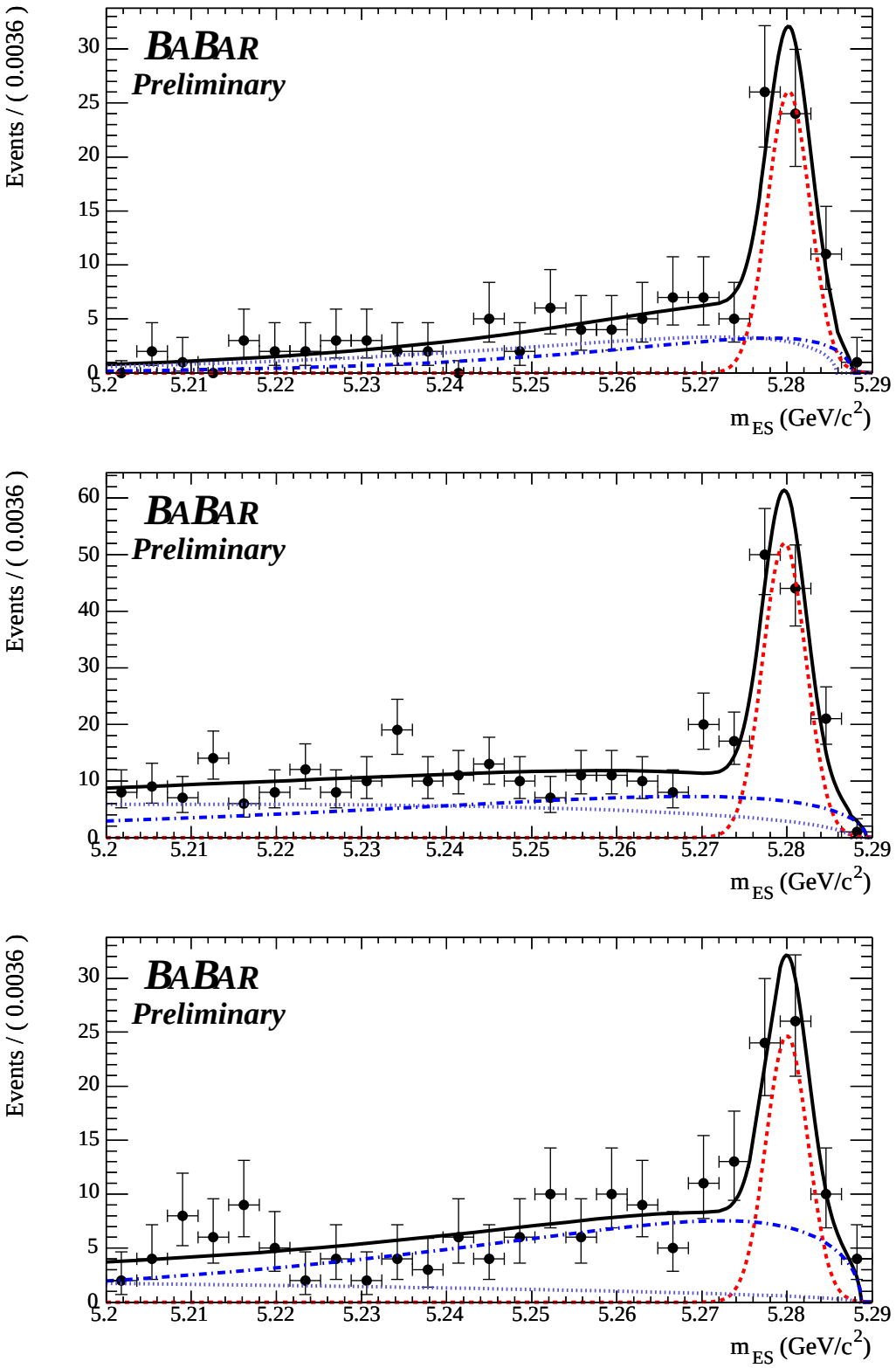

Figure 5.37: [Data - same sign] Projections of the fit over the variables m_{ES} after a cut on Fisher is applied (Fisher$>$ 0.5 for $K\pi$, Fisher$>$ 0.7 for $K\pi\pi^0$ and Fisher$>$ 1. for $K\pi\pi\pi$), to visually enhance the signal, for $K\pi$ (top), $K\pi\pi^0$ (middle) and $K\pi\pi\pi$ (bottom) same sign events. The points with error bars are data, and the superimposed curves are the result of the fit procedure as described in sec. 5.4. The dashed, dotted and dash-dotted lines represent the signal, continuum background and $B\bar{B}$ background contributions respectively.

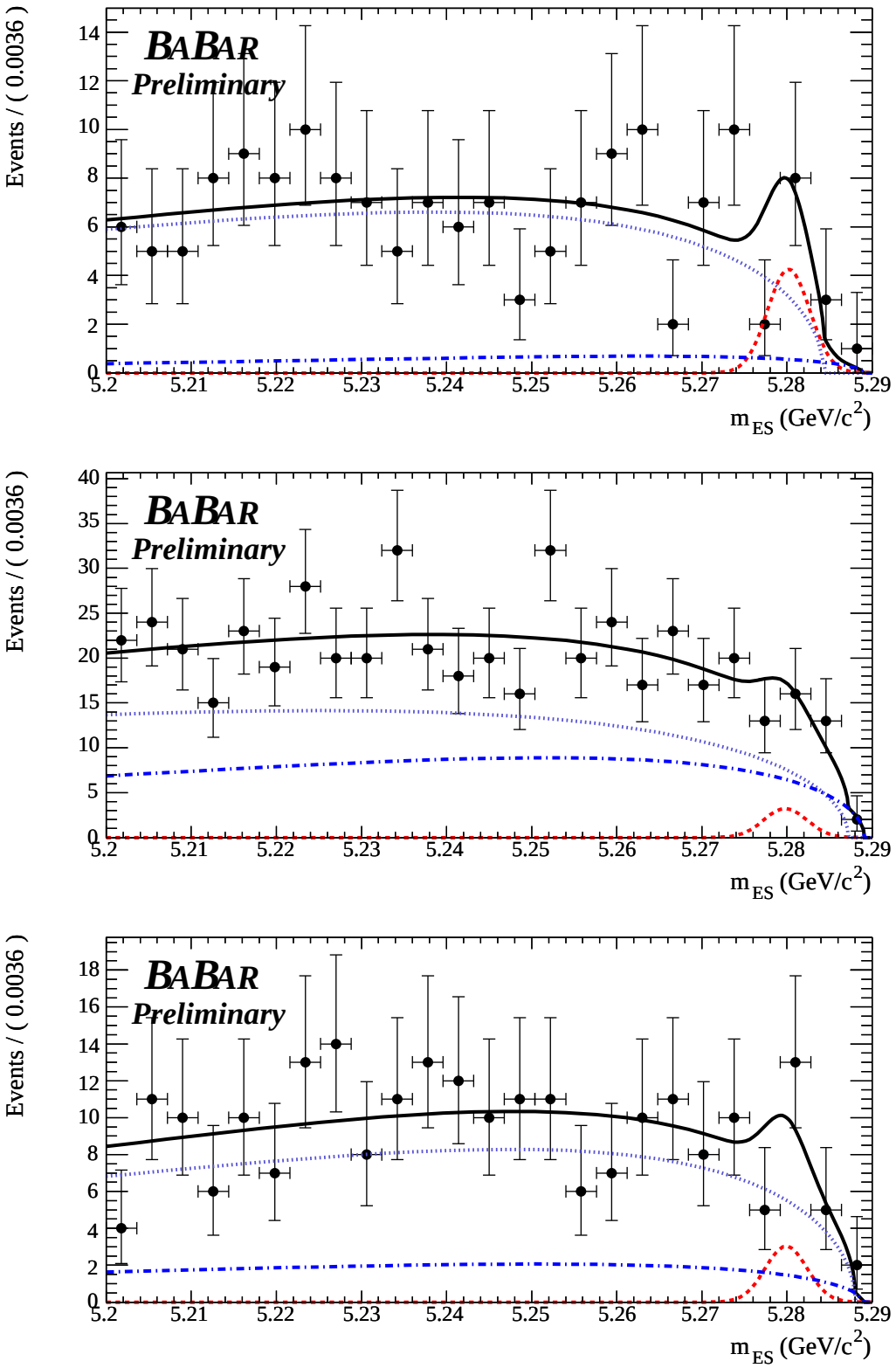

Figure 5.38: [Data - opposite sign] Projections of the fit over the variables m_{ES} after a cut on Fisher is applied (Fisher$>$ 0.5 for $K\pi$, Fisher$>$ 0.7 for $K\pi\pi^0$ and Fisher$>$ 1. for $K\pi\pi\pi$), to visually enhance the signal, for $K\pi$ (top), $K\pi\pi^0$ (middle) and $K\pi\pi\pi$ (bottom) opposite sign events. The points with error bars are data, and the superimposed curves are the result of the fit procedure as described in sec. 5.4. The dashed, dotted and dash-dotted lines represent the signal, continuum background and $B\bar{B}$ background contributions respectively.

5.5.2 Likelihood scan for R_{ADS}

In order not to depend on any Gaussian assumption, a likelihood scan with respect to the variable R_{ADS} has been performed: R_{ADS} is fixed to different values in a reasonable interval and for each value the fit is repeated letting all the other floating parameters free to vary. Each time the fit returns the likelihood value. Fig. 5.39 shows the scan of the $-\Delta ln\mathcal{L}$ (where the difference is calculated with respect to the value obtained when R_{ADS} is left floating) and of the likelihood itself, for the three channels.

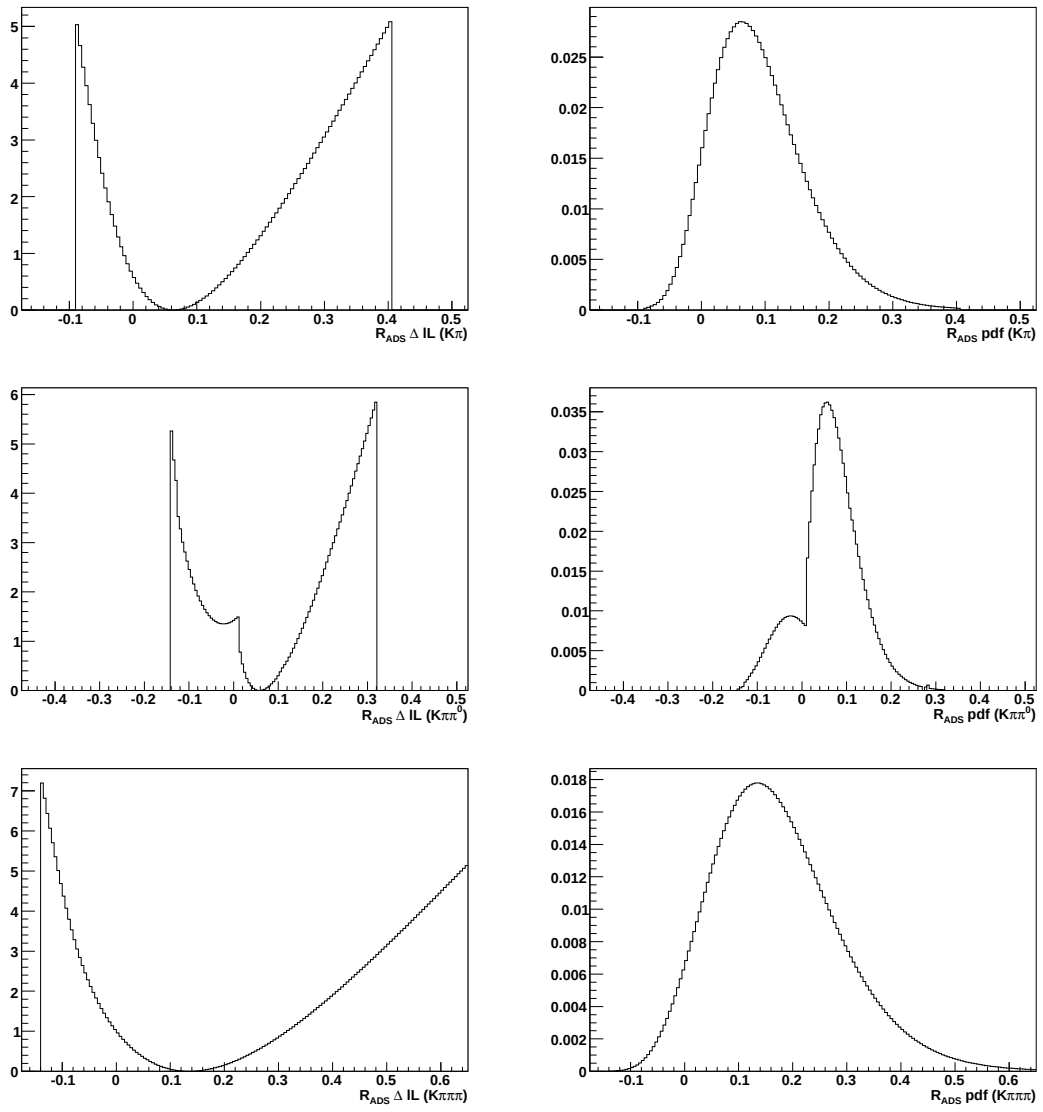

Figure 5.39: [Data - likelihood scan] Scan of $-\Delta ln\mathcal{L}$ (left plots) and of the likelihood $\mathcal{L}$ (right plots) for $K\pi$ (up), $K\pi\pi^0$ (middle) and $K\pi\pi\pi$ (bottom).

The second minimum for the likelihood of $R_{ADS}(K\pi\pi^0)$ has been investigated and found to be due to a fluctuation in the number of opposite-sign events for negative values. Since

it is well above the principal one, it is not particularly worrying.

5.5.3 Comparison with the expected sensitivity

The errors we would expect on R_{ADS} from toy Monte Carlo studies (see sec. 5.4.3), for the central values we find on data are summarized in Tab. 5.20. All the values obtained on data are within less than 1.5 standard deviation from toy Monte Carlo expectations.

Parameter	expected range	value on data
$R_{ADS}^{K\pi}$ negative error	0.044 ± 0.010	0.059
$R_{ADS}^{K\pi}$ positive error	0.055 ± 0.011	0.067
$R_{ADS}^{K\pi\pi^0}$ negative error	0.048 ± 0.010	0.037
$R_{ADS}^{K\pi\pi^0}$ positive error	0.056 ± 0.010	0.046
$R_{ADS}^{K\pi\pi\pi}$ negative error	0.139 ± 0.030	0.098
$R_{ADS}^{K\pi\pi\pi}$ positive error	0.160 ± 0.038	0.107

Table 5.20: Expected negative and positive errors on R_{ADS} ratios from toy Monte Carlo studies are compared with the errors found in the fit on data.

5.5.4 Systematic uncertainties on the R_{ADS} ratios

The systematic uncertainties on the fitted values for R_{ADS} can arise from the following sources:

- m_{ES} and $Fisher$.
  All the parameters fixed in the fit are varied by $\pm 1\sigma$ and the fit is repeated. The corresponding variation on the central value of R_{ADS} is taken as systematic uncertainty.

- Peaking background assumptions.
  The number of peaking background events is evaluated on simulated events and on M_{D^0} sidebands data trough a fit to the m_{ES} distribution. The different sources of peaking backgrounds are found to be compatible with zero within the errors and fixed to zero in the fit. The fit is performed letting the number of peaking events vary within its error and the corresponding variation of the central value of R_{ADS} is taken as systematic uncertainty.

- Crossfeed between same sign and opposite sign events.
  In sec. 5.2.7, the efficiency of the cross-feed between opposite sign and same sign events, ϵ^{CF} has been evaluated for the three D channels. The associated systematic uncertainty on R_{ADS} is calculated according to the following expression:

$$R_{ADS} = \frac{N^{OppS} \pm N^{SameS}\epsilon^{CF}}{N^{SameS} \pm N^{OppS}\epsilon^{CF}} \sim \frac{N^{OppS}}{N^{SameS}} \pm \epsilon^{CF},$$

  where the approximation results from neglecting the effect of opposite sign events wrongly reconstructed as same sign events.

- Efficiency ratio for same sign and opposite sign events.
  As explained in section 5.2.8, it has been verified that the efficiencies for same sign and opposite sign events are the same within a precision of 3% for $K\pi\pi^0$. We hence assign as systematic error on $R_{ADS}^{K\pi\pi^0}$ the variation of $R_{ADS}^{K\pi\pi^0}$ when we fit assuming the efficiencies ratio to be 1.03 and 0.97. For $K\pi\pi\pi$ we evaluated on MC studies that the average variation of the efficiency ratio due to an eventual different Dalitz distribution for CA and DCS decays is around 3%. We assign as systematic error on $R_{ADS}^{K\pi\pi\pi}$ the variation of $R_{ADS}^{K\pi\pi\pi}$ when we fit assuming the efficiencies ratio to be 1.03 and 0.97.

The systematic uncertainties on R_{ADS} are summarized in tabs. 5.21, 5.22 and 5.23. The different contributions are considered to be Gaussian and uncorrelated and for this reason we sum them in quadrature.

Source	systematics on R_{ADS} $\times 10^{-2}$
Sig. PDF parameters	0.19
Cont. PDF parameters	0.32
$B\bar{B}$ PDF parameters	0.57
Peaking bkg	1.70
SS-OS cross-feed	0.04
TOTAL	1.80

Table 5.21: [Data $K\pi$ mode] Summary of systematic uncertainties, evaluated on 423 fb^{-1} $K\pi$ events.

Source	systematics on R_{ADS} $\times 10^{-2}$
Sig. PDF parameters	0.11
Cont. PDF parameters	0.02
$B\bar{B}$ PDF parameters	0.16
$\epsilon_{CA}/\epsilon_{DCS}$	0.17
Peaking bkg	0.87
SS-OS cross-feed	0.05
TOTAL	0.91

Table 5.22: [Data $K\pi\pi^0$ mode] Summary of systematic uncertainties, evaluated on 423 fb^{-1} $K\pi\pi^0$ events.

The systematics on R_{ADS} from the variations of the PDF parameters are also shown in Fig. 5.40.

The likelihood obtained for R_{ADS}, for each channel, is convoluted with a Gaussian of width equivalent to the total systematic uncertainty. Since the measurements for the R_{ADS} ratios are not statistically significant, 95% probability limits are calculated by integrating the likelihoods, starting from $R_{ADS} = 0$, obtaining $R_{ADS}(K\pi) < 0.244$, $R_{ADS}(K\pi\pi^0) < 0.181$

Source	systematics on R_{ADS} $\times 10^{-2}$
Sig. PDF parameters	0.82
Cont. PDF parameters	0.29
BB PDF parameters	1.48
$\epsilon_{CA}/\epsilon_{DCS}$	0.39
Peaking bkg	1.40
SS-OS cross-feed	0.02
TOTAL	2.20

Table 5.23: [Data $K\pi\pi\pi$ mode] Summary of systematic uncertainties, evaluated on 423 fb^{-1} $K\pi\pi\pi$ events.

and $R_{ADS}(K\pi\pi\pi) < 0.391$ at 95% probability. The 68% probability regions are also calculated, limited by the two values of R_{ADS} for which $\mathcal{L} = \mathcal{L}_{min}$ and $68\% = \int_{\mathcal{L}(R_{ADS})>\mathcal{L}_{min}} \mathcal{L}(R_{ADS})dR_{ADS}$, obtaining:

$$\begin{aligned} R^{K\pi}_{ADS} &= 0.067^{+0.071}_{-0.057}; \\ R^{K\pi\pi^0}_{ADS} &= 0.060^{+0.055}_{-0.038}; \\ R^{K\pi\pi\pi}_{ADS} &= 0.137^{+0.114}_{-0.097}. \end{aligned} \tag{5.43}$$

The likelihood distributions, and the 68% and 95% probability regions, are shown in Fig. 5.41.

The results for $R^{K\pi}_{ADS}$, $R^{K\pi\pi^0}_{ADS}$ and $R^{K\pi\pi\pi}_{ADS}$, are summarized in Fig. 5.42. The total number of opposite sign signal events in the three channels, as obtained from the fit, is $N^{OppS}_{sig} = 24.4^{+13.7}_{-10.9}$. Although strictly speaking making an average of the three R_{ADS} has no meaning, since they are different observables, it is useful to have an idea of the probability with which we exclude zero from the combination of the three measurements. Making this average corresponds to neglect differences in the r_D parameters and in the strong phases between the three channels. The statistical average of the three R_{ADS} measurements, including the systematic errors, is $0.078^{+0.037}_{-0.035}$, indicating a signal with a 2.2 σ significance.

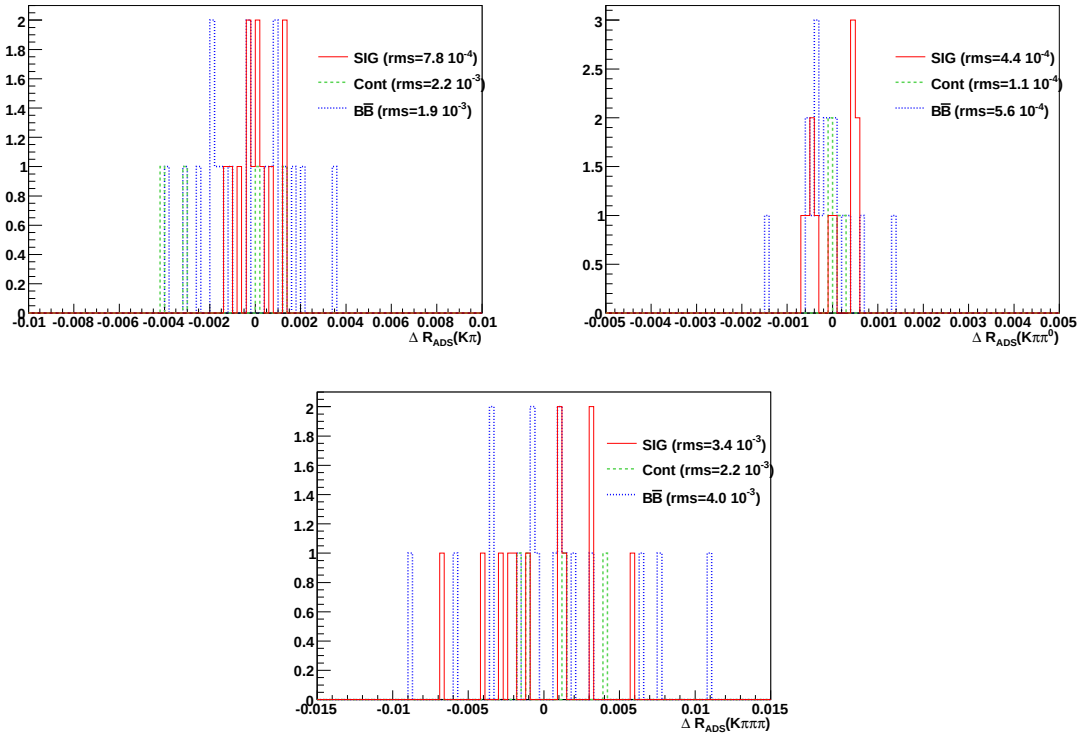

Figure 5.40: Variation of the fitted value of R_{ADS}, for the three D decay modes, when varying by $\pm 1\sigma$ the m_{ES} and Fisher pdf parameters that are fixed in the fit, for signal, continuum background and $B\bar{B}$ background components. In the legenda, we also quote the resolution (rms) of the distributions.

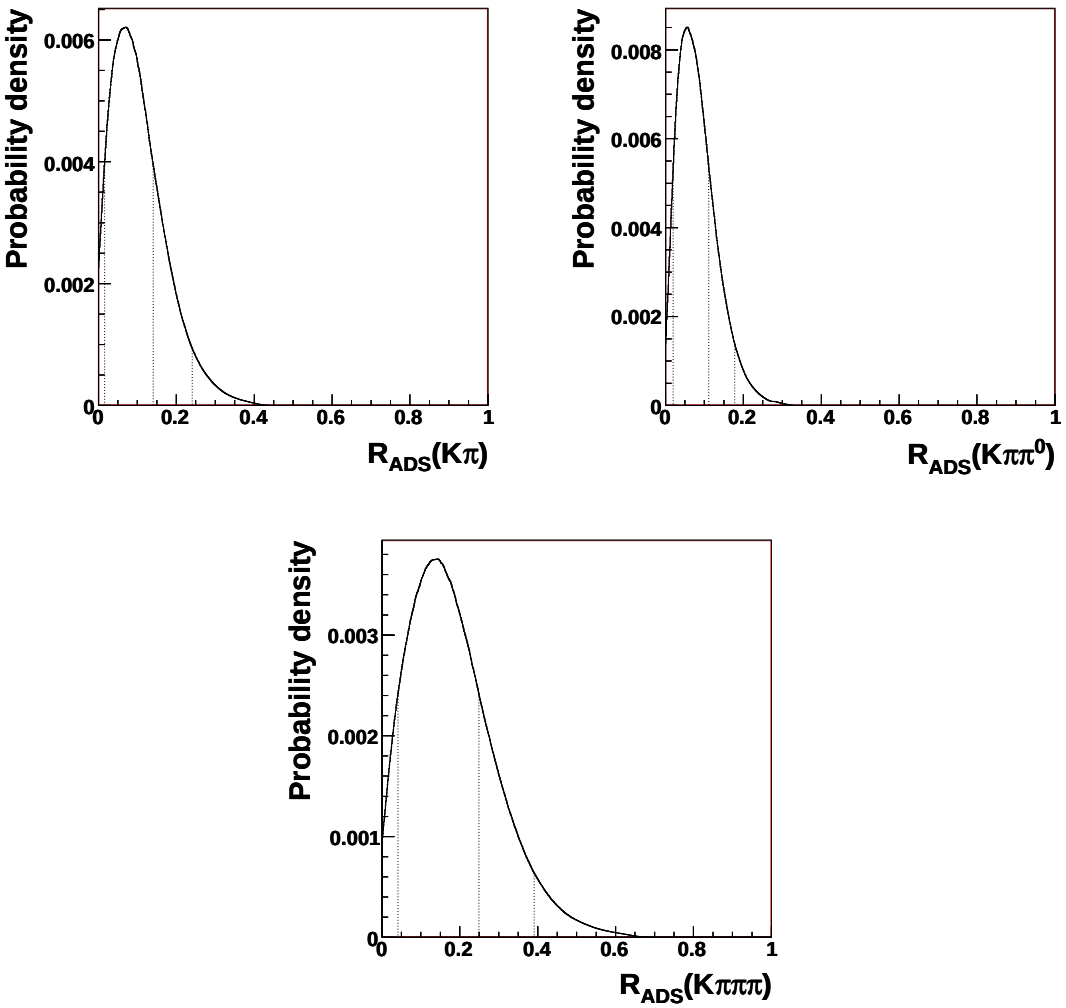

Figure 5.41: [Data - likelihood scan] Scan of $-\Delta ln\mathcal{L}$ (left plots) and of the likelihood $\mathcal{L}$ (right plots) for $K\pi$ (up), $K\pi\pi^0$ (middle) and $K\pi\pi\pi$ (bottom).

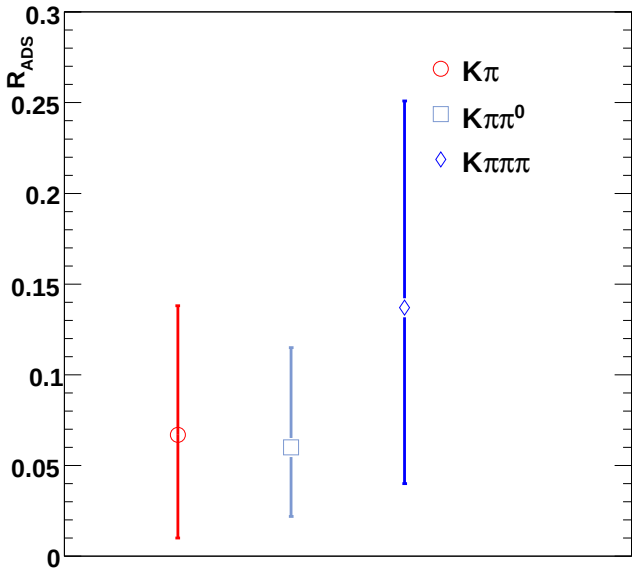

Figure 5.42: 68% probability regions for R_{ADS} for the three channels, including statistical and systematic errors.

5.6 Extraction of r_S parameter

In this chapter the procedure for the extraction of r_S from the measurements of the R_{ADS} ratios is presented. This procedure is first validated on results obtained from toy Monte Carlo (shown in sec. 5.6.1) and finally applied to the results obtained on data (sec. 5.6.2).

The outcome of the analysis are the likelihood distributions for the variables $R_{ADS}^{K\pi}$, $R_{ADS}^{K\pi\pi^0}$ and $R_{ADS}^{K\pi\pi\pi}$. To convert the results on the R_{ADS} ratios into probability regions for r_S, a bayesian approach is used. The ratios R_{ADS} for the three channels can be expressed as (see equation 5.33):

$$\begin{aligned}
R_{ADS}^{K\pi} &= r_S^2 + r_{DK\pi}^2 + 2kr_S r_{DK\pi}\cos(\delta_S + \delta_{DK\pi})\cos\gamma; \\
R_{ADS}^{K\pi\pi^0} &= r_S^2 + r_{DK\pi\pi^0}^2 + 2kr_S k_{DK\pi\pi^0} r_{DK\pi\pi^0}\cos(\delta_S^{DK\pi\pi^0} + \delta_S)\cos\gamma; \\
R_{ADS}^{K3\pi} &= r_S^2 + r_{DK3\pi}^2 + 2kr_S k_{DK3\pi} r_{DK3\pi}\cos(\delta_S^{DK3\pi} + \delta_S)\cos\gamma.
\end{aligned} \tag{5.44}$$

The three observables depend on quantities that are channel-dependent, but they all depend on r_S, γ and δ_S and k. Hence, a constraint on r_S from the combination of the three measurements can be derived.

The a-posteriori pdf of r_S from an R_{ADS} measurement is defined as

$$\mathcal{L}(r_S) = \frac{\int p(r_S,\gamma,\delta_S,k,\vec{\xi})\mathcal{L}(R_{ADS}(r_S,\gamma,\delta_S,k,\vec{\xi}))d\gamma d\delta_S dk d\vec{\xi}}{\int p(r_S,\gamma,\delta_S,k,\vec{\xi})\mathcal{L}(R_{ADS}(r_S,\gamma,\delta_S,k,\vec{\xi}))d\gamma d\delta_S dk d\vec{\xi} dr_S} \tag{5.45}$$

$$\tag{5.46}$$

With $\vec{\xi} = \{r_D, \delta_D\}$ for the two-body case and $\xi = \{r_D, \delta_S^D, k_D\}$ for the multi-body cases. Here $p(r_S,\gamma,\delta_S,k,\vec{\xi})$ is the a-priori probability for the quantities $r_S,\gamma,\delta_S,k,\vec{\xi}$, which are considered uncorrelated. The ratio r_S is extracted from a flat distribution in $[0,1]$ and k_D is extracted from a flat distribution in $[0,1]$ for $K\pi\pi^0$. The a-priori distribution for $\delta_S^{DK\pi}$ is a Gaussian following the measurement presented in [55]. The parameters $\delta_S^{DK\pi\pi\pi}$ and $k_{DK\pi\pi\pi}$ are extracted following the measurement presented in [56]. All the remaining phases are sampled form a flat distribution in $[0,2\pi]$ range. All the remaining phases are extracted form a flat distribution in $[0,2\pi]$ range. The a-priori probabilities for the r_D ratios are Gaussian distributions with mean and standard deviation taken from the measurements and the a-priori distribution for k is Gaussian with mean and standard deviation equal to 0.95 and 0.03 respectively (see sec. 2.6.2). Technically, the histogram of $\mathcal{L}$ as a function of r_S is filled using a toy MC procedure:

- large number of experiments is generated by extracting $r_S,\gamma,\delta_S,k,\vec{\xi}$ within their ranges.
- in each experiment the value of R_{ADS} is computed according to eqs. 5.44.
- for each experiment a weight $\mathcal{L}(R_{ADS})$ is computed, where $\mathcal{L}(R_{ADS})$ is calculated from the experimental likelihood obtained for R_{ADS}, after convolution with the systemtic errors. An entry is added, to the content of the appropriate bin for the extracted value of r_S, with weight $p(r_S,\gamma,\delta_S,k,\vec{\xi})\mathcal{L}(R_{ADS})$.
- the histogram is normalized to unit area.

The 68% probability region is limited by the two values of r_S for which $\mathcal{L} = l_{min}$ where

$$68\% = \int_{\mathcal{L}>l_{min}} \mathcal{L}(r_S) dr_S \tag{5.47}$$

The interval is symmetrized (which means that the quoted central value is not the maximum of the likelihood).

5.6.1 Validation of r_S extraction procedure using toy Monte Carlo

The extraction procedure has been tested on toy MC results, assuming the likelihood for the three R_{ADS} to be described by bifurcated Gaussians, for simplicity. The procedure to extract r_S, as presented in 5.6 has been followed, starting from the measurements:

$$\begin{aligned} R_{ADS}^{K\pi} &= 0.090^{+0.079}_{-0.065} \\ R_{ADS}^{K\pi\pi^0} &= 0.090^{+0.088}_{-0.076} \\ R_{ADS}^{K3\pi} &= 0.090^{+0.110}_{-0.090} \end{aligned}$$

where the central values for the three ratios are calculated assuming $r_S = 0.3$ and $r_D = 0$ and the negative and positive errors are taken from the toy MC studies (see Fig. 5.25, 5.26 and 5.27). With these values, the extraction procedure for r_S leads to the result shown in Fig. 5.43, and corresponding to the 68% probability region $r_S = 0.29^{+0.08}_{-0.011}$, which is consistent with the generated value. The distribution obtained for r_S is not Gaussian, in particular the

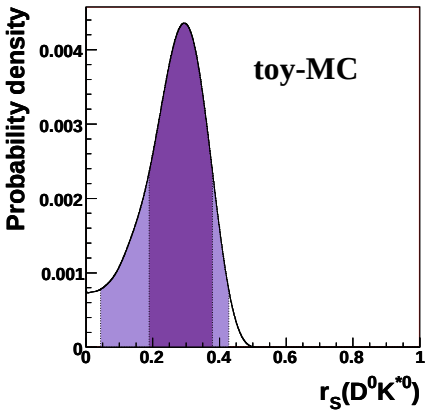

Figure 5.43: [Toy Monte Carlo] Constraint on r_S from fake $R_{ADS}^{K\pi}$, $R_{ADS}^{K\pi\pi^0}$ and $R_{ADS}^{K3\pi}$ measurements. The parameter r_S is assumed to be 0.3 and the (asymmetric) errors for the ratios R_{ADS} are taken from toy MC studies. The 68% and 95 % probability regions are shown in light and dark colors respectively.

tail observed for low r_S results from the functional dependence $R_{ADS} \sim r_S^2$ and accounts for the fact that we cannot exclude zero with a higher probability for r_S than for the combined result for R_{ADS}.

5.6.2 Extraction of r_S on real data

The 68% probability intervals obtained, on a sample of 423 fb^{-1} data and after having included systematics effects, for the R_{ADS} ratios are:

$$\begin{aligned} R_{ADS}^{K\pi} &= 0.067^{+0.071}_{-0.057}; \\ R_{ADS}^{K\pi\pi^0} &= 0.060^{+0.055}_{-0.038}; \\ R_{ADS}^{K\pi\pi\pi} &= 0.137^{+0.114}_{-0.097}. \end{aligned} \tag{5.48}$$

Following the procedure explained in sec.5.6, the information on r_S from the three R_{ADS} measurement has been extracted. The results for r_S, separately from the three channels, are the following:

$$\begin{aligned} r_S^{K\pi} &= 0.250^{+0.114}_{-0.165},\ r_S \in [0.0, 0.451] \text{ at } 95\%\text{probability}. \\ r_S^{K\pi\pi^0} &= 0.238^{+0.106}_{-0.104},\ r_S \in [0.0, 0.394] \text{ at } 95\%\text{probability}. \\ r_S^{K\pi\pi\pi} &= 0.363^{+0.149}_{-0.190},\ r_S \in [0.0, 0.579] \text{ at } 95\%\text{probability}. \end{aligned} \tag{5.49}$$

and from the combination of all the three channels:

$$\begin{aligned} &r_S = 0.26^{+0.077}_{-0.088}, \\ &r_S \in [0.05, 0.396] \text{ at } 95\%\text{probability}. \end{aligned} \tag{5.50}$$

The probability density functions for r_S from the single measurements and from their combination are shown in Fig. 5.44. The results for r_S from the three channels separately and from their combination, are shown in Fig. 5.45.

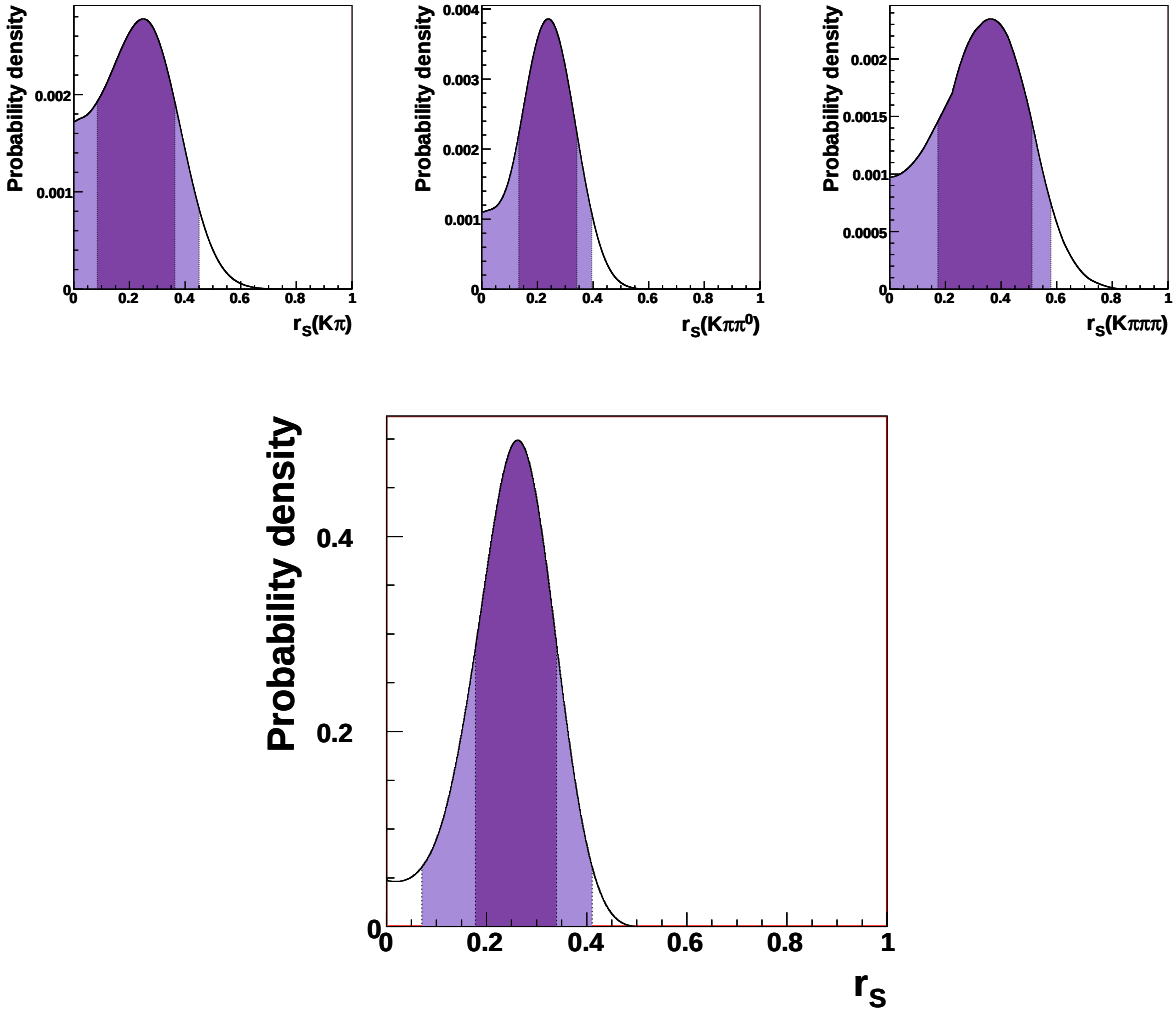

Figure 5.44: [Data] Results for r_S from the measurement of R_{ADS} in the three modes (upper plots) and from their combination (lower plot).

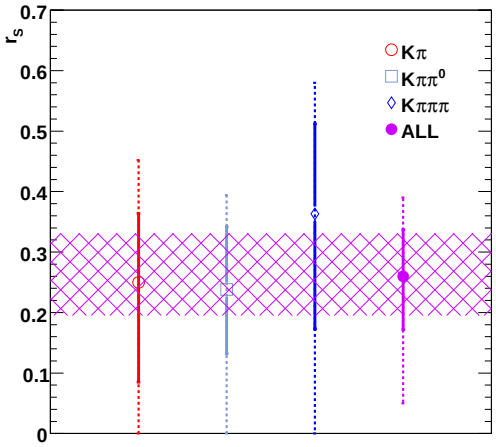

Figure 5.45: [Data] 68% (solid line) and 95% (dotted line) probability regions obtained for r_S from the measurement of R_{ADS} in the three modes and from their combination.

Chapter 6

Dalitz analysis of $B^0 \to D^0 K^{*0}$ decay channel

In this chapter we present the analysis of $B^0 \to \bar{D}^0(D^0)K^{*0}$ with $K^{*0} \to K^-\pi^+$ (and $B^0 \to D^0(\bar{D}^0)K^{*0}$ with $\bar{K}^{*0} \to K^+\pi^-$), where the neutral D is reconstructed in the $K_S\pi^+\pi^-$ *CP* eigenstate. The decay chain is analyzed with the Dalitz technique, allowing for the extraction of r_S, δ_S and γ parameters. We use a data set of 353 fb^{-1} (371 10^6 $B\bar{B}$ pairs) collected with the *BABAR* detector at the $\Upsilon(4S)$ center of mass energy.

The Dalitz method [32], presented in sec. 2.2.3, aims to measure γ from the $B \to DK$ decays with the D decaying to multi-body *CP* eigenstate final states. As shown in sec. 2.3 and 2.5, the Dalitz method is the one with highest sensitivity to the angle γ.

The interest of this measurement, as explained in sec. 2.6, is the fact that the ratio between the $b \to u$ and $b \to c$ amplitudes of the neutral B decays is expected to be higher than the one for charged B. The results shown in chapter 5 confirm this expectation.

6.1 Analysis overview: Dalitz method at work

For the case of $B^0 \to D^0 K^{*0}$ decays, as discussed in sec. 2.6.1, the natural width of the K^{*0} being not small ($\sim$50 MeV), the interference with other $B^0 \to \overline{D}^0(K\pi)^0_{\rm non-K^*}$ processes may not be negligible. For this reason, following the formalism suggested in [33], the effective quantities r_S, k and δ_S are introduced. Following this formalism, it has been shown in sec. 2.6.1 that the expression for the partial decay rate is (see eq. 2.28):

$$d\Gamma(\overline{B}^0 \to D[\to f]X^0_S) \propto A_f^2 + r_S^2 A_{\bar{f}}^2 + 2r_S k \mathcal{R}e\left(A_f A_{\bar{f}} e^{i\delta_D} e^{i\delta_S+\gamma}\right);$$

where $\delta_D = \delta_{\bar{f}} - \delta_f$. In the case of D decaying into $K_S\pi\pi$ final states,

$$A_f e^{i\delta_f} = f(m_-^2, m_+^2);$$
$$A_{\bar{f}} e^{i\delta_{\bar{f}}} = f(m_+^2, m_-^2);$$

where m_- and m_+ are the invariant masses of the systems (K_S, π^-) and (K_S, π^+) respectively. The amplitude for the process $\bar{B}^0(B^0) \to D[\to K^0_S\pi^-\pi^+]\bar{X}^0_S(X^0_S)$ can be written as follows:

$$A(\bar{B}^0(B^0) \to D[\to K^0_S\pi^-\pi^+]\bar{X}^0_S(X^0_S)) = A_c(p)e^{i\delta_c(p)} f(m_\mp^2, m_\pm^2) + A_u(p)e^{i\delta_u(p)\mp\gamma} f(m_\pm^2, m_\mp^2)\,, \tag{6.1}$$

where A_c, A_u, δ_c and δ_u vary as a function of the point p over the $B^0 \to D^0 K^{*0}$ Dalitz plane as explained in sec. 2.6.1. The rate is expressed by:

$$\begin{aligned}
&\Gamma(\bar{B}^0(B^0) \to D[\to K^0_S\pi^-\pi^+]\bar{X}^0_S(X^0_S)) \propto \\
&|f_\mp|^2 + r_S^2|f_\pm|^2 + 2kr_S\left\{\cos(\delta_S \mp \gamma)Re[f_\mp f_\pm^*] + \sin(\delta_S \mp \gamma)Im[f_\mp f_\pm^*]\right\} \equiv \\
&|f_\mp|^2 + r_S^2|f_\pm|^2 + 2kr_S|f_\mp||f_\pm|\cos(\delta_S + \delta_D(m^2_\mp, m^2_\pm) \mp \gamma)\,,
\end{aligned} \tag{6.2}$$

where $\delta_D(m^2_\mp, m^2_\pm) = \delta_{\bar{f}}(m^2_\mp, m^2_\pm) - \delta_f(m^2_\mp, m^2_\pm)$ is the strong phase difference between $f(m^2_\pm, m^2_\mp)$ and $f(m^2_\mp, m^2_\pm)$ and r_S, k and δ_S are defined as following (see eqs. **??** and 2.27):

$$\begin{aligned}
r_S^2 &= \frac{\Gamma(\overline{B}^0 \to \overline{D}^0 X^0_S)}{\Gamma(\overline{B}^0 \to D^0 X^0_S)} = \frac{\int dp\ |A_u^2(p)|}{\int dp\ |A_c^2(p)|}\,; \\
ke^{i\delta_S} &= \frac{\int dp\ A_c(p)A_u(p)e^{i\delta(p)}}{\sqrt{\int dp\ |A_c^2(p)|\ \int dp\ |A_u^2(p)|}}\,.
\end{aligned}$$

In the following we use the simplified notation $f_\pm \equiv f(m^2_\pm, m^2_\mp)$ and $f_\mp \equiv f(m^2_\mp, m^2_\pm)$.

The amplitude for the neutral D decays into $K_S\pi^+\pi^-$ final states is used as an input in this analysis, and the results obtained from the Dalitz *BABAR* analysis of charged B decays [59] have been used. In sec. 6.1.1, the technique for extracting this amplitude used in *BABAR* is briefly described, in the study presented in this thesis no original work on the subject has been done.

6.1.1 The Dalitz model for neutral D decays into $K_S\pi^+\pi^-$ final state

The $D^0 \to K_S\pi\pi$ decay amplitude is determined in *BABAR* from a Dalitz plot analysis of D^0 mesons from $D^{*+} \to D^0\pi^+$ decays produced in $e^+e^- \to c\bar{c}$ events. The charge of the low momentum π^+ from the D^{*+} decay identifies the flavor of the D^0. The signal purity for this analysis ($\pm 2\sigma$ cutoff on M_D, where σ stands for the M_D resolution) is of 97.7%, with about 500000 selected candidates.

The P- and D-waves of the $D^0 \to K_S\pi\pi$ decay amplitude are described using a total of 6 resonances leading to 8 two-body decay amplitudes: the Cabibbo allowed (CA) $K^*(892)^-$, $K^*(1680)^-$, $K_2^*(1430)^-$, the doubly-Cabibbo suppressed (DCS) $K^*(892)^+$, $K_2^*(1430)^+$, and the *CP* eigenstates $\rho(770)^0$, $\omega(782)$, and $f_2(1270)$. The contributions from these resonances are parametrized using the isobar model, as described in sec. 2.2.3. The dynamics for the $\pi\pi$ S-wave in $D^0 \to K_S\pi\pi$ decays [60] is caracterized by the overlap of several broad scalar resonances. While these contributions were parametrized with the isobar model (see for example the old *BABAR* Dalitz analysis publication [61]) it has been found that they are better described through the use of a K-matrix formalism [62] with the P-vector approximation [63]. Thus the Dalitz plot amplitude $f(m)$ (where m indicates the Dalitz plane point $m = (m^2_\pm, m^2_\mp)$) can be written as follows:

$$f(m) = F_1(s) + \sum_{r \neq (\pi\pi)_{L=0}} a_r e^{i\phi_r}\mathcal{A}_r(m) + a_{\rm NR}e^{i\phi_{\rm NR}}, \tag{6.3}$$

where $F_1(s)$ is the contribution of $\pi\pi$ S-wave states written in terms of the K-matrix formalism,

$$F_1(s) = \sum_j [I - iK(s)\rho(s)]^{-1}_{1j} P_j(s). \tag{6.4}$$

The parameter $s = m_0^2$ is the squared invariant mass of the $\pi^+\pi^-$ system, I is the identity matrix, K is the matrix describing the S-wave scattering process, ρ is the phase-space matrix, and P is the initial production vector (P-vector). The parametrization and parameter values for the K-matrix used in the *BABAR* analysis are taken from [72], where they have been obtained from a global analysis of the available $\pi\pi$ scattering data from threshold up to 1900 MeV/c^2 [72].

6.2 Selection and background caracterization

6.2.1 Selection criteria and background composition

The selection studies are based on simulated events for the signal modes and for the different backgrounds and, whenever possible, directly on data. The agreement of the relevant variables distribution between data and simulation has also been checked. The data and simulated samples used in this analysis are summarized in Tab. 6.1.

Sample	Events	$\mathcal{L}_{eq}$ (fb^{-1})
$B\overline{B}^0$	385M	733
B^+B^-	394M	751
$c\bar{c}$	267M	206
$u\bar{u}$,dd,$s\bar{s}$	324M	155
Signal	185k	$304{\cdot}10^3$
$D^0\rho^0$ MC	100k	$16 \cdot 10^3$
$D^0K^*(D^0 \to 4\pi)$ MC	10k	$48 \cdot 10^3$
Data (On-peak)		353
Data (Off-peak)		37

Table 6.1: Data and MC samples used in the analysis in terms of number of events and of equivalent integrated luminosity ($\mathcal{L}_{eq}$). The integrated luminosity for data is also given.

The assumptions for the branching fractions and cross sections used to get the values of Tab. 6.1 are summarized in Tab. 6.2. These values have been used to rescale the signal and the different background components to the integrated luminosity of data.

We reconstruct $B^0 \to \bar{D}^0(D^0)K^{*0}$ events with $K^{*0} \to K^+\pi^-$, $D^0 \to K_S\pi^+\pi^-$ and $K_S \to \pi^+\pi^-$. For this analysis, apart from the K^{*0} (and $\bar{K}^{*0}$) selection, which has been optimized and presented in sec. 4.6, we have applied standard selection criteria, also used in similar *BABAR* analyses. The K_S from the D^0 is reconstructed from pairs of oppositely charged pions and their invariant mass is required to be within $\pm$ 7 MeV/c^2 of the nominal K_S mass [8].

Quantity	Value
$Br(B^0 \to \overline{D}^0 K^{*0})$	$(5.3 \pm 0.8) \cdot 10^{-5}$ [50]
$Br(B^0 \to \overline{D}^0 \rho^0)$	$(2.3 \pm 0.9) \cdot 10^{-4}$ [50]
$Br(D^0 \to \bar{K}^0 \pi^- \pi^+)$	0.0597 ± 0.0035 [50]
$Br(D^0 \to \pi^- \pi^+ \pi^- \pi^+)$	$7.3 \pm 0.5 \cdot 10^{-3}$ [50]
$Br(\bar{K}^0 \to K_S)$	1/2
$Br(K_S \to \pi^+ \pi^-)$	0.6895 ± 0.0014 [50]

Table 6.2: Branching ratios and cross sections used to get the values of Tab. 6.1. These values have been used to normalize the signal and the different background components.

The K_S candidates are also requested to satisfy the condition $\cos\alpha_{K_S}(D^0) > 0.997$ where $\alpha_{K_S}(D^0)$ is the angle between the K_S line of flight (line between the D^0 vertex and the K_S vertex) and its momentum (reconstructed with the two pions momentum). This cut is particularly helpful in removing the $D^0 \to 4\pi$ background, as explained in sec. 6.2.5.

The D^0 is selected by combining K_S candidates with two oppositely charged pions and requiring its invariant mass to be within $\pm$ 11 MeV/c^2 of the nominal mass. Charged kaon identification, based on Cerenkov angle and dE/dx measurements, is required for the charged kaon produced in K^{*0} and $\bar{K}^{*0}$ decays. The D^0 and K^{*0} vertex fits are requested to have converged ("$P[\chi^2(D^0)_{vtx}, ndof] > 0$" and "$P[\chi^2(K^{*0})_{vtx}, ndof] > 0$" in the following). In order to suppress combinatorial background, the probability of the B vertex $\chi^2_{vtx}(B)$ per number of degree of freedom ($ndof$) is required to be greater than 0.001, $P[\chi^2(B)_{vtx}, ndof] > 0.001$. The absolute value of ΔE is required to be smaller than 25 MeV and the absolute value of the cosine of the B polar angle in the center of mass frame, $\cos\theta_B$, to be less than 0.9.

In summary, the applied selection criteria are:

- $|m_{K_S} - m_{K_S}(nominal)| < 7$ MeV/c^2
- $|m_{D^0} - m_{D^0}(nominal)| < 11$ MeV/c^2
- $P(\chi^2, D^0) > 0$, $P(\chi^2, K^*) > 0$
- $P(\chi^2, B) > 0.001$
- $\cos\alpha_{K_S} > 0.997$
- $|m_{K^*} - m_{K^*}(nominal)| < 48$ MeV/c^2
- $|\cos\theta_{Hel}| > 0.3$
- $K^\pm$ from $K^{*0}/\bar{K}^{*0}$: KLHTight
- $|\cos\theta^*_B| < 0.9$
- $|\Delta E| < 25$ MeV

- $m_{ES} > 5.2$ MeV/c^2
- $|\Delta t| < 20$ ps
- $|\Delta t_{err}| < 2.5$ ps

The selection efficiency for signal, evaluated on simulated events, is $\epsilon_{\rm sig} = (10.8 \pm 0.5)\%$. In Tab. 6.3 we list the number of expected events, on 353fb^{-1}, for signal and different background components. The significance of the signal in the final signal region $m_{ES} > 5.27\,\mathrm{GeV}/c^2$ is $S/\sqrt{S+B} = 1.7$.

Sample	Signal	$B^0\overline{B^0}$	B^+B^-	$c\overline{c}$	$u\overline{u}, d\overline{d}, s\overline{s}$
Final Selection	35	46	80	1589	671
$+m_{ES} > 5.27\,\mathrm{GeV}/c^2$	35	11	19	264	90

Table 6.3: Number of expected signal and background events, evaluated on simulated events, rescaled to an integrated luminosity of 353 fb^{-1}.

6.2.2 Efficiency variations over the Dalitz plot for signal events

The Dalitz model presented in sec. 6.1.1 has to be convoluted with the theoretical phase space distribution, namely $F(m) = f(m) \otimes PS^{theo}$. To account for possible variations of the efficiency across the Dalitz plot, the Dalitz distribution $F(m)$ we use in the final fit to extract γ, δ and r_S is:

$$F(m) = f(m) \otimes PS^{\rm theo} \frac{PS^{\rm after\ cuts}}{PS^{\rm theo}}. \tag{6.5}$$

As said before, the simulated signal events have been generated using a phase space model for the $D^0 \to K_S\pi^+\pi^-$ decay. Thus the distribution of $PS^{\rm after\ cuts}$ can be obtained using signal simulated events, and performing an unbinned fit over the Dalitz plane. The function used in this fit is a third order polynomial in two dimensions (where the variables x and y in this case are the squared invariant masses $x = m_+^2$ and $y = m_-^2$), expressed by:

$$P(x,y) = PS^{\rm after\ cuts} = 1 + a_1\,(x+y) + a_2\,(x^2+y^2+xy) + a_3\,(x^3+y^3+x^2y+xy^2)\ . \tag{6.6}$$

The parameterization has been symmetrized for $x = m_+^2$ and $y = m_-^2$. Fig. 6.1 shows the m_+^2 and m_-^2 projections for signal simulated events. The resulting coefficients from the fit are given in Tab. 6.4.

6.2.3 Background containing real neutral D mesons

The background events have been divided in two classes. The events for which the reconstructed neutral D is a real D that decays to $K_S\pi^+\pi^-$ (denoted "true D^0" in the following) and the rest, namely events not containing a "true D^0". The two classes of events have

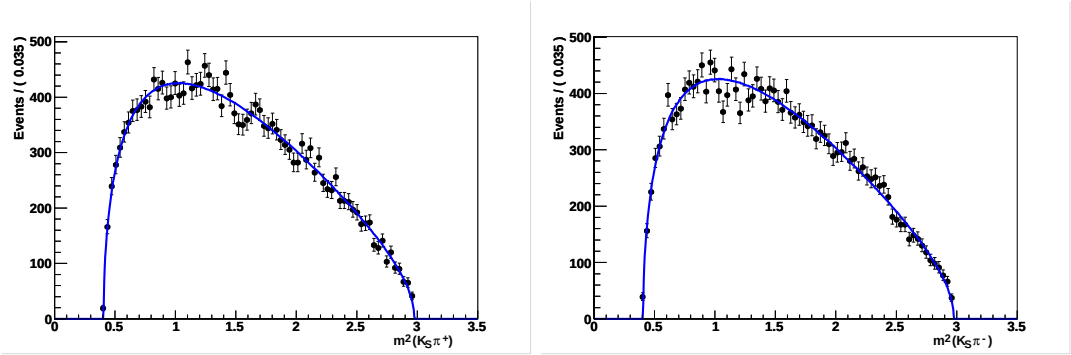

Figure 6.1: Dalitz distribution of signal simulated events (phase space). The curve is the projection on $m^2_{K_S\pi^+}$ (left) and on $m^2_{K_S\pi^-}$ (right) of the result of an unbinned likelihood fit using a third order polynomial (symmetric under $m^2_{K_S\pi^+} \to m^2_{K_S\pi^-}$, see eq. 6.6).

Parameters	a_1	a_2	a_3
Signal	1.30 ± 0.63	-0.34 ± 0.20	0.04 ± 0.03

Table 6.4: The values and the errors of the parameters of the third-order polynomial function, eq. (6.6), obtained from the unbinned likelihood fit to the Dalitz distribution of simulated signal events.

to be treated separately because of their different distribution on the D Dalitz plane. The fractions of true D^0 have been evaluated on simulated events (separately for $B\bar{B}$ and continuum background) and also on data, considering the m_{ES} sidebands. The fraction can be extracted from a fit to the D^0 invariant mass using as pdf, a Gaussian for the D^0 signal and a constant for the background. In these fits the mean of the Gaussian has been fixed to the nominal D^0 mass, $\mu_{D^0} = 1864.1\,\mathrm{MeV}/c^2$. The fractions of events with a true D^0 for $B\bar{B}$ and continuum backgrounds are found compatible within the errors and also compatible with the value found on data. In order to not depend on simulated events, we assume both the values to be equal to the one found on data. The difference will be taken into account in the systematics. The values are reported in Tab. 6.5.

Background events with final states containing $D^0h^+\pi^-$ or $\overline{D}^0h^-\pi^+$, where $h^\pm$ is a candidate $K^\pm$, can mimic $b \to u$ signal events (we recall here that the sign of the $K^\pm$ from the neutral K^* identifies the flavour of the neutral B). The fraction of these $b \to u$-like D^0 events, defined as $R^{WS} = \frac{N_{D^0h^+\pi^-} + N_{\bar{D}^0h^-\pi^+}}{N_{D^0h^-\pi^+} + N_{\bar{D}^0h^-\pi^+} + N_{D^0h^+\pi^-} + N_{\bar{D}^0h^+\pi^-}}$ is evaluated on simulated events and reported in Tab. 6.5.

The Dalitz distribution for true D^0 events is the same as the one used for signal events, described in sec. 6.1.1. The Dalitz distribution for background events with no true D^0 has been studied and parametrized using simulated events, where all the events with true D^0 have been excluded. Both for continuum and $\mathsf{B\bar{B}}$ background a third order polynomial has been used (eq. 6.6) to parametrize the distributions. In this case both for continuum and $B\bar{B}$ background we observe the presence of a $K^*(892)$ resonance in the mass projections. In

Parameters	Fitted values
R_{Cont} (true D^0 fraction in continuum)	0.268 ± 0.037
$R_{\mathsf{B\bar{B}}}$ (true D^0 fraction in $B\bar{B}$)	0.309 ± 0.072
R_{DATA} (true D^0 fraction in data)	0.289 ± 0.028
R^{WS}_{Cont} (D^0 K^+ in continuum)	0.88 ± 0.02
$R^{WS}_{\mathsf{B\bar{B}}}$ (D^0 K^+ in $B\bar{B}$)	0.45 ± 0.12

Table 6.5: Fraction of background events with a "true D^0", estimated from data and simulated events.

order to describe the presence of the K^*, a Breit-Wigner function is added to the polynomial one in the fit to the Dalitz shape and its fraction is fitted. The fraction of resonant events f_{K^*} is also extracted from the fit.

The distributions and fit results are shown in Fig. 6.2, for continuum and $B\bar{B}$ simulated events respectively. The values of the parameters, polynomial terms and fraction of K^{*0} events, are given in Tab. 6.6.

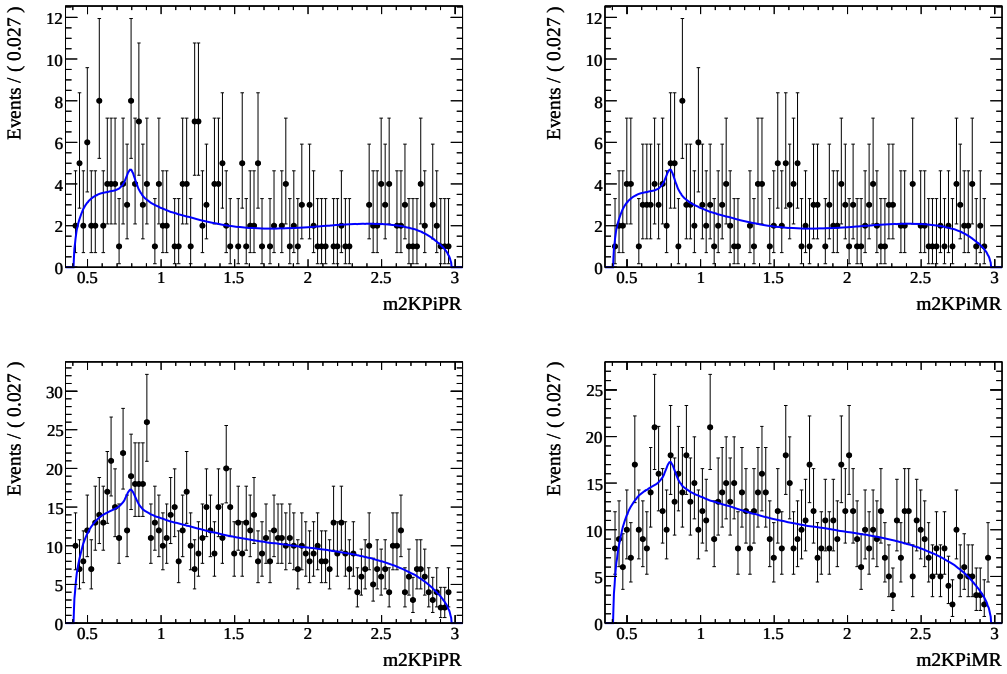

Figure 6.2: Dalitz distribution of simulated events with no true D^0, for $B\bar{B}$ (top) and continuum events (bottom). The curve is the projection on $m_{K_S\pi^+}$ (left) and on $m_{K_S\pi^-}$ (right) of the result of an unbinned likelihood fit using a third order polynomial (symmetric under $m_{K_S\pi^+} \to m_{K_S\pi^-}$) and a Breit-Wigner, to account for the presence of the K^{*0} resonance.

Samples	a_1	a_2	a_3	f_{K^*}
continuum	-0.701 ± 0.010	0.224 ± 0.007	-0.019 ± 0.016	0.029 ± 0.021
BB	-0.538 ± 0.017	0.064 ± 0.005	0.017 ± 0.002	0.062 ± 0.049

Table 6.6: Values and the errors of the parameters of the third-order polynomial function, eq. (6.6), obtained from the unbinned likelihood fit to the Dalitz distribution of background events with no true D^0 ($B\bar{B}$ and continuum separately). The fraction of K^{*0} events, fitted using a Breit-Wigner function is also given in the last column.

6.2.4 Continuum background caracterization and Fisher discriminant

As already discussed, several variables account for the fact that, in the center of mass frame, continuum events have a jet-like spatial distribution, while $B\bar{B}$ events are spherically distributed (see sec. 4.9). In this analysis, the variables $|cos(\theta_{thrust})|$, L_{10} and L_{12}, defined in sec. 4.9, are combined into a Fisher discriminant, that is used in the final maximum likelihood fit. The discriminant has been trained (see sec. 4.9) using simulated signal events and off-resonance data. The distributions for these three variables are shown in Fig. 6.3, for signal MC, off-resonance data and $B\overline{B}$ background simulated events. The distribution of the Fisher discriminant, for signal simulated events and for off-resonance data, is shown in Fig. 6.4 (left). The efficiency of a cut on the Fisher on off-resonance events as a function of the efficiency on simulated signal events is also shown in Fig. 6.4 (right). The expression for the Fisher is:

$$Fisher = 2.484 - 0.7811|cos(\theta_{thrust})| + 0.1884L_{10} - 1.2567L_{12}.$$

To further discriminate between signal and continuum background events, the variable Δt, introduced in sec. 4.9, is used in the likelihood fit.

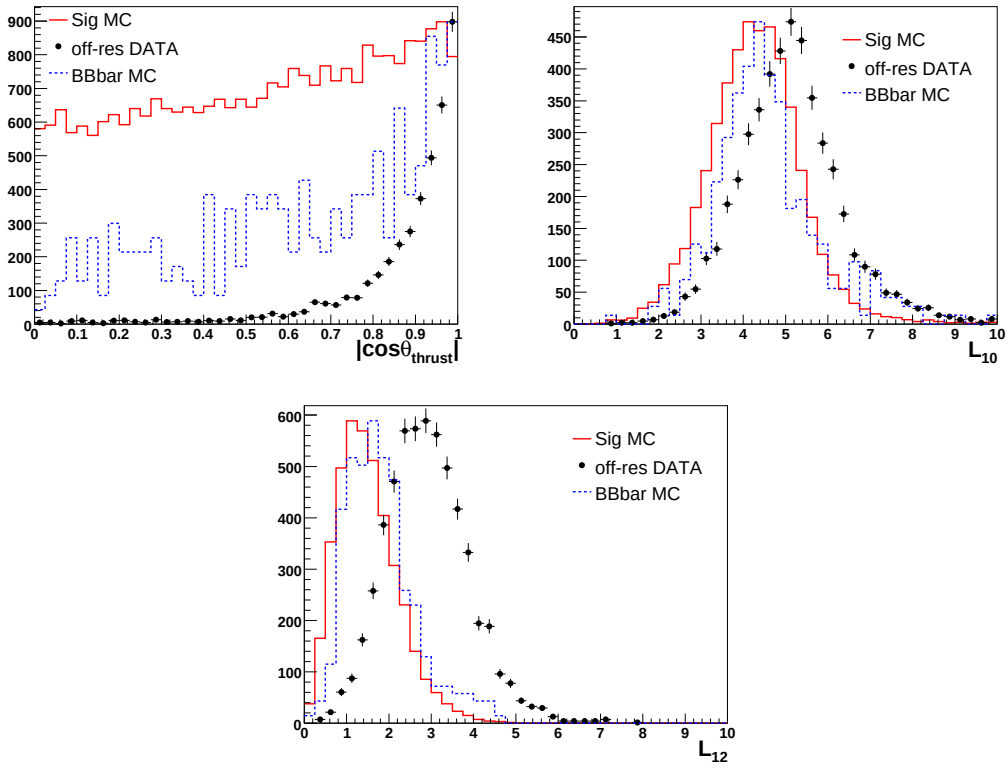

Figure 6.3: Distributions of simulated signal events (solid histograms), off-resonance data (points with error bars) and $B\overline{B}$ background simulated events (dashed histograms) for the three variables used in the Fisher: $|cos(\theta_{thrust})|$, L_{10} and L_{12}.

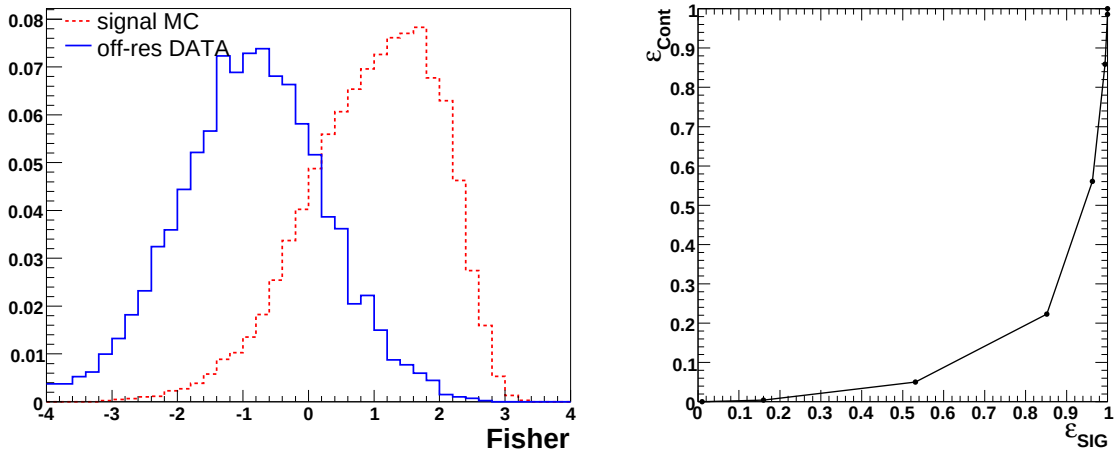

Figure 6.4: Left: distribution of the Fisher discriminant for simulated signal events (dashed histogram) and off-resonance data (solid histogram). Right: efficiency on off-resonance events as a function of the efficiency on signal events.

6.2.5 Studies of peaking background events

A special attention has been put, within the $B\bar{B}$ background, on possible sources of peaking background events. Peaking background consists of processes that lead to the same final state as for the reconstructed signal. The final state we are considering is:

$$D^0 K^{*0} \quad = \quad [(\pi^+\pi^-)_{K_S}\pi^+\pi^-]_{D^0} \quad [K^+\pi^-]_{K^{*0}}.$$

From simulated events studies we identified three possible sources of peaking $B\bar{B}$ background:

- $B^0 \to \overline{D^0}K^{*0}$ events with $K^{*0} \to K^+\pi^-$ and $\overline{D^0} \to \pi^+\pi^-\pi^+\pi^-$,
- $B^0 \to \overline{D^0}\rho^0$ events with $\rho^0 \to \pi^+\pi^-$ and $\overline{D^0} \to K_S\pi^+\pi^-$,
- charmless events of the kind $B^0 \to K^{*0}K_SK_S$.

As far as the first two categories are concerned, dedicated simulation studies give a selection efficiency of $(0.036 \pm 0.019)\%$ for the $D^0\rho^0$ channel and a selection efficiency of $(0.18 \pm 0.04)\%$ for the D^0K^{*0} with $D^0 \to \pi^+\pi^-\pi^+\pi^-$. In the latter case, the cut on α_{K_S} is very important, while for the $D^0\rho^0$ the cuts on ΔE and the PID of the $K^\pm$ are the most effective ones. With these efficiencies, we expect about 0.9 $D^0\rho^0$ events and 0.1 $D^0[\pi^+\pi^-\pi^+\pi^-]K^{*0}$ events (assuming the branching fraction in Tab. 6.2) on 353 fb^{-1} . The results are summarized in Tab. 6.7.

$D^0\rho^0$	
Selection cuts except the cuts on ΔE and KLHTight	76.0 ± 4.6
$\lvert\Delta E\rvert < 0.025$ GeV/c^2	9.7 ± 1.6
KLHTight	0.9 ± 0.6
$D^0 \to 4\pi$	
Selection cuts except the cut on α_{K_S}	0.8 ± 0.5
$\alpha_{K_S} > 0.997$	0.1 ± 0.2

Table 6.7: Number of expected $D^0\rho^0$ and $D^0[\pi^+\pi^-\pi^+\pi^-]K^{*0}$ peaking background events.

The number of peaking charmless events is evaluated from a fit to the m_{ES} variable, using data in the M_{D^0} sidebands (i.e. events that satisfy the condition $|M_{D^0} - M_{D^0}^{\rm nominal}| > 0.025\,{\rm GeV}/c^2$). In Fig. 6.5 we show the distribution of the neutral D mass, after we have applied all the cuts but the cut on M_{D^0}. The projection of the fit over the variable m_{ES} is shown in Fig. 6.5. The number of peaking events, rescaled to the selected region ($|M_{D^0} - M_{D^0}^{\rm nominal}| < 0.011\,{\rm GeV}/c^2$) is $N_{peak} = -5 \pm 7$.

The total number of peaking events in the $B\bar{B}$ background is then assumed to be negligible and fixed to zero in the fit. The effect of this assumption is taken into account in the evaluation of the systematic uncertainties.

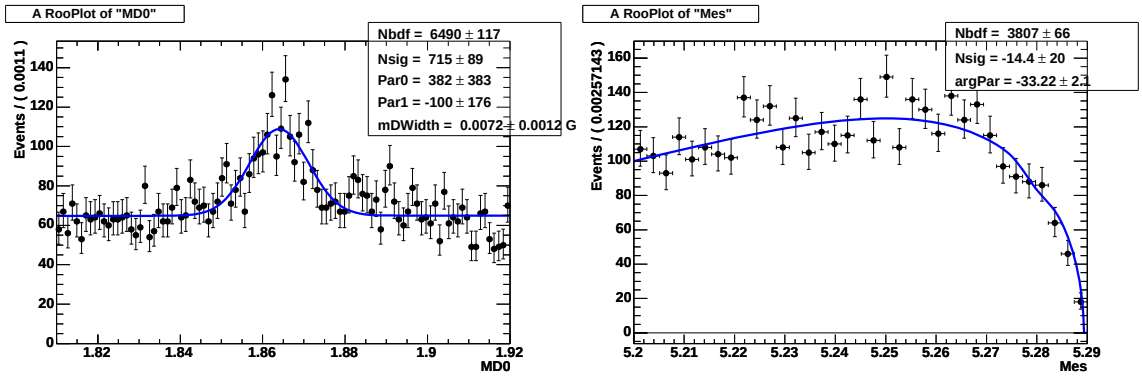

Figure 6.5: Left: D^0 mass distribution in data after all selection cuts are applied (except the cut on M_{D^0}). Right: m_{ES} distribution in data of events in the M_{D^0} sidebands ($|M_{D^0} - M_{D^0}^{\rm nominal}| > 0.025\,{\rm GeV}/c^2$), after all selection criteria are applied. No evidence of peaking events is found.

6.3 Comparison between data and simulated events

The agreement between data and simulated distributions of the relevant variables used in this analysis has been checked after all cuts are applied but the one on the showed variable (see Figs. 6.6 and 6.7). The colored histograms represent the different Monte Carlo components and the points with error bars are the data. Each component is rescaled to 353 fb^{-1}, the luminosity of the on-resonance data. In each case the agreement is satisfactory.

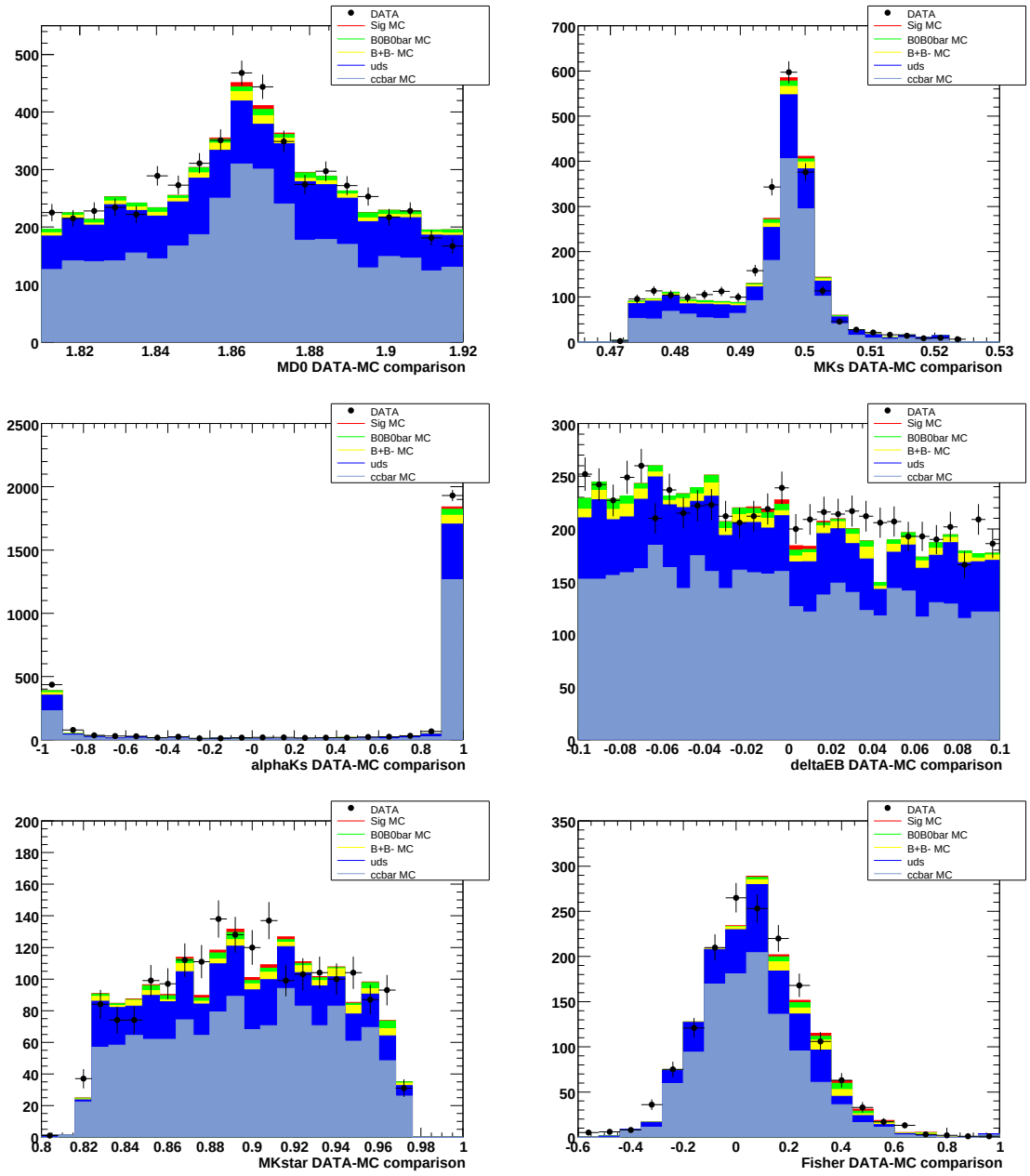

Figure 6.6: Comparison between data and simulation for the relevant variables used in the selection. From the top left to the bottom right the following quantities are shown: M_{D^0}, M_{K_S}, α_{K_S}, ΔE, M_{K^*} and $Fisher$. The events each plot are selected applying all the cuts but the one on the displayed variable.

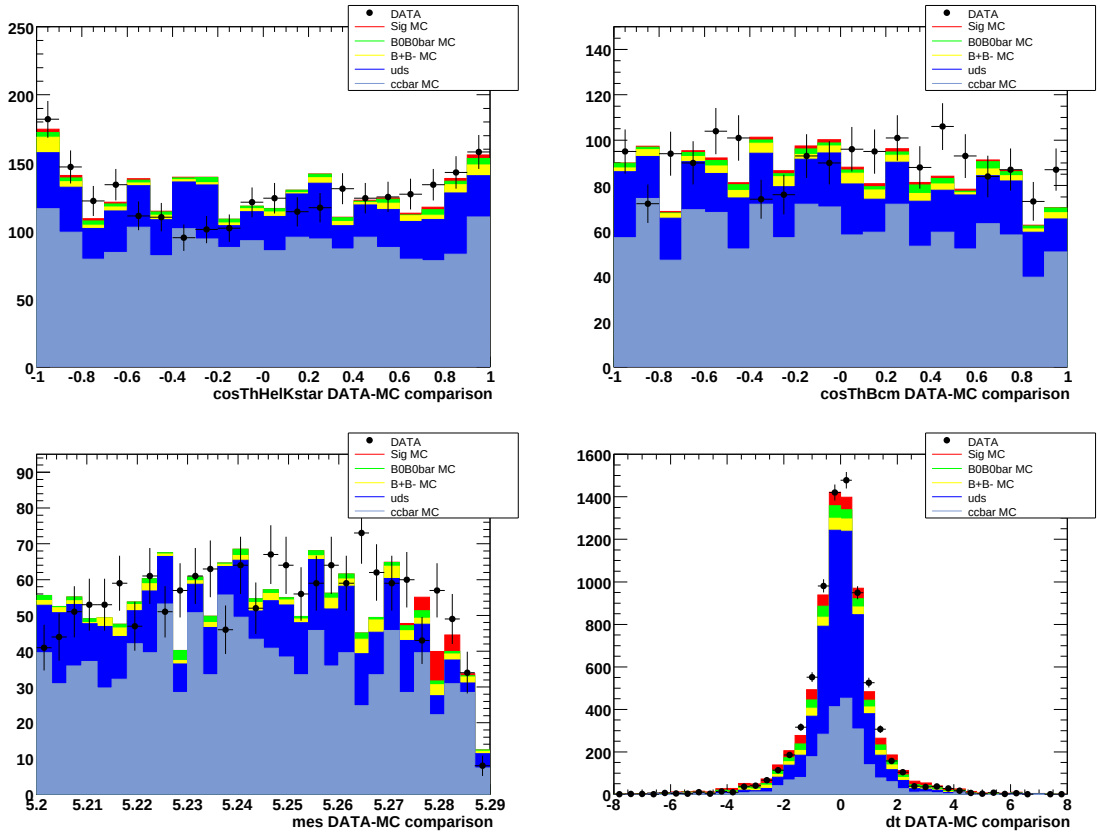

Figure 6.7: Comparison between data and simulation for the relevant variables used in the selection. From the top left to the bottom right the following quantities are reported: $\cos\theta_{Hel}$, $\cos\theta^*_B$, m_{ES} and Δt. The events in each plot are selected applying all the cuts but the one on the displayed variable.

6.4 Maximum likelihood fit

6.4.1 Structure of the fit model

The extraction of the number of signal and background events and *CP* parameters is performed maximizing an extended unbinned likelihood function

$$\mathcal{L}_{ext} = \frac{e^{-\eta}\eta^N}{N!}\prod_{i=1}^{N}\mathcal{P}(\mathbf{x}_i)\ , \tag{6.7}$$

where $\mathcal{P}(i)$ is the total probability density function (pdf) given by eq. (6.8) for event i and $\mathbf{x}$ indicates the set of variables used in the likelihood fit $\mathbf{x} = \{m_{ES}, Fisher, \Delta t, m_+^2, m_-^2\}$. Here N is the total number of observed events and η its expected value according to Poisson statistics.

Based on the background caracterization, we consider three different components in the probability density function: signal (sig), continuum (Cont) and $B\bar{B}$ ($\mathsf{B\bar{B}}$) events. Both the continuum and $B\bar{B}$ background component are subdivided into two categories, which differ only in the term depending on $\{m_+^2, m_-^2\}$:

- combinatorial (not true) D^0 (Comb);
- true D^0 (D^0). Inside this category, we distinguish between real D^0 mesons with a right sign (RS) random K^* (i.e. D^0K^- or $\overline{D}^0K^+$) or a wrong sign (WS) random K^* (i.e. D^0K^+ or $\overline{D}^0K^-$). This splitting is needed in order to account for the misinterpretation of D^0 decays as $\overline{D}^0$ (and vice versa), relevant to parametrize correctly the Dalitz structure. This background component does not contain *CP*-violating effects.

The total pdf $\mathcal{P}$ can then be written as:

$$\begin{aligned}\mathcal{P} = {} & f_{\rm sig}\mathcal{P}_{\rm sig} + \\ & f_{\mathsf{Cont}}\left\{(1-R_{\mathsf{Cont}})\mathcal{P}^{\mathsf{Comb}}_{\mathsf{Cont}} + R_{\mathsf{Cont}}\left[R^{RS}_{\mathsf{Cont}}\mathcal{P}^{\alpha}_{\mathsf{Cont}} + (1-R^{RS}_{\mathsf{Cont}})\mathcal{P}^{\overline{\alpha}}_{\mathsf{Cont}}\right]\right\} + \\ & f_{\mathsf{B\bar{B}}}\left\{(1-R_{\mathsf{B\bar{B}}})\mathcal{P}^{\mathsf{Comb}}_{\mathsf{B\bar{B}}} + R_{\mathsf{B\bar{B}}}\left[R^{RS}_{\mathsf{B\bar{B}}}\mathcal{P}^{\alpha}_{\mathsf{B\bar{B}}} + (1-R^{RS}_{\mathsf{B\bar{B}}})\mathcal{P}^{\overline{\alpha}}_{\mathsf{B\bar{B}}}\right]\right\}\end{aligned} \tag{6.8}$$

where

- $\mathcal{P}_{\rm sig} \equiv \mathcal{P}_{\rm sig}(m_{ES})\mathcal{P}_{\rm sig}(Fisher)\mathcal{P}_{\rm sig}(\Delta t)\mathcal{P}(m_+^2, m_-^2)$ with $\mathcal{P}(m_+^2, m_-^2) = |f_-|^2 + r_S^2|f_+|^2 + 2kr_S\left\{\cos(\delta_S-\gamma)Re[f_-f_+^*] + \sin(\delta_S-\gamma)Im[f_-f_+^*]\right\}$ in the case of $\bar{B}^0$ and $\mathcal{P}(m_+^2, m_-^2) = |f_+|^2 + r_S^2|f_-|^2 + 2kr_S\left\{\cos(\delta_S+\gamma)Re[f_+f_-^*] + \sin(\delta_S+\gamma)Im[f_+f_-^*]\right\}$ in the case of B^0 and f_+ is given by eq. (6.3),
- $\alpha = \mathsf{D}^0$ in the case of $\bar{B}^0$ and $\bar{\mathsf{D}}^0$ in the case of B^0, and $\overline{\alpha}$ denotes the *CP* conjugate state of α;
- f_k is the fraction for component $k = \mathrm{sig}, \mathsf{Cont}, \mathsf{B\bar{B}}$ over the expected value of total events;

- R_{Cont} ($R_{\mathsf{B\bar{B}}}$) is the fraction of real $D^0/\overline{D}^0$ in Cont ($\mathsf{B\bar{B}}$) background component;
- $R^{\mathsf{RS}}_{\mathsf{Cont}}$ ($R^{\mathsf{RS}}_{\mathsf{B\bar{B}}}$) is the fraction of right sign $D^0/\overline{D}^0$ in Cont ($\mathsf{B\bar{B}}$) background component;
- $\mathcal{P}^{\alpha}_{k}$ is the pdf for component k and real D^0 ($\alpha = \mathsf{D}^0$) or $\overline{D}^0$ ($\alpha = \bar{\mathsf{D}}^0$), while $\mathcal{P}^{\mathsf{Comb}}_{k}$ is the pdf for the component k and fake D^0.

$\mathcal{P}^{\alpha}_{k}$ (and similarly $\mathcal{P}^{\mathsf{Comb}}_{k}$) is parametrized as follows:

$$\mathcal{P}^{\alpha}_{k} \equiv \mathcal{P}^{\alpha}_{k}(m_{ES})\mathcal{P}^{\alpha}_{k}(Fisher)\mathcal{P}^{\alpha}_{k}(\Delta t)\mathcal{P}^{\alpha}_{k}(m^2_+, m^2_-) \ , \tag{6.9}$$

.

The pdf is the product of a "yield" pdf $\mathcal{P}^{\alpha}_{j}(m_{ES})\mathcal{P}^{\alpha}_{j}(\mathcal{F})\mathcal{P}^{\alpha}_{j}(\Delta t)$ (written as a product of one-dimensional pdfs since m_{ES}, $\mathcal{F}$ and Δt are not correlated) and of the Dalitz plot dependent part: $\mathcal{P}^{\alpha}_{j}(m^2_+, m^2_-)$, multiplied by the phase space distribution after selection criteria, $P(m^2_+, m^2_-) = PS^{\text{after cuts}}$. $\mathcal{P}^{\alpha}(m^2_+, m^2_-) = f(m)$ is given by eq. (6.3) for true-D^0 events and is parametrized by a third order polynomial for non true-D^0 events (see sec. 6.2.3). In the following, with "yield fit", we refer to the fit using only the "yield" pdf, that will allow for the extraction of the number of signal and background events. Similarly, the term "*CP* fit" refers the fit using the Dalitz plot dependent pdf (and hence giving sensitivity to γ). The yield fit is first performed and validated (see sec. 6.5.1, 6.5.2 and 6.5.3), the number of events and the *CP* parameters (r_S, δ_S, γ) are then determined in the *CP* fit. The validation of the *CP* fit are shown in sec. 6.5.4.

6.4.2 Parametrizations of the distributions of the variables used in the fit: m_{ES}, Fisher and Δt

The variable m_{ES} is parametrized as a Gaussian for the signal and as an Argus both for continuum and $B\bar{B}$ background events. The Fisher discriminant is parametrized using a bifurcate Gaussian for the signal and $B\bar{B}$ background and using the sum of two Gaussians for the continuum background. For the signal, Δt is parametrized (see equation 6.10) with a resolution function convoluted with an exponential in which $\tau = \tau_{B^0}$. For the backgrounds, to parametrize the fraction of events in which a B is misreconstructed, we convolve the resolution function with an exponential with effective lifetime τ_0 and, for events in which there is no real neutral B ($frac_{\text{Short}}$), we convolve the resolution function with an exponential in which $\tau = 0$. The resolution function $\mathcal{R}(\Delta t, \sigma_{\Delta t})$ is a sum of a core Gaussian (whose sigma depends on the error on Δt event per event), a tail Gaussian and an outlier Gaussian:

$$\mathcal{R}(\Delta t, \sigma_{\Delta t}) = (1 - \phi_{tail} - \phi_{out})G(\Delta t, \mu_{core}, s_{core}\sigma_{\Delta t}) + \phi_{tail}G(\Delta t, \mu_{tail}, \sigma_{tail}) + \\ +\phi_{out}G(\Delta t, \mu_{out}, \sigma_{out})$$

The parametrizations have been obtained on simulated events for signal and $B\bar{B}$ background and, for continuum background, using off-resonance data. Fig. 6.8, 6.9 and 6.10 show the distributions so obtained for m_{ES} Fisher and Δt for signal, $B\bar{B}$ and continuum background events respectively.

Tab. C.1 (in appendix C) shows the values of the parameters determined in the parametrization fits and used in the final fit on data.

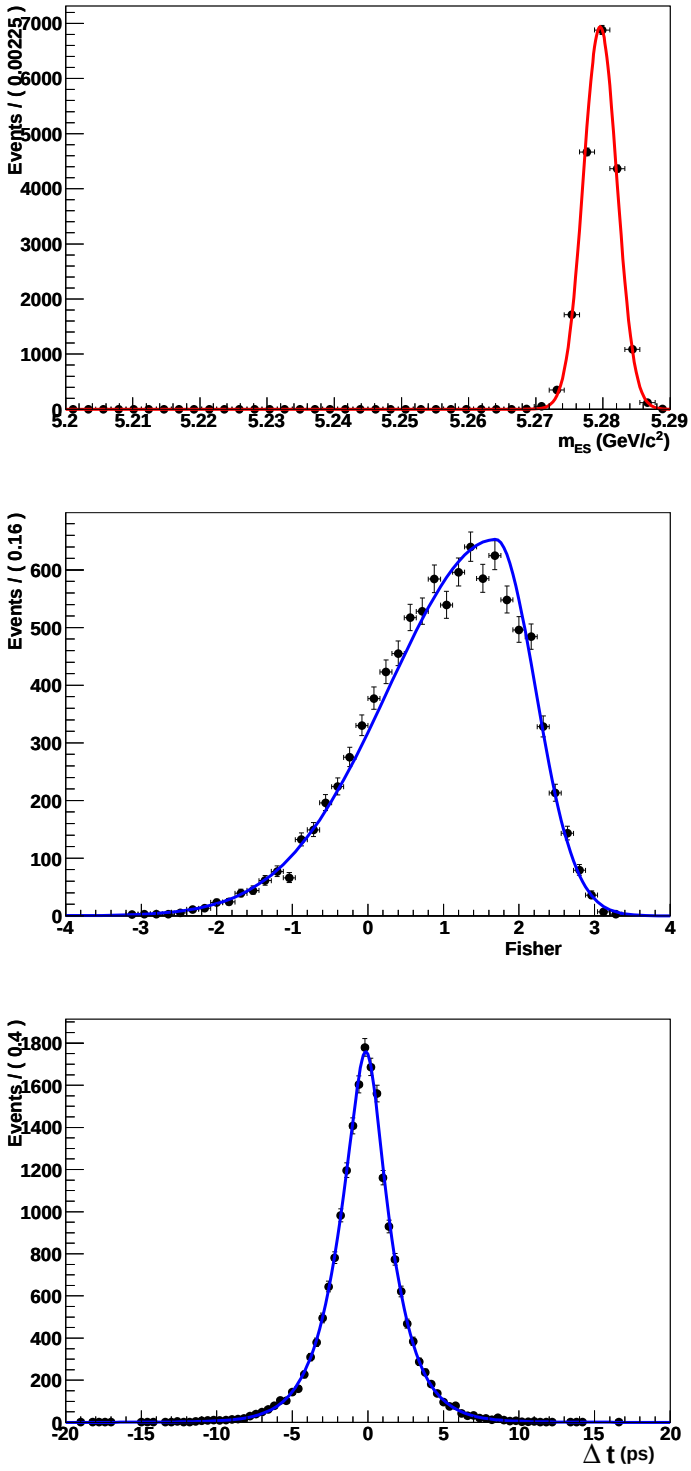

Figure 6.8: m_{ES} (top), Fisher (middle) and Δt (bottom) distributions of simulated signal events.

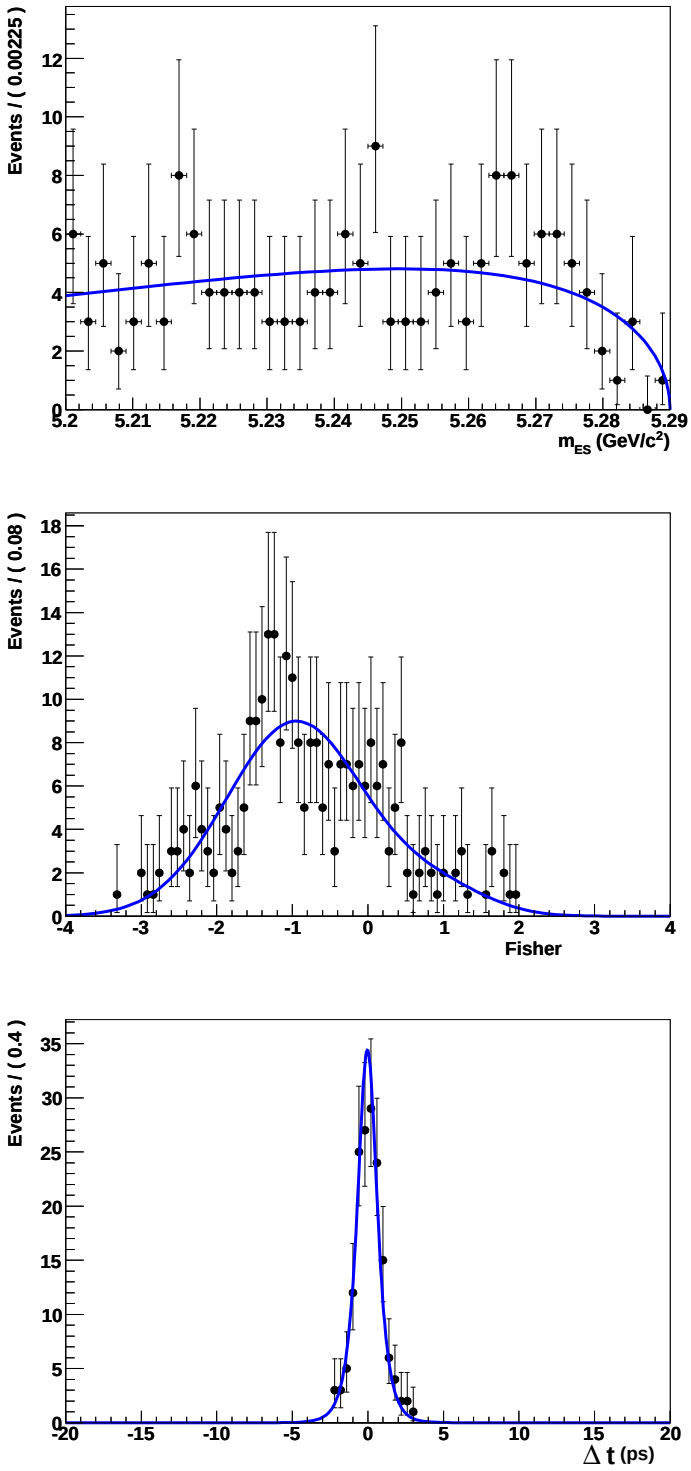

Figure 6.9: m_{ES} (top), Fisher (middle) and Δt (bottom) distributions of off-resonance events.

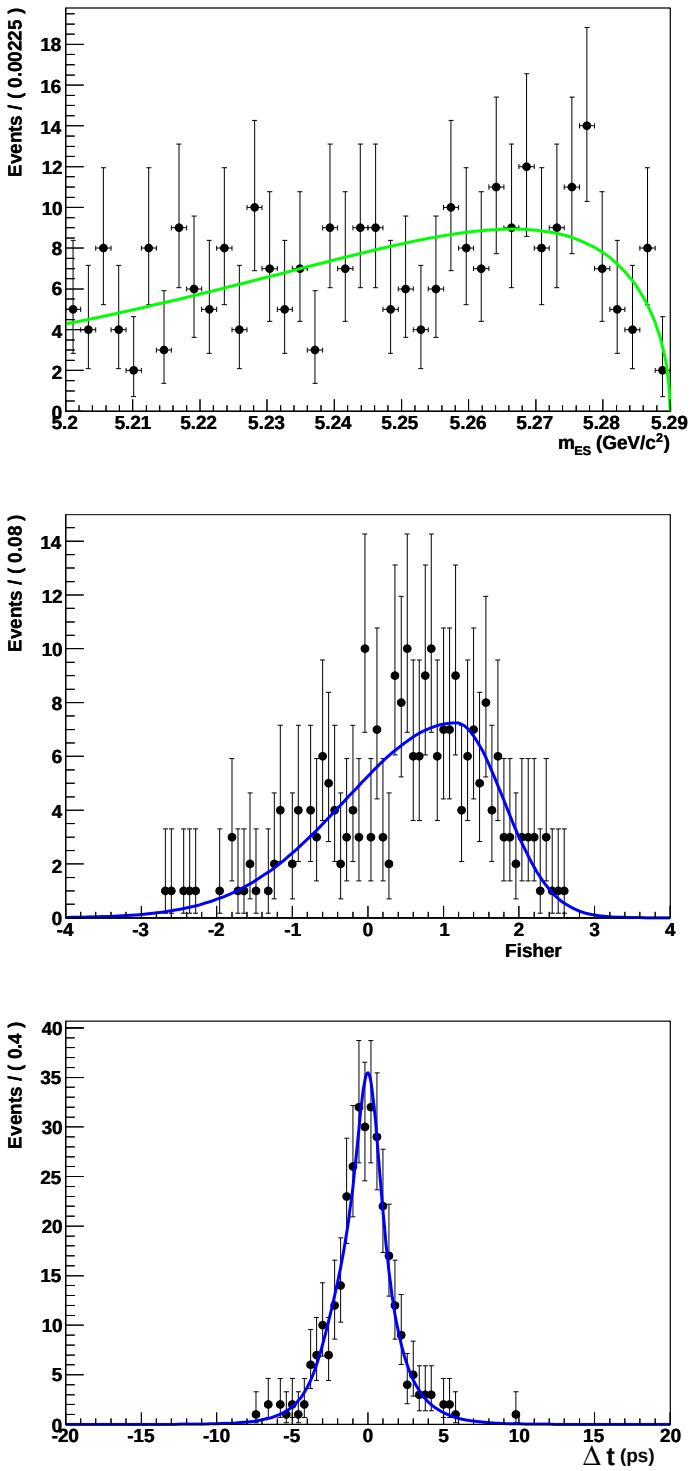

Figure 6.10: m_{ES} (top), Fisher (middle) and Δt (bottom) distributions of simulated $B\bar{B}$ events.

The correlation between m_{ES}, $\mathcal{F}$ and Δt have been found to be negligible for all the background components (of the order of a few percent). For signal the correlations are at the level of -1.5%, -0.1% and 1.0% respectively for m_{ES} as a function of Fisher, m_{ES} as a function of Δt and Δt as a function of Fisher. This allows to write the total pdf in the likelihood fit as a product of one-dimensional pdfs for the single variables.

6.5 Results on real data

6.5.1 Fit on data: results for the yields

A first fit has been performed on data (fit of the "yields") to extract the number of signal and background events. The parameters left free to vary in the fit procedure on data are:

- the number of signal events, N_{SIG};
- the number of continuum and $B\bar{B}$ events, N_{CONT} and N_{BB} respectively;
- the mean value for the Gaussian describing m_{ES} for signal events;
- the parameters of the Argus function describing m_{ES} for $B\bar{B}$ background events.

The fit projections for m_{ES}, $\mathcal{F}$ and Δt are shown in Fig. 6.11. The corresponding results of the fit are given in Tab. 6.8: we find 39 ± 9 signal events with a purity of $\frac{N_{SIG}}{\sigma_{N_{SIG}}{}^2} \approx 0.48$. In Fig. 6.12 we show the projection of the "yield" fit over the variable m_{ES}, after a cut on Fisher> 0.4 has been applied, in order to visually enhance the signal.

Parameter	Fitted value
N_{SIG}	39 ± 9
N_{CONT}	1772 ± 48
$N_{B\overline{B}}$	231 ± 28
Sig m_{ES} μ $[GeV/c^2]$	$5.2798 \pm 0.0001\,\mathrm{GeV}/c^2$
BB m_{ES} shape	-64.97 ± 14.69

Table 6.8: [Data - yield fit] Results for the yield fit on 353 fb^{-1} on-resonance data.

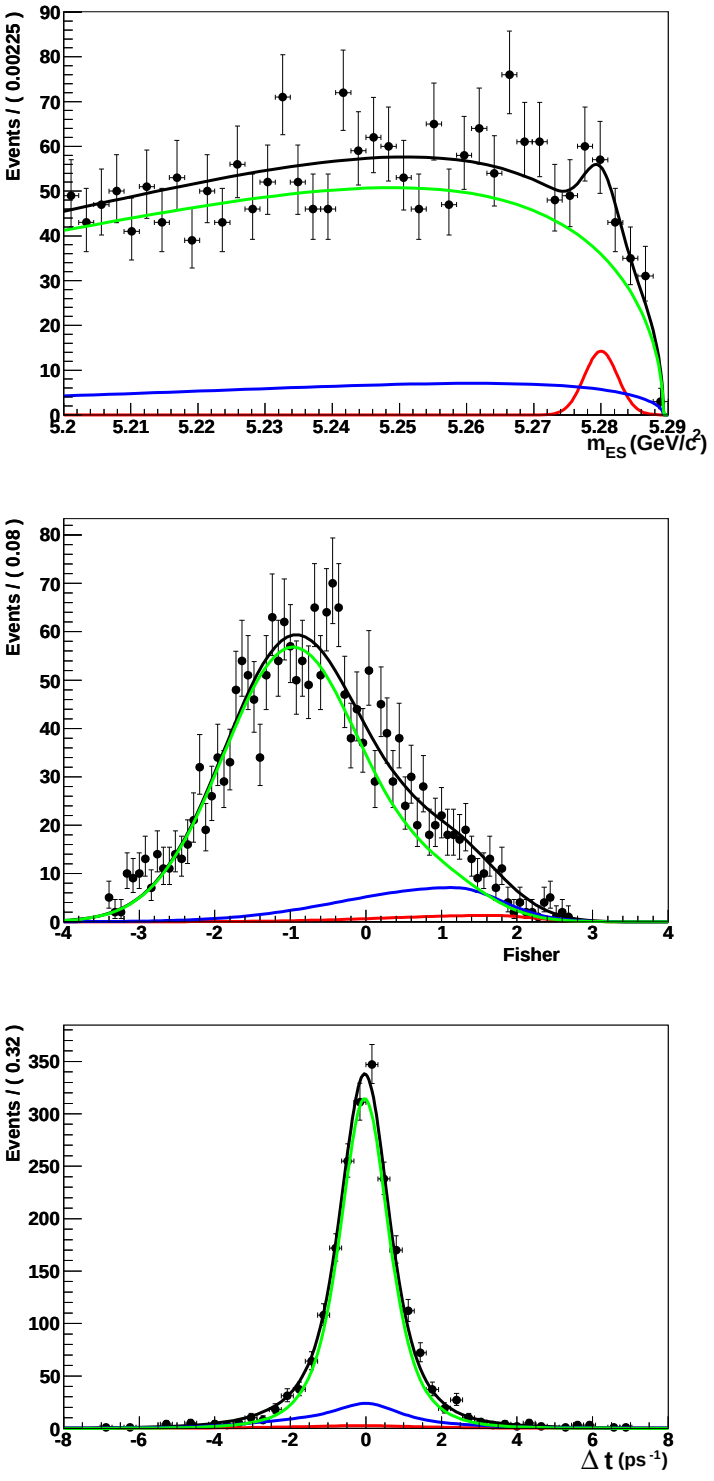

Figure 6.11: [Data - yield fit] Projections of the "yield" fit over the variables m_{ES}, Fisher and Δt. The fit has been performed on $353 fb^{-1}$ on-resonance data. The different fit components are shown: sig (red), $B\bar{B}$ (blue) and Cont (green).

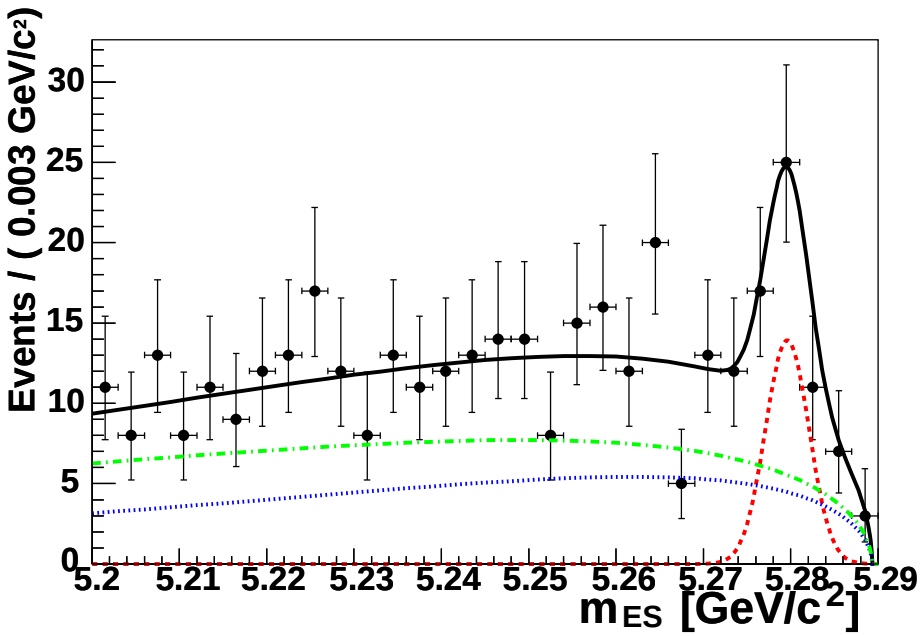

Figure 6.12: [Data - yield fit] Projections of the "yield" fit over the variable m_{ES}, after a cut on Fisher$>$ 0.4 in order to visually enhance the signal. The fit has been performed on $353 fb^{-1}$ on-resonance data. The different fit components are shown: signal (red dashed), $B\bar{B}$ (blue dotted) and continuum (green dash-dotted).

6.5.2 Validation for the yields fit using a Toy-Monte Carlo procedure

The "yield" fit has been validated with a toy Monte Carlo procedure. We generate 1000 experiments from the fit model, using the values in Tab. C.1 (in appendix C) for the parameters describing the different pdfs (m_{ES}, Fisher, Δt). The number of events are generated according to Poisson distributions with expected values equal to the values found on data (see Tab. 6.8). These samples are then fitted using the same fit model used for their generation. In Fig. 6.13 we show the distribution of N_{SIG}, its error and pull, obtained from this study. The pull for the number of signal events is well behaved, its mean value is consistent with zero and its resolution with unity. The fit procedure tends to overestimate the number

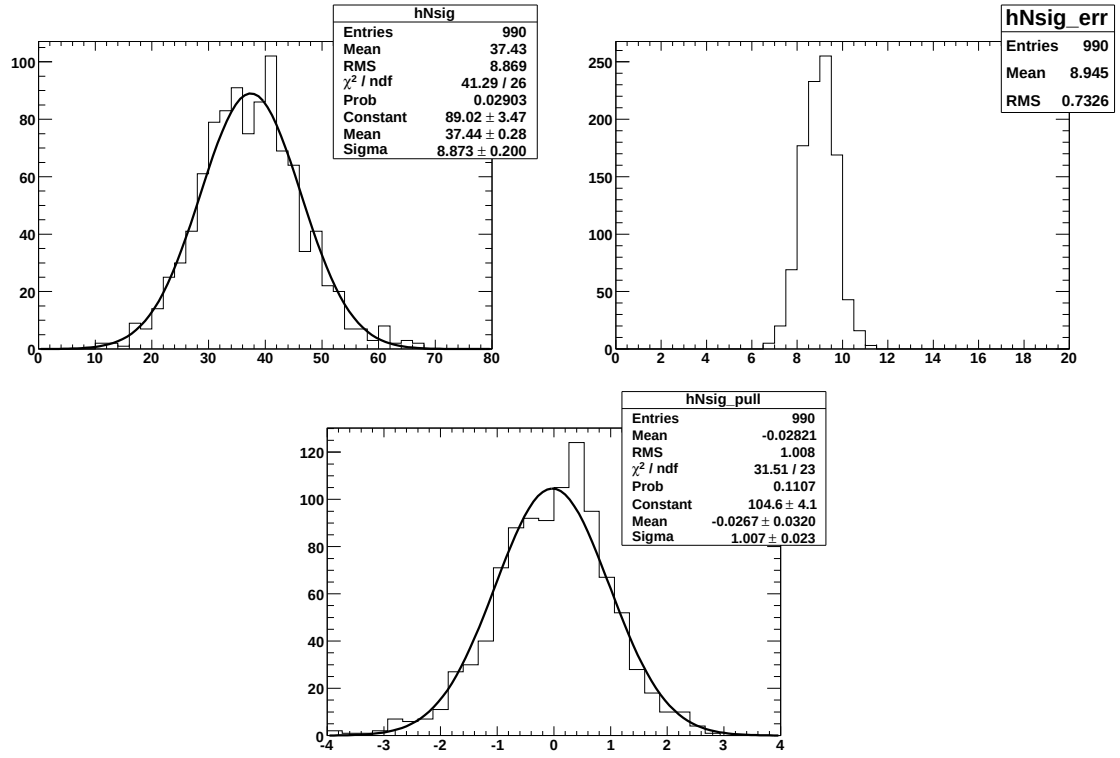

Figure 6.13: [Validation - toy Monte Carlo]. Distributions of the fitted value (top left), the error (top right) and the pull (bottom) for N_{SIG} obtained from 1000 toy Monte Carlo experiments.

of $B\bar{B}$ events (and consequently underestimate the number of continuum events). The pull distribution for the number of $B\bar{B}$ events has a bias of about 15%. The only impact of that is on the total fraction of $b \to u$-like real D^0 events, which will be fixed in the final fit. In continuum background events, the number of $b \to u$-like real D^0 events is almost twice that in $B\bar{B}$ events (see Tab. 6.5). This effect is taken into account in the systematic error evaluation.

6.5.3 Crosschecks for the yield fit using the sPlot technique

A qualitative agreement of the presence of real signal events in the data can be obtained using the sPlot technique [58]. In this technique, each event is reweighted using a weight $W_{\rm sig}$ defined as following:

$$W^i_{\rm sig} \equiv \frac{\sum_j \mathbf{V}_{{\rm sig},j}\, P_{ij}(m^i_{ES}, \Delta t^i)}{\sum_j N_j\, P_{ij}(m^i_{ES}, \Delta t^i)}, \tag{6.10}$$

where N_j is the number of events of each component j (signal, continuum, $B\overline{B}$) and P_{ij} is the product of probability density functions of m^i_{ES} and Δt^i for the event i, $\mathbf{V}_{{\rm sig},j}$ is the signal row of the covariance matrix of the component yields. The covariance matrix $\mathbf{V}_{{\rm sig},j}$ is obtained from a yield fit in which all the parameters (but the yields) are fixed to the values obtained in the nominal fit.

The sPlots of the variables Δt and m_{ES} are shown (for signal, $B\bar{B}$ and continuum background) in Fig. 6.14 and Fig. 6.15 respectively. The curves are illustration of the expected shapes for the different components. For the signal, the error bars are quite large (reflecting the small signal yield) but the data distributions weighted by $W_{\rm sig}$ are in reasonable agreement with the simulated events shapes for signal, $B\bar{B}$ and continuum components.

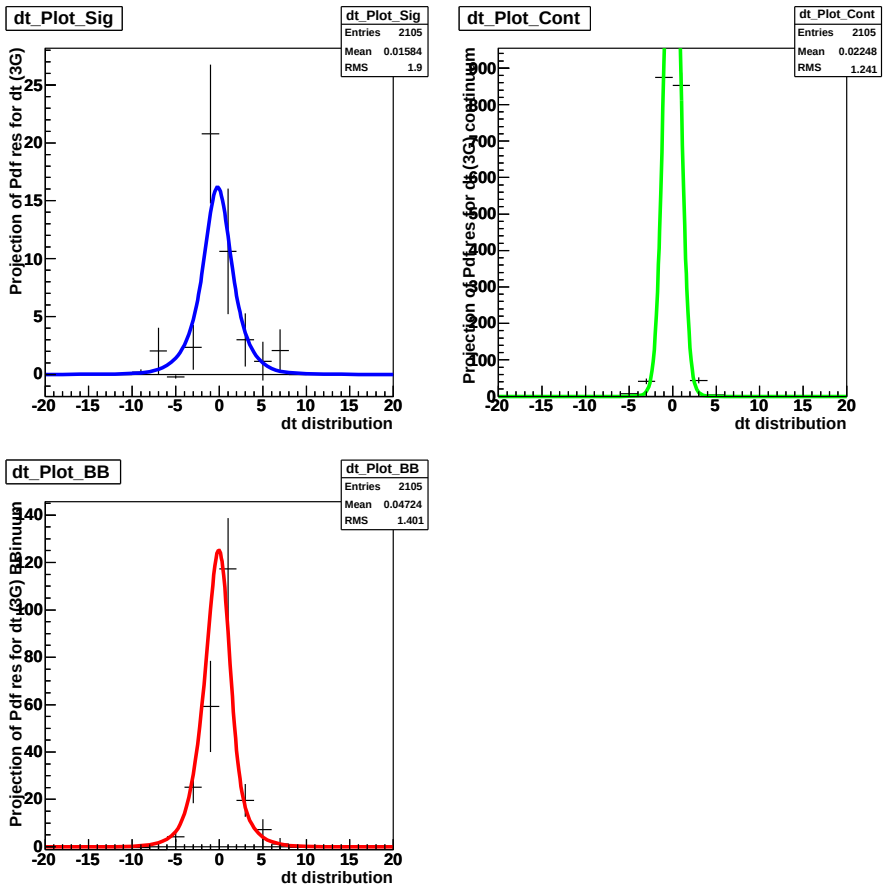

Figure 6.14: [Data - sPlot]. sPlot distributions of Δt in data for signal, continuum and $B\bar{B}$ background. Shapes obtained from signal MC, $B\bar{B}$ MC and off-resonance data are superimposed for comparison.

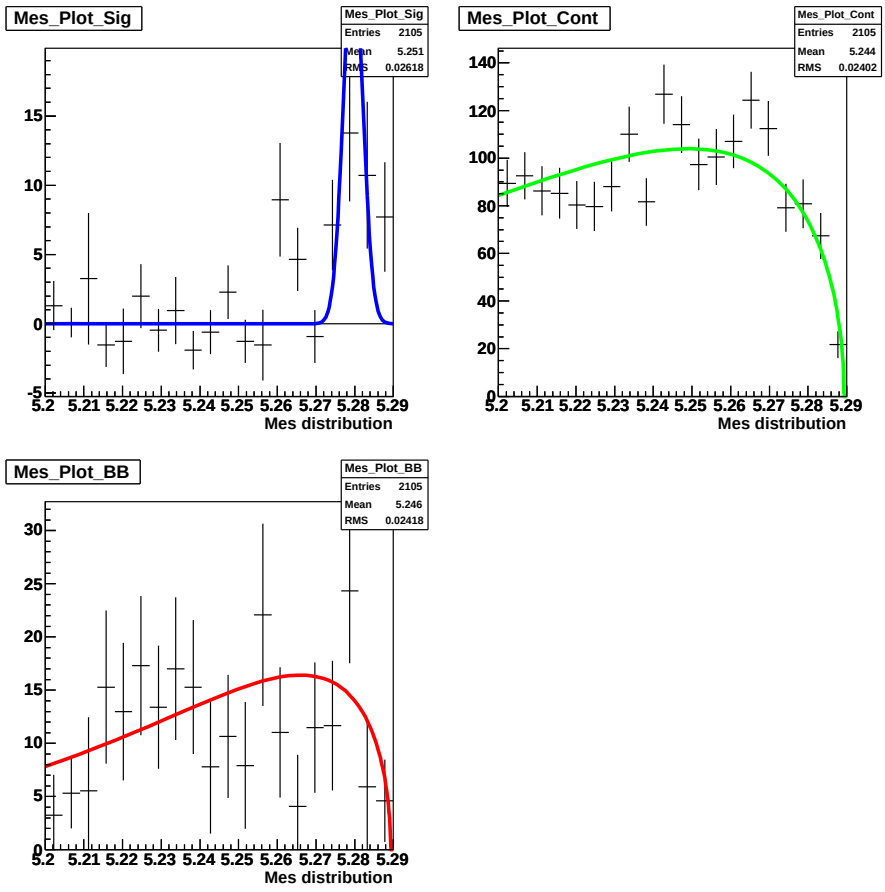

Figure 6.15: [Data - sPlot]. sPlot distributions of m_{ES} in data for signal, continuum and $B\bar{B}$ background. Shapes obtained from signal MC, $B\bar{B}$ MC and off-resonance data are superimposed for comparison.

6.5.4 Validation of the *CP* Dalitz fit: testing the polar coordinates

In order to validate the *CP* fit, we made many toy-MC tests both in polar and cartesian coordinates (defined in chapter 2.2). All the tests are made using the number of signal and background events obtained on data and summarized in Tab. 6.8.

Toy-MC tests have been first performed in polar coordinates, r_S, γ and δ_S: these three parameters are all floated in the fit in addition to the number of signal and background events, to the mean value for the Gaussian describing m_{ES} for the signal and the shape parameter of the Argus pdf describing m_{ES} for the $B\bar{B}$ background. The parameter k is fixed in the fit to $k = 0.95$ (see 2.6.2).

Due to the dependence of the likelihood on r_S, we tend to get from the fit a value of r_S larger than the generated one and consequently, since r_S leads the sensitivity to γ, to underestimate the error on γ, this feature is known as the "linearity problem".

In Fig. 6.16 (left plot), we summarize the results of many toy Monte Carlo tests made generating different values for r_S. The number of signal and background events are generated according to the yields found in 353 fb^{-1} of data. The plots show the fitted value r_S^{fit} as a function of the generated one r_S^{GEN}.

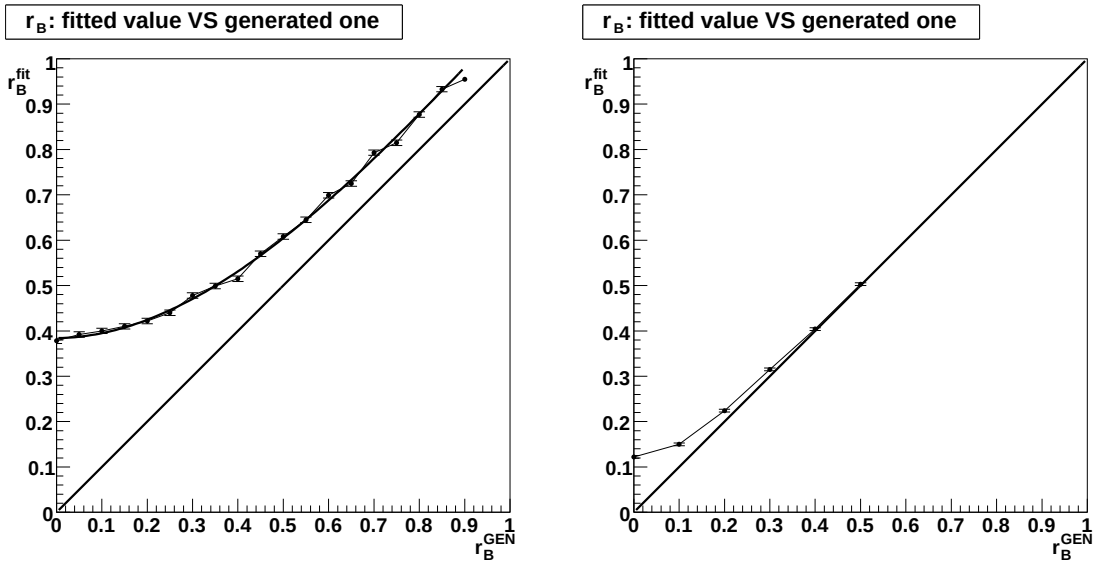

Figure 6.16: Distribution of r_S^{FIT} vs r_S^{GEN} from toy MC for different generated values. The toy-MC samples have been generated assuming for the yields the results obtained with 353 fb^{-1} of on-resonance data ($N_{SIG} = 37$, $N_{Cont} = 1810$ and $N_{BB} = 258$) (left) and for ten times the statistics (right).

In Fig. 6.16 (left) it can be seen that, also for high values of r_S^{GEN}, the results for r_S^{fit} as a function of r_S^{GEN} do not converge to the curve $r_S^{fit} = r_S^{GEN}$ (the black curve in the plots). We name this feature "low statistics problem", since it disappears in the results of toy Monte Carlo with ten times the statistics (Fig. 6.16, right).

In conclusion, with the available statistics for this analysis, the fit in polar coordinates is not feasible (with r_S, γ and δ_S floating) because of the two effects: the "linearity" and

the "low statistics" problems, and that, for r_S of order $r_S \approx 0.3$, it is the second one that dominates.

Tests have also been performed in polar coordinates for r_S fixed in the fit. For different values of r_S^{GEN} we fit fixing r_S each time to the generated value. In this configuration, also for the available statistics, the fit shows a good behaviour for γ and δ_S.

6.5.5 Validation for the *CP* Dalitz fit: testing the cartesian coordinates

Toy-Monte Carlo studies have been performed also using in the fit the cartesian coordinates (already defined in eq. 2.5 in chapter 2.2):

$$x_\pm = r_B \cos(\delta \pm \gamma) \; ; \; y_\pm = r_B \sin(\delta \pm \gamma). \tag{6.11}$$

The use of these coordinates has become usual for the Dalitz analyses of charged B mesons, since it solves the "linearity problem" [61].

In Tab. 6.9, we summarize the results of toy Monte Carlo corresponding to 353 fb^{-1} of on-resonance data (left column) and with ten times larger statistics (right column). From the simulation, with the present statistics, the four variables $(x_\pm, y_\pm)$ show a non-Gaussian behaviour and appear to be biased; the mean values of their pull distributions are not consistent with zero and the resolutions are not compatibles with unity. This effect disappears at high statistics (right column). We conclude that, with the available statistics, we cannot perform the measurement in cartesian coordinates either.

-	353 fb^{-1}	3.5 ab^{-1}
$\mu_{x_+}^{PULL}$	-0.52 ± 0.05	-0.04 ± 0.05
$\sigma_{x_+}^{PULL}$	0.82 ± 0.03	0.97 ± 0.04
$\mu_{x_-}^{PULL}$	-0.07 ± 0.05	-0.02 ± 0.05
$\sigma_{x_-}^{PULL}$	0.78 ± 0.04	0.99 ± 0.04
$\mu_{y_+}^{PULL}$	-0.18 ± 0.05	-0.05 ± 0.06
$\sigma_{y_+}^{PULL}$	0.79 ± 0.04	1.01 ± 0.04
$\mu_{y_-}^{PULL}$	0.40 ± 0.05	-0.03 ± 0.05
$\sigma_{y_-}^{PULL}$	0.79 ± 0.04	1.03 ± 0.04

Table 6.9: Pull distributions for cartesian coordinates obtained from 500 toy-MC in a configuration similar to the one we find on data (left column) and for ten times the statistics (right column).

6.5.6 Adopted strategy for the *CP* fit

As shown in section 6.5.4, given the available statistics, an unbiased fit cannot be performed neither in polar coordinates, with γ, δ and r_S floating, neither in cartesian coordinates. The performed simulation studies show that the problem for the *CP* fit is mostly due to the lack of signal statistics.

To avoid this problem, we extract from the fit a three-dimensional likelihood for the variables γ, δ and r_S and we combine it with an additional r_S measurement, as the one obtained from the ADS analysis. The combination is obtained from the product of the two pdf: the three-dimensional pdf ($100 \times 360 \times 360$ bins in r_S, γ and δ) and the one-dimensional Gaussian pdf for r_S from the ADS analysis. The height of each bin (r_{Si}, γ_j, δ_k) is multiplied by the corresponding height of the ADS pdf for r_{Si} and the three-dimensional distribution obtained in this way is the pdf for the combined measurements. Whenever the pdf is projected on any of the three variables (or on a set of them), an integral is performed on the other variables.

This procedure has been tested on ten different samples, generated with a toy-Monte Carlo procedure, using for the yields the values found on data and assuming $r_S = 0.3$. For each sample, the three-dimensional likelihood has been extracted and combined with an hypothetical Gaussian measurement of $r_S = 0.30 \pm 0.15$, where the central value is consistent with the one generated for the ten samples. The results of these tests show that γ, δ and r_S can be extracted with no bias, provided that it is combined with an additional r_S measurement, even with an error of 50%. The precision we get from the ADS measurement is better than that, being $r_S = 0.271^{+0.060}_{-0.076}$.

In conclusion, the output of the Dalitz measurement presented here, for the reasons explained above, is a three dimensional likelihood scan in r_S, γ and δ. Simulation studies show that results on the single variables can be safely obtained by projecting the three-dimensional likelihood, provided that it has been combined with an external information on r_S, as the one from the $B^0 \to D^0(\overline{D}^0)K^{*0}$ ADS analysis.

6.5.7 Fit on real data: results for the *CP* parameters: γ, r_S, δ_S

A three-dimensional likelihood scan for γ, δ and r_S is extracted from the fit to 353 fb^{-1} of on-resonance data. The three-dimensional likelihood is an histogram with $100 \times 360 \times 360$ bins in (r_S, γ, δ).

In Fig. 6.17 we show the 68% probability regions obtained for γ, at different r_S values (we divide the interval $[0, 1]$ for r_S in 20 bins, $r_S = 0$; 0.05; 0.1....0.95). As expected, moving the value of the (fixed) r_S does not affect the central value of γ, but only its error. For example, for r_S fixed at 0.35, we obtain $\gamma = (162 \pm 45)^\circ$. On toy-MC for the same fit configuration, the average error is 39° with a RMS of 12°. All the distributions shown in the following are obtained after the combination of the three-dimensional likelihood with the experimental likelihood for r_S from ADS analysis (see eq. 5.50). The projection of the three-dimensional likelihood on the two-dimensional plane r_S vs γ is shown in Fig. 6.18. The projection of the three-dimensional likelihood on the three variables, r_S, γ and δ, are shown in Fig. 6.19. The dark and light colored zones are the 68% and 95% probability regions.

The corresponding values we obtain are:

$$\begin{aligned}
&\gamma = (162 \pm 56)^\circ or (342 \pm 56)^\circ; \\
&\delta_S = (62 \pm 56)^\circ or; (242 \pm 56)^\circ \\
&r_S = 0.273^{+0.058}_{-0.071}\ ,\ r_S \in [0.12, 0.38]@95\%.
\end{aligned}$$

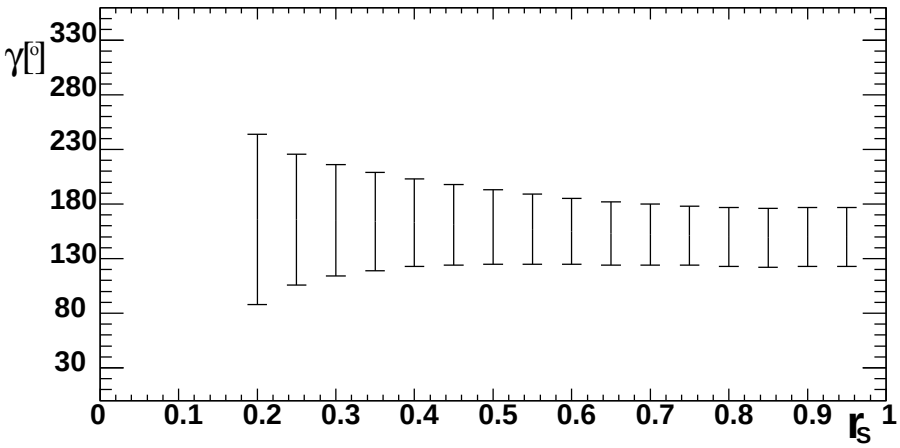

Figure 6.17: 68% probability regions obtained for γ, at different values of r_S. A 68% probability region cannot be obtained at values of r_S lower than 0.2. The results are obtained on 353 fb^{-1} on-resonance data.

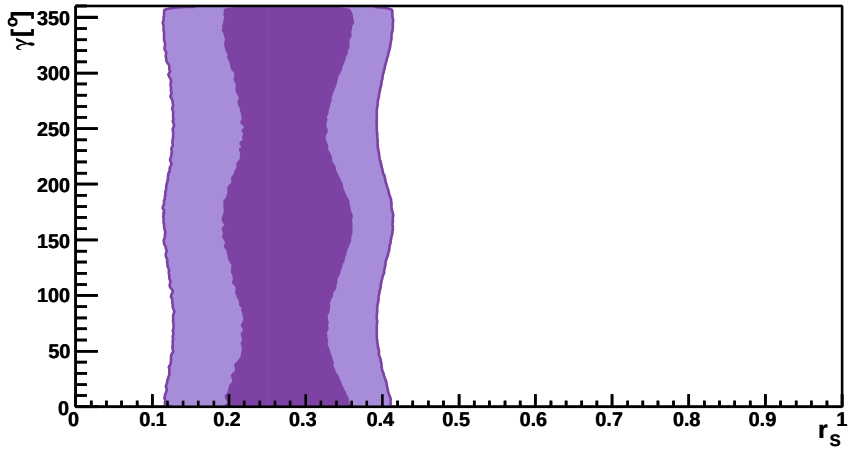

Figure 6.18: Projections, on the two-dimensional plane γ vs r_S, of the three-dimensional likelihood, combined with the measurement of r_S. The dark and light colored zones are the 68% and 95% probability regions.

6.5.8 Systematic uncertainties

In this section we discuss the sources of systematic uncertainties. These effects are assumed to be Gaussian and uncorrelated between the three variables r_S, γ and δ_S. The total systematic error is calculated for each variable separately. After that a 3-dimensional Gaussian is built having as width, for each variable, the value of its systematic uncertainty. The three-dimensional likelihood from the fit is then convoluted with this three-dimensional Gaussian

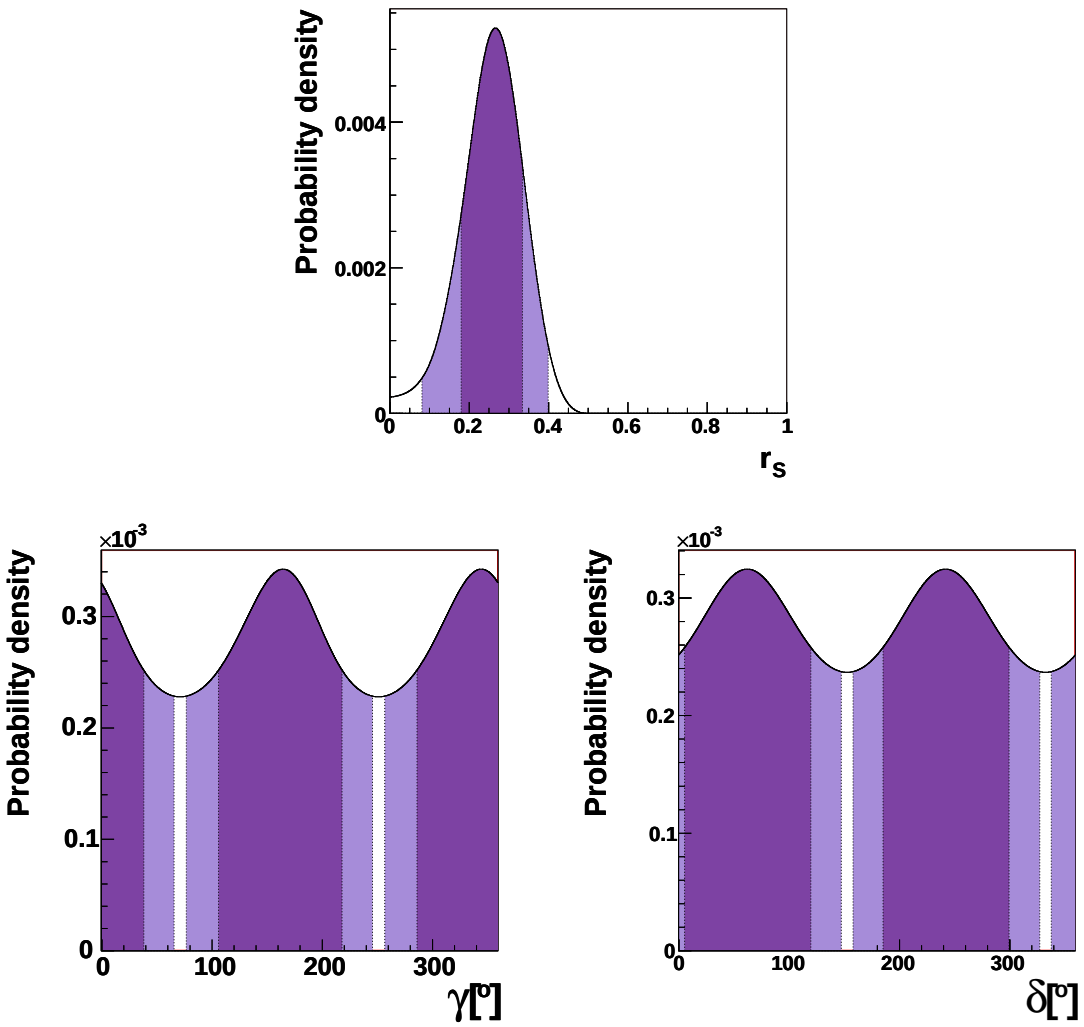

Figure 6.19: Projections of the three-dimensional likelihood, combined with the r_S measurement from the ADS analysis, on r_S (top plot), γ (bottom left) and δ_S (bottom right). The dark and light colored zones are the 68% and 95% probability regions.

to obtain the final three-dimensional pdf.

In order not to be sensitive to problems due to the low statistics of the sample in the evaluation of the systematics, we evaluate the uncertainties on high statistics toy-MC. For γ and δ, we study the systematics using a toy-MC for a fixed value of r_S. As a matter of fact, the systematics do not depend on the r_S value: the only difference between different r_S values is the number of $b \to u$ events and so the number of events that we should generate in order to be in a "high statistic" condition.

- m_{ES} **and** *Fisher* **shapes and parameters in yields fit.**
  The systematics from pdfs shapes are evaluated by varying all the fixed parameters by $\pm 1\sigma$. In addition, for continuum background, the fit is also performed using the

parameters obtained on simulated events (instead of off-resonance data).

- **Peaking background assumptions**
  The number of peaking background events, evaluated on simulated events and on M_{D^0} sidebands data trough a fit to the m_{ES} distribution, is found consistent with zero and fixed to zero in the fit. The systematic due to this assumption are evaluated by varying the number of peaking background events within their statistical errors.

- **True-D^0 fractions in background**
  The background true-D^0 fraction is evaluated on data through a D^0 mass fit in the m_{ES} sidebands region. The uncertainty due to this assumption is evaluated by varying the value within its statistical error.

- **$b \to c$-like events fractions in background**
  The $b \to c$-like (and complementary the $b \to u$-like) events fractions for combinatorial background are evaluated on simulated events. This value is bigger for the case of continuum background than for the case of $B\bar{B}$ background (it is almost the double, see Tab. 6.5). Toy-Monte Carlo studies show that the yield fit tends to overestimate the number of $B\bar{B}$ background events and so to underestimate the number of $b \to u$-like events in combinatorial background (see sec. 6.2.3). The systematic uncertainty due to this effect is evaluated by fixing the number of $B\bar{B}$ to the MC one and repeating the CP-fit.

- **Signal efficiency over the Dalitz plot**
  The variations of the efficiency over the Dalitz have been considered by using a phase space distribution corrected after having applied the selection criteria. For the evaluation of the systematic effect the fit has been repeated using only the phase space distribution PS^{theo} (see eq. 6.5).

- **Dalitz shape for fake-D^0 background**
  The Dalitz shape for combinatorial background are evaluated on simulated events (see sec. 6.2.3). To evaluate the systematic effect due to this assumption, we repeat the fit assuming a flat Dalitz distribution (without the presence of a K^* contribution).

- **Systematics from the assumptions on the k parameter**
  The k parameter is fixed in the fit to 0.95. We evaluate the systematics effect of this assumption by varying the value to which we fix k in the interval $[0.88, 1.]$ as determined in 2.6.2.

- $D^0 \to K_s\pi^+\pi^-$ **Dalitz model parametrization** The systematic uncertainty coming from the parametrization of the D Dalitz model is evaluated by performing the fit on data assuming different Dalitz models, including or not the K-matrix formalism or parametrizing the $\pi\pi$ S-wave component using the scalar resonances σ_1 and σ_2.

The systematic uncertainties are summarized in Tab. 6.10, and a detail of the different contributions can be found in Tab. D.1 in appendix D.

Systematics source	$\Delta\gamma[^o]$	$\Delta\delta_S[^o]$	$\Delta r_S(10^{-2})$
pdf shapes	1.5	2.5	5.2
Peaking background	0.14	0.12	0.04
True D^0 in the background	0.05	0.03	1.0
$R_{b\to u}$	0.01	1.1	1.9
Dalitz not true D^0	0.31	0.62	0.61
Dalitz background param.	0.03	0.27	0.2
k parameter	0.07	1.2	7.1
Dalitz model for signal	6.5	15.8	6.0
Total	6.7	16.1	11

Table 6.10: [Data - systematics] Systematic uncertainties on γ , δ_S , and r_S.

The results for γ, r_S and δ_S, taking into account the systematic effects and after the combination with the r_S measurement from the ADS analysis presented in chapter 5 are:

$$\begin{aligned} \gamma &= (162 \pm 56)^\circ \text{ or } (342 \pm 56)^\circ; \\ \delta_S &= (62 \pm 57)^\circ \text{ or } (242 \pm 57)^\circ; \\ r_S &= 0.273^{+0.058}_{-0.071} \; ; \in [0.120, 0.381] \;\; \text{at } 95\% \text{ probability.} \end{aligned} \tag{6.12}$$

6.5.9 Tests on B^0 and $\bar{B}^0$ samples separately

In Dalitz analyses the phases γ and δ are constrained by the simultaneous use of B^0 and $\bar{B}^0$ samples, which are sensitive to $\delta+\gamma$ and $\delta-\gamma$ respectively (see eqs.2.11 and 2.11). Fig. 6.20 shows the pdf of γ as a function of δ as obtained on data, after having integrated on r_S. It is evident that for this measurement the sensitivity is higher on the combination $\delta+\gamma$ than on the combination $\delta-\gamma$. To better understand this feature, some tests have been made on data considering separately the B^0 and $\bar{B}^0$ samples. In Fig. 6.21 we show the yield fit results

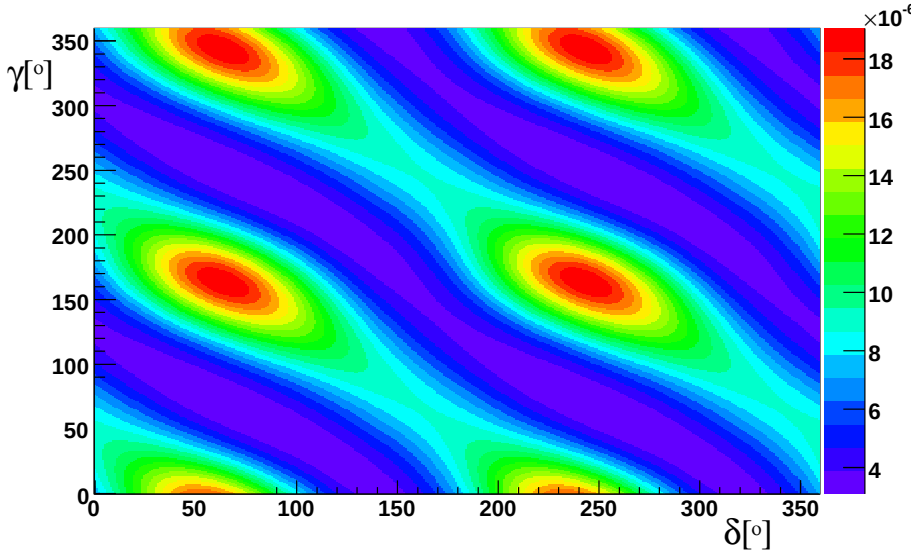

Figure 6.20: Projections, on the two-dimensional plane γ vs r_S of the three-dimensional pdf, combined with the r_S measurement from the ADS measurement.

on the B^0 and $\bar{B}^0$ samples respectively. The results of this fit are summarized in Tab. 6.11.

parameter	B^0 sample	$\bar{B}^0$ sample
N_{SIG}	16 ± 6	18 ± 6
N_{CONT}	897 ± 35	898 ± 34
$N_{B\overline{B}}$	111 ± 21	106 ± 20

Table 6.11: Results of the yield fit, separately for B^0 and $\bar{B}^0$, on $353 fb^{-1}$ on-resonance data.

Fig. 6.22 shows the likelihood scan [1] for γ as a function of δ, for r_S fixed to 0.35, for the B^0 and for the $\bar{B}^0$ sample respectively. The tests show that, despite the fact that the number of signal events is comparable in the two samples, the $\bar{B}^0$ sample is less sensitive to γ and δ_S than the B^0 one. That is probably due to the different position, for the two

[1] The plots show the $-\Delta ln\mathcal{L}$, hence the preferred value is the minimum and the $-\Delta ln\mathcal{L}$=0.5 determines the 1σ region

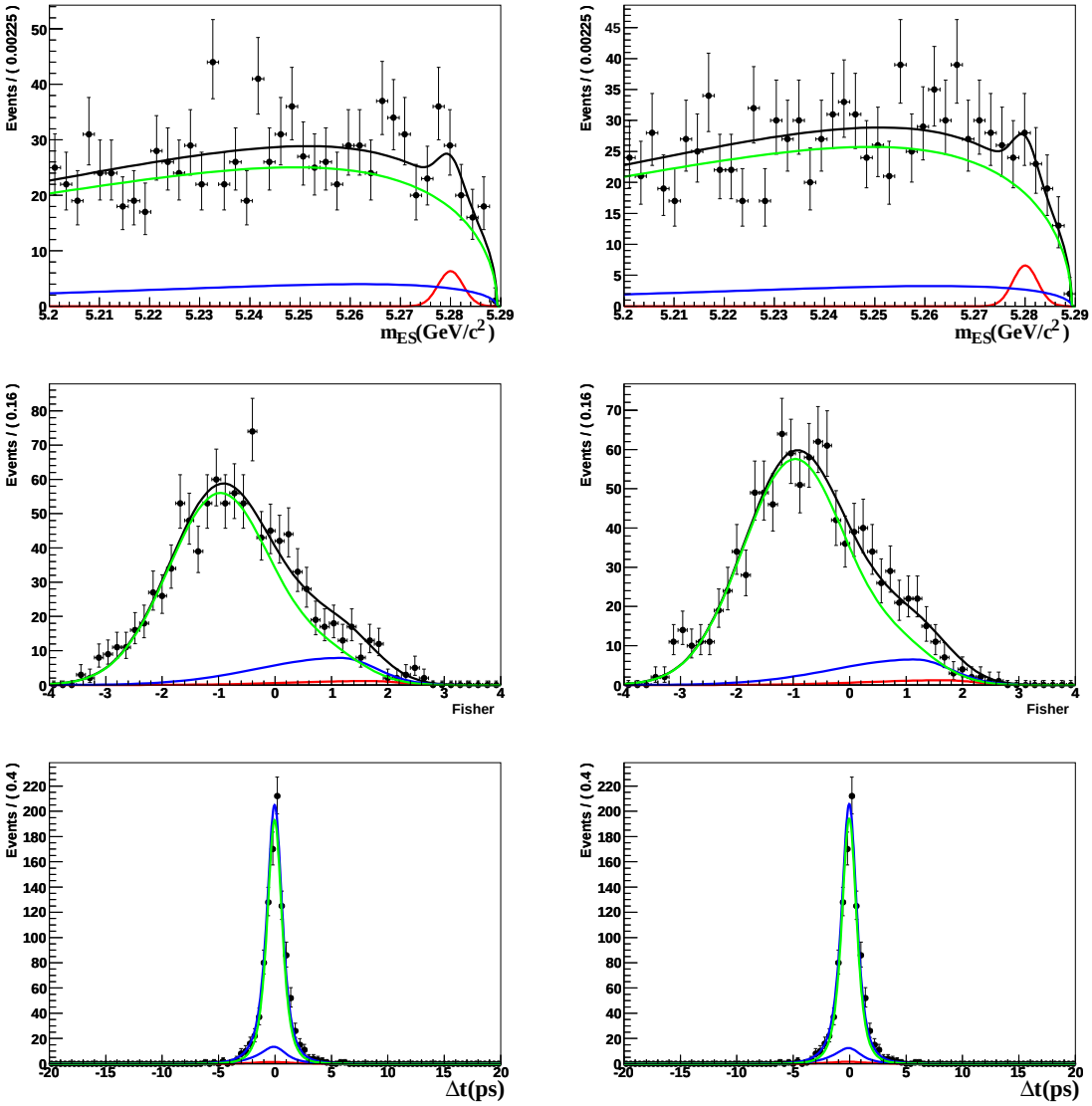

Figure 6.21: m_{ES} (top), Fisher (middle) and Δt (bottom) distributions extracted from the fit on 353 fb^{-1} of on-resonance data for B^0 only (left) and $\bar{B}^0$ only (right). The different components are also shown: signal (red), $B\bar{B}$ (blue) and continuum (green).

samples, of the signal and background events in the Dalitz plot plane and is an effect that is expected to disappear when more data are used.

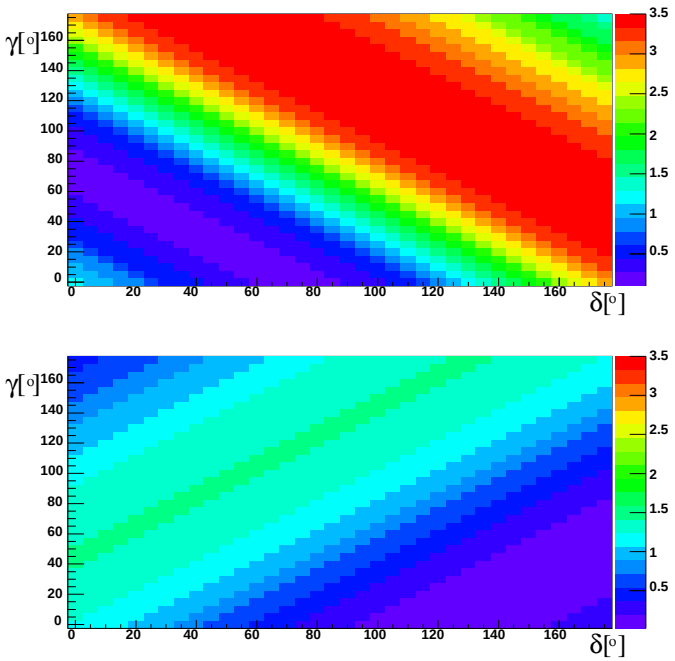

Figure 6.22: $-\Delta ln\mathcal{L}$ as a function of γ and δ_S for r_S fixed in the fit, for B^0 only (top) and for $\bar{B}^0$ only (bottom). The distribution is obtained on 353 fb^{-1} B^0 on-resonance data.

6.5.10 Comparison with expected sensitivity

Despite the large value of r_S (around 0.3), the obtained error on γ is large. A partial explanation of this effect is given in the previous paragraph (6.5.9). To further clarify this situation, we have generated 1000 toy Monte Carlo experiments with the same generation and fit configuration as the one used for the data. The number of signal and background events and all the parameters that are free to vary in the fit are generated according to the values we find on data and r_S is generated, according to the result of the ADS analysis, $r_S = 0.26$ and fixed in the fit. In Fig. 6.23 we show the distribution of the error on γ. The error on γ obtained on data (displayed as a red dotted line in Fig. 6.23) is $\sigma_\gamma = 56^o$, while the mean value of the distribution for the 1000 toy Monte Carlo experiments is $< \sigma_\gamma >= 41^o$. The test has been repeated assuming values at plus and minus one standard deviation from $r_S = 0.26$: $r_S = 0.17$ and $r_S = 0.34$. The mean values and rms of the distributions of the error on γ, assuming $r_S = 0.17$ and $r_S = 0.34$, are $(51 \pm 13)^o$ and $(38 \pm 10)^o$ respectively.

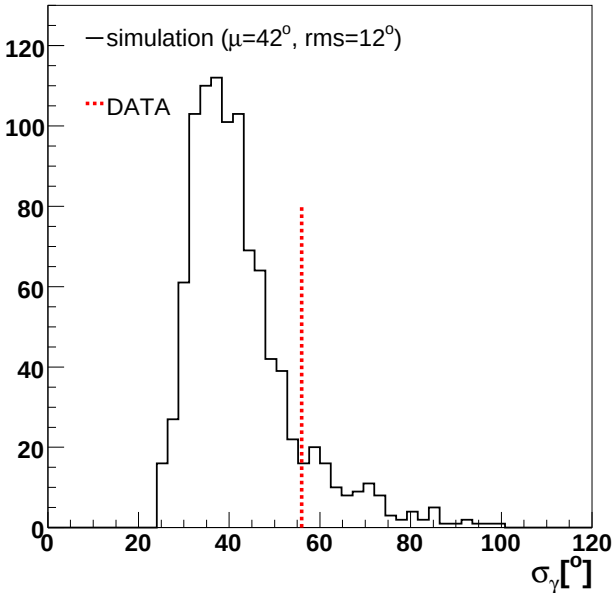

Figure 6.23: Distribution of the error on γ obtained on 1000 different toy Monte Carlo experiments for the Dalitz analysis in which r_S has been generated at the value $r_S = 0.26$ and fixed in the fit. The error obtained in the fit on data is also shown with the dotted line at $\sigma_\gamma = 56^o$.

Chapter 7

Conclusions and perspectives

7.1 Summary of the results

In this thesis the first measurement of r_S and of the angle γ from neutral $B^0 \to D^0(\bar{D}^0)K^{*0}$ decays has been presented. As a first result (see chapter 5), the ratios R_{ADS} for the $B^0 \to D^0(\bar{D}^0)K^{*0}$, with $D^0 \to K^{\pm}\pi^{\mp}$, $K^{\pm}\pi^{\mp}\pi^0$ and $K^{\pm}\pi^{\mp}\pi^{\mp}\pi^{\pm}$ have been measured with the ADS technique using 423 fb^{-1} of data, resulting in the following 68% probability intervals:

$$\begin{aligned} R_{ADS}^{K\pi} &= 0.067^{+0.071}_{-0.057}; \\ R_{ADS}^{K\pi\pi^0} &= 0.060^{+0.055}_{-0.038}; \\ R_{ADS}^{K\pi\pi\pi} &= 0.137^{+0.114}_{-0.097}. \end{aligned} \tag{7.1}$$

Since the single measurements for the R_{ADS} ratios are not statistically significant, 95% probability limits are calculated by integrating the likelihoods, starting from $R_{ADS} = 0$, obtaining $R_{ADS}(K\pi) < 0.244$, $R_{ADS}(K\pi\pi^0) < 0.181$ and $R_{ADS}(K\pi\pi\pi) < 0.391$ at 95% probability. The statistical average of the three R_{ADS} measurements, including the systematic effects and ignoring differences in the r_D parameters and in the strong phases between the three channels, is $0.078^{+0.037}_{-0.035}$, thus indicating a signal with a 2.2 σ significance.

From these results we infer the ratio r_S to be [1]:

$$\begin{aligned} &r_S = 0.26^{+0.077}_{-0.088}, \\ &r_S \in [0.05, 0.396] \text{ at } 95\% \text{ probability}. \end{aligned}$$

This result is consistent with the expectations for a larger value of this parameter in case of neutral B decays, with respect to charged B decays and clearly states the interest of studies of $B^0 \to D^0(\bar{D}^0)K^{*0}$ decays to measure γ.

A first step in this direction, the Dalitz analysis of $B^0 \to D^0(\bar{D}^0)K^{*0}$ with neutral D decaying into $K_s\pi^+\pi^-$ final states based on 353 fb^{-1} data, is presented in chapter 6 of the thesis. The information on the r_S parameter is very helpful for extracting γ from this Dalitz

[1] Which is consistent with the only experimental information on r_S, the upper bound ($r_S < 0.4$) put on this parameter from a low statistics *BABAR* analysis [73].

analysis. Indeed, the analysis suffers from low statistics effects and simulation studies have proved that, only when combining the three-dimensional likelihood obtained from the Dalitz measurement with the external information on r_S, the weak phase γ can be safely extracted. The values obtained for r_S, γ and δ_S from the combination of the ADS and Dalitz analyses are:

$$\begin{aligned} \gamma &= (162 \pm 56)^\circ \text{ or } (342 \pm 56)^\circ; \\ \delta_S &= (62 \pm 57)^\circ \text{ or } (242 \pm 57)^\circ; \\ r_S &= 0.259^{+0.073}_{-0.079} \; ; \in [0.08, 0.397] \;\; \text{at } 95\% \text{ probability}. \end{aligned} \tag{7.2}$$

As commented in sec. 6.5.10, the error (of 56^o) on γ is rather large (see Fig. 6.23), being expected in average to be around 41^o from data driven simulation studies. In Fig. 7.1, the value obtained for r_S is compared with the equivalent ratios for charged B channels. In Fig. 7.2, we show the comparison of the measured value with the expectation for r_S evaluated as explained in sec. 2.4.

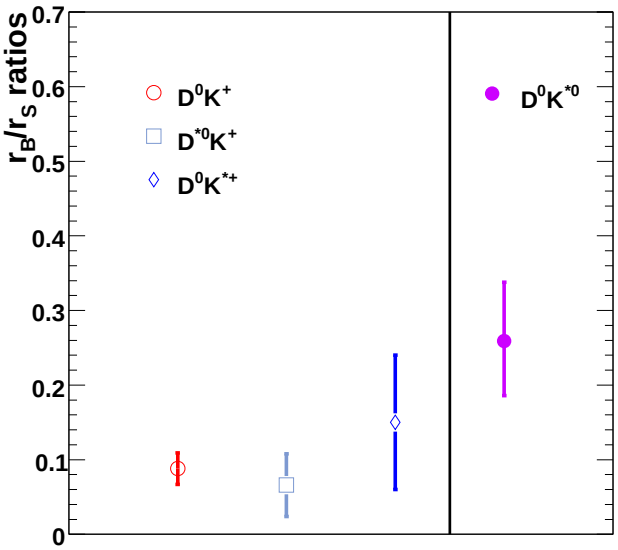

Figure 7.1: Values for the r_B (r_S) ratios for different charged channels, D^0K^+, $D^{*0}K^+$ and D^0K^{*+} ([25]) and for our analysis D^0K^{*0}.

7.2 Perspectives

In the following we show some extrapolations to higher luminosity scenarios for the measurements presented in this thesis.

In Fig. 7.3 (left plot), the evolution of the error on r_S from an ADS analysis using separately the three channels studied in this thesis ($K\pi$, $K\pi\pi^0$ and $K\pi\pi\pi$) is shown. The

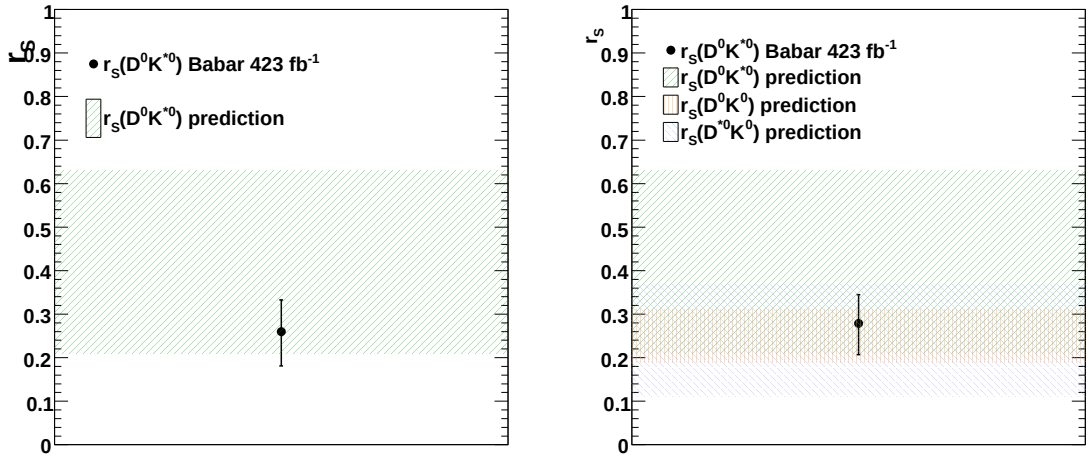

Figure 7.2: The measured value for r_S, represented by the point with error bars, is compared with the 68% probability region expected for r_S for D^0K^{*0} decays from the evaluation presented in sec. 2.4 (left plot). In the right plot, the 68% probability regions expected for r_S for D^0K^0 and $D^{*0}K^0$ decays are also shown.

error on r_S is analytically calculated (up to a scenario of 10 ab^{-1}) according to the expression obtained in 2.16. In this test, r_S is assumed to be $r_S = 0.26$, the relative errors on the R_{ADS} ratios are taken from the measurement presented in chapter 5 and they are assumed to scale with the luminosity ($\propto 1/\sqrt{N}$). The "limit" error on R_{ADS}, $r_D/\sqrt{(3)}$, is also shown in the plot. This term being proportional to r_D, it is lower for $K\pi\pi^0$ than for the other two D decay modes. Fig. 7.3 (right plot) shows the variation, up to a scenario of 10 ab^{-1}, of the error on r_S from the combination of the three D channels.

In Fig. 7.4 (left plot), the variation of the error on γ from the Dalitz analysis of $B^0 \to D^0(\bar{D}^0)K^{*0}$ decays is shown. The values are obtained (for a statistics of 353 fb^{-1}, 450 fb^{-1} and 1 ab^{-1}) from toy Monte Carlo studies, for three different values of r_S, corresponding to the central value found on data and values at plus and minus one standard deviation from it ($r_S = 0.17$, $r_S = 0.26$ and $r_S = 0.34$). In the toy Monte Carlo procedure r_S is fixed in the fit, while γ, δ_S and the yield parameters are left free to vary. With a statistics of 1 ab^{-1}, and for $r_S = 0.26$, an error of $\sim 25^o$ can be obtained on γ from this analysis. In Fig. 7.4 (right plot), the variation of the error on γ from the Dalitz analysis of $B^0 \to D^0(\bar{D}^0)K^{*0}$ decays (for $r_S = 0.26$, corresponding to the central value found on data), for a statistics of 353 fb^{-1}, 450 fb^{-1} and 1 ab^{-1}, is compared with the variation of the error on γ from the Dalitz analysis of D^0K^{*+}, D^0K^+ and $D^{*0}K^+$, with $D^0 \to K_S\pi^+\pi^-$. The values for the errors on γ from the D^0K^{*+}, D^0K^+ and $D^{*0}K^+$ measurements separately are evaluated from the results of the Dalitz *BABAR* analysis [59] for the number of events, the ratios r_B, r_B^* and r_S and γ. It can be noted that the use of neutral B meson decays, $B^0 \to D^0(\bar{D}^0)K^{*0}$, proposed in this thesis, has the second best single-channel sensitivity for measuring γ.

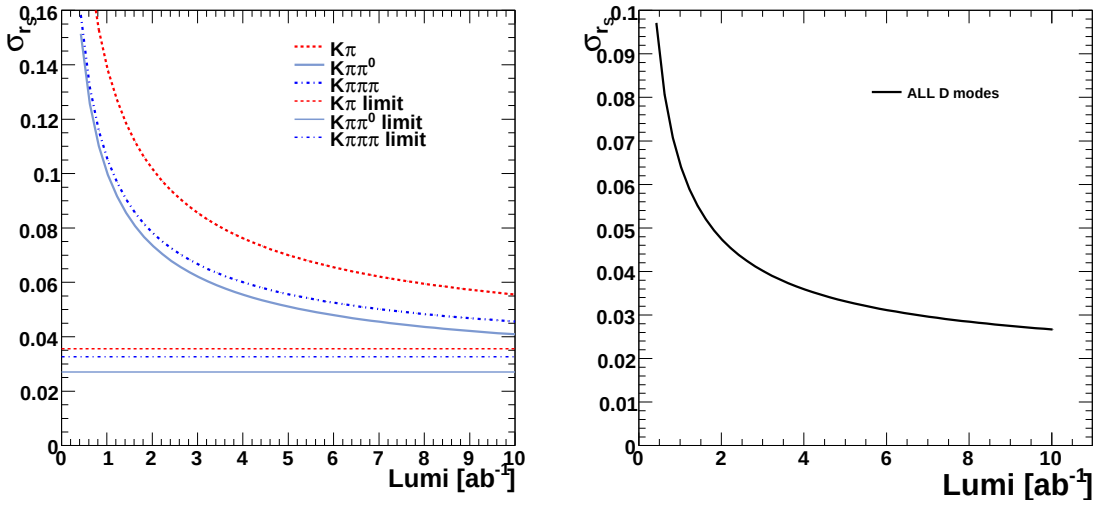

Figure 7.3: Left plot: evolution of the error on r_S from the ADS analysis using separately the three D modes studied in this thesis ($K\pi$, $K\pi\pi^0$ and $K\pi\pi\pi$). The error on r_S is analytically calculated (up to a scenario of 10 ab^{-1}). The "limit" error on R_{ADS} coming from the term containing the phases is also shown. Right plot: variation of the error on r_S from an ADS analysis combining the three channels studied in this thesis ($K\pi$, $K\pi\pi^0$ and $K\pi\pi\pi$). The error on r_S is analytically calculated (up to a scenario of 10 ab^{-1}).

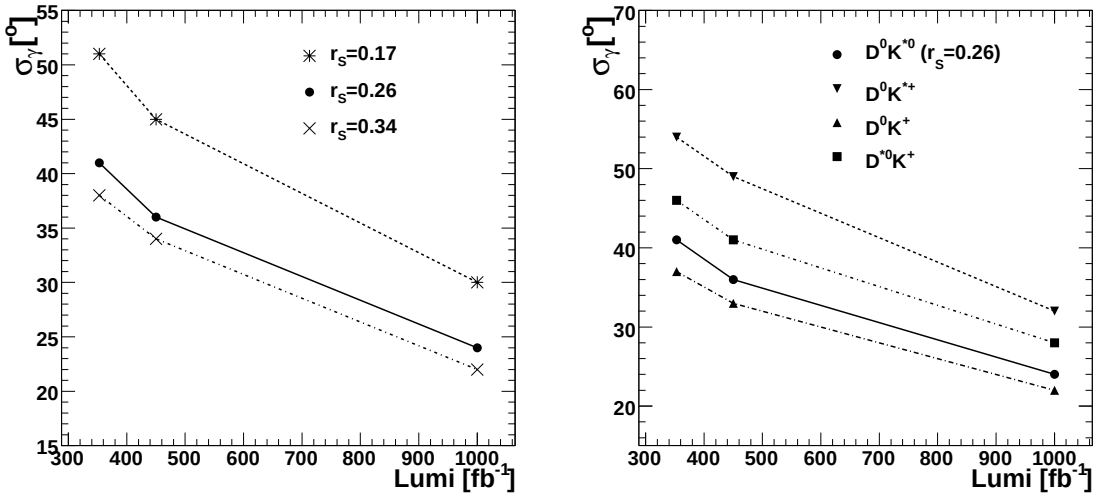

Figure 7.4: Left plot: variation of the error on γ from the Dalitz analysis of $B^0 \to D^0(\bar{D}^0)K^{*0}$ decays, for a statistics of 353 fb^{-1}, 450 fb^{-1} and 1 ab^{-1}, for three different values of r_S ($r_S = 0.17$, $r_S = 0.26$ and $r_S = 0.34$). Right plot: variation of the error on γ from the Dalitz analysis of $B^0 \to D^0(\bar{D}^0)K^{*0}$ decays (for $r_S = 0.26$), for a statistics of 353 fb^{-1}, 450 fb^{-1} and 1 ab^{-1}, is compared with the variation of the error on γ from the Dalitz analysis of D^0K^{*+}, D^0K^+ and $D^{*0}K^+$, with $D^0 \to K_S\pi^+\pi^-$.

Appendix A

Values of the pdf parameters for m_{ES} and Fisher used in the ADS analysis

In Tabs. A.1, A.2 and A.3 we show the values of the pdf parameters, as obtained on MC, for the $K\pi$, $K\pi\pi^0$ and $K\pi\pi\pi$ modes respectively. The choice of the fitting functions are described in sec. 5.4.2, where the plots for the distributions of m_{ES} and Fisher are also shown (Figs. 5.19–5.23). The values shown for the fixed parameters are used for the fit validation with a toy Monte Carlo procedure as explained in sec. 5.4.3 and on a fully simulated sample (sec. 5.4.4). The fitted values (marked as "floated" in the tables, left free to vary in the fit) can be compared with those obtained in the fits to fully simulated samples (see tabs. 5.14–5.16).

Parameter	value	In final fit
Sig m_{ES} $\mu[GeV/c^2]$	5.27950 ± 0.00002	floated
Sig m_{ES} $\sigma[GeV/c^2]$	0.002480 ± 0.000014	fixed
Sig Fisher μ_1	1.135 ± 0.022	fixed
Sig Fisher μ_2	1.708 ± 0.020	fixed
Sig Fisher σ_1	0.571 ± 0.024	fixed
Sig Fisher σ_2	1.024 ± 0.014	fixed
Sig Fisher frac	0.356 ± 0.034	fixed
Same Sign Cont m_{ES} cutoff $[GeV/c^2]$	5.2886 ± 0.0004	floated
Same Sign Cont m_{ES} shape	-39.5 ± 5.5	floated
Opposite Sign Cont m_{ES} cutoff $[GeV/c^2]$	5.2892 ± 0.0001	floated
Opposite Sign Cont m_{ES} shape	-49.3 ± 2.7	floated
Cont Fisher μ	-0.88 ± 0.02	fixed
Cont Fisher σ	0.964 ± 0.015	fixed
Same Sign $B\bar{B}$ m_{ES} cutoff $[GeV/c^2]$	5.2876 ± 0.0006	fixed
Same Sign $B\bar{B}$ m_{ES} shape	-136.5 ± 13.2	fixed
Opposite Sign $B\bar{B}$ m_{ES} cutoff $[GeV/c^2]$	5.2889 ± 0.0009	fixed
Opposite Sign $B\bar{B}$ m_{ES} shape	-50.5 ± 9.8	fixed
$B\bar{B}$ Fisher μ_1	0.93 ± 0.15	fixed
$B\bar{B}$ Fisher μ_2	0.65 ± 0.08	fixed
$B\bar{B}$ Fisher σ_1	0.33 ± 0.12	fixed
$B\bar{B}$ Fisher σ_2	1.01 ± 0.06	fixed
$B\bar{B}$ Fisher frac	0.13 ± 0.08	fixed

Table A.1: [ADS analysis - $K\pi$ mode] Fitted and fixed parameters for the pdf of m_{ES} and Fisher, for $K\pi$ mode, obtained on simulated events.

Parameter	value	In final fit
Sig m_{ES} $\mu[GeV/c^2]$	5.2795 ± 0.00002	floated
Sig m_{ES} $\sigma[GeV/c^2]$	0.002540 ± 0.000023	fixed
Sig Fisher μ_1	0.787 ± 0.029	fixed
Sig Fisher μ_2	1.131 ± 0.041	fixed
Sig Fisher σ_1	1.015 ± 0.024	fixed
Sig Fisher σ_2	0.564 ± 0.051	fixed
Sig Fisher frac	0.685 ± 0.066	fixed
Same Sign Cont m_{ES} cutoff $[GeV/c^2]$	5.28910 ± 0.00015	floated
Same Sign Cont m_{ES} shape	-29.3 ± 2.1	floated
Opposite Sign Cont m_{ES} cutoff $[GeV/c^2]$	5.28900 ± 0.00004	floated
Opposite Sign Cont m_{ES} shape	-33.4 ± 1.2	floated
Cont Fisher μ	-0.852 ± 0.009	fixed
Cont Fisher σ	0.948 ± 0.006	fixed
Same Sign $B\bar{B}$ m_{ES} cutoff $[GeV/c^2]$	5.2893 ± 0.0004	fixed
Same Sign $B\bar{B}$ m_{ES} shape	-63.5 ± 5.0	fixed
Opposite Sign $B\bar{B}$ m_{ES} cutoff $[GeV/c^2]$	5.2891 ± 0.0003	fixed
Opposite Sign $B\bar{B}$ m_{ES} shape	-35.3 ± 4.1	fixed
$B\bar{B}$ Fisher μ_1	0.73 ± 0.08	fixed
$B\bar{B}$ Fisher μ_2	0.26 ± 0.20	fixed
$B\bar{B}$ Fisher σ_1	0.74 ± 0.08	fixed
$B\bar{B}$ Fisher σ_2	1.2 ± 0.1	fixed
$B\bar{B}$ Fisher frac	0.72 ± 0.19	fixed

Table A.2: [ADS analysis - $K\pi\pi^0$ mode] Fitted and fixed parameters for the pdf of m_{ES} and Fisher, for the $K\pi\pi^0$ mode, obtained on simulated events.

Parameter	value	In final fit
Sig m_{ES} $\mu[GeV/c^2]$	5.2795 ± 0.00003	floated
Sig m_{ES} $\sigma[GeV/c^2]$	0.002462 ± 0.000020	fixed
Sig Fisher μ_1	0.75 ± 0.03	fixed
Sig Fisher μ_2	1.05 ± 0.03	fixed
Sig Fisher σ_1	1.03 ± 0.02	fixed
Sig Fisher σ_2	0.56 ± 0.04	fixed
Sig Fisher frac	0.64 ± 0.05	fixed
Same Sign Cont m_{ES} cutoff $[GeV/c^2]$	5.2887 ± 0.0002	floated
Same Sign Cont m_{ES} shape	-34.0 ± 2.6	floated
Opposite Sign Cont m_{ES} cutoff $[GeV/c^2]$	5.2891 ± 0.0001	floated
Opposite Sign Cont m_{ES} shape	-35.6 ± 1.5	floated
Cont Fisher μ	-0.86 ± 0.01	fixed
Cont Fisher σ	0.930 ± 0.007	fixed
Same Sign $B\bar{B}$ m_{ES} cutoff $[GeV/c^2]$	5.2887 ± 0.0004	fixed
Same Sign $B\bar{B}$ m_{ES} shape	-80.0 ± 5.2	fixed
Opposite Sign $B\bar{B}$ m_{ES} cutoff $[GeV/c^2]$	5.2888 ± 0.0006	fixed
Opposite Sign$B\bar{B}$ m_{ES} shape	-34.3 ± 4.6	fixed
$B\bar{B}$ Fisher μ_1	0.59 ± 0.05	fixed
$B\bar{B}$ Fisher μ_2	0.24 ± 0.14	fixed
$B\bar{B}$ Fisher σ_1	0.72 ± 0.07	fixed
$B\bar{B}$ Fisher σ_2	1.2 ± 0.1	fixed
$B\bar{B}$ Fisher frac	0.71 ± 0.15	fixed

Table A.3: [ADS analysis - $K\pi\pi\pi$ mode] Fitted and fixed parameters for the pdf of m_{ES} and Fisher, for $K3\pi$ mode, obtained on simulated events.

Appendix B

More details on toy Monte Carlo results for the ADS analysis

The fit validation using a toy Monte Carlo procedure is presented in sec. 5.4.3. More details are given in the following. In Fig. B.1, B.2 and B.3, we show the distribution of N_{DK^*} and of its error for the three D^0 channels. For the three D modes, we also show the pull distributions for continuum and $B\bar{B}$ background events are shown in Fig. B.4, B.5 and B.6.

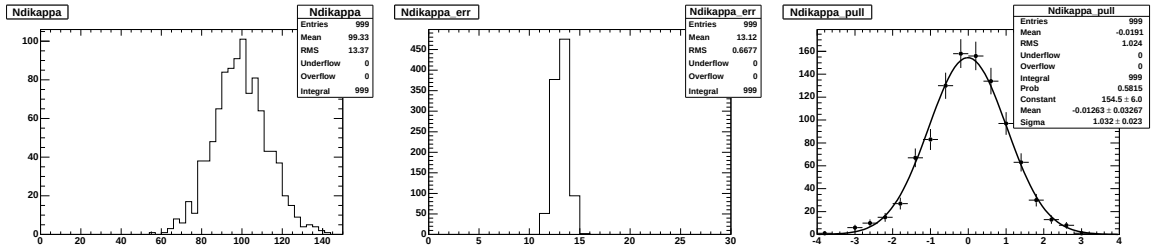

Figure B.1: [$K\pi$ mode] Distributions of the fitted value (left), the error (middle) and the pull (right) for N_{DK^*} obtained with the toy MC described in the text for the $K\pi$ channel.

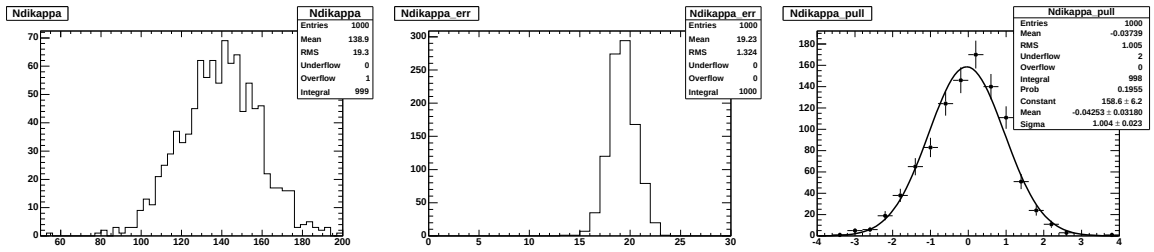

Figure B.2: [$K\pi\pi^0$ mode] Distributions of the fitted value (left), the error (middle) and the pull (right) for N_{DK^*} obtained with the toy MC described in the text for the $K\pi\pi^0$ channel.

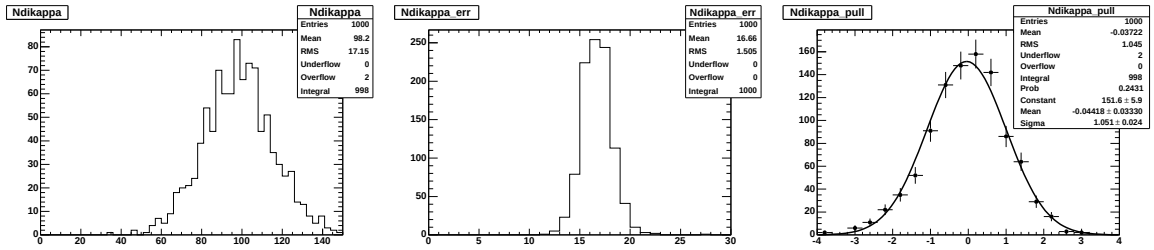

Figure B.3: [$K\pi\pi\pi$ mode] Distributions of the fitted value (top left), the error (top right) and the pull (bottom) for N_{DK^*} obtained with the toy MC described in the text for the $K3\pi$ channel.

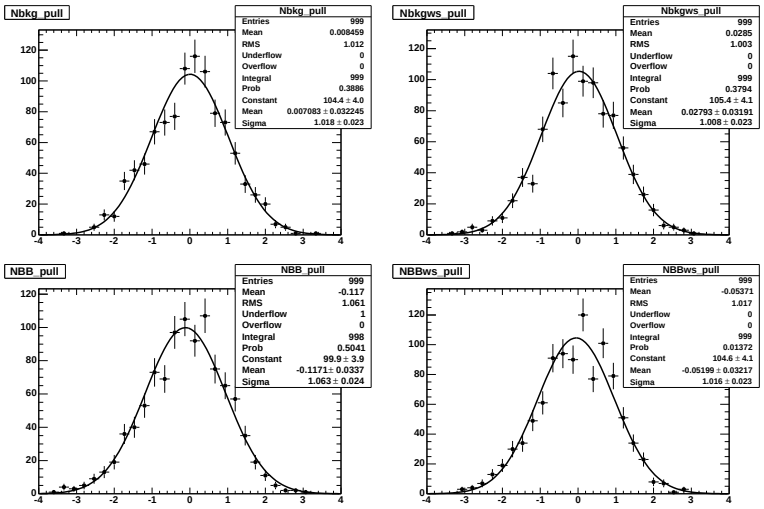

Figure B.4: [$K\pi$ mode] Pull distributions for continuum same sign (top left), continuum opposite sign (top right), $B\bar{B}$ same sign background (bottom left) and $B\bar{B}$ opposite sign background (bottom right) for the $K\pi$ channel.

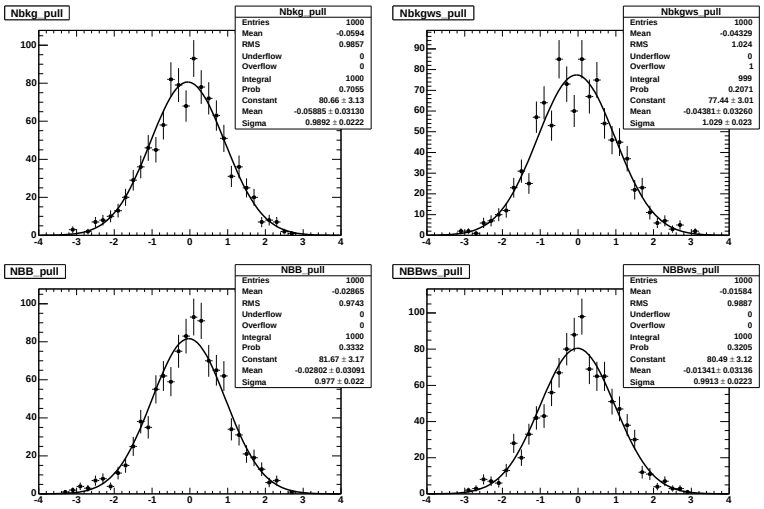

Figure B.5: [$K\pi\pi^0$ mode] Pull distributions for continuum same sign (top left), continuum opposite sign (top right), $B\bar{B}$ same sign background (bottom left) and $B\bar{B}$ opposite sign background (bottom right) for the $K\pi\pi^0$ channel.

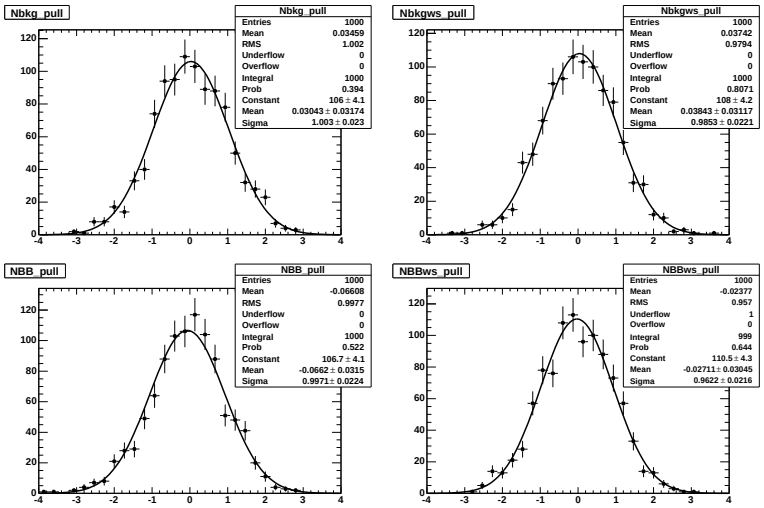

Figure B.6: [$K\pi\pi\pi$ mode] Pull distributions for continuum same sign (top left), continuum opposite sign (top right), $B\bar{B}$ same sign background (bottom left) and $B\bar{B}$ opposite sign background (bottom right) for the $K3\pi$ channel.

Appendix C

Values of the pdf parameters for m_{ES}, Fisher and Δt used in the Dalitz analysis

Tab. C.1 summarizes the values of the pdf parameters used in the "yield" fit for the Dalitz analysis. The table also shows which of these parameters are floated in the final fit on data (in addition to the number of events for sig, Cont and $B\bar{B}$).

The choice of the fitting functions are described in sec. 6.4.2, where the plots for the distributions of m_{ES}, Fisher and Δt are also shown (Figs. 6.8, 6.9 and 6.10). The values shown for the fixed parameters are used for the fit validation with a toy Monte Carlo procedure as explained in sec.6.5.2. The shapes of the distributions have been checked with an sPlot technique (sec. 6.5.3). The fitted values (marked as "floated" in the tables, left free to vary in the fit) can be compared with those obtained in the fit on real data (see tab. 6.8).

Shape parameter	value	status in final fit on data
m_{ES}		
Sig μ_{mES}	5.27957 ± 0.00002 GeV/c^2	floated
Sig σ_{mES}	2.48 ± 0.01 MeV/c^2	fixed
Cont $cutoff_{mES}$	5.29 GeV/c^2	fixed
Cont $slope_{mES}$	-32.5 ± 8.2	fixed
$B\bar{B}$ $cutoff_{mES}$	5.29 GeV/c^2	fixed
$B\bar{B}$ $slope_{mES}$	-56.0 ± 6.7	floated
$\mathcal{F}$		
Sig μ_{Fish}	1.69 ± 0.02	fixed
Sig $\sigma_{L\ Fish}$	1.41 ± 0.01	fixed
Sig $\sigma_{R\ Fish}$	0.52 ± 0.01	fixed
Cont f_{Fish}	0.08 ± 0.03	fixed
Cont $\mu_{1\ Fish}$	1.0 ± 0.6	fixed
Cont $\mu_{2\ Fish}$	-9.68 ± 0.07	fixed
Cont $\sigma_{1\ Fish}$	0.63 ± 0.12	fixed
Cont $\sigma_{2\ Fish}$	0.92 ± 0.55	fixed
$B\bar{B}$ μ_{Fish}	1.19 ± 0.19	fixed
$B\bar{B}$ $\sigma_{L\ Fish}$	1.46 ± 0.13	fixed
$B\bar{B}$ $\sigma_{R\ Fish}$	0.63 ± 0.11	fixed
Δt		
Sig Δt μ_{Core}	$(-0.3087 \pm 0.102) \cdot 10^{-12}$s	fixed
Sig Δt $scale_{\sigma\ Core}$	1.269 ± 0.166	fixed
Sig Δt μ_{Tail}	$(-7.21 \pm 0.85) \cdot 10^{-12}$s	fixed
Sig Δt σ_{Tail}	$(1.36 \pm 1.7) \cdot 10^{-12}$s	fixed
Sig Δt μ_{Out}	$0. \cdot 10^{-12}$s	fixed
Sig Δt σ_{Out}	$8. \cdot 10^{-12}$s	fixed
Sig Δt f_{Tail}	0.0079 ± 0.0060	fixed
Sig Δt f_{Out}	0.0053 ± 0.0100	fixed
$\tau_{B^+B^-}$	$1.53 \cdot 10^{-12}$s	fixed
Cont Δt μ_{Core}	$(-0.0717 \pm 0.365) \cdot 10^{-12}$s	fixed
Cont Δt $scale_{\sigma\ Core}$	0.146 ± 0.22	fixed
Cont Δt f_{Short}	0.897 ± 0.112	fixed
$B\bar{B}$ Δt μ_{Core}	$(0.074 \pm 0.365) \cdot 10^{-12}$s	fixed
$B\bar{B}$ Δt $scale_{\sigma\ Core}$	1.773 ± 0.222	fixed
$B\bar{B}$ Δt μ_{Tail}	$(-0.73 \pm 0.56) \cdot 10^{-12}$s	fixed
$B\bar{B}$ Δt σ_{Tail}	$(1.52 \pm 0.35) \cdot 10^{-12}$s	fixed
$B\bar{B}$ Δt f_{Tail}	0.36 ± 0.19	fixed
$B\bar{B}$ Δt f_{Out}	0.72 ± 0.13	fixed

Table C.1: PDF parameters as extracted from the m_{ES} $\mathcal{F}$ and Δt fit on MC and offresonance data.

Appendix D

Details on Dalitz analysis systematic uncertainties

The systematic uncertainties for the Dalitz analysis are presented in sec. 6.5.8 and summarized in Tab. 6.10. In Tab. D.1 we give more details on the single contributions.

Parameter	val $\pm$ err	$\Delta\gamma[^o]$	$\Delta\delta[^o]$	Δr_S
Sig m_{ES} pdf TOT sys		$4.7\ 10^{-1}$	$9.4\ 10^{-1}$	$5.3\ 10^{-3}$
Sig Fisher pdf TOT sys		$3.7\ 10^{-2}$	$1.\ 10^{-1}$	$8.9\ 10^{-4}$
Sig Δt pdf TOT sys		$2.5\ 10^{-1}$	$2.5\ 10^{-1}$	$1.6\ 10^{-3}$
Cont m_{ES} pdf TOT sys	-32.5 ± 8.2	$1.8\ 10^{-1}$	$1.1\ 10^{-1}$	$8.5\ 10^{-3}$
Cont Fisher pdf TOT sys		$8.8\ 10^{-1}$	1.15	$5\ 10^{-2}$
Cont Δt pdf TOT sys		1.0	1.5	$7.3\ 10^{-3}$
BB m_{ES} pdf TOT sys	-48.3 ± 10.0	$2.1\ 10^{-2}$	$4.5\ 10^{-2}$	$1.5\ 10^{-3}$
BB Fisher pdf TOT sys		$3.5\ 10^{-1}$	1.1	$1.2\ 10^{-2}$
BB Δ t pdf TOT sys		$3.9\ 10^{-1}$	$5.9\ 10^{-1}$	$1.8\ 10^{-3}$
TOT sys from pdf		1.5	2.5	$5.2\ 10^{-2}$
Peaking bkg assumptions		$1.4\ 10^{-1}$	$1.2\ 10^{-1}$	$3.5\ 10^{-4}$
$fracD0_{C}ontandBB$	0.289 ± 0.028	$5.2\ 10^{-2}$	$3.2\ 10^{-2}$	$1.0\ 10^{-2}$
k parameter	0.95	$7.2\ 10^{-2}$	1.2	$7.1\ 10^{-2}$
Dalitz model (K-matrix)		2.9	5.5	$3\ 10^{-3}$
Dalitz model (no σ_1 and σ_2)		6.4	15.8	$6\ 10^{-2}$
Sig eff. over the Dalitz plot		$3.1\ 10^{-1}$	$6.2\ 10^{-1}$	$6.0\ 10^{-3}$
Dalitz shape for fake-D^0 bkg		$3.0\ 10^{-2}$	$2.7\ 10^{-1}$	$2.0\ 10^{-3}$
BB V_{cb}-like evt fraction		$1.0\ 10^{-2}$	$1.0\ 10^{-1}$	$4.7\ 10^{-3}$
Cont V_{cb}-like evt fraction		$5.0\ 10^{-3}$	$3.5\ 10^{-2}$	$1.9\ 10^{-2}$
TOT syst		(3.2) 6.6	(6.2) 16.1	(8.9) $1.0\ 10^{-1}$

Table D.1: Systematics contributions to the determination of γ, δ and r_S.

Bibliography

[1] J. Wess, *"The Cpt Theorem And Its Significance For Fundamental Physics,"* Nucl. Phys. Proc. Suppl. **8** (1989) 461.

[2] N. Cabibbo, *"Unitary Symmetry And Leptonic Decays,"* Phys. Rev. Lett. **10** (1963) 531; M. Kobayashi and T. Maskawa, *" CP Violation In The Renormalizable Theory Of Weak Interaction,"* Prog. Theor. Phys. **49** (1973) 652.

[3] J. H. Christenson, J. W. Cronin, V. L. Fitch and R. Turlay, *Phys. Rev. Lett.* **13** (1964) 138.

[4] S. Weinberg, *"Mixing Angle In Renormalizable Theories Of Weak And Electromagnetic Interactions,"* Phys. Rev. D **5** (1972) 1962.

[5] L. L. Chan and W. L. Keung, *Phys. Rev. Lett.* **53** (1984) 1802.

[6] L. Wolfenstein, *Phys. Rev. Lett.* **51** (1983) 1945.

[7] A. J. Buras, M. E. Lautenbacher and G. Ostermaier, Phys. Rev. D **50** (1994) 3433.

[8] W. M. Yao *et al.* (Particle Data Group), J. Phys. G **33**, 1 (2006).

[9] M. Ciuchini *et al.*, JHEP **0107**, 013 (2001) [arXiv:hep-ph/0012308].

[10] G. Buchalla, A. J. Buras and M. E. Lautenbacher, *" Weak Decays Beyond Leading Logarithms,"* Rev. Mod. Phys. **68** (1996) 1125 `hep-ph/9512380`.

[11] C. Jarlskog, Phys. Rev. Lett, **55**, 1039 (1985)

[12] T.Inami and C.S.Lim, *Prog.Theor.Phys.* **65** (1981) 297; *ibid.* **65** (1981) 1772.

[13] A.J. Buras, M. Jasmin and P.H. Weisz, *Nucl. Phys.* **B347** (1990) 491.

[14] T. T. E. Group *et al.* [CDF Collaboration], arXiv:0803.1683 [hep-ex].

[15] S. Herrlich and U. Nierste, *Nucl. Phys.* **B419** (1994) 192.

[16] F. Parodi, P. Roudeau and A. Stocchi, Nuovo Cim. A **112**, 833 (1999) [arXiv:hep-ex/9903063].

[17] J. Charles *et al.* [CKMfitter Group], Eur. Phys. J. C **41**, 1 (2005) [arXiv:hep-ph/0406184].

[18] S. Plaszczynski and M. H. Schune, arXiv:hep-ph/9911280; Y. Grossman, Y. Nir, S. Plaszczynski and M. H. Schune, Nucl.Phys.B **511** (1998) 69; G. P. Dubois-Felsmann, D. G. Hitlin, F. C. Porter and G. Eigen, CALT 68-2396 (2002).

[19] M. Bona *et al.* [UTfit Collaboration], JHEP **0507**, 028 (2005) [arXiv:hep-ph/0501199].

[20] M. Bona *et al.* [UTfit Collaboration], JHEP **0610**, 081 (2006) [arXiv:hep-ph/0606167].

[21] M. Beneke, G. Buchalla, M. Neubert and C.T. Sachrajda, *" QCD factorization for exclusive, non-leptonic B meson decays: General arguments and the case of heavy-light final states,"* Nucl. Phys. B **591** (2000) 313; *" QCD factorization for B –¿ pi K decays,"* hep-ph/0007256.

[22] J. D. Bjorken, *" Topics in B Physics,"* Nucl. Phys. Proc. Suppl. **11** (1989) 325.

[23] A. J. Buras and L. Silvestrini, *" Non-leptonic two-body B decays beyond factorization,"* Nucl. Phys. B **569** (2000) 3, hep-ph/9812392.

[24] M. Ciuchini, E. Franco, G. Martinelli and L. Silvestrini, *" Charming penguins in B decays,"* Nucl. Phys. B **501** (1997) 271, hep-ph/9703353; M. Ciuchini, R. Contino, E. Franco, G. Martinelli and L. Silvestrini, *" Charming-penguin enhanced B decays,"* Nucl. Phys. B **512** (1998) 3, hep-ph/9708222.

[25] Updated results on the web page **http://www.utfit.org**.

[26] M. Gronau and J. L. Rosner, Phys. Lett. B **439**, 171 (1998) [arXiv:hep-ph/9807447]. B. Blok, M. Gronau and J. L. Rosner, Phys. Rev. Lett. **78**, 3999 (1997) [arXiv:hep-ph/9701396].

[27] G. Cavoto *et al.*, Proceedings of the CKM 2005 Workshop (WG5), UC San Diego, 15-18 March 2005 [arXiv:hep-ph/0603019].

[28] M. Gronau, D. Wyler, Phys. Rev. Lett. **B253** (1991) 483.

[29] M. Gronau, D. London, Phys. Rev. Lett. **B265** (1991) 172.

[30] I. Dunietz, Phys. Rev. Lett. **B270** (1991) 75; Phys. Rev. Lett. **D52** (1995) 3048.

[31] D. Atwood, I. Dunietz and A. Soni, *"Enhanced CP violation with B → K D0 (anti-D0) modes and extraction of the CKM angle gamma,"* Phys. Rev. Lett. **78**, 3257 (1997) [arXiv:hep-ph/9612433].

[32] A. Giri, Y. Grossman, A. Soffer and J. Zupan, *"Determining gamma using B+- → D K+- with multibody D decays,"* Phys. Rev. D **68** (2003) 054018 [arXiv:hep-ph/0303187].

[33] M.Gronau, Phys.Lett. B557 (2003) 198-206.

[34] M. Gronau, *Phys. Lett.* **B557**, 198-206 (2003).

[35] B. Aubert *et al.*, *BABAR* Collaboration, Nucl. Instr. and Methods A **479**, 1 (2002).

[36] *PEP II - An Asymmetric B Factory, Conceptual Design Report*, SLAC-418, LBL-5379 (1993).

[37] P.F. Harrison, *et al.*, *BABAR* Collaboration, *The BABAR physics book: Physics at an asymmetric B factory.*, SLAC-R-0504 (1998).

[38] J. Seeman *et al.*, *Results and Plans of the PEP-II B Factory*, SLAC-PUB-10547, Contribution to EPAC 2004 (2004).

[39] B. Aubert *et al.*, *BABAR* Collaboration, *The First Year of the BABAR experiment at PEP-II*, BABAR-CONF-00/17, Contribution to XXX^{th} International Conference of High Energy Physics, Osaka (Japan) (2000).

[40] C. Bozzi *et al.*, Nucl. Instr. and Method A **453**, 78 (2000).

[41] V. Re *et al.*, Nucl. Instr. and Method A **511**, 1 (2003).

[42] V. Re *et al.*, Nucl. Instr. and Method A **501**, 14 (2003).

[43] G. Sciolla *et al.*, Nucl. Instr. and Method A **419**, 310 (1998).

[44] M. H. Kelsey *et al.*, Nucl. Instr. and Method A **536**, 206 (2004).

[45] I. Adam *et al.*, IEEE Trans. Nucl. Sci. 45, 657 (1998).

[46] I. Adam *et al.*, SLAC-PUB-8783 (2001).

[47] B. Lewandowski *et al.*, Nucl. Instr. and Method A **494**, 302 (2002).

[48] F. Anulli *et al.*, Nucl. Instr. and Method A **409**, 542 (1998).

[49] CLEO Collaboration, S. Kopp *et al.*, Phys. Rev. D **63**, 092001 (2001); CLEO Collaboration, H. Muramatsu *et al.*, Phys. Rev. Lett. **89**, 251802 (2002); erratum-ibid: **90** 059901 (2003).

[50] Particle Data Group, S. Eidelman et al., **592**, 1 (2004).

[51] BABAR Collaboration, B. Aubert *et al.*, Phys. Rev. Lett. **95** 171802 2005.

[52] F. Polci, M.-H. Schune and A. Stocchi [arXiv:hep-ph/0605129].

[53] R. A. Fisher, Annals Eugen. **7**, 179 (1936).

[54] N. Cabibbo and A. Maksymowicz, Phys. Rev. Lett. **352**, 9 (1964).

[55] D. M. Asner *et al.* [CLEO Collaboration], arXiv:0802.2268 [hep-ex].

[56] A. S. Powell, arXiv:0805.1722 [hep-ex].

[57] BaBar Collaboration, B. Aubert *et al.*, Phys. Rev. Lett. **97**, 221803 (2006).

[58] M. Pivk and L. Le Diberder, Nucl.Instrum.Meth.A555:356-369,2005

[59] B. Aubert [The BABAR Collaboration], arXiv:0804.2089 [hep-ex].

[60] Review on Scalar Mesons in Ref. [8].

[61] B. Aubert *et al.* (*BABAR* Collaboration), Phys. Rev. Lett. **95**, 121802 (2005).

[62] E. P. Wigner, Phys. Rev. **70**, 15 (1946); S. U. Chung *et al.*, Ann. Phys. **4**, 404 (1995).

[63] I. J. R. Aitchison, Nucl. Phys. A **189**, 417 (1972).

[64] B. Aubert *et al.* [BABAR Collaboration],Phys. Rev. D **77**, 111102 (2008) [arXiv:0802.4052 [hep-ex]].
B. Aubert *et al.* [BABAR Collaboration],Phys. Rev. D **71**, 031102 (2005) [arXiv:hep-ex/0411091].
B. Aubert *et al.* [BABAR Collaboration],Phys. Rev. D **72**, 071103 (2005) [arXiv:hep-ex/0507002].

[65] K. Abe *et al.* [BELLE Collaboration], Phys. Rev. D **73**, 051106 (2006) [arXiv:hep-ex/0601032].

[66] BaBar Collaboration, B. Aubert *et al.*, Phys. Rev. D **72** (2005) 032004.

[67] BaBar Collaboration, B. Aubert *et al.*, Phys. Rev. D **76** (2007) 111101.

[68] Y. Horii *et al.* [Belle Collaboration], arXiv:0804.2063 [hep-ex].

[69] B. Aubert *et al.* [BABAR Collaboration], arXiv:0804.2089 [hep-ex].

[70] A. Poluektov *et al.* [Belle Collaboration], Phys. Rev. D **73**, 112009 (2006) [arXiv:hep-ex/0604054].

[71] B. Aubert *et al.* [BaBar Collaboration], Phys. Rev. Lett. **99**, 251801 (2007) [arXiv:hep-ex/0703037].

[72] V. V. Anisovich and A. V. Sarantsev, Eur. Phys. Jour. **A16**, 229 (2003).

[73] B. Aubert *et al.* (BABAR Collaboration), Phys. Rev. **D74**, 031101 (2006).

Abstract

In this thesis we present *CP* violation studies in the B mesons system, and in particular measurements of the angle γ of the Unitarity Triangle, using data collected by the *BABAR* experiment. The angle γ is the relative weak phase between the V_{ub} and V_{cb} elements of the CKM matrix. A crucial parameter, which drives the sensitivity to γ, is the ratio r between $b \to u$ and $b \to c$ transition amplitudes.

In the first part of the thesis, general issues on γ studies and the status of the present measurements are introduced.

The experimental work is then detailed. It is composed of two different analyses of $B^0 \to D^0(\bar{D}^0)K^{*0}$. In the first analysis, these decays are studied through the ADS method, where the neutral D mesons are reconstructed into $K^{\pm}\pi^{\mp}$, $K^{\pm}\pi^{\mp}\pi^0$ and $K^{\pm}\pi^{\mp}\pi^{\pm}\pi^{\mp}$ final states. This analysis allows to determine, for the first time, the ratio r for $B^0 \to D^0(\bar{D}^0)K^{*0}$, which is found to be $r = 0.260^{+0.077}_{-0.088}$. The large value for the parameter r makes the use of this channel interesting for present and future facilities, for the determination of γ.

In the second analysis, tha channel $B^0 \to D^0(\bar{D}^0)K^{*0}$ is studied with a Dalitz method and the neutral D mesons are reconstructed into $K_S\pi^+\pi^-$ final states. The determination of γ from this analysis is $\gamma = (162 \pm 56)^\circ$, with a 180° ambiguity. The result for r from the combination of the two analyses is: $r = 0.259^{+0.073}_{-0.079}$. These results represent the first contraints on γ and r obtained from neutral B decays.

Finally, data driven simulation studies are discussed, which show that the study of the $B^0 \to D^0(\bar{D}^0)K^{*0}$ is competitive, for the determination of γ, with the other analysis aiming to extract γ from charged B decays.

Key words: *CP* violation, CKM, *BABAR* experiment, UTfit, weak phase γ, $b \to u$ amplitude, ADS method, Dalitz method

Résumé

Cette thèse porte sur l' étude de la violation de *CP* dans le secteur des mésons B et en particulier les mesures de l'angle γ du Triangle d'Unitarité, en utilisant les données enregistrées par le détecteur *BABAR* . L'angle γ est la phase relative entre les éléments V_{ub} et V_{cb} de la matrice CKM. Un paramètre très important dans les mesures de γ est le rapport r entre les amplitudes des désintégrations qui comportent une transition des quarks $b \to u$ et les désintégrations qui comportent une transition $b \to c$. La sensibilité à γ est proportionelle à la valeur de ce paramètre.

Dans la première partie de cette thèse, les problematiques liées à l'étude de l'angle γ ainsi que l'état actuel des mesures sont presentés.

Le travail experimental est ensuite présenté, il comporte deux analyses en utilisant les désintégrations $B^0 \to D^0(\bar{D}^0)K^{*0}$. Dans la première analyse, le canal $B^0 \to D^0(\bar{D}^0)K^{*0}$ est étudié en utilisant une méthode ADS et les mésons D neutres sont reconstruits dans les états finals $K^{\pm}\pi^{\mp}$, $K^{\pm}\pi^{\mp}\pi^0$ et $K^{\pm}\pi^{\mp}\pi^{\pm}\pi^{\mp}$. Cette analyse permet de mesurer, pour la première fois, le rapport r pour le canal $B^0 \to D^0K^{*0}$. On obtient: $r = 0.260^{+0.077}_{-0.088}$. La grande valeur obtenue pour r rend l'utilisation de ce canal très intéressante pour les expériences présentes et futures, pour la détermination de l'angle γ.

Dans la deuxième analyse, le canal $B^0 \to D^0(\bar{D}^0)K^{*0}$ est étudié avec une méthode Dalitz et les mésons D neutres sont reconstruits dans l'état final $K_S\pi^+\pi^-$. Cette analyse permet une mesure de l'angle γ. On obtient $\gamma = (162 \pm 56)^\circ$ avec une ambiguité de 180°. La détermination du paramètre r par les deux analyses combinées est: $r = 0.259^{+0.073}_{-0.079}$. Ces analyses donnent les premièrs resultats sur γ et r obtenus à partir des études des mésons B neutres.

Finalement, des études de simulation, basés sur les données, sont presentés. Ces études montrent que l'utilisation des canaux $B^0 \to D^0(\bar{D}^0)K^{*0}$ peut donner une sensitivité a γ comparable avec celle des autres analyses, qui utilisent les mésons B chargés.

Key words: violation de *CP*, CKM, experience *BABAR* , UTfit, phase faible γ, amplitude $b \to u$, méthode ADS, méthode Dalitz

Remerciements, Ringraziamenti, Acknowledgements

Je veux premièrement remercier les institutions qui m'ont permis de faire cette thèse de doctorat, en cotutelle entre France et Italie: l'Université franco-italienne, l'école doctorale *constituants élémentaires et systemes complexes* (ED381), le Laboratoire de l'Accélérateur Linéaire et L'Università di Roma La Sapienza. Cette miraculeuse et délicate cooperation entre les deux administrations a exigé l'effort et l'application de plusieurs personnes, en premiers mes deux directeurs de thèse: Achille Stocchi e Fernando Ferroni, que je remercie pour ca d'abord.

Du point de vue scientifique, par contre, la cooperation a eté beacoup plus simple et enrichissante, je veux remercier tous les gens qui m'ont aidé et avec lesquelles j'ai travaillé. Je remercie d'abord la commission de thèse, et en particulier les rapporteurs, Jean-Pierre et Olivier: votre aide a eté très précieuse. Many thanks to Hassan, who came from faraway for this thesis defense. Grazie ai grandi capi di sempre Ferroni e Martinelli. Merci à Guy et Achille.

Merci au groupe Babar du LAL: Anne-Marie, Marie-Hélène, Achille, Patrick, Michel, Nicolas, Guy, Gilbert et Stéphane (qui maintenant est parti, mais qui m'a beaucoup aidé avec son expertise de programmation). Et, dans le goupe du LAL, je remercie mes co-thésards: Francesco (bon, pour une période!), Justine et Joao, pour leur soutien et parce que a eté un plaisir de partager cette aventure avec vous. Nicolas, merci pour tous ce que tu m'as appris a SLAC (et pas seulement) et pour avoir toujours fait attention à moi. Marie-Hélène, merci pour m'avoir montré comment un physicien expérimentateur devrait être, j'ai appris plein des choses en travaillant avec toi (et je me suis amusée en plus!).

Je dois ensuite remercier la groupe de Rome, la baita: Betta, non solo per la convivenza a SLAC, i margarita e le chiacchierate in piscina leggendo Cosmopolitan, Francesco per la sua creativitá nella scelta degli sfondi del laptop, Mao per l'attenzione, la compagnia e il sostegno anche da lontano, Luca per i suoi mille consigli e per l'aiuto sulle analisi e non solo, Sha per essere sempre disponibile a rispondere alle mie strane domande su root, Cecilia che mi ha seguita da quando ero una piccola laureanda, Daniele per i consigli, Alessia infallibile organizzatrice e Marco per avermi portata sulle piste nere e non avermi costretta ad ascoltare troppo le sue doti canore durante le lunghe ore di lavoro. Un ringraziamento speciale a Baffo, che mi ha aiutata tantissimo dal punto di vista tecnico e morale e a Maurizio, che è insostituibile e sempre pronto ad aiutarmi (e anche a lamentarsi!). Infine voglio ringraziare Riccardo Faccini per il suo costante aiuto e sostegno anche da lontano (anche quando era PAC e avevamo appuntamento telefonico tutti i martedí mattina mentre andava a SLAC in

macchina!): Ric, ho imparato tantissimo da te e so che ho ancora tantissimo da imparare.

Come non parlare inoltre della collaborazione UTfit, un'esperienza da cui ho imparato tante cose, voglio ringraziare in particolare Luca, Marco, Marcella (grazie per i mille aiuti sulle macro!), Maurizio, Achille.

Many thanks to the people at SLAC that taught me many things (also if they will probably never read this thesis!): the Run6 coordination team (Nicolas and Gigi for first), all the people in ir2 and PEP II with their infinite and different knowledges, the *BABAR* online data acquisition group.

Grazie a tutti i vari personaggi che hanno popolato il mio mondo in questi tre anni, per lo piú incontrati a SLAC e poi rivisti a conferenze nei luoghi piú improbabili in giro per il mondo: Salvati prima di tutto, il mio coinquilino che "i coltelli nella lavastoviglie vanno messi a testa in giù", MaVio, Cervelli, Cenci, Silvano, Elisa, Tina, Antonio, Bomben, Simi, Giovanni varii, Roberto e santo cielo non so se ho nominato tutti. Grazie a tutti per youtube, per le serate al rose and crown e tutto il resto. Thanks to all the people in the rob, at the coffee machines or eating outside in the sun, complaining about the Friday meeting and the US food.

And here we come to family and friends, that I am sure will read this part with particular interest. Grazie alla mia famiglia e specialmente ai miei genitori Fiammetta e Stefano che sopportano tutti i miei spostamenti e mi sostengono sempre. Grazie alle amichette Maria, Giulia e Susanna che ci sono sempre, grazie a Kristina-Kenobi, Julie, Paolino. Grazie a tutti quelli che sono venuti a Parigi per la mia tesi.

Merci aux copains de voyage des ces années de thèse à Paris: le kernel Yasmine et Joao (shoukran e muito obrigada!), merci pour être là toujours, pour les bières a Bourg la Reine (c'est juste a coté de La Croix de Berny), pour les mails débiles, pour l'écoute, je vous aime vraiment bien. Merci à Dimitris avec tous ses grecs, à Marcel avec ses chemises, à Clément pour la musique et l'escalade et le ski: c'etait tres beau de partager avec vous le travail, le stress, les soirées, les voyages (parfois). Francesco grazie per le mille chiacchierate e per avermi capita tante volte (e qualche volta anche no!), per le mattine in RER, per titeuf, per ascoltare le mie lamentele, per chiedermi le domande sui tree. Justine, merci pas seulement pour ton aide et soutien psicologique pendant la thèse (fondamental!), merci pour la piscine à SLAC, pour avoir organisé avec moi la fête où la Cenci-dance a eté inventé (tu te rappelles les courses chez cotsco!), pour les voyages qu'on a fait et pour les voyages qu'on va faire. Merci à tous vraiment.

Avant de terminer, je veux remercier en particulier Achille, je le fais en italien, car c'est plus approprié. Achille, è stato un onore lavorare con te, dal punto di vista scientifico e umano. Ti voglio ringraziare per avermi seguita, stimolata con il tuo entusiasmo, la fantasia, le mille idee. Mi hai insegnato a credere nelle cose che faccio e a renderle così appassionanti. Grazie grazie mille.

In summary, the thesis was a very intense, stressing, learning, fun, experiencing period for me, and it was thanks to many people, I hope I have mentioned all of them here.